LIGHT-DRIVEN HYDRIDE TRANSFER FROM IRIDIUM HYDRIDE COMPLEXES

Seth M. Barrett

A dissertation submitted to the faculty at the University of North Carolina at Chapel Hill in partial fulfillment of the requirements for the degree of Doctor of Philosophy in the Department of Chemistry.

Chapel Hill
2016

Approved by:

Alexander J. M. Miller

Cynthia K. Schauer

Maurice S. Brookhart

Michel R. Gagné

Scott C. Warren

ABSTRACT

Seth M. Barrett: Light-Driven Hydride Transfer from Iridium Hydride Complexes
(Under the direction of Alexander J. M. Miller)

Light-triggered hydride transfer is an emerging class of chemical transformations that is increasingly being applied to systems previously promoted with elevated reaction temperatures. The excited state of $[Cp^*Ir(bpy)(H)]^+$ can drive chemical reactivity. The strength of the Ir-H bond can be determined through hydricity in both the ground and excited states to predict reactivity with substrates. Using thermochemical cycles, the excited state hydride is predicted to become a much stronger hydride donor, with nearly a 20 kcal· mol^{-1} enhancement in the experimentally measured excited state hydricity compared to the ground state hydricity. Using $[Cp^*Ir(bpy)(H)]^+$ and 460 nm light, hydride transfer to methylnicotinamide results in the formation of singly and doubly reduced products. Notably, the doubly reduced product is traditionally formed using harsh reaction conditions. Instead, the doubly reduced product can be exclusively formed using visible light.

Moving beyond stoichiometric hydride transfer, $[Cp^*Ir(bpy)(H)]^+$ excited state reactivity can be applied to photocatalytic dehydrogenation of formic acid. By the careful study of a new $[Cp^*Ir(bpy\text{-}OMe)(H)]^+$ photocatalyst, the reaction mechanism can be better understood in order to improve catalytic performance. Deactivation pathways, including light-induced ligand loss, are reduced in order to achieve more than 500 TON of H_2. Additionally, the hydride catalyst is

stable across a wide pH range, promoting the reaction at both acidic and basic pH. Between pH 7 – 11, 96% pure H_2 is collected by trapping evolved CO_2 in solution.

Catalytic hydrodehalogenation of dichloromethane is also promoted using the excited state reactivity of $[Cp^*Ir(bpy)(H)]^+$. A biphasic reaction setup allows for the *in situ* formation of the hydride catalyst, which is irradiated to form chloromethane-d_2. Formate regenerates the active hydride to promote catalytic turnover, with greater than 3 TON of chloromethane. UV-Vis reaction monitoring and kinetic analysis using the method of initial rates determines the hydrodehalogenation to be second order in iridium. A proposed mechanism consistent with this observation is discussed herein. In hydrodehalogenation of dichloromethane, light-induced hydride transfer is harnessed towards another chemical transformation and contributes to a better mechanistic understanding of excited state reactivity.

ACKNOWLEDGEMENTS

I first thank my family for all of their support and encouragement in graduate school and throughout my life. My parents, Mike and Carolyn, my sister Lindsey, my aunts Julia, Bobbi, and Weezie, and my uncle Michael have helped me more than I can ever convey. Thank you. I appreciate you always being there for me.

I must also thank my advisor, Alex Miller, for all his help, support, and knowledge during my time at UNC. I am grateful to you for giving me the chance to work in your lab and to continue my studies at UNC. I have learned so much and accomplished much more than I thought was possible. To Joe Templeton, Cindy Schauer, and Maurice Brookhart: thank you for your encouragement and advice on a variety of issues, I greatly appreciate it.

I finally thank all my friends in the Miller group, at UNC, and beyond. I could not have completed this journey without you. I could not have asked for more welcoming labmates in Andrew, Kate, and Kita upon my arrival to the Miller group. To Javier, Jacob, Brian, Andrew, Ali, Lauren, Kelsey, Matt, and Sam; it has been a pleasure working with you. To my former labmates Rachel, Kathryn, Wave, Joe, Zekai, Chris, Teng, Stephanie, KD, Marcela, and Carter; I greatly value your friendship and wish we had more time together. Cory, Amy, John, Steven, Marsha, Chrissy, Pippa, Dustin, and Doug; thank you for your patience and listening to me rant way too much. I greatly appreciate your friendship and the shenanigans we found ourselves in.

TABLE OF CONTENTS

LIST OF FIGURES

LIST OF TABLES

LIST OF SCHEMES

LIST OF EQUATIONS

LIST OF SYMBOLS AND ABBREVIATIONS

dppe	1,2-bis-(diphenyl-phosphino)ethane)
phen	1,10-phenanthroline
ppy	2-phenylpyridine
tpy	2,2':6'2"-terpyridine
bpy	2,2'-bipyridine
TEMPO	(2,2,6,6-Tetramethylpiperidin-1-yl)oxyl
thbpym	4,4',6,6'-tetrahydroxy-2,2'-bipyrimidine
$AcrH_2$	9,10-dihydro-10-methylacridine
A	Absorbance
Å	Angstrom
OAc	Acetate
HOAc	Acetic acid
K_a	Acid dissociation constant
$AcrH^+$	Acridinium
aq	Aqueous
atm	Atmosphere
BD_4^-	Borodeuteride
BH_4^-	Borohydride
^{11}B	Boron NMR
cal	Calories
^{13}C	Carbon NMR
C-X	Carbon-halide bond

C	Celsius
CV	Cyclic voltammetry
^{o}	Degree
D	Deuterium
DMF	Dimethylformamide
e^-	Electron
ESI	Electrospray ionization
E_{00}	Energy difference between lowest vibration states of ground and excited state
OEt	Ethoxy
K_a*	Excited state acid dissociation constant
E^o	Formal potential
HCO_2^-	Formate
HCO_2H	Formic acid
ΔG_{H+}	Free energy, acidity
$\Delta G_{H\bullet}$	Free energy, homolysis
ΔG_{H-}	Free energy, hydricity
g	Gram
GC	Gas chromatography
$E_{1/2}$	Half wave potential
Hz	Hertz
PF_6^-	Hexafluorophosphate
h	Hour
OH	Hydroxy

Ir-H	Iridium-hydrogen bond
J	Joule
KIE	Kinetic isotope effect
LED	Light emitting diode
hv	Light irradiation
LMCT	Ligand to metal charge transfer
MS	Mass spectrometry
M-H	Metal-hydrogen bond
MLCT	Metal to ligand charge transfer
OMe	Methoxy
MNA^+	Methylnicotinamide
µL	Microliter
mg	Milligram
mL	Milliliter
mM	Millimolar
mmol	Millimole
min	Minute
M	Molar
ε	Molar extinction coefficient
Mol	Mole
nm	Nanometer
NP	Nanoparticle
NADH	Nicotinamide adenine dinucleotide

NMR	Nuclear magnetic resonance
R	Organic subsituent
ppm	Parts per million
Pa	Pascal
Cp*	Pentamethylcyclopentadienyl
^{31}P	Phosphorous NMR
PTFE	Polytetrafluoroethylene
KOH	Potassium hydroxide
^{1}H	Proton NMR
Hpy	Pyridinium
QY	Quantum yield (as a decimal)
•	Radical
s	Second
TBA^{+}	Tetrabutylammonium
TMEDA	Tetramethylethylenendiamine
$HBEt_3^{-}$	Triethylborohydride
TOF	Turnover frequency
TON	Turnover number
OTf^{-}	Triflate
PPh_3	Triphenylphosphine
OTs^{-}	Tosylate
UV	Ultraviolet
Vis	Visible

W	Watt
λ	Wavelength
cm^{-1}	Wavelength, inverse centimeters
λ_{max}	Wavelength maximum
wt%	Weight percent

Chapter 1: TRANSITION METAL COMPLEXES: FROM THERMAL REACTIVITY TO PHOTOCHEMICAL ROUTES

1.1 Introduction to Cp*Ir Reactivity

Transition metal complexes have long been studied for their ability to promote chemical transformations, including hydride transfer, hydrogenation, and dehydrogenation. Pentamethylcyclopentadienyl (Cp*Ir) iridium bipyridine (bpy) complexes have been used to catalyze a variety of chemical transformations since their discovery in 1988 by Ziessel,[1] building upon similar catalysts from Maitlis and Crabtree.[2, 3] The Cp*Ir complexes have been utilized in several transformations, including hydrogenation, [4-17] dehydrogenation,[18-29] and dehalogenation.[30] The reactivity of Cp*Ir catalysts has been attributed to a reactive hydride intermediate.[1, 31-35] Importantly, catalysis has been promoted primarily using thermal methods, but emerging reports of photochemical reactivity motivate the development of new directions while also identifying potential areas for improvement. Specific, prominent examples of these transformations will be explored in more detail below.

Toward hydrogenation using Cp*Ir catalysts, perhaps one of the most highlighted transformations is the conversion of carbonyl functional groups to alcohol groups.[36, 37] Cp*Ir complexes have also been used to promote hydride transfer from biological cofactor nicotinamide adenine dinucleotide (NADH) to pyruvate[38] and quinones[39] in water/methanol solutions. In another example, catalytic hydride transfer has been promoted using an iridium catalyst to an organic acceptor, converting benzaldehyde to benzyl alcohol with up to 91% yield,

using NADH as the hydride donor.[37] Similar reactions performed with sodium formate as the hydrogen source exhibited shorter reaction times. Catalytic transfer hydrogenation was also applied to an array of aldehydes and ketones, with near quantitative yields (up to 99%) for many substrates. Carbonate and CO_2 hydrogenation has also been promoted with Cp*Ir-based complexes,[5-7, 9, 20, 22, 23, 40-47] with up to 222,000 TON and 42,000 h^{-1} TOF using $[Cp^*Ir(phen\text{-}OH)(Cl)]^+$ (phen-OH is 4,7-dihydroxy-1,10-phenanthroline) and $[Cp^*Ir(bpy\text{-}OH)(Cl)]^+$ (bpy-OH is 4,4'-dihydroxy-2,2'-bipyridine) catalysts.[8, 9, 43]

Dehydrogenation reactions have also been catalyzed using Cp*Ir complexes.[18-29] Formic acid dehydrogenation has been reported, where Cp*Ir complexes have been used at elevated temperatures to achieve catalytic turnover.[19] The volume of H_2 and CO_2 gaseous products could be controlled by temperature, with greater performance at high temperatures. The reaction can also be controlled by pH, as more acidic solutions exhibited dramatically improved performance (consistent with the pK_a of formic acid, 3.8). For example, $[Cp^*Ir(bpy\text{-}OH)(OH_2)]^{2+}$ was found to catalyze the dehydrogenation of 1 M formic acid in acidic water (pH 2.5-4).[19]

Hydrodehalogenations are useful synthetic transformations important to selective organic synthesis[48] and decontamination of halogenated species in water sources.[49-60] While hydrodehalogenation activity for other transition metal hydride complexes have been reported, Cp*Ir activity towards hydrodehalogenation has not been well explored. One of the few reports of Cp*Ir-promoted activity includes the hydrodehalogenation of bromo- and chloropropanoic acid substrates in water.

In hydrogenation, dehydrogenation, and hydrodehalogenation reactivity, an *in situ* generated hydride is traditionally proposed as the catalytic intermediate.[7, 11, 30, 61-64] Ogo and Steckhan propose a direct chemical method for hydride formation (Scheme 1.1).[30, 65] Isolation

and structural determination of the hydride was made possible through reaction of the aquo precursor in pH 5 aqueous formic acid to yield the hydride species.[61]

Scheme 1.1 Proposed mechanism of formation for $[Cp^*Ir(bpy)(H)]^+$ through β-hydride elimination and release of CO_2 upon reaction with formate.[30]

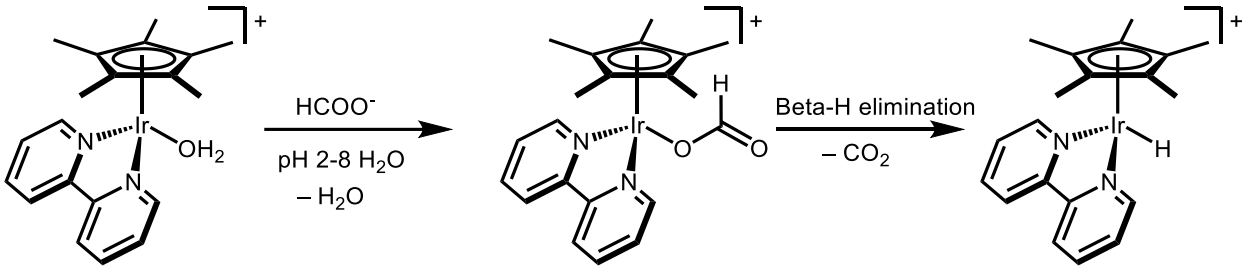

Beyond thermal activity, Cp*Ir complexes have also shown photochemical activity. Photochemical activation typically requires milder conditions and frequently can help prevent side reactions, resulting in cleaner product formation.[66] Enhanced reactivity with visible light has been previously attributed to a MLCT transition to describe the observed photoactivity.[18, 67, 68] The possibility of reactivity through a LMCT has also been discussed.[34] The promising potential of light-driven reactivity was discussed in the $[Cp^*Ir(bpy)(Cl)]^+$ complex's first report, highlighting the photoactivity with small molecules and photosensitizer applications.[1, 67] Light-driven reactivity with Cp*Ir was shown in the photochemical water-gas shift reaction (Equation 1.1).[1, 18, 32, 35] The $[Cp^*Ir(bpy)(Cl)]^+$ precursor, $[Cp^*Ir(phen)(Cl)]^+$ precursor, and $[Cp^*Ir(bpy)(H)]^+$ demonstrated light promoted production of H_2 through the water-gas shift reaction under 1 atm CO.[1] The complexes have also been applied towards photochemical dehydrogenation of formic acid, with up to 53 TON of H_2 after two hours of irradiation.[18] Excited state deprotonation[68] and photoelectrochemical production of H_2[69] have also been shown using Cp*Ir complexes.

$$CO(g) + H_2O(g) \leftrightarrow CO_2(g) + H_2(g) \quad \text{(Equation 1.1)}$$

The versatility of Cp*Ir catalysts towards an array of hydrogenation, dehydrogenation, and hydrodehalogenation reactions combined with known photoactivity of the complexes provides a promising potential for Cp*Ir-catalyzed light-driven transformations. Moving beyond thermal conditions, reactivity with light can provide alternative mechanisms and allow reactions to proceed under mild reaction conditions. The thermochemical aspect of hydride transfer and excited state reactions will be discussed first, followed by more detailed background on two key reactions than can be improved by using photochemical methods: dehydrogenation and hydrodehalogenation.

1.2 Hydricity

In discussing hydride transfer, it is convenient to consider the ability of a compound to donate a hydride to a hydride acceptor species, called hydricity. The particular strength of a species to react and donate a hydride can be measured, quantified, and compared against other hydride donors. This convenient, direct comparison of hydricity values enables the prediction of reactivity between different hydride donor and acceptor species and improves our understanding of hydride transfer reactions. The thermodynamic hydricity values for hydride materials are reported according to the reaction solvent, much like pK_a. Acetonitrile is one of the most commonly used solvents due to enhanced solubility of many transition metal complexes.[70-73]

While Cp*Ir has been used in many hydrogenation and transfer hydrogenation processes that invoke a hydride transfer mechanism, understanding and predicting hydride transfer activity was previously not well understood. Through the construction of thermochemical cycles and measurements of hydricities, hydride transfer reactivity can be understood, predicted, and observed.[74-78] At the basis of Cp*Ir hydride reactivity is hydricity, the thermodynamic strength of

the Ir-H bond that determines whether hydride transfer reactions will proceed. The concept of hydricity is similar to acidity, where hydricity is the thermodynamic value of heterolytic dissociation of a hydride anion from a parent metal complex (Equation 1.2). Also like acidity, the hydricity of a complex changes with solvent.[79, 80] Beyond hydricity and acidity, the third manner of splitting a M-H bond, homolysis, is included below for completeness. Further explanations on modes of metal hydride bond cleavage can be found in the literature.[17, 74, 81]

Hydricity:	$M\text{-}H \rightarrow M^+ + H^-$	ΔG_{H^-}	(Equation 1.2)
Acidity	$M\text{-}H \rightarrow M^- + H^+$	ΔG_{H^+}	(Equation 1.3)
Homolysis	$M\text{-}H \rightarrow M^\bullet + H^\bullet$	$\Delta G_{H^\bullet}$	(Equation 1.4)

There are three common ways to determine the hydricity of a compound in a particular solvent, depending on what information is known or can be obtained for the desired reaction. The potential-pK_a thermochemical cycle (Scheme 1.2) requires the pK_a and redox potential of the complex as well as the two electron reduction of a proton.[82] The derivations and explanations for the potential-pK_a thermochemical cycle are explained in detail in an excellent review by DuBois.[74, 82] Another method to determine hydricity is the relative hydricity from equilibrium (Scheme 1.3), in which a species with a known hydricity is added to a species of unknown hydricity and by determining the equilibrium between the two species, the unknown hydricity can be determined. Finally, hydricity can be calculated by reacting the metal hydride with an acid of a known pK_a (Scheme 1.4). Reactions with a series of acids of varying strengths provide a ballpark value of the hydricity.

Scheme 1.2. Potential-pK_a method to determine hydricity. Adapted from ref.[80]

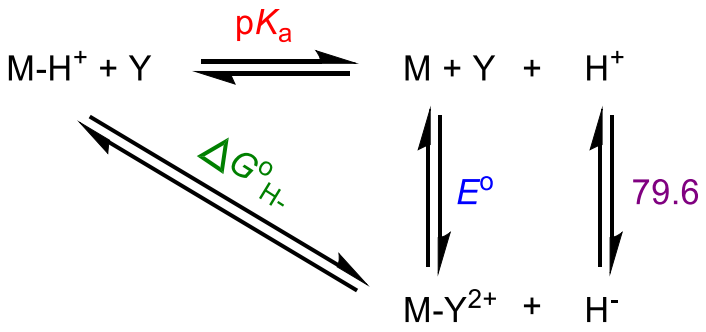

$$\Delta G^{o}_{H-} = (1.37)pK_a - (-46.12)E^{o} + 79.6 \text{ kcal•mol}^{-1}$$

Scheme 1.3. Relative hydricity from equilibrium using a reference hydricity value. Adapted from ref.[80]

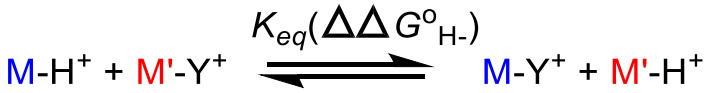

$$\Delta G^{o}_{H-} = (1.37)pKeq + \Delta G^{o}_{H-}$$

Scheme 1.4. Acid reactivity to determine hydricity.

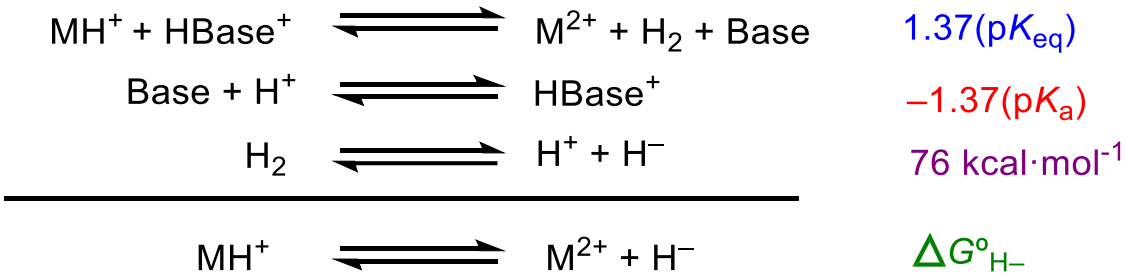

$$\Delta G^{o}_{H-} = -1.37\log(K_{eq}) - 1.37(pK_a) + 76$$

It is also important to consider hydricity in context by establishing a scale of strong and weak hydride donors within a particular solvent. Once the hydricity is determined for a species in a solvent, acetonitrile as a common example, the hydride donor ability can then be compared to other species (transition metals and main groups) of known hydricity values in acetonitrile. The

placement of a compound's hydricity on a scale provides a quick, convenient, and reliable method to predict reactivity between two or more species (Figure 1.1).

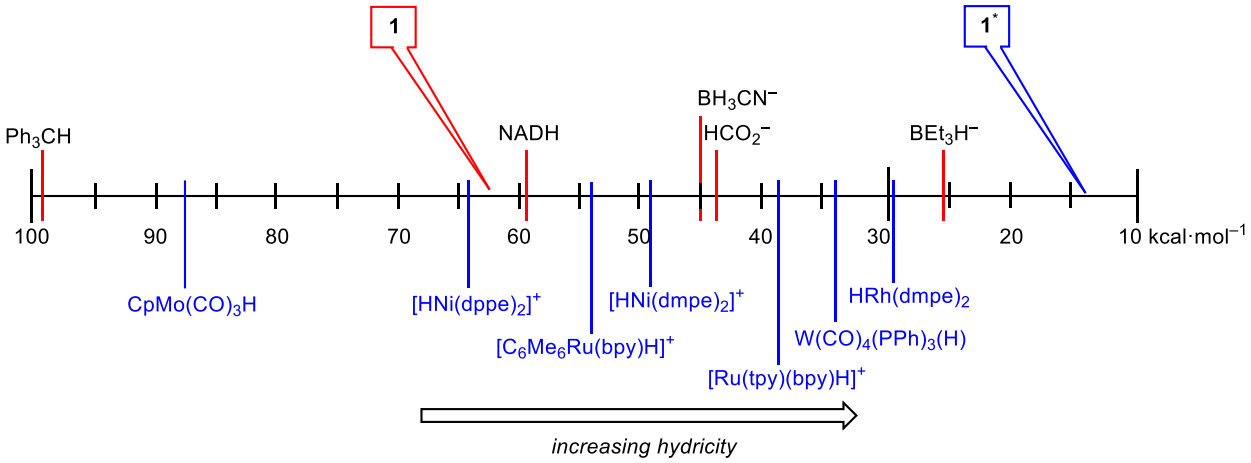

Figure 1.1. Hydricity scale in acetonitrile. Stronger hydride donors are found to the right of the scale.

Hydricities in organic solvents, particularly acetonitrile, are well known. A recent review has compiled over 130 main group hydrides plus several transition metal hydrides into an all-encompassing hydricity scale from 0.5 – 160 kcal/mol in acetonitrile.[83] Less well known, however, are hydricities in water.[81, 84, 85] Many relevant chemical transformations are performed in water, such as H_2 evolution and CO_2 reduction, and rely on aqueous hydride transfer. Gaining a better understanding of aqueous hydricity values has great potential in further improving these transformations. However, one of the most challenging aspects of aqueous hydricity measurements is the water-insolubility of the conjugate base needed for traditional hydricity calculations. Therefore, some aqueous hydricities have been determined via a challenging equilibrium method (Scheme 1.5).

Scheme 1.5. Aqueous hydricity determination through equilibrium in water.[81]

$$Ru(H_2O)^{2+} + HCO_2^- \underset{k_{-A}}{\overset{k_A}{\rightleftharpoons}} Ru(HCO_2)^+ \underset{k_{-B}}{\overset{k_B}{\rightleftharpoons}} RuH^+ + CO_2$$

$$K_{AB} = \frac{[RuH^+][CO_2]}{[Ru(H_2O)^{2+}][HCO_2^-]} = K_A K_B = \frac{k_A k_B}{k_{-A} k_{-B}}$$

Recently, however, the Miller lab has developed a new method to measure aqueous hydricities.[80] Rather than relying on the potential-pK_a method for all hydride species, many of which have insoluble conjugate bases in water, instead a reference hydride that is well behaved in water is first studied using the potential-pK_a method. All other hydricities are determined relative to this reference hydricity. In addition to nearly doubling the known hydricity values in the literature, the report also shows how the hydride donating ability of a species can be tuned not only by substituent effects but also by the reaction solvent.

The hydricity calculations shown above, however, do not account for changes in excited state reactivity. Photochemical methods, previewed above and described in additional detail later in this chapter, require a new series of thermochemical equations to determine the excited state hydricity (Scheme 1.6). While at first glance, the thermochemical equations seem very similar to the ground state hydricity equations (Scheme 1.2), the one key difference between the two schemes is the excited state deprotonation, pK_a*, step in the excited state hydricity equation. The pK_a* value can be determined from the ground state pK_a and E_{00}, the energy difference between the lowest vibrational states of the ground and excited state species. Additional information on the derivation of these thermochemical equations, as well as experimental data matching predicted reactivity from the use of these equations, is presented in Chapter 2.

Scheme 1.6. Thermochemical cycles for determination of excited state hydricity.

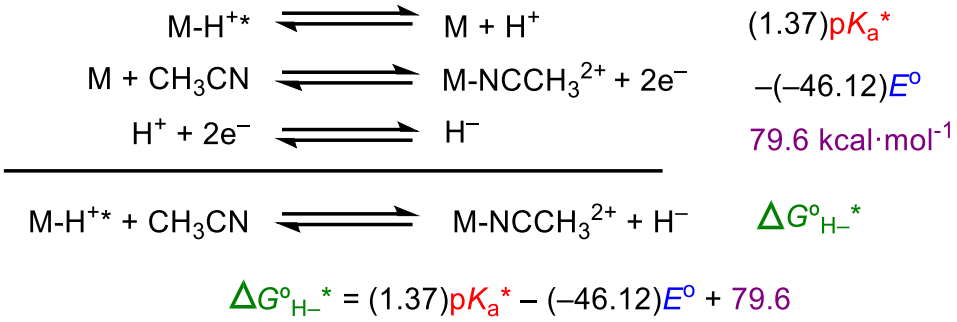

$$\Delta G^{\circ}_{H^-}{}^{*} = (1.37)pK_a{}^{*} - (-46.12)E^{\circ} + 79.6$$

1.3 Formic Acid Dehydrogenation

Utilizing hydricity, hydride transfer reactivity towards organic substrates can be predicted and tested experimentally. From the hydricity scale in Figure 1.1, $[Cp^*Ir(bpy)(H)]^+$ (**1**) in the ground state is not predicted to promote hydride transfer to formic acid, as formic acid is anticipated to be the stronger hydride donor. However, the excited state of the complex, **1***, becomes much more hydridic (a stronger hydride donor) upon irradiation and is thermodynamically capable of hydride transfer to formic acid to release H_2. Importantly, formic acid dehydrogenation coupled with CO_2 hydrogenation (both shown to be catalyzed by Cp*Ir complexes) can be employed to reversibly produce and store H_2.

CO_2 is considered a promising H_2 storage material capable of storing 4.3 wt% H_2 in formic acid and 12 wt% H_2 in methanol and water.[86-90] In supporting a hydrogen-fueled economy, challenges in hydrogen storage and transportation must be addressed. Towards hydrogen's low energy density and transportation difficulties in gas form, storage issues and potential explosion hazards must be overcome.[86] Hydrogen storage materials have been heavily studied in recent years, applying physical and materials-based strategies to store hydrogen more efficiently in liquid or solid materials. The Department of Energy has set forth a series of hydrogen storage targets to encourage development of these storage materials (Figure 1.2).[91]

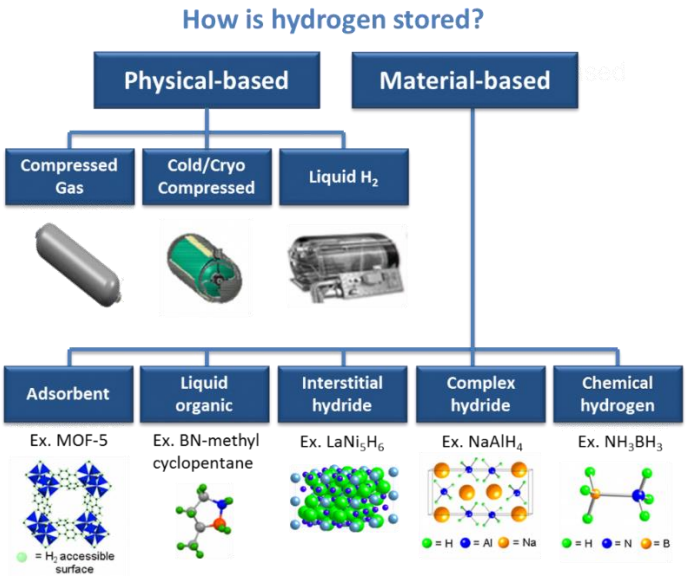

Figure 1.2. DOE strategies towards physical and materials-based hydrogen storage materials.[91]

In chemical-based solutions, H_2 can be stored in a liquid and can be activated and released from the solvent when desired. As a chemical-based solution to hydrogen storage, formate can be used to reversibly produce hydrogen by undergoing dehydrogenation to give bicarbonate and to store hydrogen by the hydrogenation of bicarbonate in solution (Equation 1.5).[86]

$$HCO_2^- + H_2O \leftrightarrow HCO_3^- + H_2 \qquad \text{(Equation 1.5)}$$

The reverse reaction, hydrogenation of bicarbonate, can be promoted to utilize formic acid as a hydrogen storage material (Scheme 1.7).

Scheme 1.7. Reversible H_2 storage using the formate/bicarbonate couple for storage and production of H_2. Adapted from ref.[86]

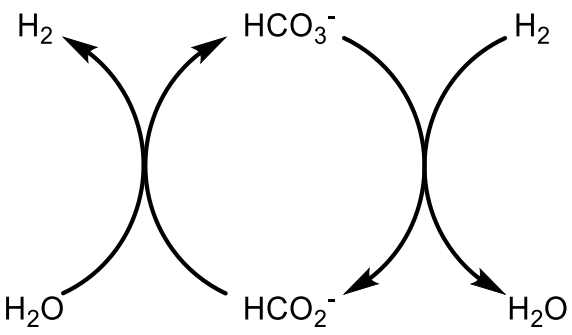

1.3.1 Thermal Formic Acid Dehydrogenation and Carbonate Hydrogenation

Taking inspiration from this H_2-producing strategy with formic acid, Cp*Ir has been shown to both hydrogenate bicarbonate/CO_2[5-7, 9, 20, 22, 23, 40-47] and dehydrogenate formic acid. [18-29] Several examples of thermal formic acid dehydrogenation and carbonate hydrogenation can be found below, with temperature, pH, and pressure modulating reactivity.

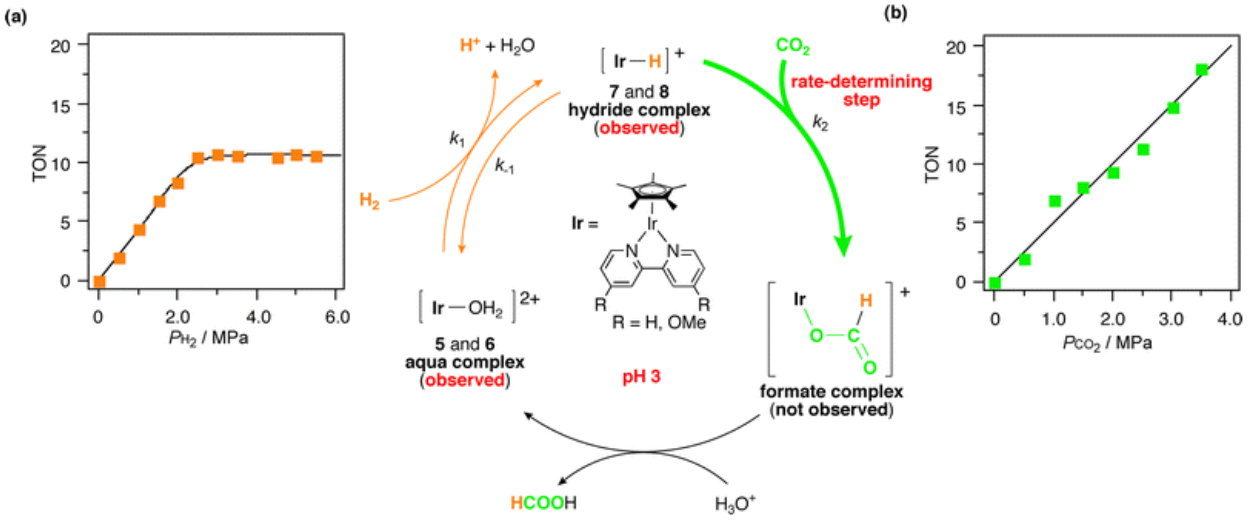

Figure 1.3. Mechanistic study with $[Cp^*Ir(bpy\text{-}R)(OH_2)]^{2+}$ precatalyst under varying H_2 and CO_2 pressures. The *in situ* generated hydride was observed and the following carboxylation step was determined to be rate limiting.[7]

Iridium aquo precatalysts have been studied for the hydrogenation of CO_2.[7] Iridium catalysts, $[Cp^*Ir(bpy\text{-}R)(OH_2)]^{2+}$, where R = bpy and bpy-OMe), were used under acidic aqueous conditions at 40°C under varying H_2 and CO_2 pressures in pH 3 citrate buffer solution to achieve CO_2 hydrogenation. In mechanistic studies, increasing H_2 pressures gave saturation behavior in TON while increasing CO_2 pressures gave a linear relationship in TON (Figure 1.3). This linear relationship between CO_2 pressure and TON, as well as the observation and isolation of the hydride intermediate, illustrated that the next step, carboxylation leading to the formation of the formato complex (not observed), must be the rate determining step.

In another report, the Cp*Ir complex (and an analogous Cp*Rh complex) containing a 1,10-phenanthroline ligand was shown to catalyze CO_2 hydrogenation.[5] The 4,7-dihydroxy substituted phen ligand was also tested for catalytic activity, with significant enhancements in performance noted. At 120°C under 6 MPa of H_2:CO_2 pressure in degassed 1 M aqueous KOH solution for 10 hours, the iridium catalyst exhibited the greatest performance with up to 21,000 TON and 23,000 h^{-1} TOF (over the initial 20 min). No induction period was required, nor was CO observed as a reaction byproduct. The dihydroxy ligand, especially upon deprotonation, was a much better catalyst thanks to its strong electron donating ability and enhanced water solubility (Scheme 1.8). A later article and microreview detailed even higher activity, with up to 222,000 TON and 42,000 h^{-1} TOF using Ir phen and bpy catalysts.[8, 9, 43]

Scheme 1.8. Cp*Ir and Rh catalysts towards CO_2 hydrogenation. Adapted from ref.[5]

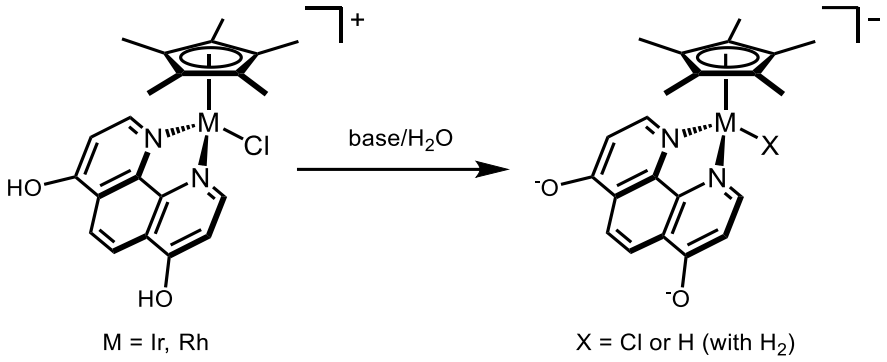

The thermal activity of Cp*Ir can be used to promote the reverse reaction, formic acid dehydrogenation. $[Cp^*Ir(bpy\text{-}OH)(H_2O)]^{2+}$ was used in 2 M aqueous formic acid at temperatures varying from 40-90°C.[19] The volume of H_2 and CO_2 gaseous products could be controlled by temperature, with high temperature 90°C reactions yielding the highest performance, with up to 14000 h^{-1} TOF. This study also illustrated the importance of pH on the thermal formic acid dehydrogenation (Figure 1.4a), as more acidic solutions exhibited dramatically improved performance (consistent with the pK_a of formic acid). The reaction is dependent upon the protonation state of the acid, with the acid form being more reactive. The importance of formic acid concentration was also demonstrated (Figure 1.4b), with activity increasing up to 4 M formate and decreasing quickly at higher formate concentrations. In the Miller lab, we have also observed this lower performance beyond 4 M formate, with solubility of the iridium catalysts becoming troublesome with high formate concentrations.[27]

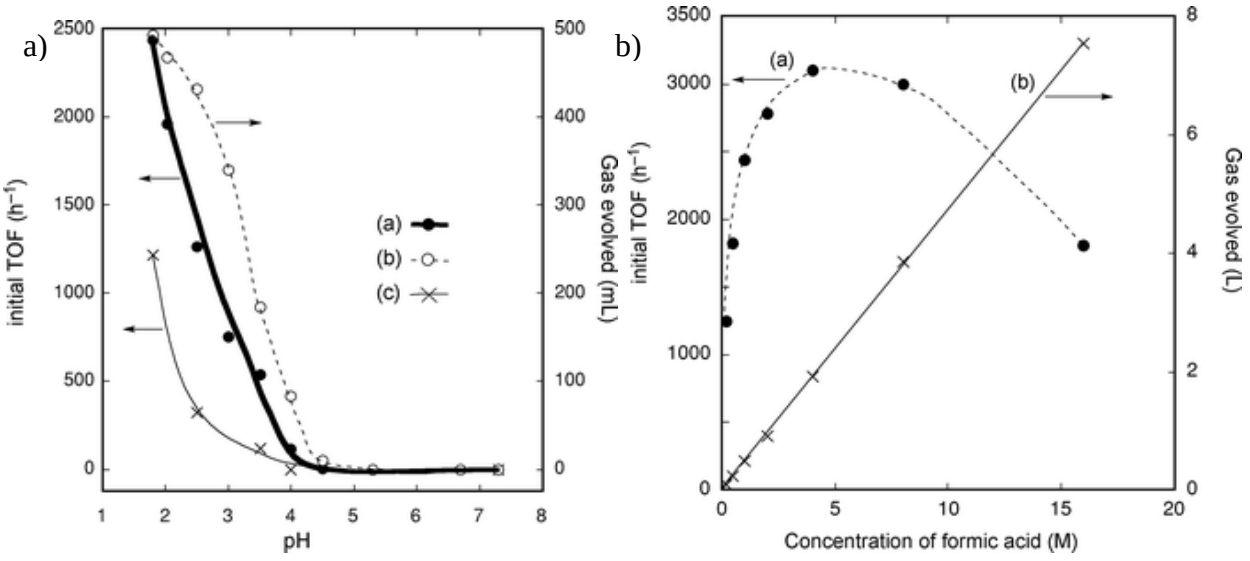

Figure 1.4. a) Effect of pH and b) formic acid concentration on catalytic activity for thermal formic acid dehydrogenation.[19]

Combining insights from Cp*Ir-promoted hydrogenation of CO_2 and dehydrogenation of formic acid, both hydrogenation and dehydrogenation can be promoted with the same catalyst.[20, 22, 23, 92-95] However, the pH of the solution and the headspace gas of the reaction are changed in order to promote the desired reaction. $[Cp^*Ir(bpy\text{-}OH)(OH_2)]^{2+}$ catalyzed the hydrogenation of CO_2 under basic pH (1 M KOH) at 80°C using a 1 MPa H_2/CO_2 headspace.[20] The aquo precatalyst catalyzed the dehydrogenation of 1 M formic acid under acid pH (2.5-4).[19] Using a Ru catalyst, consecutive bicarbonate hydrogenation and formate dehydrogenation was achieved.[93] While the same catalyst was used for both reactions, the headspace and solvent were removed in between the two experiments. Another Ru catalyst was utilized in a similar manner, with release of the headspace pressure triggering formate decomposition.[92] Using $[(Cp^*IrCl)_2(thbpym)]^{2+}$, where thbpym is 4,4',6,6'-tetrahydroxy-2,2'-bipyrimidine, as a precatalyst (Figure 1.5), a truly reversible system was reported with the stepwise consumption of H_2 through hydrogenation of bicarbonate followed immediately by production of H_2 through dehydrogenation of formic acid.[22] The catalyst was evaluated in 2 M $KHCO_3$ under a continuous

flow of 1:1 H_2/CO_2 at atmospheric pressure for 136 h. The reaction was then cooled and pH adjusted to 1.7 using 4 M sulfuric acid to protonate the catalyst to form $[(Cp^*IrOH_2)_2(thbpym)]^{4+}$. The solution was slowly warmed to 50°C, promoting dehydrogenation activity. No CO by-product was detected. The cycle was repeated once more, cooling the reaction and adjusting the pH with $KHCO_3$. The recyclability and reversibility of this system is the first of its kind (Table 1.1).

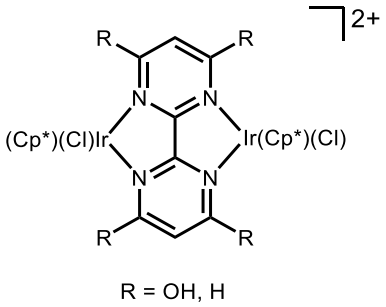

Figure 1.5. Precatalyst $[(Cp^*IrCl)_2(thbpym)]^{2+}$ towards reversible formic acid dehydrogenation.

Table 1.1. $[(Cp^*IrCl)_2(thbpym)]^{2+}$ precatalyst and recyclability towards CO_2 hydrogenation and formic acid dehydrogenation, demonstrated by concertation of formate and formic acid. Adapted from ref.[22]

Cycle	Hydrogenation of CO_2		Dehydrogenation of formic acid		
	Time (h)	Generated formate (M)	Time (h)	Gas Produced (MPa)	Formic acid remaining (M)
1	136	0.48	8	2.34	0.017
2	182	0.38	8	1.93	0.024

A similarly reversible systems for carbonate hydrogenation and formic acid dehydrogenation was reported using a Ru catalyst.[95] To drive hydrogenation, the system was placed under 140 bar H_2 gas. After heating and hydrogenation, the pressure dropped to 100 bar. The reaction vessel was then cooled to room temperature and the atmosphere was flushed with N_2 gas. The vessel was once again heated and the catalyst then coverts the formic acid to H_2.

This hydrogenation and dehydrogenation cycle could be repeated for 5 cycles. While this recyclable example works well and efficiently, we desired similar recyclability without having to depressurize the system.

1.3.2 Photochemical Formic Acid Dehydrogenation

We wanted to promote this reversible reactivity without altering reaction conditions, including solution pH and vessel pressure. One way of doing this is to take advantage of Cp*Ir's known thermal reactivity towards the hydrogenation of CO_2 in the dark, as shown in examples above, while promoting the reverse reaction, dehydrogenation of formic acid, using light. (Scheme 1.9) In this manner, we can regulate reactivity without chemical additives by instead using light as a reactivity switch. Furthermore, unlike thermal activity, light-driven dehydrogenation is not limited to acid pH near the pK_a of formic acid. By taking advantage of photochemical reactivity, the pH limitations from thermal methods can be overcome, improving the dehydrogenation process. Beyond significantly widening reaction conditions under both acidic and basic pH ranges, this important change also allows for the trapping of evolved CO_2 as bicarbonate in aqueous solution, yielding pure H_2

Scheme 1.9. Hydrogenation of CO_2 (bicarbonate) can be promoted using Cp*Ir in the dark, storing H_2, while dehydrogenation of formic acid can be promoted with light.

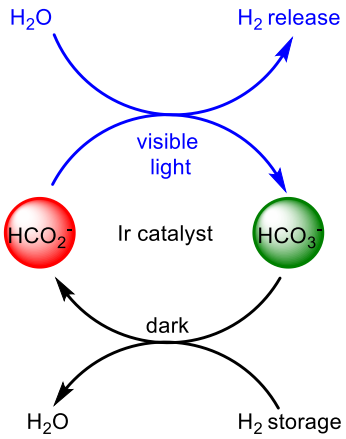

Photochemical formic acid dehydrogenation has been shown in the literature. An early report of photochemical formic acid dehydrogenation used a $[Co^{I}H(PPh(OEt)_2)_4]$ precatalyst in THF to photocatalytically produce H_2 and CO_2 gaseous products using a 400W mercury lamp.[96] The *in situ* generated $Co^{III}H_2(PPh(OEt)_2)_4]^+$ was determined to be the active catalyst. In another early report, a chromium carbonyl species was also used for photochemical formic acid dehydrogenation.[97] The $Cr(CO)_6$ species was used as a precatalyst to generate a $[Cr(CO)_5][HCO_2]$ intermediate, bicarbonate, and H_2 using a 100 W mercury lamp. More recently, Beller and coworkers have shown a $[RuCl_2(benzene)_2]$/dppe (where dppe = 1,2-bis-(diphenyl-phosphino)ethane) catalyst that is capable of higher formic acid dehydrogenation activity, with TON up to 2800 using a xenon-arc lamp with 380 nm and Ir cutoff filters.[98] Notably, this system exhibited nearly double the activity of the best non-light promoted system of the time. Beller next applied this photochemical on and off switch to an earth abundant Fe catalyst.[99] The triirondodecacarbonyl catalyst, $Fe_3(CO)_{12}$, was found to be the best catalyst; in the presence of triphenylphosphine (PPh_3), tpy (2,2':6'2"-terpyridine) and DMF at 60^{o}C under xenon-arc lamp irradiation. Up to 126 TON of H_2 was achieved, the highest activity of a nonprecious metal based system.

In one example, Ziessel reports the dehydrogenation of aqueous formate using Cp*Ir catalysts with up to 53 TON of H_2 after two hours of irradiation.[18] Several Cp*Ir(bpy) and (tpy) complexes were evaluated for activity towards photochemical formic acid dehydrogenation using a 250 W halogen lamp. Initial formic acid dehydrogenation activity was probed using a series of substituted bpy and phen ligands to gauge substituent effects on photochemical reactivity. At the time of the report, formic acid dehydrogenation was only performed using temperatures above 100^{o}C.[100-103] Iridium chloride precursor was used as a precatalyst, generating the reactive and

photoactive hydride intermediate upon addition to aqueous sodium formate. Using a NMe_2 substituted $[Cp^*Ir(bpy\text{-}R)(Cl)]^+$ complex, the best activity was achieved; irradiation over two hours yielded up to 53 TON of H_2 (159 maximum TON over longer irradiation times), yielding H_2 and CO_2 in a 1:1 ratio (Scheme 1.10)

Scheme 1.10. Photochemical dehydrogenation of formic acid using $[Cp^*Ir(bpy\text{-}R)(Cl)]^+$ precatalysts and visible light. R = COOH, NO_2, NMe_2.

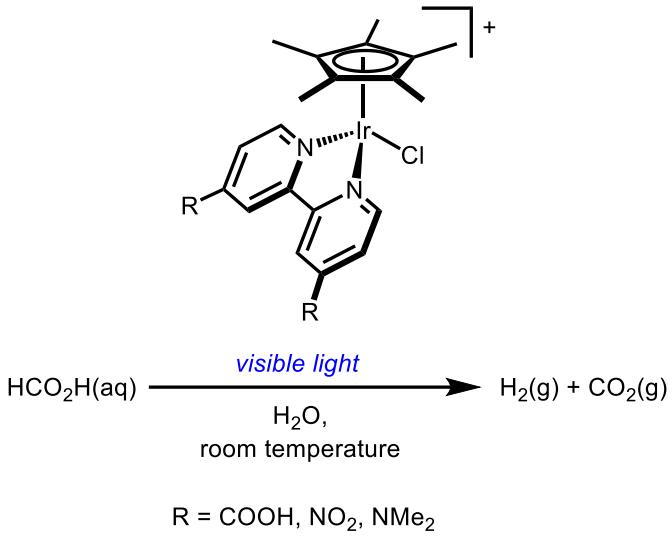

Kinetic studies were performed on the system in order to gain a mechanistic understanding of the observed photochemical reactivity. Activation energies for the dehydrogenation of formic acid (46.3 and 39.3 $kJ \cdot mol^{-1}$ for R = NO_2 and NMe_2 respectively) were found to be much higher than those determined for the photochemical water-gas shift reaction (14.6 $kJ \cdot mol^{-1}$)[32] but were dramatically lower than those determined for thermal formic acid decomposition (146 $kJ \cdot mol^{-1}$).[104, 105]

Traditionally, catalysts for photochemical formic acid dehydrogenation are thought to be slow and less stable than thermal catalysts.[89, 106, 107] However, deeper mechanistic understanding of these light-driven systems shows great potential for substantially improving catalytic activity. For example, the initial iron carbonyl catalyst described above was found to be active towards

light-driven dehydrogenation,[99] but dissociation of CO quickly deactivated the catalyst. Addition of surrounding phosphine ligands dramatically improved (by an order of magnitude) activity and reduced deactivation pathways in photochemical formic acid dehydrogenation.[108] Deeper mechanistic understanding of photochemical formic acid dehydrogenation provides helpful guidance in improving systems to offer a promising mild alternative to reversible hydrogen storage reactions controlled by changes in pressure or pH. In the Miller lab, we have carefully studied the mechanism of photochemical formic acid dehydrogenation to achieve significant improvements in catalytic activity, with greater than 500 TON of H_2.[27] Approaches to these mechanistic studies, including identifying and shutting down deactivation pathways, are described in Chapter 3.

1.4 Hydrodehalogenation Reactions

In addition to formic acid dehydrogenation, hydride transfer reactivity can be utilized in hydrodehalogenation reactions. Dehalogenation reactions have been the focus of many recent studies due to their application in selective organic synthesis[48] and in the decontamination of halogenated pollutants in water.[49-60] Dehalogenations (Scheme 1.11) have also been invoked in biological applications, where bacteria have been found to promote dehalogenation of halogenated substrates.[109]

Scheme 1.11. General hydrodehalogenation scheme with aromatic and aliphatic substrates.

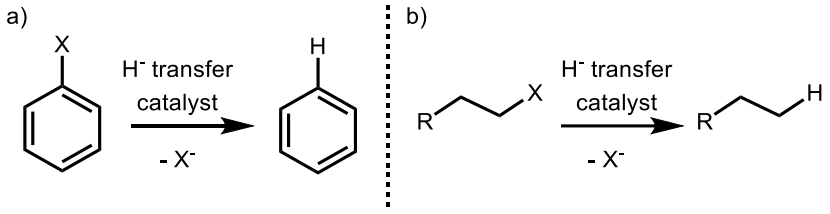

Several plausible mechanisms for hydrodehalogenation have been invoked using different substrates and hydride sources. Oxidative or reductive quenching pathways have been

proposed,[110, 111] while other systems invoke hydride transfer mechanism to aromatic, aliphatic, and allylic substrates from a metal or metalloid hydride.[49, 112-118] From these metal and metalloid hydrides, there are several different mechanisms that have been proposed, including radical chain mechanisms, nucleophilic attack, and direct hydridic attack.[114, 119-121]

1.4.1 Thermal Hydrodehalogenation.

Several transition metal hydride species have been reported to catalyze hydrodehalogenation. However, only one report utilizes Cp*Ir complexes to promote catalysis. Hydrodehalogenation has been shown using a $[Cp^*Ir(bpy)(OH_2)]^{2+}$ complex and three water soluble alkyl halides using formic acid as a hydrogen donor.[30] Using 2-bromopropanoic acid, 2-chloropropanoic acid, and 3-bromopropanoic acid at room temperature, the catalyst promotes up to 9 turnovers of propanoic acid after 6 hours. The transformation is proposed to proceed through an S_N2 mechanism, where the generated $[Cp^*Ir(bpy)(H)]^+$ species forms a bound transition state species with the halogenated substrate, prior to hydride transfer and the breaking of the C-X bond of the substrate (Scheme 1.12). The dehalogenation is pH-dependent, with the highest activities achieved at pH 5. KIE experiments confirm deuterium incorporation into the dehalogenated product when using deuterated formic acid as the hydrogen donor to form the active iridium hydride (deuteride) catalyst.

Scheme 1.12. Proposed transition state of the hydrodehalogenation of 2-bromopropanoic acid using $[Cp^*Ir(bpy)(H)]^+$. Adapted from ref.[30]

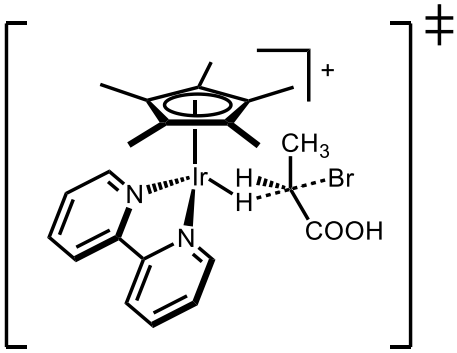

Other transition metal hydrides have been used for hydrodehalogenation. Using $Cp^*_2ZrH_2$, a radical chain mechanism was proposed for aliphatic substrates, while aryl substrates exhibited direct hydridic attack from the metal hydride to the aromatic ring.[114] In aliphatic hydrodehalogenation, fluorohexane was used with the zirconium complex to produce hexane and Cp^*_2ZrHF. Sodium and naphthalene were added to initiate the radical reaction, allowing the reaction to proceed three times faster than the rate without the radical initiators. Strong evidence for the proposed radical mechanism was made possible through reaction with cyclopropylcarbinyl fluoride (Scheme 1.13). The cyclopropylcarbinyl radical undergoes irreversible ring-opening to form the butenyl radical if radicals are present in a reaction.[122] After 15 minutes, Cp^*_2ZrHF and Cp^*_2Zr(n-butyl)H were observed in the reaction. No methylcyclopropane was detected. These observations support a mechanism where a fluorine radical is abstracted by the $Cp^*_2ZrH^{\bullet}$ to form the cyclopropylcarbinyl radical and Cp^*_2ZrHF. The cyclopropylcarbinyl radical quickly undergoes ring opening to form the butenyl radical which abstracts a hydrogen atom from $Cp^*_2ZrH_2$ to propagate the radical chain. Butene then inserts into a second equivalent of $Cp^*_2ZrH_2$ to form the zirconium butyl hydride complex.

Scheme 1.13. Proposed radical chain mechanism for the hydrodehalogenation of aliphatic substrates using $Cp^*_2ZrH_2$. Adapted from ref.[114]

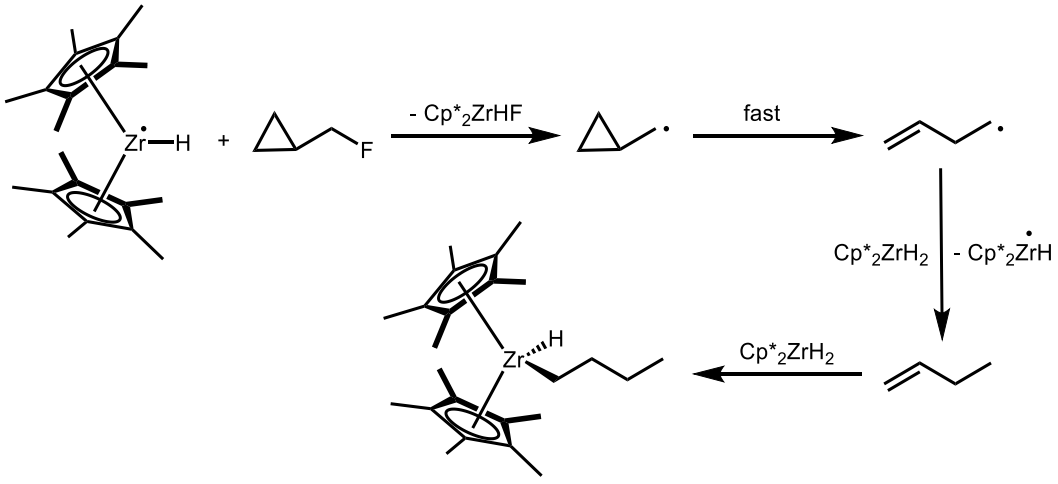

In aromatic hydrodehalogenation, fluorobenzene was used with the zirconium complex to produce benzene, Cp^*_2ZrHF, and $Cp^*_2Zr(C_6H_5)F$. The reaction was not inhibited with radical traps 9,10-dihydroanthracene or triphenylmethane. Furthermore, the reaction was not promoted with sodium or naphthalene radical initiators. Therefore, the aromatic hydrodehalogenation activity is best described as a direct nucleophilic attack by hydride on the aromatic ring, an S_NAr mechanism. Fluoride can then be abstracted by the zirconium complex to form the benzene product (Scheme 1.14).

Scheme 1.14. Proposed direct hydridic attach mechanism for the hydrodehalogenation of aromatic substrates using $Cp^*_2ZrH_2$. Adapted from ref.[114]

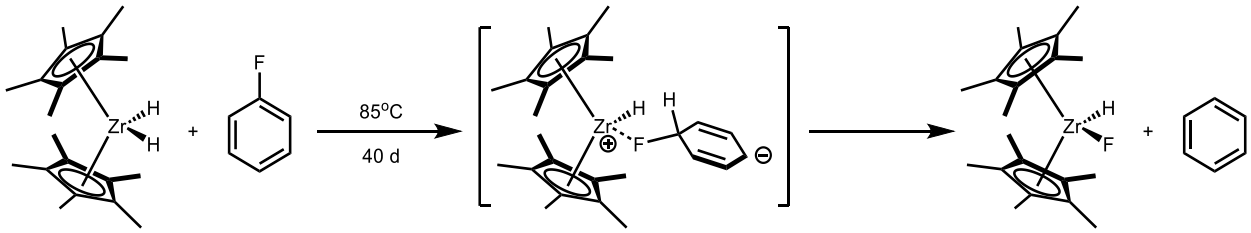

Another mechanistic study was provided using nickel as the transition metal catalyst to a series of geminal dihalide substrates.[123] As shown in Schemce 1.15, the system utilizes two different oxidation states of the nickel pincer catalyst, as the Ni^I and Ni^{II}-H complexes. A Ni^I complex was prepared to serve as a halogen atom abstractor from the geminal dihalide, generating a Ni^{II}-Cl complex and a radical halide. The radical halide can then reversibly coordinate to the generated Ni^{II}-Cl. Finally, the radical is trapped by the Ni^{II}-H complex, which undergoes H atom transfer to the radical species (Scheme 1.15).

Scheme 1.15. Proposed reaction scheme for the hydrodehalogenation of geminal dihalides using a Ni^{I}/Ni^{II}-H catalyst combination. Adapted from ref.[123]

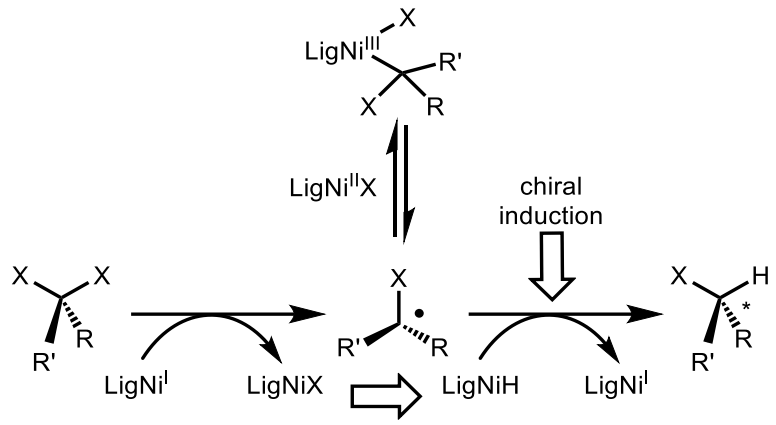

Supporting this proposed mechanism, addition of TEMPO radical trap immediately halted product formation. Bromomethylcyclopropane, known to ring open under radical conditions, was added to the Ni^{I} complex, resulting in the formation of a Ni-Br complex and bound n-butene (Scheme 1.16). In another experiment, $LiEt_3BH$ was added to a labeled Ni-D complex to test the isotopic composition of the hydrodehalogenation product by determining the source of the hydrogen atom (Scheme 1.17). Incorporation of deuterium in the product was clearly observed, suggesting the Ni^{II}-D complex is the hydrogen atom source for the reaction.

Scheme 1.16. Bromomethylcyclopropane radical test for the hydrodehalogenation of geminal dihalides using a Ni^{I}/Ni^{II}-H catalyst combination yields bound n-butene and the Ni-Br complex. Adapted from ref.[123]

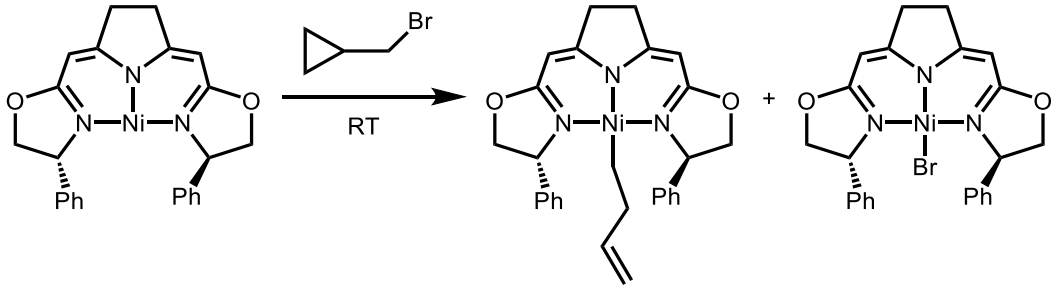

Scheme 1.17. Deuterium incorporation test to determine the hydrogen source in the hydrodehalogenation reaction. Adapted from ref.[123]

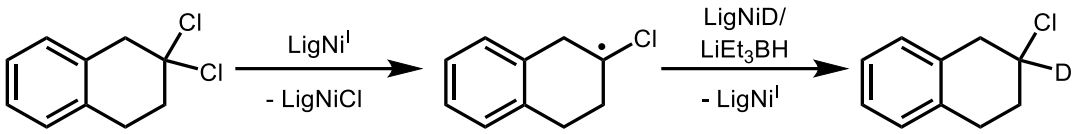

1.4.2 Photochemical Hydrodehalogenation.

Instead of promoting hydrodehalogenation under harsh conditions with strong oxidants or reductants, we wanted to see if photochemical hydrodehalogenation activity could be achieved using Cp*Ir complexes. Under mild reaction conditions, direct light-triggered hydride transfer has the potential to promote hydrodehalogenation more cleanly, and without the need for radical initiators or multiple catalysts in the same reaction. There have been no reports of Cp*Ir reactivity towards photochemical hydrodehalogenation, but several reports of photoredox catalysis using iridium photosensitizing complexes have been shown to promote the reaction.

In recent years, photoredox catalysis has been used to achieve photo-assisted dehalogenation transformations.[48, 124, 125] Ru and Ir based polypyridyl complexes have been utilized as photoredox catalysts for atom transfer radical addition reactions. While many organic molecules lack visible light absorption properties, a separate visible light absorbing photocatalyst can be used as a photosensitizer for the organic substrates to promote the desired chemical transformation. $Ru(bpy)_3Cl_2$ is often used as the photosensitizer, thanks to its well-known photochemical properties, straightforward synthesis, and commercial availability.

$Ru(bpy)_3^{2+}$ photocatalyst, 9,10-dihydro-10-methylacridine ($AcrH_2$) electron donor, and phenacyl halide electron acceptor substrate was used by Fukuzumi in a dehalogenation scheme using 452 nm light.[110] The excitation of $Ru(bpy)_3^{2+}$ generates $AcrH^+$ and acetophenone, serving as the photosensitizer towards the photoreduction of phenacyl bromide by the electron donor, $AcrH_2$. A reaction scheme is depicted below in Scheme 1.18. The reaction mechanism was

carefully studied in the absence and presence of a Bronsted acid, $HClO_4$. In the absence of $HClO_4$, a reductive quenching pathway is proposed (Scheme 1.19), where the excited state $Ru(bpy)_3^{2+}$* is quenched by electron transfer from $AcrH_2$ to produce the ground state $Ru(bpy)_3^{+}$ and $AcrH_2^{\bullet+}$. The generated $Ru(bpy)_3^{+}$, a strong reductant, readily reduces the phenacyl bromide to yield acetophenone and regenerate $Ru(bpy)_3^{2+}$.

Scheme 1.18. Hydrodehalogenation of phenacyl bromide using $AcrH_2$ electron donor, $Ru(bpy)_3^{2+}$ photosensitizer, and 452 nm light. Adapted from ref.[110]

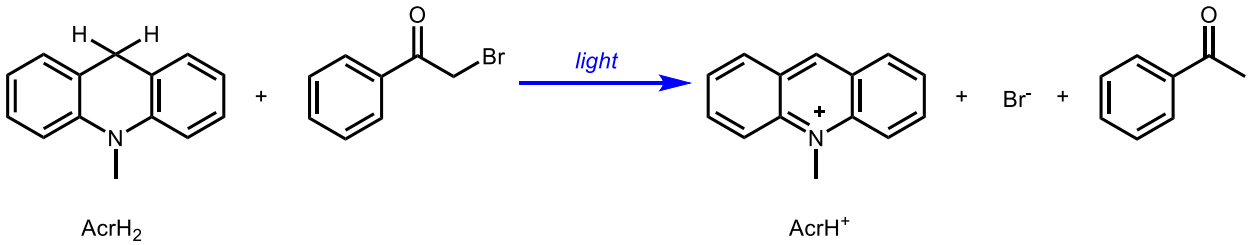

Scheme 1.19. Reductive quenching mechanism for the hydrodehalogenation of phenacyl halide in the absence of $HClO_4$. Adapted from ref.[110]

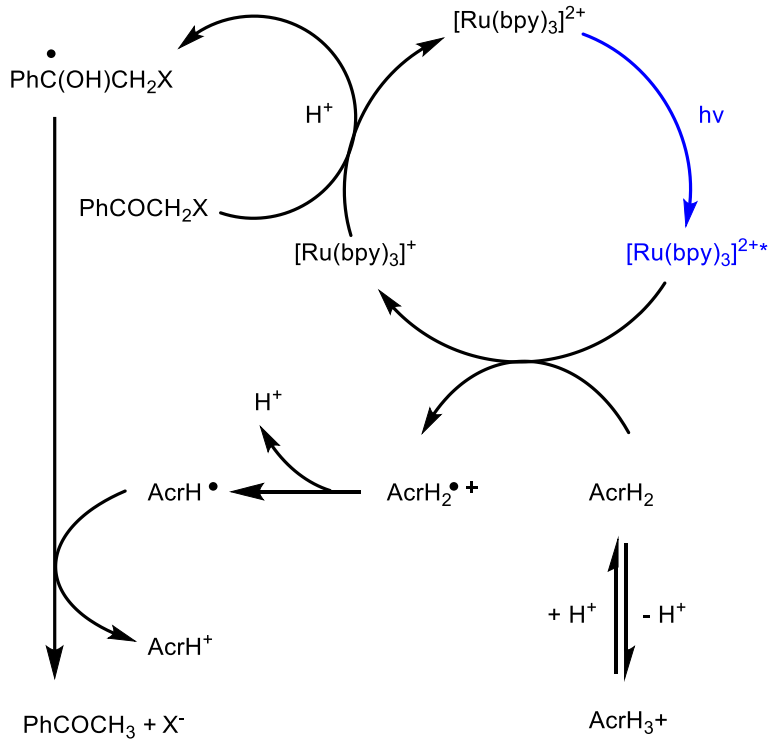

Alternatively, an oxidative quenching mechanism is proposed in the presence of $HClO_4$. (Scheme 1.20). With high acid concentrations, the rate of reductive quenching of $Ru(bpy)_3^{2+}$* by $AcrH_2$ decreases, and the oxidative quenching of $Ru(bpy)_3^{2+}$* becomes the predominant pathway. The phenacyl halide oxidizes the excited state complex to $Ru(bpy)_3^{3+}$, a very strong oxidant that can oxidize $AcrH_2$ even in the presence of acid to produce $AcrH_2^{\bullet+}$ and regenerate $Ru(bpy)_3^{2+}$. $AcrH_2^{\bullet+}$ then deprotonates and reacts with the $PhC^{\bullet}(OH)CH_2X$ to yield the dehalogenated product.

Scheme 1.20. Oxidative quenching mechanism for the hydrodehalogenation of phenacyl halide in the presence of $HClO_4$. Adapted from ref.[110]

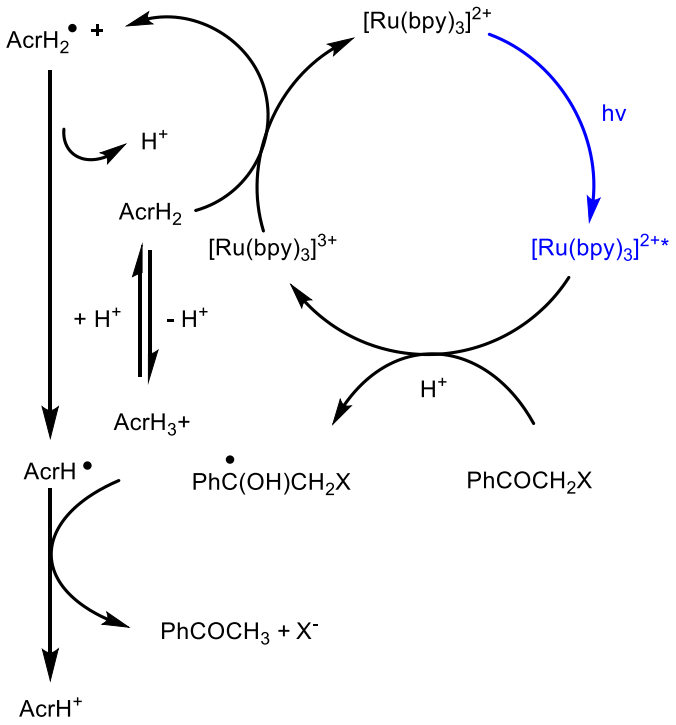

By varying reaction conditions, Fukuzumi was able to control the reaction pathway by modulating the photoredox events. Building upon this idea, Stephenson has applied photoredox dehalogenation to a broad scope of halogenated reagents, including α-halides to carbonyls and utilizing aryl groups or electron withdrawing groups (Scheme 1.21).[111] Similar to Fukuzumi's

report, the reaction mechanism is proposed to go through a reductive quenching of the excited $Ru(bpy)_3^{2+}$* to $Ru(bpy)_3^{+}$ followed by electron transfer to a C-X bond alpha to the electron withdrawing substituent. The alkyl radical is reduced through hydrogen abstraction from formic acid or from the electron donor, $^{i}Pr_2NEt$ (Scheme 1.22).

Scheme 1.21. Photoredox catalysis towards hydrodehalogenation for a variety of α-halides to carbonyls or aryl groups. Adapted from ref.[111]

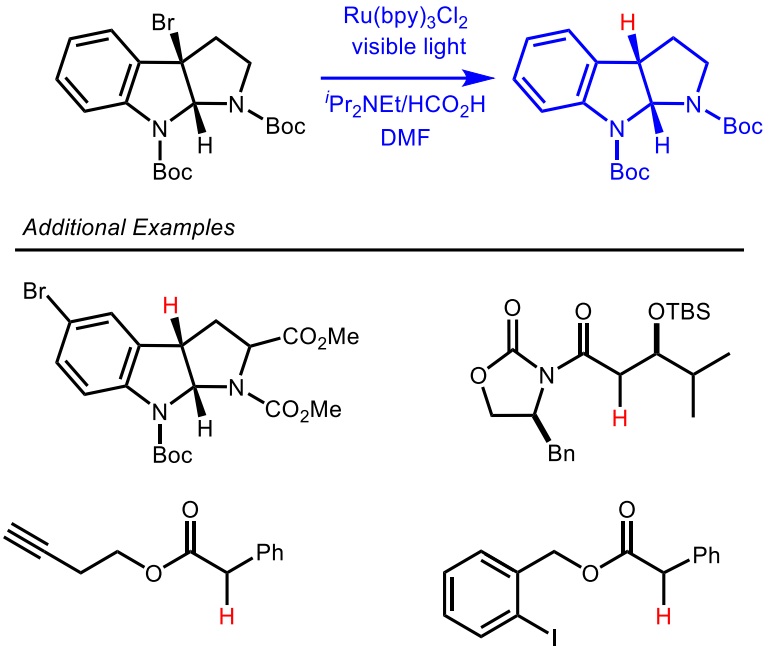

Scheme 1.22. Proposed mechanism towards reductive hydrodehalogenation of α-halides to carbonyls or aryl groups. Adapted from ref.[48, 111]

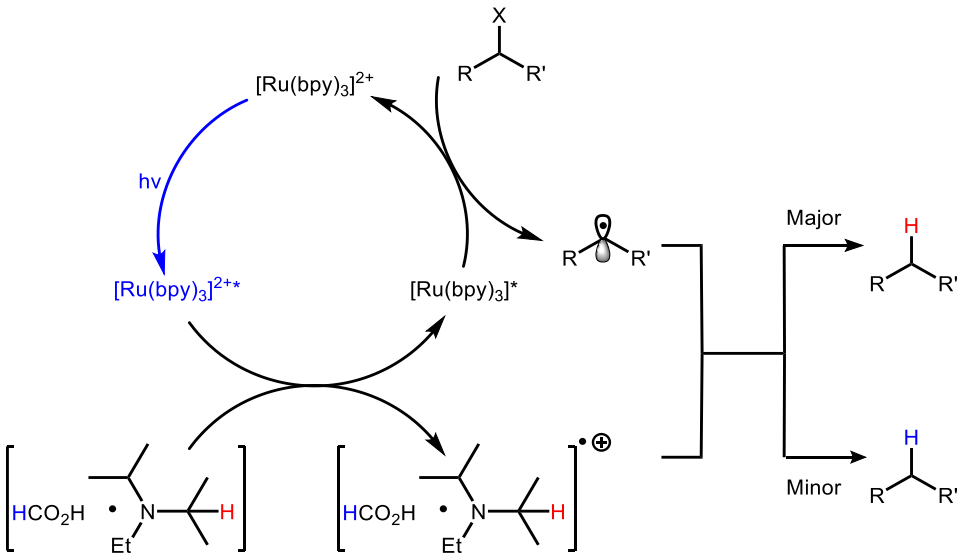

Considering a hydride transfer mechanism to halogenated substrates from a metal hydride has been proposed for hydrodehalogenation reactions,[49, 112-118] the reported dark activity of $[Cp^*Ir(bpy)(H)]^+$ with 2-bromopropanoic acid, and reported photoredox hydrodehalogenation activity using visible light, we wanted to see if Cp*Ir complexes could be used to photochemically promote hydrodehalogenation. In the Miller lab, we have shown the ability to promote hydride transfer from $[Cp^*Ir(bpy)(H)]^+$ using light;[27, 69, 80, 126] applying this technique to hydrodehalogenation we aim to discover new substrates to serve as hydride acceptors. As an additional benefit, the Cp*Ir complexes can transfer hydride using light as a reactivity switch; no strong reductants or oxidants are needed for the reaction. Applying a light-driven hydride transfer strategy for hydrodehalogenation, we report a new application of photochemistry with Cp*Ir and explore the mechanism involved in Chapter 4.

The following chapters will focus on harnessing the excited state reactivity of iridium hydride complexes to drive chemical transformations under mild conditions.

Chapter 2 – Photoswitchable Hydride Transfer

Hydride transfer from $[Cp^*Ir(bpy)(H)]^+$ to organic acids will be investigated to determine ground and excited state hydricity values. Irradiation of the catalyst with 1-methylnicotinamide enhances the reaction rate and selectivity of reduced products.

Chapter 3 – Photochemical Formic Acid Dehydrogenation

Moving from stoichiometric to catalytic hydride transfer, $[Cp^*Ir(bpy)(H)]^+$ and $[Cp^*Ir(bpy\text{-}OMe)(H)]^+$ catalysts will be used to promote the photocatalytic dehydrogenation of formic acid. Thorough investigation of the reaction mechanism will enable significant improvements in catalytic performance.

Chapter 4 – Photoinduced Hydrodehalogenation

Applying excited state hydride transfer to another application, photocatalytic hydrodehalogenation of dichloromethane is observed using $[Cp^*Ir(bpy)(H)]^+$ and $[Cp^*Ir(bpy\text{-}OMe)(H)]^+$ catalysts. Kinetic studies will allow for the proposal and discussion of mechanism.

REFERENCES

1. Ziessel, R., *J. Chem. Soc., Chem. Commun.* **1988**, 16.

2. Kang, J. W.; Maitlis, P. M., *J. Am. Chem. Soc.* **1968,** *90*, 3259.

3. Crabtree, R. H.; Dion, R. P., *J. Chem. Soc., Chem. Commun.* **1984,** 1260.

4. Caix, C.; Chardon-Noblat, S.; Deronzier, A.; Moutet, J.-C.; Tingry, S., *J. Organomet. Chem.* **1997,** *540*, 105.

5. Himeda, Y.; Onozawa-Komatsuzaki, N.; Sugihara, H.; Arakawa, H.; Kasuga, K., *Organometallics* **2004,** *23*, 1480.

6. Himeda, Y.; Onozawa-Komatsuzaki, N.; Sugihara, H.; Kasuga, K., *J. Am. Chem. Soc.* **2005,** *127*, 13118.

7. Ogo, S.; Kabe, R.; Hayashi, H.; Harada, R.; Fukuzumi, S., *Dalton Trans.* **2006,** *39*, 4657.

8. Himeda, Y.; Onozawa-Komatsuzaki, N.; Sugihara, H.; Kasuga, K., *J. Photoch. Photobio. A* **2006,** *182*, 306.

9. Himeda, Y.; Onozawa-Komatsuzaki, N.; Sugihara, H.; Kasuga, K., *Organometallics* **2007,** *26*, 702.

10. Sanz, S.; Benítez, M.; Peris, E., *Organometallics* **2010,** *29*, 275.

11. Brewster, T. P.; Miller, A. J. M.; Heinekey, D. M.; Goldberg, K. I., *J. Am. Chem. Soc.* **2013,** *135*, 16022.

12. Deng, J.; Wang, Y.; Pan, T.; Xu, Q.; Guo, Q. X.; Fu, Y., *ChemSusChem* **2013,** *6*, 1163.

13. Xu, Z.; Yan, P.; Xu, W.; Liu, X.; Xia, Z.; Chung, B.; Jia, S.; Zhang, Z. C., *ACS Catal.* **2015,** *5*, 788.

14. Wu, W.-P.; Xu, Y.-J.; Zhu, R.; Cui, M.-S.; Li, X.-L.; Deng, J.; Fu, Y., *ChemSusChem* **2016,** *9*, 1209.

15. Sasayama, A. F.; Moore, C. E.; Kubiak, C. P., *Dalton Trans.* **2016,** *45*, 2436.

16. Xu, Z.; Yan, P.; Li, H.; Liu, K.; Liu, X.; Jia, S.; Zhang, Z. C., *ACS Catal.* **2016,** *6*, 3784.

17. Bullock, R. M., *Chem. Eur. J.* **2004,** *10*, 2366.

18. Watson, K. J.; Ziessel, R., *Inorg. Chim. Acta* **1992,** *197*, 125.

19. Himeda, Y., *Green Chem.* **2009,** *11*, 2018.

20. Himeda, Y.; Miyazawa, S.; Hirose, T., *ChemSusChem* **2011,** *4*, 487.

21. Wang, W. H.; Hull, J. F.; Muckerman, J. T.; Fujita, E.; Hirose, T.; Himeda, Y., *Chem. - Eur. J.* **2012,** *18*, 9397.

22. Hull, J. F.; Himeda, Y.; Wang, W. H.; Hashiguchi, B.; Periana, R.; Szalda, D. J.; Muckerman, J. T.; Fujita, E., *Nat. Chem.* **2012,** *4*, 383.

23. Ngo, A. H.; Adams, M. J.; Do, L. H., *Organometallics* **2014,** *33*, 6742.

24. Wang, W. H.; Xu, S.; Manaka, Y.; Suna, Y.; Kambayashi, H.; Muckerman, J. T.; Fujita, E.; Himeda, Y., *ChemSusChem* **2014,** *7*, 1976.

25. Keller, S. G.; Ringenberg, M. R.; Häussinger, D.; Ward, T. R., *Eur. J. Inorg. Chem.* **2014,** *2014*, 5860.

26. Manaka, Y.; Wang, W.-H.; Suna, Y.; Kambayashi, H.; Muckerman, J. T.; Fujita, E.; Himeda, Y., *Catalysis Science & Technology* **2014,** *4*, 34.

27. Barrett, S. M.; Slattery, S. A.; Miller, A. J. M., *ACS Catal.* **2015,** *5*, 6320.

28. Iguchi, M.; Himeda, Y.; Manaka, Y.; Matsuoka, K.; Kawanami, H., *ChemCatChem* **2016,** *8*, 886.

29. Zhu, R.; Wang, B.; Cui, M.; Deng, J.; Li, X.; Ma, Y.; Fu, Y., *Green Chem.* **2016,** *18*, 2029.

30. Ogo, S.; Makihara, N.; Kaneko, Y.; Watanabe, Y., *Organometallics* **2001,** *20*, 4903.

31. Youinou, M. T.; Ziessel, R., *J. Organomet. Chem.* **1989,** *363*, 197.

32. Ziessel, R., *Angew. Chem., Int. Ed.* **1991,** *30*, 844.

33. Ziessel, R., *Angew. Chem.* **1991,** *103*, 863.

34. Ladwig, M.; Kaim, W., *J. Organomet. Chem.* **1992,** *439*, 79.

35. Ziessel, R., *J. Am. Chem. Soc.* **1993,** *115*.

36. Wang, D.; Astruc, D., *Chem. Rev.* **2015,** *115*, 6621.

37. Ngo, A. H.; Ibañez, M.; Do, L. H., *ACS Catal.* **2016,** *6*, 2637.

38. Betanzos-Lara, S.; Liu, Z.; Habtemariam, A.; Pizarro, A. M.; Qamar, B.; Sadler, P. J., *Angew. Chem., Int. Ed.* **2012,** *51*, 3897.

39. Liu, Z.; Deeth, R. J.; Butler, J. S.; Habtemariam, A.; Newton, M. E.; Sadler, P. J., *Angew. Chem., Int. Ed.* **2013,** *52*, 4194.

40. Wang, W. H.; Hull, J. F.; Muckerman, J. T.; Fujita, E.; Himeda, Y., *Energy Environ. Sci.* **2012,** *5*, 7923.

41. Wang, W. H.; Muckerman, J. T.; Fujita, E.; Himeda, Y., *ACS Catal.* **2013,** *3*, 856.

42. Dadci, L.; Elias, H.; Frey, U.; Hoernig, A.; Koelle, U.; Merbach, A. E.; Paulus, H.; Schneider, J. S., *Inorg. Chem.* **1995,** *34*, 306.

43. Himeda, Y., *Eur. J. Inorg. Chem.* **2007,** *2007*, 3927.

44. Himeda, Y.; Onozawa-Komatsuzaki, N.; Miyazawa, S.; Sugihara, H.; Hirose, T.; Kasuga, K., *Chem. - Eur. J.* **2008,** *14*, 11076.

45. Sypaseuth, F. D.; Matlachowski, C.; Weber, M.; Schwalbe, M.; Tzschucke, C. C., *Chem. - Eur. J.* **2015,** *21*, 6564.

46. Park, K.; Gunasekar , G. H.; Prakash, N.; Jung, K.-D.; Yoon, S., *ChemSusChem* **2015,** *8*, 3410.

47. Brewster, T. P.; Rezayee, N. M.; Culakova, Z.; Sanford, M. S.; Goldberg, K. I., *ACS Catal.* **2016,** *6*, 3113.

48. Narayanam, J. M. R.; Stephenson, C. R. J., *Chem. Soc. Rev.* **2011,** *40*, 102.

49. Alonso, F.; Beletskaya, I. P.; Yus, M., *Chem. Rev.* **2002,** *102*, 4009.

50. Voldner, E. C.; Li, Y. F., *Sci. Total Environ.* **1995,** *160–161*, 201.

51. Key, B. D.; Howell, R. D.; Criddle, C. S., *Environ. Sci. Technol.* **1997,** *31*, 2445.

52. de Wit, C. A., *Chemosphere* **2002,** *46*, 583.

53. Birnbaum, L. S.; Staskal, D. F., *Environ. Health Perspect.* **2004,** *112*, 9.

54. Neilson, A. H.; Allard, A.-S., Degradation and transformation of organic fluorine compounds. In *Handbook of Environmental Chemistry*, Springer: Berlin, Germany, 2002; Vol. 3, pp 137-202.

55. Breivik, K.; Sweetman, A.; Pacyna, J. M.; Jones, K. C., *Sci. Total Environ.* **2007,** *377*, 296.

56. Lohmann, R.; Breivik, K.; Dachs, J.; Muir, D., *Environ. Pollut.* **2007,** *150*, 150.

57. Adams, D. E. C.; Halden, R. U., *Contaminants of Emerging Concern in the Environment: Ecological and Human Health Considerations*. 2010; p 539.

58. O'Hagan, D., *J. Fluorine Chem.* **2010,** *131*, 1071.

59. de Wit, C. A.; Kierkegaard, A.; Ricklund, N.; Sellström, U., *Brominated Flame Retardants*. 2011; p 241.

60. Shen, Y.; Zhao, R.; Wang, J.; Chen, X.; Ge, X.; Chen, M., *Waste Manage.* **2016,** *49*, 287.

61. Abura, T.; Ogo, S.; Watanabe, Y.; Fukuzumi, S., *J. Am. Chem. Soc.* **2003,** *125*, 4149.

62. Gabrielsson, A.; van Leeuwen, P.; Kaim, W., *Chem. Commun.* **2006**, 4926.

63. Himeda, Y.; Miyazawa, S.; Onozawa-Komatsuzaki, N.; Hirose, T.; Kasuga, K., *Dalton Trans.* **2009**, 6286.

64. Miller, A. J. M.; Heinekey, D. M.; Mayer, J. M.; Goldberg, K. I., *Angew. Chem., Int. Ed.* **2013,** *52*, 3981.

65. Hollmann, F.; Schmid, A.; Steckhan, E., *Angew. Chem., Int. Ed.* **2001,** *40*, 169.

66. Moggi, L.; Juris, A.; Sandrini, D.; Manfrin, M. F., *Rev. Chem. Intermed.* **1981,** *4*, 171.

67. Sandrini, D.; Maestri, M.; Ziessel, R., *Inorg. Chim. Acta* **1989,** *163*, 177.

68. Suenobu, T.; Guldi, D. M.; Ogo, S.; Fukuzumi, S., *Angew. Chem., Int. Ed.* **2003,** *42*, 5492.

69. Pitman, C. L.; Miller, A. J. M., *ACS Catal.* **2014,** *4*, 2727.

70. DuBois, D. L.; Berning, D. E., *Appl. Organomet. Chem.* **2000,** *14*, 860.

71. Muckerman, J. T.; Achord, P.; Creutz, C.; Polyansky, D. E.; Fujita, E., *Proc. Natl. Acad. Sci. U.S.A.* **2012,** *109*, 15657.

72. Horn, M.; Schappele, L. H.; Lang-Wittkowski, G.; Mayr, H.; Ofial, A. R., *Chem. Eur. J.* **2013,** *19*, 249.

73. Bullock, R. M.; Appel, A. M.; Helm, M. L., *Chem. Commun.* **2014,** *50*, 3125.

74. DuBois, M. R.; DuBois, D. L., *Chem. Soc. Rev.* **2009,** *38*, 62.

75. Kreevoy, M. M.; Ostovic, D.; Lee, I. S. H.; Binder, D. A.; King, G. W., *J. Am. Chem. Soc.* **1988,** *110*, 524.

76. Anne, A.; Moiroux, J., *J. Org. Chem.* **1990,** *55*, 4608.

77. Cheng, J. P.; Lu, Y.; Zhu, X.; Mu, L., *J. Org. Chem.* **1998,** *63*, 6108.

78. Sarker, N.; Bruno, J. W., *J. Am. Chem. Soc.* **1999,** *121*, 2174.

79. Tsay, C.; Livesay, B. N.; Ruelas, S.; Yang, J. Y., *J. Am. Chem. Soc.* **2015,** *137*, 14114.

80. Pitman, C. L.; Brereton, K. R.; Miller, A. J. M., *J. Am. Chem. Soc.* **2016,** *138*, 2252.

81. Creutz, C.; Chou, M. H., *J. Am. Chem. Soc.* **2009,** *131*, 2794.

82. Berning, D. E.; Noll, B. C.; DuBois, D. L., *J. Am. Chem. Soc.* **1999,** *121*, 11432.

83. Heiden, Z. M.; Lathem, A. P., *Organometallics* **2015,** *34*, 1818.

84. Creutz, C.; Chou, M. H., *J. Am. Chem. Soc.* **2007,** *129*, 10108.

85. Connelly, S. J.; Wiedner, E. S.; Appel, A. M., *Dalton Trans.* **2015,** *44*, 5933.

86. Zaidman, B.; Wiener, H.; Sasson, Y., *Int. J. Hydrogen Energy* **1986,** *11*, 341.

87. Johnson, T. C.; Morris, D. J.; Wills, M., *Chem. Soc. Rev.* **2009,** *39*, 81.

88. Enthaler, S.; von Langermann, J.; Schmidt, T., *Energy Environ. Sci.* **2010,** *3*, 1207.

89. Grasemann, M.; Laurenczy, G., *Energy Environ. Sci.* **2012,** *5*, 8171.

90. Fukuzumi, S.; Suenobu, T., *Dalton Trans.* **2013,** *42*, 18.

91. Department of Energy. Hydrogen Storage. Online, **2016**.

92. Papp, G.; Csorba, J.; Laurenczy, G.; Joó, F., *Angew. Chem., Int. Ed.* **2011,** *50*, 10433.

93. Boddien, A.; Gärtner, F.; Federsel, C.; Sponholz, P.; Mellmann, D.; Jackstell, R.; Junge, H.; Beller, M., *Angew. Chem., Int. Ed.* **2011,** *50*, 6411.

94. Boddien, A.; Federsel, C.; Sponholz, P.; Mellmann, D.; Jackstell, R.; Junge, H.; Laurenczy, G.; Beller, M., *Energy Environ. Sci.* **2012,** *5*, 8907.

95. Hsu, S. F.; Rommel, S.; Eversfield, P.; Muller, K.; Klemm, E.; Thiel, W. R.; Plietker, B., *Angew. Chem., Int. Ed.* **2014,** *53*, 7074.

96. Onishi, M., *J. Mol. Catal.* **1993,** *80*, 145.

97. Linn, D. E.; King, R. B.; King, A. D., *J. Mol. Catal.* **1993,** *80*, 151.

98. Loges, B.; Boddien, A.; Junge, H.; Noyes, J. R.; Baumann, W.; Beller, M., *Chem. Commun.* **2009,** *28*, 4185.

99. Boddien, A.; Loges, B.; Gärtner, F.; Torborg, C.; Fumino, K.; Junge, H.; Ludwig, R.; Beller, M., *J. Am. Chem. Soc.* **2010,** *132*, 8924.

100. King, A. D.; King, R. B.; Yang, D. B., *J. Am. Chem. Soc.* **1981,** *103*, 2699.

101. Coffey, R. S., *Chem. Commun.* **1967,** 923b-924.

102. Forster, D.; Beck, G. R., *J. Chem. Soc. Chem. Comm.* **1971,** 1072.

103. Collin, J. P.; Sauvage, J. P., *Nouv. J. Chim.* **1985,** *9*, 395.

104. King, A. D.; King, R. B.; Yang, D. B., *J. Am. Chem. Soc.* **1980,** *102*, 1028.

105. Choudhury, D.; Cole-Hamilton, D. J., *J. Chem Soc. Dalton* **1982,** 1885.

106. Boddien, A.; Mellmann, D.; Gartner, F.; Jackstell, R.; Junge, H.; Dyson, P. J.; Laurenczy, G.; Ludwig, R.; Beller, M., *Science* **2011,** *333*, 1733.

107. Bielinski, E. A.; Lagaditis, P. O.; Zhang, Y.; Mercado, B. Q.; Würtele, C.; Bernskoetter, W. H.; Hazari, N.; Schneider, S., *J. Am. Chem. Soc.* **2014,** *136*, 10234.

108. Boddien, A.; Gärtner, F.; Jackstell, R.; Junge, H.; Spannenberg, A.; Baumann, W.; Ludwig, R.; Beller, M., *Angew. Chem., Int. Ed.* **2010,** *49*, 8993.

109. Muller, E. E. L.; Bringel, F.; Vuilleumier, S., *Res. Microbiol.* **2011,** *162*, 869.

110. Fukuzumi, S.; Mochizuki, S.; Tanaka, T., *J. Phys. Chem.* **1990,** *94*, 722.

111. Narayanam, J. M. R.; Tucker, J. W.; Stephenson, C. R. J., *J. Am. Chem. Soc.* **2009,** *131*, 8756.

112. Grushin, V. V.; Alper, H., *Chem. Rev.* **1994,** *94*, 1047.

113. Kiplinger, J. L.; Richmond, T. G.; Osterberg, C. E., *Chem. Rev.* **1994,** *94*, 373.

114. Kraft, B. M.; Lachicotte, R. J.; Jones, W. D., *J. Am. Chem. Soc.* **2001,** *123*, 10973.

115. Grushin, V. V.; Alper, H., *Activation of otherwise unreactive CCl bonds*. Springer-Verlag: 1999; Vol. 3.

116. Schrick, B.; Blough, J. L.; Jones, A. D.; Mallouk, T. E., *Chem. Mater.* **2002,** *14*, 5140.

117. Aresta, M.; Caramuscio, P.; De Stefano, L.; Pastore, T., *Waste Manage.* **2003,** *23*, 315.

118. Maron, L.; Werkema, E. L.; Perrin, L.; Eisenstein, O.; Andersen, R. A., *J. Am. Chem. Soc.* **2005,** *127*, 279.

119. Artamkina, G. A.; Egorov, M. P.; Beletskaya, I. P., *Chem. Rev.* **1982,** *82*, 427.

120. Vlasov, V., *J. Fluorine Chem.* **1993,** *61*, 193.

121. Sadowsky, D.; McNeill, K.; Cramer, C. J., *Environ. Sci. Technol.* **2014,** *48*, 10904.

122. Mathew, L.; Warkentin, J., *J. Am. Chem. Soc.* **1986,** *108*, 7981.

123. Rettenmeier, C.; Wadepohl, H.; Gade, L. H., *Chem. – Eur. J.* **2014,** *20*, 9657.

124. Chelucci, G.; Baldino, S.; Pinna, G. A.; Pinna, G., *Current Org. Chem.* **2012,** *16*, 2921.

125. Wallentin, C.-J.; Nguyen, J. D.; Stephenson, C. R. J., *CHIMIA* **2012,** *66*, 394.

126. Barrett, S. M.; Pitman, C. L.; Walden, A. G.; Miller, A. J. M., *J. Am. Chem. Soc.* **2014,** *136*, 14718.

Chapter 2: PHOTOSWITCHABLE HYDRIDE TRANSFER FROM IRIDIUM TO 1-METHYLNICOTINAMIDE RATIONALIZED BY THEROCHEMICAL CYCLES

2.1 Introduction

Hydride transfer between a transition metal and an organic substrate is involved in numerous catalytic transformations, especially hydrogenations and dehydrogenations.[1-4] To improve hydride transfer catalysis, one can tune the hydride donor ability (hydricity) of the catalyst. This strategy is empowered by thermodynamic measurements of hydricity (the free energy required for heterolytic M–H bond cleavage) that have emerged over the last 15 years as a quantitative guide in catalyst design.[5-9] The hydricity of a catalytic intermediate is typically tuned through synthetic modification, such as installing more strongly donating ligands to generate more hydridic intermediates.

This work pursues an alternative strategy for tuning reactivity while avoiding synthetic modification: harnessing visible light to enhance hydricity. Hydride $[Cp^*Ir(bpy)(H)]^+$ (**1**) releases H_2 in the presence of weak acids only under visible light illumination. Photohydride thermochemical cycles and experimental studies are both consistent with net hydride transfer being greatly promoted by light. In reactions with the organic acceptor 1-methylnicotinamide, illumination dramatically accelerates hydride transfer and exhibits photo-switchable product selectivity.

Hydride **1** was investigated because it is commonly invoked as a catalytic intermediate in hydrogenation and dehydrogenation reactions, among other transformations.[10-16] While most of these reactions proceed without any influence of light, **1** also exhibits photochemical reactivity, including stoichiometric light-promoted proton transfer[17] and photocatalytic water-gas shift reactivity.[18-21] Photochemical H_2 release involving formal H^- donation from a metal hydride to a proton source is rare.[18-25] Photohydride transfer from an M−H bond to an organic substrate is apparently unprecedented, despite the potential utility of light-triggered reductions.

2.2 Results and Discussion

We recently harnessed the proclivity of **1** to release H_2 under illumination to realize a photoelectrocatalytic water reduction cycle.[26] Hydride **1** is produced in an electrochemical step before undergoing light-triggered H_2 evolution. The action of light is striking: no catalytic activity is observed in the dark, but visible light illumination triggers catalysis. The formal photohydride reactivity of **1** sparked our interest in understanding the difference between ground state and excited state hydricity and expanding such photohydride reactivity to organic substrates.

Thermodynamic calculations were a useful starting point in rationalizing the reactivity of **1** and its excited state, **1***. All thermodynamic values are determined and reported in CH_3CN solvent, in order to facilitate comparisons with values previously established for other hydrides.[27-30] The ground state hydricity of **1** (ΔG°_{H-}) can be determined by obtaining the pK_a of **1** and the reduction potential of $[Cp^*Ir(bpy)(NCCH_3)]^{2+}$ (**2**), according to Equation 2.1.[31] The constant C_{H-} (79.6 kcal·mol^{-1}) is the formal potential for 2e$^-$ reduction of H^+ to H^-.[31]

$$\Delta G^{o}_{H-} = 1.37\cdot(pK_a) - (-46.12)\cdot(E_{1/2}) + C_{H-} \qquad \text{(Equation 2.1)}$$

Spectrophotometric titration of hydride **1** in CH_3CN with 1,8-diazabicyclo[5.4.0]undec-7-ene (DBU) provided a pK_a value of 23.3.(See Experimental Section for additional information) Cyclic voltammetry (CV) of CH_3CN complex **2** revealed a quasi-reversible $2e^-$ reduction at –1.07 V *vs.* $Cp_2Fe^{+/0}$. The ground state hydricity of **1** was determined according to Equation. 2.1: $\Delta G^{o}_{H-} = 62$ kcal·mol^{-1}. This value is similar to the ubiquitous biological hydride transfer reagent NADH.[32, 33]

Scheme 2.1. Hydricity of Complex **1**.

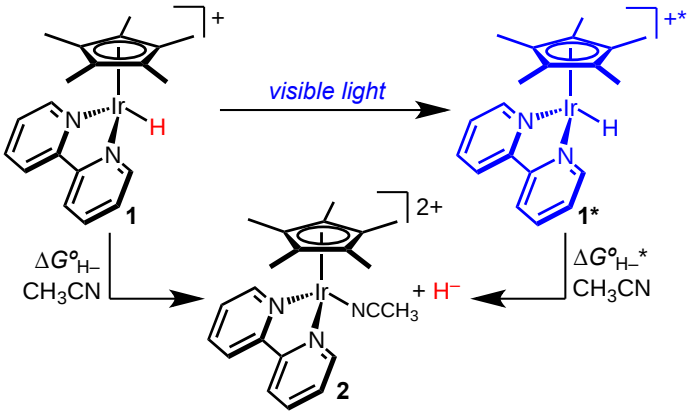

The relatively weak ground state hydricity of **1** leads to good stability even in quite acidic environments when protected from light. In the dark, hydride **1** showed no reaction after 1 hour when mixed with acetic acid (pK_a 23.5),[34] triethylammonium (pK_a 18.8),[35] or pyridinium (pK_a 12.5).[35] Even after 2 months in the dark, only 35% of **1** had reacted with $[Hpy]^+$, and heating **1** and $[Hpy]^+$ to 80 ºC for 3 h led to only ~10% consumption of **1**. Only moving to the stronger methanesulfonic acid (pK_a = 10.0)[36] was rapid H_2 release observed (along with complete consumption of **1** and formation of **2**). These observations are consistent with the determined hydricity of **1**, according to DuBois' equations for predicting H_2 release from a hydride and an acid.[37] The relative acid stability of **1** may explain the high activity of Cp*Ir-based catalysts for hydrogenation of carboxylic acids and disproportionation of formic acid.[15, 16]

A thermodynamic measure of excited state hydricity was developed next. Thermodynamic studies of photohydrides (unlike photoacids)[38-40] are lacking, but an excited state hydricity, ΔG^{o}_{H-}*, can be considered in the context of ΔG^{o}_{H-}, as shown in Scheme 2.1. The excited state hydricity (Equation 2.5) is provided by Equation 2.2 through Equation 2.4. The thermochemical cycle assumes that hydride transfer is coupled to ground state relaxation, in analogy to excited-state electron transfer and some photoacid reactions (Scheme 2.2).[41, 42]

1* ⇆ Cp*Ir(bpy) + H^+ (Equation 2.2)

Cp*Ir(bpy) + CH_3CN ⇆ **2** + $2e^-$ (Equation 2.3)

$H^+ + 2e^- \leftrightarrows H^-$ (Equation 2.4)

1* + CH_3CN ⇆ **2** + H^- (Equation 2.5)

The pK_a* of **1** (Equation 2.2) was estimated based on the energy difference between the lowest vibrational states of **1** and **1*** (E_{00}). Hydride **1** exhibited featureless emission ($\lambda_{em,max}$ = 708 nm = 14,100 cm^{-1}) in CH_3CN that did not overlap with the excitation spectrum appreciably, consistent with previously reported triplet emission from a charge transfer transition.[17-21] The low energy edge of the emission spectrum was used to estimate E_{00} = 16,900 cm^{-1}, providing pK_a* = –12. (See Experimental Section for additional details) The strongly photoacidic excited state is consistent with the reported ability of **1** to protonate CH_3OH.[17]

$$\Delta G^{o}_{H-}* = -(E_{00}/350) + 1.37\cdot(pK_a) - (-46.12)\cdot(E_{1/2}) + C_{H-} \quad \text{(Equation 2.6)}$$

The excited state hydricity of **1** can be predicted using Equation 2.6: ΔG°_{H-}* = 14 kcal·mol^{-1}. The predicted value of ΔG°_{H-}* suggests that **1** is a much stronger hydride donor in its triplet excited state than in its ground state, consistent with observed photocatalysis.[26] Strikingly, excited state **1*** is predicted to be an incredibly potent hydride donor − thermodynamically

stronger than the "super hydride" $[HBEt_3]^-$ (~26 kcal· mol^{-1}) used extensively in organic reductions.[43]

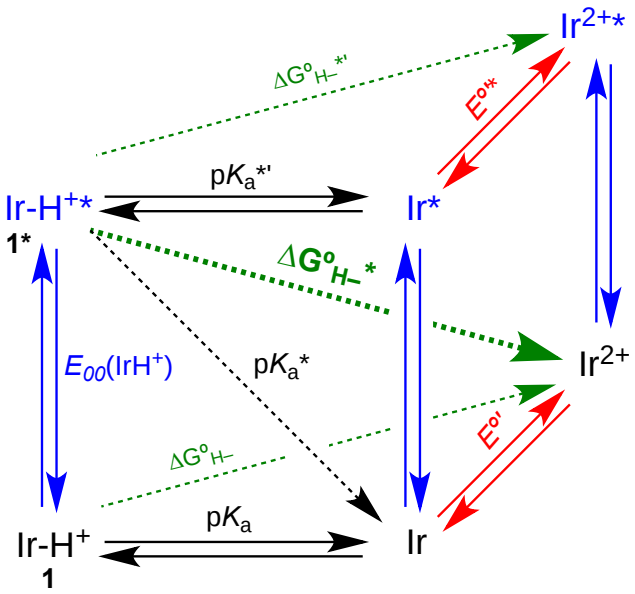

Scheme 2.2. "Cube scheme" diagram showing thermochemical relationships between excited state and ground state species. In the scheme above, Ir represents Cp*Ir(bpy).

It is noteworthy that the thermochemical cycles predict that **1*** should *both* be a stronger acid *and* a stronger hydride donor. The strongly hydridic excited state, in particular, poses a paradox: the excited state **1*** was previously assigned as originating from a MLCT transition in which transfer of electron density on the bpy ligand leads to formal oxidation of the Ir center,[17, 44] seemingly indicating an *acidic* (rather than hydridic) excited state. This paradox can be rationalized by noticing that while **1*** is a strong acid, the reduced bpy ligand is simultaneously a strong reductant, rendering the net transfer of a hydride ($H^+/2e^-$) thermodynamically favorable.

Scheme 2.3. Reactivity of Complex **1** with Organic Acids.

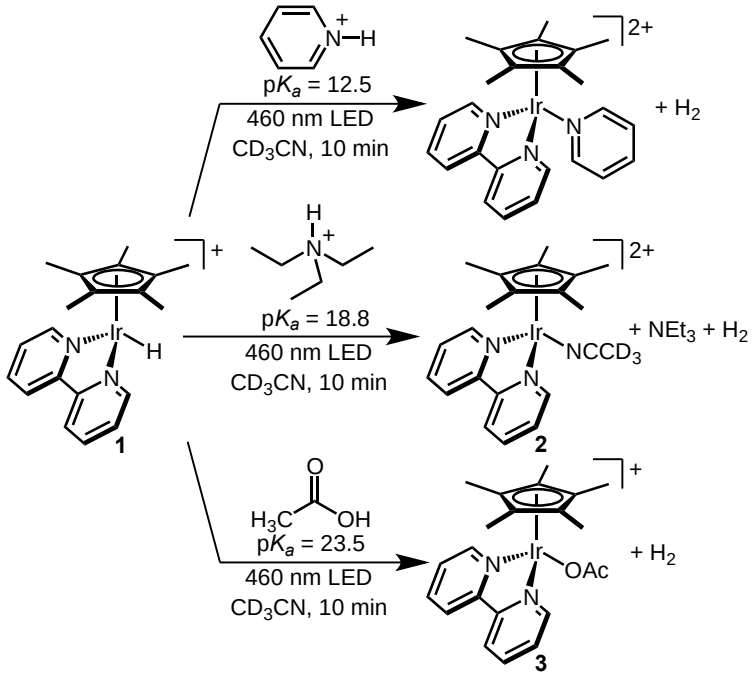

Experimental validation of the thermodynamic predictions was sought through photoreactivity of **1** with organic acids (Scheme 2.3), with **1** as a formal source of H^-. H_2 release is favorable if the sum of the hydricity (ΔG^o_{H-}) and the free energy of proton loss ($1.37 \cdot pK_a$) is less than 76 kcal·mol^{-1} (the free energy of heterolytic H_2 cleavage), see Equation. 2.29. As discussed above, no H_2 release was observed in the dark with pyridinium ($[Hpy]^+$), $HNEt_3^+$, or HOAc over 1 h at room temperature. If the hydricity of **1** is sufficiently enhanced upon photoexcitation, however, H_2 release should be observed.

Illuminating solutions of **1** and [Hpy][OTs] (Hpy = pyridinium, OTs = tosylate) in CD_3CN with a 460 nm LED lamp led to rapid H_2 release within 1 h at room temperature. Complete conversion to $[Cp^*Ir(bpy)(py)]^{2+}$, as judged by ^1H NMR spectroscopy and electrospray ionization–mass spectrometry (ESI–MS), was accompanied by the formation of H_2 gas (^1H NMR δ 4.57 ppm).

Photohydride reactivity was also observed with the weaker acid $[HNEt_3][BF_4]$, with complete consumption of **1** (and formation of **2**) in less than 10 minutes of illumination (Scheme 2.3). The quantum yield for this reaction was assessed using the ferrioxalate actinometer.[45-47] The photon flux passing through an NMR tube was determined to be 2.18 x 10^{-8} mol·photons·s^{-1}, providing a quantum yield $\Phi = 0.29$.

Even acetic acid, an acid of similar strength to **1**, gave high yields of H_2 gas in less than 10 min. The Ir-containing product was $[Cp^*Ir(bpy)(OAc)]^+$ (**3**) according to ESI-MS, as further confirmed based on an independent synthesis of **3**. A 74% yield of H_2 was quantified by headspace gas chromatography.

Photoexcitation clearly enhances the ability of **1** to perform a net hydride transfer. Only a hydride featuring $\Delta G^o_{H-} < 43$ kcal·mol^{-1} is thermodynamically capable of H_2 release with acetic acid. Accordingly, irreversible H_2 photoevolution from **1** and the weak acid HOAc establishes a limiting hydricity value, according to Equation 2.32 through Equation 2.34: $\Delta G^o_{H-}* < 43$ kcal·mol^{-1}. *This represents an almost 20 kcal·mol^{-1} enhancement in experimentally measured hydricity relative to the ground state hydricity*.

Scheme 2.4. Formation of Iminoacyl Complex.

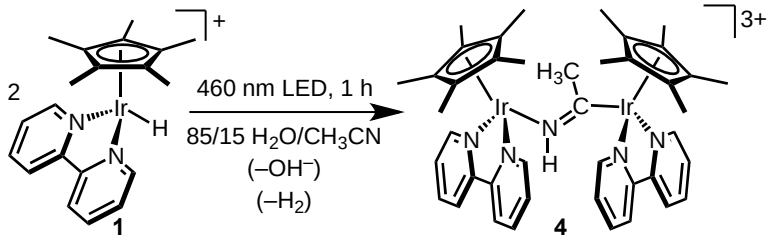

The experimental hydricity value is apparently limited by the acidity of **1** ($pK_a = 23.3$). When acids weaker than acetic acid are employed, decomposition to a mixture of species is observed upon illumination, suggesting that **1** may also be acting as a sacrificial proton donor in these reactions. The major product from this mixture was produced cleanly upon photolysis of **1**

in water/acetonitrile mixtures in the presence of a chloride source (Scheme 2.4). No discernible reaction took place in the dark. NMR spectroscopy of the resulting product revealed two distinct sets of Cp* and bpy resonances in a 1:1 ratio. X-ray diffraction of yellow single crystals of the product revealed an unusual bridging iminoacyl structure [Cp*Ir(bpy)(μ-N(H)C(CH_3))(bpy)IrCp*][PF_6]$_3$ (**4**, Figure 2.1).[48-52] The mechanism by which **4** is formed is unclear at this time (as is the role of chloride), but **4** is commonly observed as a side product in reactions that do not undergo clean H^- transfer. A plausible mechanism toward formation of the bridging iminoacyl complex is depicted in Scheme 2.5. Upon irradiation, an excited **1*** is proposed to react with a ground state **1**, releasing H_2 and yielding Cp*Ir^I(bpy) as well as [Cp*Ir(bpy)(NCCH_3)]$^{2+}$. Nucleophilic attack from Ir^1 to the nitrile carbon on the acetonitrile-bound complex in the presence of an acid source yields **4**. Independent synthesis of Cp*Ir^I(bpy) and [Cp*Ir(bpy)(NCCH_3)]$^{2+}$, followed by mixing in acetonitrile solvent does indeed yield **4**, providing support for the proposed mechanism.

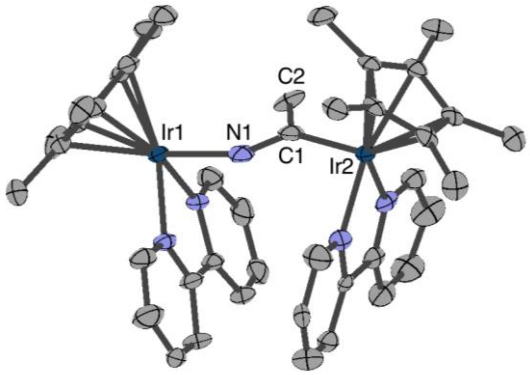

Figure 2.1. Structural representation of **4** (ellipsoids at 50% probability). Three PF_6 ions, two CH_3CN molecules, and H atoms omitted for clarity. A H-bond between one CH_3CN and the imine NH is observed (N-N: 3.201 Å).[12] Selected bond distances (Å) and angles (º): Ir1–N1 2.149, Ir2–C1 2.126, N1–C1 1.245, C1–C2 1.503, Ir1–N1–C1 131.8, Ir2–C1–N1 119.7, Ir2–C1–C2 129.5.

Scheme 2.5. Proposed mechanism for the formation of **4**.

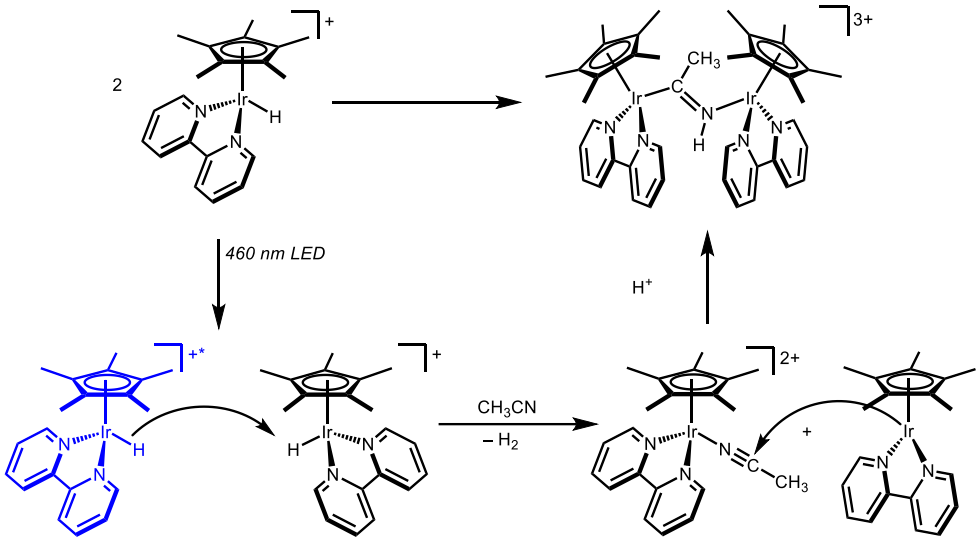

With a better understanding of the thermodynamics of photohydride transfer in hand, the ability of **1** to reduce organic substrates was assessed using nicotinamide derivatives. The calculated hydricity of 1,4-dihydro-1-methylnicotinamide (MNA-H) is $\Delta G^{o}_{H-} = 56$ kcal·mol^{-1},[28] similar to other 1,4-dihydronicotinamide derivatives ($\Delta G^{o}_{H-} \sim 56$–$64$ kcal·mol^{-1}),[23, 32, 33] suggested that hydride transfer from **1** would be unfavorable while hydride transfer from **1*** would be highly favorable. Mixtures of **1** and [MNA][BF_4] (MNA is 1-methylnicotinamide) showed no detectable reaction after 6 hours in the dark, consistent with the thermodynamic predictions. After 1 h illumination, however, significant conversion to the *doubly-reduced* product, 1-methyl-1,4,5,6-tetrahydronicotinamide (MNA-H_3, ~10% yield) was observed. The reduction of a nicotinamide derivative to the tetrahydro product by a homogeneous transition metal hydride is extremely rare.[53] Typical conditions for the double reduction of pyridinium salts include strong main group hydride donors (e.g. $NaBH_4$)[54] or Pd/C under H_2.[55-58] Transition metal hydride complexes, including strong hydride donors such as [Cp*Rh(ppy)(H)]$^+$ ($\Delta G^{o}_{H-} = 49$ kcal·mol^{-1}, ppy = 2-phenylpyridine)[59, 60] and [Ru(tpy)(bpy)(H)]$^+$ ($\Delta G^{o}_{H-} = 39$ kcal·mol^{-1}, tpy = 2,2':6',2"-terpyridine)[61] give only 1,4- and 1,6-reduced species.[62-64] The double reduction of

MNA^+ in a fashion analogous to borohydride reagents is further evidence of the greatly enhanced excited state hydricity of **1***.

Table 2.1. Visible light-promoted hydride transfer from [Cp*Ir(bpy)(H)][OTf] (**1**) to [MNA][I].[a]

Strategies to tune the product selectivity were considered next. To provide more

Table 1. Visible light-promoted hydride transfer from [Cp*Ir(bpy)(H)][OTf] (**1**) to [MNA][I].[a]

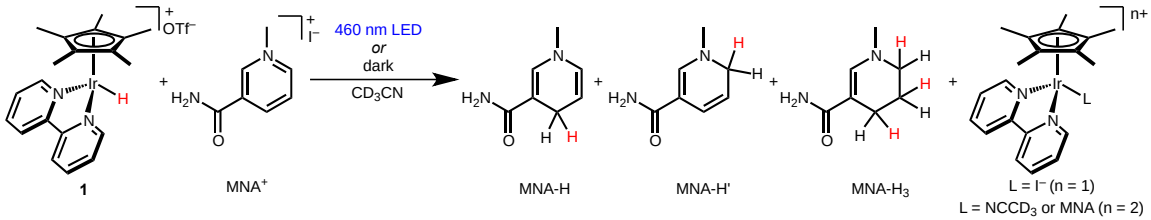

[**1**]:[MNA^+]	Time (min)	Yield of MNA-H (%)		Yield of MNA-H' (%)		Yield of $MNA\text{-}H_3$ (%)	
		Dark	Light	Dark	Light	Dark	Light
1:4.4	10	0	52	0	7	0	3[b]
	20	0	59	0	10	0	7[b]
4.8:1	10	9	21	6	3	0	15
	60	24	0	15	0	0	24

[a]Yields determined by ^1H NMR and calculated relative to limiting reagent. [b]Maximum yield is 50%. See the Supporting Information for full details.

thermodynamic driving force (and avoid possible reversion in the dark), the iodide salt of MNA^+ was utilized in order to produce a more stable Ir–I product. As shown in Table 1.1, mixtures of **1** and excess [MNA][I] (1:4.4) produced the normally observed 1,4-reduced product MNA-H in 52% yield (with respect to **1**) after just 10 min of illumination. Only small amounts of 1,6-reduced MNA-H' (10%) and doubly-reduced $MNA\text{-}H_3$ (7%) were observed, even after 20 minutes. The major Ir-containing product was $[Cp^*Ir(bpy)(I)]^+$; the adduct of the conjugate base of MNA^+, $[Cp^*Ir(bpy)(MNA)]^{2+}$, was also observed in small quantities.[64] The quantum yield for production of MNA-H and MNA-H' was determined to lie in the range $0.03 < \Phi < 0.20$, depending on reaction conditions. No reduced products were observed in the dark, even after 1 hour.

Upon photolysis of MNA^+ in the presence of excess **1**, doubly-reduced MNA-H_3 was the sole reduced nicotinamide product after 60 min of illumination (24% yield with respect to MNA^+, Table 1.1). When the same mixture is allowed to react in the dark for 60 minutes, only singly-reduced products are formed — no MNA-H_3 is observed in reactions carried out in the dark, even with reaction times up to 6 hours. Doubly reduced MNA-H_3 is apparently formed by two sequential H^- transfers, in addition to one proton transfer. MNA-H and MNA-H' are observed as intermediates at early times (Table 2.1 and Appendix A). The product forms in the absence of water, so MNA^+ or **1** itself may be acting as an acid source. Under conditions of high concentrations of **1**, H_2 release and formation of bimetallic **4** become competitive.

2.3 Conclusions

The photohydride strategy offers powerful tunability of nicotinamide reductions. First, dramatic *rate enhancements* are observed under illumination relative to dark reactions: in ~1:1 mixtures of **1**:MNA^+, visible light illumination accelerated the production of 1,4-reduced product (MNA-H) by a factor of ~200 compared to reactions carried out in the dark (Appendix A). Second, *selectivity* can be photo-switched from singly-reduced to doubly-reduced products with complete fidelity (Table 1.1).

In summary, visible light has been shown to promote hydride transfer reactions from $[Cp^*Ir(bpy)(H)]^+$ to several organic acids and to 1-methylnicotinamide. A method for determining excited state hydricity was presented, revealing an increase in thermodynamic hydride donor ability upon light absorption of at least 18 kcal·mol^{-1}. In reactions with nicotinamide derivatives, illumination accelerates production of 1,4-reduced species. Under conditions of excess hydride, illumination leads to a complete switch in selectivity, producing an unusual doubly-reduced product. The products are consistent with net photohydride reactivity,

but questions remain concerning the detailed mechanism: the reaction could proceed *via* concerted H^- transfer, separate transfer of H^+ and $2e^-$, or even stepwise H• and e^- transfer. Deeper mechanistic understanding and the promise of utilizing light to activate catalytic hydrogenations motivate future research.

2.4 Experimental Section

General Considerations.

Manipulations were performed under the inert nitrogen atmosphere of a Schlenk line or a glovebox, except as noted. Water and formic acid were thoroughly degassed by sparging with nitrogen before use. Organic solvents were dried and degassed with argon using a Pure Process Technology solvent system. D_2O was purchased from Cambridge Isotope Laboratories, Inc. and sparged with nitrogen before being stored in a glovebox. CD_3CN was purchased from Cambridge Isotope Laboratories, Inc. and degassed by three freeze-pump-thaw cycles before drying by passage through a small column packed with activated alumina. $[Cp^*Ir(Cl)_2]_2$,[65] $[Cp^*Ir(bpy)(Cl)][Cl]$,[66] $[Cp^*Ir(bpy)(H_2O)][OTf]_2$,[15] $[Cp^*Ir(bpy)(H)][PF_6]$,[16] reduced MNA products (MNA-H, MNA-H', and MNA-H_3),[67-69] and $[K_3][Fe(C_2O_4)_3]$[70] were synthesized following established procedures. Tetrabutylammonium hexafluorophosphate ($[Bu_4N][PF_6]$, VWR, 98%) was twice recrystallized from ethanol. All other materials were readily commercially available and were used as received. The hydrides $[Cp^*Ir(bpy)(H)][PF_6]$ and [Cp*Ir(bpy)(H)][OTf] were utilized interchangeably in these studies, and showed similar behavior. The OTf salt was preferred for most hydride transfer studies due to enhanced solubility in CH_3CN and CH_3CN/H_2O mixtures.

^1H and $^{13}C(^1H)$ NMR spectra were recorded on 400 or 600 MHz spectrometers at 25 ºC. Chemical shifts are reported with respect to residual proteo solvent.[71] ESI-MS data was acquired

on a Micromass Triple Quadrupole Mass Spectrometer with a Z-spray nano-electrospray source and an Advion TriVersa NanoMate sampling system. UV-Vis spectra were obtained with either a Cary 60 spectrophotometer or an Ocean Optics USB2000+ spectrometer with a DT-MINI-2GS deuterium/tungsten halogen light source controlled by OceanView software. Infrared spectroscopy was carried out with a Bruker Alpha FT-IR equipped with an ATR module. Single-crystal X-ray diffraction (XRD) was performed with a Bruker SMART APEX II diffractometer using Cu radiation. Visible light photolysis was carried out using an EagleLight 460 nm (± 12 nm at half-max intensity) LED lamp (500 lumens at 15 W). A Coherent FieldMax$_{II}$ Laser Power/Energy Meter (photodiode) was used for electronic photon flux measurements. Electrochemical measurements were performed in a nitrogen glovebox with a Pine Instruments WaveNow potentiostat controlled by Aftermath software. All potentials are reported with respect to $Cp_2Fe^{+/0}$ internal standard.

Steady-state emission and excitation spectra were recorded on a Photon Technology International, Inc. Quantamaster 4SE-NIR5 spectrometer PC-controlled by FeliX32 software. Excitation light was provided by a 75 W Xenon light source coupled to a single monochromator outfitted with a 1200 L/mm grating blazed at 400 nm. A 300 nm long pass filter was placed before the sample to prevent deep UV excitation from a second order grating effect. Emission was collected at a right angle relative to excitation, focused into a single monochromator (grating blazed at 500 nm with 1200 L/mm) and detected by a Hamamatsu R928P photomultiplier tube used in single photon counting mode. Bandwidths for both emission and excitation monochromators were fixed at 6 nm for all experiments. All spectra were corrected for system response.

Synthetic Procedures.

Synthesis of [Cp*Ir(bpy)(H)][OTf] (1).

A 3 M formic acid solution was prepared by adding 5.8 mL 98% formic acid to 50 mL of water. The solution was adjusted to pH 5 (pH electrode meter) using potassium hydroxide. The formic acid solution was sparged prior to storage in a nitrogen-filled glovebox. Addition of 10 mL of 3 M formic acid at pH 5 to 119.2 mg (0.149 mmol) $[Cp^*Ir(bpy)(H_2O)][OTf]_2$ in a 20 mL scintillation vial produced a yellow solution that was protected from light and stirred for 2 h. After the first hour, the reaction vessel cap was vented to release any CO_2 generated during the reaction. The cap was then replaced and the solution was stirred for an additional hour. The product was extracted with 3 x 3 mL CH_2Cl_2. The extract was then washed with 3 x 3 mL aqueous LiOTf solution (155.3 mg, 0.995 mmol, in 10 mL water). The product was next washed with 3 x 3 mL of water. The final water wash was extracted with CH_2Cl_2 to recover any product lost to the aqueous layer. The yellow product was dried *in vacuo* to afford pure **1** (87.9 mg, 93% yield). Spectroscopic data closely matched the previously reported hexafluorophosphate salt.[11] ^{1}H NMR (CD_3CN): δ 8.89 (d, *J* = 5.7 Hz, 2H), 8.39 (d, *J* = 8.1 Hz, 2H), 8.07 (td, *J* = 8.0, 1.3 Hz, 2H), 7.59 (ddd, *J* = 7.3, 5.7, 1.4 Hz, 2H), 1.83 (s, 15H), –11.56 (s, 1H).

Synthesis of [Cp*Ir(bpy)(NCCH$_3$)][PF$_6$]$_2$ (2).

In a nitrogen-filled glovebox, a 20 mL scintillation vial was charged with 12.5 mg (0.0225 mmol) [Cp*Ir(bpy)(Cl)][Cl]. A second 20 mL scintillation vial was charged with 12.0 mg (0.0475 mmol) $AgPF_6$ and 5 mL CH_3CN. The $AgPF_6$ solution was added to the vial containing [Cp*Ir(bpy)(Cl)][Cl], and the mixture was stirred for 30 min. The AgCl precipitate was removed from the solution via filtration. The pale yellow filtrate was dried *in vacuo* to afford 11.8 mg of **2** (64% yield). In CD_3CN solution the bound nitrile is deuterated, as evidenced by the presence of

free acetonitrile (δ 1.96).[71] ^{1}H NMR (CD_3CN): δ 8.93 (d, *J* = 5.5 Hz, 2H), 8.52 (d, *J* = 8.1 Hz, 2H), 8.34 (td, *J* = 7.9, 1.4 Hz, 2H), 7.89 (ddd, *J* = 7.3, 5.7, 1.3 Hz, 2H), 1.68 (s, 15H). $^{13}C(^{1}H)$ NMR (CD_3CN): δ 157.09, 153.34, 142.65, 130.58, 125.72, 93.40, 8.71. ESI-MS: calcd. m/z for $C_{22}H_{26}F_6IrN_3P^+$ ([Cp*Ir(bpy)(NCCH$_3$)][PF$_6$]$^+$): 670.14, observed m/z: 670.21. Anal. calcd. for $C_{22}H_{26}F_{12}IrN_3P_2$: C, 32.44; H, 3.22; N, 5.16. Found: C, 32.24; H, 2.95; N, 5.00.

Independent Synthesis of [Cp*Ir(bpy)(OAc)][OAc] (3).

In a nitrogen-filled glovebox, a 20 mL scintillation vial was charged with 5.7 mg (0.0103 mmol) [Cp*Ir(bpy)(Cl)][Cl], and 3.7 mg (0.0222 mmol) AgOAc, and 1 mL of CD_3CN. The reaction mixture was protected from light and stirred for 1 h. The AgCl precipitate was removed from the solution via pipette filtration, yielding a yellow solution. Spectroscopic analysis confirmed that **3** was the product of the photochemical reaction of **1** with HOAc (*vide infra*). ^{1}H NMR (CD_3CN): δ 9.12 (d, *J* = 5.4 Hz, 2H), 8.46 (d, *J* = 8.1 Hz, 2H), 8.22 (td, *J* = 7.9, 1.5 Hz, 2H), 7.77 (ddd, *J* = 7.4, 5.7, 1.5 Hz, 2H), 1.63 (s, 15H), 1.53 (s, 3H). $^{13}C(^{1}H)$ NMR (CD_3CN): δ 176.65, 156.82, 153.27, 141.33, 129.07, 124.80, 88.81, 23.26, 8.85. ESI-MS: calcd. m/z for $C_{22}H_{26}IrN_2O_2^+$ ([Cp*Ir(bpy)(OAc)]$^+$): 543.16, observed m/z: 543.21.

Synthesis of [Cp*Ir(bpy)(μ-N(H)C(CD$_3$))(bpy)IrCp*][OTf]$_3$ (4-OTf).

In a nitrogen-filled glovebox, 6.0 mg (0.0095 mmol) **1** and 0.1 mL CD_3CN (containing mesitylene internal standard) were added to a 20 mL scintillation vial. A second 20 mL scintillation vial was charged with 3.6 mg (0.0616 mmol) sodium chloride and 0.5 mL D_2O. The sodium chloride solution was added to the vial containing **1**, and the mixture was transferred to an NMR tube. Upon 1 h of irradiation, near-complete consumption of **1** was observed along with formation of the [Cp*Ir(bpy)(μ-N(H)C(CD$_3$))(bpy)IrCp*]$^{3+}$ (**4**-OTf) iminoacyl product. See below for a preparative-scale synthesis of the corresponding PF_6 salt, **4**-PF_6. ^{1}H NMR (CD_3CN):

δ 8.88 (d, *J* = 5.1 Hz, 2H), 8.64 (d, *J* = 5.4 Hz, 2H), 8.47 (d, *J* = 7.9 Hz, 2H), 8.40 (d, *J* = 7.9 Hz, 2H), 8.34 (t, *J* = 8.6 Hz, 2H), 8.25 (t, *J* = 7.9 Hz, 2H), 7.82 (t, *J* = 6.4 Hz, 2H), 7.73 (t, *J* = 6.8 Hz, 2H), 1.47 (s, 15H), 1.44 (s, 15H). ESI-MS: calcd. for m/z $C_{43}H_{47}D_3F_3Ir_2N_5O_3S^{2+}$ ([Cp*Ir(bpy)(μ-N(H)C(CD_3))(bpy)IrCp*][OTf]$^{2+}$): 580.15, observed m/z: 580.24.

Synthesis of [Cp*Ir(bpy)(μ-N(H)C(CH_3))(bpy)IrCp*][PF_6]$_3$ (4-PF_6).

In a nitrogen-filled glovebox, a stock solution of sodium chloride was prepared in a 20 mL scintillation vial by dissolving 9.5 mg (0.163 mmol) sodium chloride in 1.0 ml H_2O. Another 20 mL scintillation vial was charged with 0.1 mL of the 0.1625 M stock solution of sodium chloride (0.0162 mmol) in H_2O and an additional 0.9 mL of H_2O. To this vial was added 0.4 mL of a 0.079 M stock solution of **1** (0.0316 mmol) in CH_3CN. A stirbar was added, and the solution was irradiated for 1 h under constant stirring. After photolysis, the vial was brought back into the glovebox and 15.4 mg (0.0945 mmol) ammonium hexafluorophosphate was added to the solution, which resulted in formation of a precipitate. The yellow solids were collected on a glass filter and rinsed with H_2O, followed by CH_2Cl_2. The solids were dissolved in CH_3CN and solvent was removed *in vacuo* to afford [Cp*Ir(bpy)(μ-N(H)C(CH_3))(bpy)IrCp*][PF_6]$_3$ (**4-PF_6**). ^{1}H NMR (CD_3CN): δ 8.78 (d, *J* = 5.5 Hz, 2H), 8.55 (d, *J* = 5.5 Hz, 2H), 8.33 (d, *J* = 7.9, 2H), 8.28 (m, 4H), 8.19 (t, *J* = 7.4 Hz, 2H), 7.77 (t, *J* = 6.2 Hz, 2H), 7.70 (t, *J* = 6.3 Hz, 2H). 1.86 (s, 3H), 1.40 (s, 15H), 1.36 (s, 15H). ^{13}C(^{1}H) NMR (CD_3CN): δ 217.06, 155.97, 155.74, 153.42, 152.51, 142.55, 141.59, 130.68, 130.58, 125.68, 125.40, 93.86, 91.86, 38.28, 8.68, 8.25. ESI-MS: calcd. for $C_{42}H_{50}F_6Ir_2N_5P^{2+}$ ([Cp*Ir(bpy)(μ-N(H)C(CH_3))(bpy)IrCp*][PF_6]$^{2+}$): 576.65, observed. m/z: 576.70. Anal. calcd. for $C_{42}H_{50}F_{18}Ir_2N_5P_3$: C, 34.93; H, 3.49; N, 4.85. Found: C, 34.84; H, 3.24; N, 5.01. IR (cm^{-1}): 1609w, 1536m, 1451m, 1388w, 1031w, 826vs, 765s, 555vs.

Thermodynamic Considerations

Ground State Thermodynamic Calculations.

The ground state hydricity of **1** was determined using previously reported methodology,[31] according to Equation 2.7 to Equation 2.10.

$$[Cp^*Ir(bpy)(H)]^+ \leftrightarrows Cp^*Ir(bpy) + H^+ \qquad \Delta G^o = 1.37\cdot(pK_a) \qquad \text{(Eq. 2.7)}$$

$$Cp^*Ir(bpy) + CH_3CN \leftrightarrows [Cp^*Ir(bpy)(NCCH_3)]^{2+} + 2e^- \qquad \Delta G^o = -(-46.12)\cdot(E^{o\prime}) \qquad \text{(Eq. 2.8)}$$

$$H^+ + 2e^- \leftrightarrows H^- \qquad C_{H^-} = \Delta G^o = (-46.12)\cdot(E^{o\prime}{}_{H^-}) \qquad \text{(Eq. 2.9)}$$

$$[Cp^*Ir(bpy)(H)]^+ + CH_3CN \leftrightarrows [Cp^*Ir(bpy)(NCCH_3)]^{2+} + H^- \qquad \Delta G^o{}_{H^-} \qquad \text{(Eq. 2.10)}$$

The standard conditions for the free energy values are acetonitrile solvent at 298 K, with reduction potentials referenced to the $Cp_2Fe^{+/0}$ couple. The constant C_{H^-} is the free energy for the $2e^-$ reduction of a proton in acetonitrile (C_{H^-} = 79.6 kcal·mol^{-1}).[5, 72] Conversion factors: 1.37 is RT at 298 K (plus a factor of 2.303 to convert log_{10} to log_e) in kcal·mol^{-1}; 46.12 is nF at 298 K for a $2e^-$ process.

To determine the ground state hydricity of **1**, the pK_a of hydride complex **1** and formal potential ($E^{o\prime}$) of acetonitrile complex **2** are required. The half-wave potential ($E_{1/2}$) determined experimentally by cyclic voltammetry is taken to be approximately equal to the formal potential ($E^{o\prime}$) under the standard conditions above. The required thermodynamic values were obtained according to the following procedures.

Determination of the pK_a of **1** in CH_3CN. Spectrophotometric titrations were carried out under N_2 in a glove box using the Cary 60 spectrometer fitted with a fiber optic coupler, fiber optic cables passing through a KF-40 feedthrough, and a cuvette holder inside the glovebox.

A 25 mL solution of **1** (as the PF_6^- salt) was prepared by dissolving 3.7 mg (0.0059 mmol) of **1** in 25 mL of CH_3CN. A 2 mL sample of this solution was added to a cuvette and an initial absorbance spectrum was taken. Additional spectra were taken after additions of 10 μL of

a 0.675 M solution of DBU (DBU = 1,8-diazabicyclo[5.4.0]undec-7-ene, pK_a = 24.34 for conjugate acid HDBU) in CH_3CN (Appendix A, Figure A.10).[35]

The pK_a of **1** was determined by the method outlined by Saouma *et al.*[73] Plots of $([Ir]_t/[IrH]_t)*[HDBU]_t$ vs $[DBU]_t$ at three different wavelengths (550, 620 and 750 nm) were generated, an example of which is shown in Appendix A, Figure A.11. The pK_a was determined at three different wavelengths using the following equation:

$$pK_a(\mathbf{1}) = pK_a(\text{HDBU}) - \log(\text{slope}). \quad \text{(Eq. 2.11)}$$

From the average value at three different wavelengths, **1** has pK_a = 23.3.

Determination of Half-wave Potential, $E_{1/2}$. Solid $[Cp^*Ir(bpy)(NCCH_3)][PF_6]_2$ (9.4 mg, 0.012 mmol) was added to 15 mL 0.1 M $[Bu_4N][PF_6]$ in CH_3CN. A glassy carbon working electrode, platinum counter electrode, and Ag/Ag^+ (10 mM $AgNO_3$ in 0.1 M $[Bu_4N][PF_6]$) reference electrode were used in an undivided cell. Cp_2Fe was added as an internal reference at the end of the experiment. Cyclic voltammetry of $[Cp^*Ir(bpy)(NCCH_3)]^{2+}$ produces a quasi-reversible $2e^-$ redox couple at −1.07 V vs. $Cp_2Fe^{+/0}$ (ΔE_p = 135 mV; ΔE_p for Cp_2Fe = 80 mV).

Determination of hydricity, ΔG^o_{H-}. The ground state hydricity of **1** was determined by conversion of the measured pK_a and $E_{1/2}$ values to free energy values, according to Equation 2.12. The solved equation is provided in Equation 2.13. Hydricity values determined in this way are considered to have uncertainty of roughly ±1 kcal·mol^{-1}.

$$\Delta G^o_{H-} = 1.37\cdot(pK_a) - (-46.12)\cdot(E_{1/2}) + C_{H-} \quad \text{(Eq. 2.12)}$$

$$\Delta G^o_{H-} = 1.37\cdot(23.3) - (-46.12)\cdot(-1.07) + 79.6 = 62 \text{ kcal·mol}^{-1} \quad \text{(Eq. 2.13)}$$

Excited State Thermodynamic Considerations and Calculations.

A new method for determining excited state hydricity is presented, based on the ground state methods just discussed. Scheme 2.2 portrays a “cube scheme” showing the possible

pathways for the release of H^- from excited state **1***. Note that, unlike ground state hydricity, there are *two possible definitions* of excited state hydricity according to Scheme 2.2: (a) hydride transfer from **1*** with simultaneous relaxation to the ground state ($\Delta G^o_{H^-}$*); (b) hydride transfer from **1*** without relaxation ($\Delta G^o_{H^-}$*'). Analogous mechanistic distinctions have been made in photoacid reactions.[42] We favor $\Delta G^o_{H^-}$* in analogy to excited state electron transfer reactions, which are always considered as occurring with concomitant relaxation to the ground state.[41] Further evidence comes Fukuzumi's report of very strong photoacidity, consistent with proton transfer coupled to relaxation.[17]

Equation 2.14 to Equation 2.17 correspond to the situation of Scheme 2.2. The standard conditions were chosen to match those of the ground state hydricity determination. The formal potentials for Equations 2.15 and Equation 2.16 were already established above. Thus, only the excited state acidity, pK_a*, must be estimated.

$$[Cp^*Ir(bpy)(H)]^+* \leftrightarrows Cp^*Ir(bpy) + H^+ \qquad \Delta G^o = 1.37(pK_a^*) \qquad \text{(Eq. 2.14)}$$

$$Cp^*Ir(bpy) + CH_3CN \leftrightarrows [Cp^*Ir(bpy)(NCCH_3)]^{2+} + 2e^- \qquad \Delta G^o = -(-46.12)\cdot(E^{o\prime}) \qquad \text{(Eq. 2.15)}$$

$$H^+ + 2e^- \leftrightarrows H^- \qquad C_{H^-} = \Delta G^o = (-46.12)\cdot(E^{o\prime}_{H^-}) \qquad \text{(Eq. 2.16)}$$

$$[Cp^*Ir(bpy)(H)]^+* + CH_3CN \leftrightarrows [Cp^*Ir(bpy)(NCCH_3)]^{2+} + H^- \qquad \Delta G^o_{H^-}* \qquad \text{(Eq. 2.17)}$$

$$\Delta G^o_{H^-}* = 1.37\cdot(pK_a^*) - (-46.12)\cdot(E_{1/2}) + C_{H^-} \qquad \text{(Eq. 2.18)}$$

Determination of Excited State Acidity of 1, pK_a*.* As shown in Scheme 2.2, the pK_a* of **1** can be estimated based on the energy difference between the lowest vibrational states of **1** and **1***, E_{00}, and the ground state pK_a. This relationship is also written in Equation 2.19 to Equation 2.21. To determine E_{00}, the excitation and emission spectra of **1** were obtained. In a nitrogen-filled glovebox, 4 mL of 1.8 x 10^{-5} M solution of **1** in CH_3CN was added to a quartz fluorescence cuvette. An emission spectrum was recorded between 500 and 800 nm by exciting at 428 nm. An excitation spectrum was recorded between 360 and 600 nm by monitoring emission at 680

nm. An emission maximum was observed at 708 nm, featuring no overlap with the excitation spectrum. The low-energy edge of the emission spectrum was estimated as the x-intercept value of a linear fit to the rising edge of the emission feature: E_{00} = 16,900 cm^{-1}. The excited state acidity was determined to be pK_a* = –12 using Equation 2.22. A conversion factor of 1/350 converts wavenumbers to kcal·mol^{-1}.

$[Cp^*Ir(bpy)(H)]^{+}$* ⇆ $[Cp^*Ir(bpy)(H)]^{+}$ $\Delta G^o = -(1/350)\cdot(E_{00})$ (Eq. 2.19)

$[Cp^*Ir(bpy)(H)]^{+}$ ⇆ $[Cp^*Ir(bpy)(H)]^{+} + H^+$ $\Delta G^o = 1.37\cdot(pK_a)$ (Eq. 2.20)

$[Cp^*Ir(bpy)(H)]^{+}$* ⇆ $Cp^*Ir(bpy) + H^+$ $\Delta G^o = 1.37\cdot(pK_a^*)$ (Eq. 2.21)

$1.37\cdot(pK_a^*) = -(1/350)\cdot(E_{00}) + 1.37\cdot(pK_a)$ (Eq. 2.22)

Determination of Excited State Hydricity. With an estimate for the excited state acidity, pK_a*, the excited state hydricity can in turn be estimated using Equation 2.23. The numerical solution is provided in Equation 2.24.

$\Delta G^o_{H^-}{}^* = -(1/350)\cdot E_{00} + 1.37\cdot(pK_a) - (-46.12)\cdot(E_{1/2}) + C_{H^-}$ (Eq. 2.23)

$\Delta G^o_{H^-}{}^* = -(1/350)\cdot(16{,}900) + 1.37\cdot(pK_a) - (-46.12)\cdot(E_{1/2}) + C_{H^-} = 14$ kcal·mol^{-1} (Eq. 2.24)

Determination of Alternate Excited State Hydricity ($\Delta G^o_{H^-}{}^{*\prime}$). The alternative hydricity, $\Delta G^o_{H^-}{}^{*\prime}$, can be estimated by adding E_{00}(**2**) to the value of $\Delta G^o_{H^-}{}^*$. As such, the numerical value will be larger, suggesting that it is less favorable to undergo hydride transfer without simultaneous relaxation to the ground state. The acetonitrile complex $[Cp^*Ir(bpy)(NCCH_3)]^{2+}$ (**2**) is apparently non-emissive,[74] so only very crude estimates of E_{00}(**2**) can be made. One such estimate involves taking the difference in λ_{max} of **1** (λ_{max} = 433 nm) and **2** (λ_{max} = 312 nm), and adding that energy difference to E_{00}(**1**). According to this gross simplification, one can estimate E_{00}(**2**) = 26,300 cm^{-1}. Adding this energy to the $\Delta G^o_{H^-}{}^*$ gives $\Delta G^o_{H^-}{}^{*\prime}$ = 88 kcal·mol^{-1}. This value would indicate a *weaker* excited state hydride donor — contrary to experimental observations.

Experimental Evaluation of Hydricity Based on H_2 Evolution.

The ground state hydricity has also been determined by establishing equilibrium between H_2 bond formation and cleavage.[37] According to Equation. 2.25 through Equation 2.27, the propensity of a specific hydride/acid pair to release H_2 is related to the hydricity and the acidity of each species. In the present context, this method has been used simply to establish reaction favorability. The previously determined hydricity can be used to predict which acids will react with the hydride of interest to release H_2. The 76 kcal·mol^{-1} value is derived from the bond dissociation free energy of H_2, the ionization energy of H and the electron affinity of H.[37]

$$MH^+ + HBase^+ \leftrightarrows M^{2+} + H_2 + Base \quad \Delta G^o = 1.37\cdot(pK_{eq}) \quad \text{(Eq. 2.25)}$$

$$Base + H^+ \leftrightarrows HBase^+ \quad \Delta G^o = -1.37\cdot(pK_a) \quad \text{(Eq. 2.26)}$$

$$\underline{H_2 \leftrightarrows H^+ + H^-} \quad \underline{\Delta G^o = 76 \text{ kcal}\cdot\text{mol}^{-1}} \quad \text{(Eq. 2.27)}$$

$$MH^+ \leftrightarrows M^{2+} + H^- \quad \Delta G^o_{H-} \quad \text{(Eq. 2.28)}$$

This method can be used to check either the ground state hydricity or excited state hydricity. For example, the hydricity of **1** was determined to be 62 kcal·mol^{-1}, so the reaction with methanesulfonic acid (pK_a = 10.0)[36] is predicted to be favorable.

$$\Delta G^o_{H-} = -1.37\cdot\log(K_{eq}) - 1.37\cdot(pK_a) + 76 \quad \text{(Eq. 2.29)}$$

$$\Delta G^o_{H-} = \Delta G^o_{rxn} - 1.37\cdot(10.0) + 76 = 62 \text{ kcal}\cdot\text{mol}^{-1} \quad \text{(Eq. 2.30)}$$

$$\Delta G^o_{rxn} = -0.3 \text{ kcal}\cdot\text{mol}^{-1} \quad \text{(Eq. 2.31)}$$

As predicted, solutions of **1** react with methanesulfonic acid in the dark to produce H_2 and $[Cp^*Ir(bpy)(NCCH_3)]^{2+}$. On the other hand, solutions of **1** and pyridinium *p*-toluenesulfonate (pK_a = 12.5)[35] were not observed to react in the dark, consistent with the predicted ΔG^o_{rxn} = +3 kcal·mol^{-1}.

Based on the excited state hydricity estimate of 14 kcal·mol^{-1}, acids as weakly acidic as pK_a = 46 would be expected to release H_2 under photolysis! This prediction could only be tested

experimentally up to a pK_a value of 23.5 for acetic acid.[34] The use of weaker acids led to decomposition reactions (see Results and Discussion above).

The same set of equations can be used to put an experimental upper limit on the numerical value of the excited state hydricity, ΔG^o_{H-}*, based on the irreversible reaction observed with acetic acid. No attempts to establish equilibrium with H_2 were made. Rather, the hydrogen evolving reaction with acetic acid that proceeded to completion was assigned a minimum value of K_{eq} = 10. Based on this assumption, Equation 2.32 to Equation 2.33 were used to provide a hydricity estimate of ΔG^o_{H-}* < 43 kcal·mol^{-1}.

$$\Delta G^o_{H-}* < -1.37 \cdot \log(K_{eq}) - 1.37 \cdot (pK_a) + 76 \quad \text{(Eq. 2.32)}$$

$$\Delta G^o_{H-}* < -1.37 \cdot \log(10) - 1.37 \cdot (23.3) + 76 \quad \text{(Eq. 2.33)}$$

$$\Delta G^o_{H-}* < 43 \text{ kcal} \cdot \text{mol}^{-1} \quad \text{(Eq. 2.34)}$$

NMR Scale Reactions: Organic Acids

General Procedure.

Reactions with organic acids were carried out on an NMR scale. Reaction mixtures in NMR tubes were prepared in a nitrogen-filled glovebox as described in specific cases below, and the tubes were sealed and wrapped with parafilm. After initial NMR spectra were taken, one (light) sample was illuminated with the 460 nm LED lamp for the desired time. The other (dark) sample was protected from light. The given reaction times for light samples are the time under active irradiation (time protected from light, where no background reaction was observed, is not counted); for dark samples, it is the total reaction time from initial reactant mixing. The reaction was monitored by NMR spectroscopy periodically. Product yields were determined from NMR integrations relative to a mesitylene internal standard and are based upon the amount of **1** at the beginning of the reaction. The yield of H_2 and the photochemical quantum yield were established in representative examples as described below.

Reactions with Organic Acids

Reaction of 1 with methanesulfonic acid. A 20 mL scintillation vial was charged with 2.0 mg (0.0032 mmol) **1** and 0.5 mL of CD_3CN (containing mesitylene internal standard). Methanesulfonic acid (1.3 µL, 0.0200 mmol) was added to the reaction mixture and the contents were transferred to an NMR tube, protected from light. Within 10 minutes in the dark, conversion to $[Cp^*Ir(bpy)(NCCD_3)]^{2+}$ (**2**) exceeded 70%. After 1 h in the dark, complete conversion to **2** was observed.

Reaction of 1 with pyridinium p-toluenesulfonate. A 20 mL scintillation vial was charged with 1.9 mg (0.0074 mmol) pyridinium p-toluenesulfonate. A 0.333 mL aliquot of a 0.011 M stock solution of **1** (0.0037 mmol) was added using a micropipette. To this solution was added 0.666 mL of CD_3CN (containing mesitylene internal standard). The mixture was divided into two NMR tubes (~0.5 mL per tube) and monitored by NMR spectroscopy. In the dark, no reaction was observed over 1 h. Upon 1 h of irradiation, complete consumption of **1** was observed along with formation of the $[Cp^*Ir(bpy)(py)]^{2+}$ product. Spectroscopic details for $[Cp^*Ir(bpy)(py)]^{2+}$: ^1H NMR (CD_3CN): δ 9.17 (d, J = 5.5 Hz, 2H), 8.47 (d, J = 8.0 Hz, 2H), 8.31 (td, J = 7.8, 1.2 Hz, 2H), 8.29 (dd, J = 6.6, 1.2 Hz, 2H), 8.01 (ddd, J = 7.3, 5.7, 1.2 Hz, 2H), 7.89 (tt, J = 7.8, 1.2 Hz, 1H), 7.43 (td, J = 6.6, 1.2 Hz, 2H), 1.55 (s, 15H). ESI-MS: calcd. for $C_{25}H_{28}IrN_3^{2+}$ ($[Cp^*Ir(bpy)(py)]^{2+}$): 281.60, observed m/z: 281.54.

Reaction of 1 with pyridinium p-toluenesulfonate: thermal stability. A 20 mL scintillation vial was charged with 4.3 mg (0.0068 mmol) **1**. A second 20 mL scintillation vial was charged with 0.216 mL CD_3CN (containing mesitylene internal standard) and 0.284 mL of a 0.036 M stock solution of pyridinium p-toluenesulfonate (0.0102 mmol). The pyridinium solution was added to the vial containing **1**, and the mixture was transferred to a J. Young NMR

tube, protected from light. Upon heating at 80 ºC for 3 h under foil protection, ~10% of the $[Cp^*Ir(bpy)(py)]^{2+}$ product had formed.

Reaction of 1 with triethylammonium tetrafluoroborate. A 20 mL scintillation vial was charged with 0.352 mL of a 0.049 M stock solution of triethylammonium tetrafluoroborate (0.0173 mmol) and 0.103 mL CD_3CN (containing mesitylene internal standard). To this mixture was added 0.045 mL of a 0.035 M stock solution of **1** (0.0016 mmol). The reaction mixture was transferred to an NMR tube and protected from light. An initial (dark) spectrum was obtained before illumination with 460 nm LED light for 10 min, after which time nearly quantitative formation of $[Cp^*Ir(bpy)(NCCD_3)]^{2+}$ (**2**) was observed. In similar experiments that were fully protected from light, no reaction was observed over 1 hour in the dark.

Reaction of 1 with acetic acid. A 20 mL scintillation vial was charged with 0.5 mL of CD_3CN (containing mesitylene internal standard) and 0.029 mL of a 0.107 M stock solution of **1** (0.0032 mmol). To this mixture was added 3.0 µL (0.0525 mmol) acetic acid and the contents were transferred to an NMR tube, protected from light. After an initial NMR spectrum was obtained, the sample was illuminated with 460 nm LED light for 10 min, after which time nearly quantitative conversion of **1** to the acetate complex $[Cp^*Ir(bpy)(OAc)]^+$ (**3**) was observed. In similar experiments protected from light, no reaction was observed after 1 h.

Reaction of 1 with acids weaker than acetic acid. Attempts to observe H_2 release from very weak acids, in analogous fashion to reactions shown above, resulted in complex mixtures of products. The conjugate acid of *tert*-butyliminotripyrrolidino)phosphorane (HP_1^+; p*K*a = 28.42),[35] synthesized by addition of HBF_4•OEt_2 to P_1 in ether under N_2 to form a precipitate that was isolated by filtration, was irradiated with **1**. After 1 hour, a mixture of products was

observed, including iminoacyl complex **4** along with other unidentified species. Irradiation of *n*-butanol (p*K*a > 30) and **1** for 1 h led to a similar mixture of products.

NMR Scale Reactions: MNA^+ Salts

General Procedure.

Reactions with MNA^+ salts were carried out on an NMR scale. Reaction mixtures in NMR tubes were prepared in a nitrogen-filled glovebox as described in specific cases below, and the tubes were sealed and wrapped with parafilm. Initial NMR spectra were obtained. The salt [MNA][I] is not highly soluble in CD_3CN, so the exact ratio of **1**:MNA^+ was determined by integration relative to the internal standard at the start of the reaction. The light sample was then illuminated using the 460 nm LED lamp for the desired time. The dark sample was protected from light. The given reaction times for light samples are the time under active irradiation (time protected from light, when minor background reactions do occur in some cases, are not counted); for dark samples, it is the total reaction time. The reactions were monitored by NMR spectroscopy. Yields for products were determined from NMR integrations relative to the mesitylene internal standard and are based upon the limiting reagent. Because MNA-H_3 is formed from two hydride transfers, the maximum theoretical yield of MNA-H_3 is 50% in reactions where **1** is the limiting reagent. The products MNA-H, MNA-H', and MNA-H_3 were assigned by comparison to independently synthesized samples (see General Considerations section for details) that displayed diagnostic methyl resonances at δ 2.89, 2.79, and 2.85, respectively. The other commonly observed nicotinamide-containing product was the complex of the conjugate base of MNA^+, $[Cp^*Ir(bpy)(MNA)]^{2+}$. The methyl resonance for $[Cp^*Ir(bpy)(MNA)]^{2+}$ appears at δ 4.18, while the corresponding Cp* peaks appears at δ 1.69.

Further support for the structure was obtained by ESI-MS: calcd. for $C_{27}H_{31}IrN_4O^{2+}$ ($[Cp^*Ir(bpy)(MNA)]^{2+}$): 310.11, observed m/z: 310.16.

Reactions with MNA^+ Salts.

Reaction of 1 with [MNA][BF_4] (1:1.7). A 20 mL scintillation vial was charged with 0.5 mL of a 0.011 M stock solution of **1** (0.0055 mmol) in CD_3CN and 1.0 mL of CD_3CN (containing mesitylene internal standard). Solid [MNA][BF_4] (2.1 mg, 0.0094 mmol) was added to the vial, and ~0.5 mL was added to each of two NMR tubes, protected from light. One tube was continuously protected from light, and one tube was illuminated with the 460 nm LED lamp for the desired amount of time. The reaction was monitored by NMR spectroscopy. No reaction was observed in the dark over 1 h. After 1 h of illumination, the major product was MNA-H_3 (~10% yield).

Reaction of 1 with [MNA][I] (1:1.5). A stock solution of [MNA][I] was prepared in a 20 mL scintillation vial by dissolving 10.7 mg (0.0405 mmol) [MNA][I] in 1.0 mL CD_3CN. Another 20 mL scintillation vial was charged with 0.779 mL of the 0.0405 M stock solution of [MNA][I] (nominally 0.0316 mmol) in CD_3CN and 0.221 mL of CD_3CN (containing mesitylene internal standard). To this vial was added 0.178 mL of a 0.035 M stock solution of **1** (nominally 0.0063 mmol) in CD_3CN. The mixture was divided equally into two NMR tubes, protected from light. Initial NMR spectra provided the actual concentration of MNA^+ (9.0 mM) and **1** (6.0 mM). The reaction was monitored by ^1H NMR spectroscopy. In the dark, significant amounts of MNA-H and MNA-H' were observed only after 6 h. No MNA-H_3 was observed in the dark. After 3 min of illumination, 37% yield of MNA-H was observed. See Appendix A for additional details.

Reaction of 1 with [MNA][I] (1:4.4). A stock solution of [MNA][I] was prepared in a 20 mL scintillation vial by dissolving 6.0 mg (0.0227 mmol) [MNA][I] in 1.0 mL CD_3CN. Another

20 mL scintillation vial was charged with 0.126 mL CD_3CN (containing mesitylene internal standard) and 0.763 mL of the 0.0227 M stock solution of [MNA][I] (nominally 0.0173 mmol) in CD_3CN. To this vial was added 0.111 mL of a 0.014 M stock solution of **1** (nominally 0.0016 mmol) in CD_3CN. The mixture was divided equally into two NMR tubes, protected from light. Initial NMR spectra provided the actual concentration of MNA^+ (5.6 mM) and **1** (1.3 mM). The reaction was monitored by ^1H NMR spectroscopy. In the dark, no reduced products were observed after 1 h. Under illumination, moderate yields of reduced products were achieved after 10 min. See Appendix A for additional details.

Reaction of 1 with [MNA][I] (4.0:1). A 20 mL scintillation vial was charged with 5.1 mg (0.0080 mmol) **1**. A stock solution of [MNA][I] was prepared in another 20 mL scintillation vial by dissolving 1.8 mg (0.0068 mmol) [MNA][I] in 0.3 mL CD_3CN. Another 20 mL scintillation vial was charged with 0.787 mL CD_3CN (containing mesitylene internal standard) and 0.212 mL of the 0.0227 M stock solution of [MNA][I] (nominally 0.0048 mmol) in CD_3CN. The mixture was added to the vial containing **1**, and the mixture was divided equally into two NMR tubes, protected from light. Initial NMR spectra provided the actual concentration of MNA^+ (1.7 mM) and **1** (6.8 mM). The reaction was monitored by ^1H NMR spectroscopy. In the dark, a minor background reaction was observed, with singly reduced products MNA-H (21% yield) and MNA-H' (13% yield) formed after 1 h (no doubly-reduced product was observed). Under illumination, after initial formation of MNA-H and MNA-H', the only observed product was doubly-reduced MNA-H_3 (21% yield) after 1 h. See Appendix A for additional details.

Determining H_2 Yield

H_2 quantification was performed using a Varian 450-GC with a pulsed discharge helium ionizer detector. A calibration curve was made from samples of 0.5, 1.0, 3.0, and 5.0 v/v% H_2 in

air.[26] Samples of **1** and HOAc were prepared in NMR tubes, each equipped with a pierceable septum. Once the septum was covered in grease and parafilm to avoid H_2 leakage from the NMR tube, the samples were irradiated for 20 min and allowed to sit for 20 min (allowing dissolved H_2 to enter the headspace in the NMR tube) prior to analysis. A 1.0 mL Vici Pressure-Lok Precision Analytical syringe was used to sample the headspace and the NMR septum cap was pierced only once to prevent H_2 leakage. From the H_2 calibration curve, H_2 yield was determined to be 74%.

Quantum Yield Using Chemical Actinometry

The excited state hydride transfer efficiency can be determined, at least in part, by the quantum yield of the reaction. In determining the photon flux of the 460 nm LED lamp, it is essential to directly mimic NMR reaction conditions described above by maintaining the same light source and distance from the light. Chemical actinometry provides a convenient means to exactly replicate prior experimental conditions, as the actinometer can be placed inside an NMR tube and be treated as a traditional sample. Potassium ferrioxalate, $[K_3][Fe(C_2O_4)_3]$, was selected as the chemical actinometer, based on the wavelength of irradiated light and well-characterized properties (molar absorptivity and known quantum yield at a variety of wavelengths and concentrations).

Potassium ferrioxalate was synthesized by stirring potassium oxalate and iron (III) chloride in H_2O heated at 70 ºC for 30 min under light protection. The product was recrystallized three times in an ice bath, followed by filtration and solvent removal in vacuo. IR spectroscopy was used to confirm product identity, with the spectrum matching well with the literature.[75] Chemical actinometry using potassium ferrioxalate was performed according to literature.[45-47, 76] In a typical experiment, 0.5 mL of 0.2 M potassium ferrioxalate were added to an NMR tube and irradiated for 2 min. After 2 min, the irradiated sample was transferred to a cuvette containing DI

H_2O and the absorbance spectrum was obtained. Afterwards, a developer solution of sodium acetate, 1,10-phenanthroline, and H_2SO_4 was added to the irradiated sample. The solution was transferred to a cuvette and the absorbance spectrum of the $Fe(phen)_3^{2+}$ complex was found to match the literature, with strong absorbance at 510 nm (ε = 11,100 $M^{-1}\cdot cm^{-1}$). From the absorbance value at 510 nm, the concentration of $Fe(phen)_3^{2+}$ was determined and using the known quantum yield of the actinometer at an irradiation wavelength of 460 nm, photon flux can be calculated. From a series of seven samples, the average photon flux was determined to be 2.179 x 10^{-8} mol photons$\cdot s^{-1}$.

To confirm the photon flux value obtained from chemical actinometry, photon flux was also measured using a Coherent LM-2VIS photodiode with a Coherent $FieldMax_{II}$ Laser Power/Energy Meter. The photodiode was positioned at the same distance from the 460 nm LED lamp as the NMR tubes, and a piece of glass was used to approximate the conditions of the NMR tube. Irradiance (mW/cm^2) was measured six times, averaged, and converted to photon flux (mol photons/s). At 2.159 x 10^{-8} mol photons$\cdot s^{-1}$, the photon flux value measured from the photodiode was in great agreement with the photon flux obtained from chemical actinometry.

Once the photon flux determined from chemical actinometry had been verified using the photodiode, quantum yield was calculated for different NMR tube reactions by determining the mol of product from NMR spectroscopy and dividing by the photon flux (multiplied by the irradiation time, in seconds).

Table 2.2. Quantum yield for visible light-promoted hydride transfer reactions from $[Cp^*Ir(bpy)(H)]^+$ to MNA^+.[a]

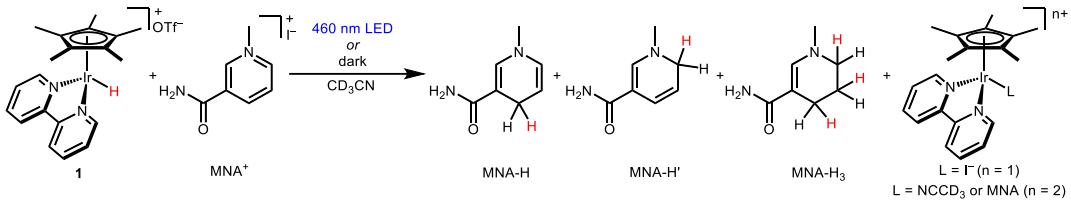

[**1**]:[MNA^+]	Time (min)	Φ MNA-H	Φ MNA-H'	Φ MNA-H_3	Φ Total Reduced MNA
1:1.5	10	0.169	0.031	0.046	0.246
1:4.4	10	0.049	0.007	0.003	0.059
4.0:1	10	0.023	0.003	0.016	0.043

[a]Φ determined from moles of product (from ^1H NMR relative to mesitylene internal standard) and photon flux after 10 min of irradiation (obtained from chemical actinometry).

Crystallographic Details

Single crystals of **4**-PF_6 [sb106_c] were grown from slow vapor diffusion of ether into a CH_3CN solution of the complex at room temperature. A suitable crystal was selected and mounted using polymer tips and paratone oil. Single-crystal X-ray diffraction of **4**-PF_6 was collected on a Bruker APEX-II CCD diffractometer. The crystal was kept at 100.15 K during data collection. The frames were integrated with the Bruker SAINT software in APEX II. A numerical absorption correction was used, and the structure was solved by direct methods using the SHELXTL software suite. Final structural refinement was performed with the SHELXL refinement program in Olex2[77] using Least Squares minimization. Initially, the bridged N1 and C1 atoms appeared to be disordered. This was determined to be the result of a 63:37 inversion twin which was included in the refinement using a TWIN parameter, with a BASF of 0.37(2). All non-NH hydrogens were calculated and refined with a riding model. The imine NH hydrogen

was positioned geometrically and refined with a riding model. See Appendix A for additional details.

2.5 Acknowledgements

C.L.P. performed electrochemical and photophysical experiments. A.G.W. performed spectrophotometric titrations. S.M.B. performed all other experiments. We gratefully acknowledge funding from The University of North Carolina at Chapel Hill, the NSF Center for Enabling New Technologies Through Catalysis (CHE-0650456), a NSF Graduate Research Fellowship to S.M.B. (DGE-1144081), and the Royster Society of Fellows (C.L.P.). The authors would like to thank Peter White for crystallographic assistance and discussion. This research made use of instrumentation funded by the UNC EFRC: Center for Solar Fuels, and Energy Frontier Research Center supported by the U.S. Department of Energy, Office of Science, Office of Basic Energy Sciences, under award number DE-SC0001011.

2.6 Associated Content

Appendix A: Additional experimental details, crystallographic data, GC traces, details of chemical actinometry.

REFERENCES

1. Bullock, R. M., *Chem. Eur. J.* **2004,** *10*, 2366.

2. Clapham, S. E.; Hadzovic, A.; Morris, R. H., *Coord. Chem. Rev.* **2004,** *248*, 2201.

3. Samec, J. S. M.; Bäckvall, J. E.; Andersson, P. G.; Brandt, P., *Chem. Soc. Rev.* **2006,** *35*, 237.

4. Dub, P. A.; Ikariya, T., *ACS Catal.* **2012,** *2*, 1718.

5. DuBois, M. R.; DuBois, D. L., *Chem. Soc. Rev.* **2009,** *38*, 62.

6. Kreevoy, M. M.; Ostovic, D.; Lee, I. S. H.; Binder, D. A.; King, G. W., *J. Am. Chem. Soc.* **1988,** *110*, 524.

7. Anne, A.; Moiroux, J., *J. Org. Chem.* **1990,** *55*, 4608.

8. Cheng, J. P.; Lu, Y.; Zhu, X.; Mu, L., *J. Org. Chem.* **1998,** *63*, 6108.

9. Sarker, N.; Bruno, J. W., *J. Am. Chem. Soc.* **1999,** *121*, 2174.

10. Ogo, S.; Makihara, N.; Kaneko, Y.; Watanabe, Y., *Organometallics* **2001,** *20*, 4903.

11. Abura, T.; Ogo, S.; Watanabe, Y.; Fukuzumi, S., *J. Am. Chem. Soc.* **2003,** *125*, 4149.

12. Gabrielsson, A.; van Leeuwen, P.; Kaim, W., *Chem. Commun.* **2006**, 4926.

13. Ogo, S.; Kabe, R.; Hayashi, H.; Harada, R.; Fukuzumi, S., *Dalton Trans.* **2006**, 4657.

14. Himeda, Y.; Miyazawa, S.; Onozawa-Komatsuzaki, N.; Hirose, T.; Kasuga, K., *Dalton Trans.* **2009**, 6286.

15. Miller, A. J. M.; Heinekey, D. M.; Mayer, J. M.; Goldberg, K. I., *Angew. Chem., Int. Ed.* **2013,** *52*, 3981.

16. Brewster, T. P.; Miller, A. J. M.; Heinekey, D. M.; Goldberg, K. I., *J. Am. Chem. Soc.* **2013,** *135*, 16022.

17. Suenobu, T.; Guldi, D. M.; Ogo, S.; Fukuzumi, S., *Angew. Chem., Int. Ed.* **2003,** *42*, 5492.

18. Ziessel, R., *J. Chem. Soc., Chem. Commun.* **1988**, 16.

19. Ziessel, R., *Angew. Chem., Int. Ed.* **1991,** *30*, 844.

20. Watson, K. J.; Ziessel, R., *Inorg. Chim. Acta* **1992,** *197*, 125.

21. Ziessel, R., *J. Am. Chem. Soc.* **1993,** *115*.

22. Wang, W.; Rauchfuss, T. B.; Bertini, L.; Zampella, G., *J. Am. Chem. Soc.* **2012,** *134*, 4525.

23. McSkimming, A.; Colbran, S. B., *Chem. Soc. Rev.* **2013,** *42*, 5439.

24. Polyansky, D.; Cabelli, D.; Muckerman, J. T.; Fujita, E.; Koizumi, T.; Fukushima, T.; Wada, T.; Tanaka, K., *Angew. Chem., Int. Ed.* **2007,** *46*, 4169.

25. Yang, X.; Walpita, J.; Zhou, D.; Luk, H. L.; Vyas, S.; Khnayzer, R. S.; Tiwari, S. C.; Diri, K.; Hadad, C. M.; Castellano, F. N.; Krylov, A. I.; Glusac, K. D., *J. Phys. Chem. B* **2013,** *117*, 15290.

26. Pitman, C. L.; Miller, A. J. M., *ACS Catal.* **2014,** *4*, 2727.

27. DuBois, D. L.; Berning, D. E., *Appl. Organomet. Chem.* **2000,** *14*, 860.

28. Muckerman, J. T.; Achord, P.; Creutz, C.; Polyansky, D. E.; Fujita, E., *Proc. Natl. Acad. Sci. U.S.A.* **2012,** *109*, 15657.

29. Horn, M.; Schappele, L. H.; Lang-Wittkowski, G.; Mayr, H.; Ofial, A. R., *Chem. Eur. J.* **2013,** *19*, 249.

30. Bullock, R. M.; Appel, A. M.; Helm, M. L., *Chem. Commun.* **2014,** *50*, 3125.

31. Berning, D. E.; Noll, B. C.; DuBois, D. L., *J. Am. Chem. Soc.* **1999,** *121*, 11432.

32. Zhu, X. Q.; Li, H. R.; Li, Q.; Ai, T.; Lu, J. Y.; Yang, Y.; Cheng, J. P., *Chem.-Eur. J.* **2003,** *9*, 871.

33. Ellis, W. W.; Raebiger, J. W.; Curtis, C. J.; Bruno, J. W.; DuBois, D. L., *J. Am. Chem. Soc.* **2004,** *126*, 2738.

34. Kütt, A.; Leito, I.; Kaljurand, I.; Sooväli, L.; Vlasov, V. M.; Yagupolskii, L. M.; Koppel, I. A., *J. Org. Chem.* **2006,** *71*, 2829.

35. Kaljurand, I.; Kuett, A.; Soovaeli, L.; Rodima, T.; Maeemets, V.; Leito, I.; Koppel, I. A., *J. Org. Chem.* **2005,** *70*, 1019.

36. Eckert, F.; Leito, I.; Kaljurand, I.; Kütt, A.; Klamt, A.; Diedenhofen, M., *J. Comput. Chem.* **2009,** *30*, 799.

37. Curtis, C. J.; Miedaner, A.; Ellis, W. W.; DuBois, D. L., *J. Am. Chem. Soc.* **2002,** *124*, 1918.

38. Shizuka, H., *Acc. Chem. Res.* **1985,** *18*, 141.

39. Arnaut, L. G.; Formosinho, S. J., *J. Photochem. Photobiol., A* **1993,** *75*, 1.

40. Tolbert, L. M.; Solntsev, K. M., *Acc. Chem. Res.* **2002,** *35*, 19.

41. Vlček, A., *Coord. Chem. Rev.* **2000,** *200–202*, 933.

42. Dempsey, J. L.; Winkler, J. R.; Gray, H. B., *J. Am. Chem. Soc.* **2010,** *132*, 16774.

43. Mock, M. T.; Potter, R. G.; O'Hagan, M. J.; Camaioni, D. M.; Dougherty, W. G.; Kassel, W. S.; DuBois, D. L., *Inorg. Chem.* **2011,** *50*, 11914.

44. Ladwig, M.; Kaim, W., *J. Organomet. Chem.* **1992,** *439*, 79.

45. Kuhn, H. J.; Braslavsky, S. E.; Schmidt, R., *Pure Appl. Chem.* **2004,** *76*, 2105.

46. Murov, S. L.; Carmichael, I.; Hug, G. L., *Handbook of Photochemistry*. 1993; p 298.

47. Gandolfi, M. T.; Moggi, L., *The Exploration of Supramolecular Systems and Nanostructures by Photochemical Techniques*. 2012; p 67.

48. Andrews, M. A.; Van Buskirk, G.; Knobler, C. B.; Kaesz, H. D., *J. Am. Chem. Soc.* **1979,** *101*, 7245.

49. Adams, R. D.; Katahira, D. A.; Yang, L. W., *J. Organomet. Chem.* **1981,** *219*, 85.

50. Clegg, W.; Feeder, N.; Martin Castro, A. M.; Nahar, S.; Raithby, P. R.; Shields, G. P.; Teat, S. J., *J. Organomet. Chem.* **1999,** *573*, 237.

51. Takagi, F.; Seino, H.; Hidai, M.; Mizobe, Y., *Organometallics* **2003,** *22*, 1065.

52. Kawashima, T.; Takao, T.; Suzuki, H., *Angew. Chem., Int. Ed.* **2006,** *45*, 485.

53. Okamoto, T.; Yamamoto, S.; Oka, S., *J. Mol. Catal.* **1987,** *39*, 219.

54. Yamada, S.; Kuramoto, M.; Kikugawa, Y., *Tetrahedron Lett.* **1969,** *10*, 3101.

55. Freifelder, M., *J. Org. Chem.* **1964,** *29*, 2895.

56. Quirion, J. C., *Science of Synthesis*. 2007; Vol. 33, p 629.

57. Rosentreter, U., *Synthesis* **1985**, 210.

58. Minato, H.; Fujie, S.; Okuma, K.; Kobayashi, M., *Chem. Lett.* **1977,** *6*, 1091.

59. Hu, Y.; Li, L.; Shaw, A. P.; Norton, J. R.; Sattler, W.; Rong, Y., *Organometallics* **2012,** *31*, 5058.

60. Hu, Y.; Norton, J. R., *J. Am. Chem. Soc.* **2014,** *136*, 5938.

61. Matsubara, Y.; Fujita, E.; Doherty, M. D.; Muckerman, J. T.; Creutz, C., *J. Am. Chem. Soc.* **2012,** *134*, 15743.

62. Ruppert, R.; Herrmann, S.; Steckhan, E., *Tetrahedron Lett.* **1987,** *28*, 6583.

63. Lo, H. C.; Buriez, O.; Kerr, J. B.; Fish, R. H., *Angew. Chem., Int. Ed.* **1999,** *38*, 1429.

64. Kobayashi, A.; Konno, H.; Sakamoto, K.; Sekine, A.; Ohashi, Y.; Iida, M.; Ishitani, O., *Chem. Eur. J.* **2005,** *11*, 4219.

65. White, C.; Yates, A.; Maitlis, P. M., *Inorg. Synth.* **1992,** *29*, 228.

66. Dadci, L.; Elias, H.; Frey, U.; Hoernig, A.; Koelle, U.; Merbach, A. E.; Paulus, H.; Schneider, J. S., *Inorg. Chem.* **1995,** *34*, 306.

67. Acheson, R. M.; Paglietti, G., *J. Chem. Soc. Perk. T. 1* **1976,** 45.

68. Paglietti, G.; Sanna, P.; Nuvole, A., *J. Chem. Res. (M)* **1983,** 2326.

69. Carelli, V.; Liberatore, F.; Scipione, L.; Rienzo, B. D.; Tortorella, S., *Tetrahedron* **2005,** *61*, 10331.

70. Johnson, R. C., *J. Chem. Ed.* **1970,** *47*, 702.

71. Fulmer, G. R.; Miller, A. J. M.; Sherden, N. H.; Gottlieb, H. E.; Nudelman, A.; Stoltz, B. M.; Bercaw, J. E.; Goldberg, K. I., *Organometallics* **2010,** *29*, 2176.

72. Wayner, D. D. M.; Parker, V. D., *Acc. Chem. Res.* **1993,** *26*, 287.

73. Saouma, C. T.; Kaminsky, W.; Mayer, J. M., *J. Am. Chem. Soc.* **2012,** *134*, 7293.

74. Sandrini, D.; Maestri, M.; Ziessel, R., *Inorg. Chim. Acta* **1989,** *163*, 177.

75. Prasad, R.; Sulaxna; Kumar, A., *J. Therm. Anal. Calorim.* **2005,** *81*, 441.

76. Kirk, A. D.; Namasivayam, C., *Anal. Chem.* **1983,** *55*, 2428.

77. Dolomanov, O. V.; Bourhis, L. J.; Gildea, R. J.; Howard, J. A. K.; Puschmann, H., *J. Appl. Crystallogr.* **2009,** *42*, 339.

Chapter 3: PHOTOCHEMICAL FORMIC ACID DEHYDROGENATION BY IRIDIUM COMPLEXES: UNDERSTANDING MECHANISM AND OVERCOMING DEACTIVATION

3.1 Introduction

Carbon dioxide is a promising hydrogen storage medium, capable of storing 4.3 wt% H_2 in formic acid (HCO_2H) and up to 12 wt% H_2 in subsequent hydrogenation products CH_3OH and H_2O.[1-5] The CO_2/HCO_2H couple (Equation 3.1) is particularly promising because the process is readily reversible, as evidenced by a substantial body of work on both the CO_2 hydrogenation[6-9] and the formic acid dehydrogenation steps.[2, 5, 10-12]

$$H_2 + CO_2 \leftrightarrows HCO_2H \qquad \text{(Equation 3.1)}$$

A few catalysts can perform both CO_2 hydrogenation and HCO_2H dehydrogenation.[13-17] Reversible storage and release is most commonly accomplished by applying high H_2/CO_2 pressures to promote hydrogenation, then releasing the pressure to trigger dehydrogenation.[13-16] Solution pH can also be used to control the reaction, with hydrogenation occurring at basic pH (where production of formate is thermodynamically favorable) and dehydrogenation occurring at acidic pH (where the thermochemistry shifts to favor H_2/CO_2 release).[17]

An alternative strategy for reversible hydrogen storage would utilize visible light to regulate the chemistry of Equation 3.1. Storage would be accomplished by thermal hydrogenation of CO_2 in the dark, followed by light-triggered hydrogen release. In pursuit of this eventual goal, and motivated by our interest in photochemical H_2 evolution,[18, 19] we considered

the very rare examples of *photocatalytic* formic acid dehydrogenation. Building on two prior studies,[20, 21] Beller and co-workers recently reported iron carbonyl catalysts that produced up to 126 turnovers of H_2:CO_2 (1:1 mixture) from formic acid in DMF solvent at 60 ºC under photolysis.[22, 23] In one of the only other examples of this reaction, Ziessel and co-workers demonstrated that Cp*Ir-based complexes produce H_2:CO_2 (1:1 mixture) from aqueous formate at pH 5, with a turnover number (TON) up to 53 after 2 h of irradiation under vacuum.[24] Under these acidic conditions (and in organic solvents), H_2 and CO_2 gas are co-evolved in a 1:1 ratio.

Little is known about the mechanism of photochemical formic acid dehydrogenation. For example, metal carbonyl-catalyzed reactions may be initiated by photochemical CO dissociation, or photochemical H_2 release may occur, or light could play multiple roles simultaneously.[25] Mechanistic information on the Cp*Ir-based photocatalysis is limited to an Arrhenius analysis,[24] which gave higher activation energies than the Cp*Ir-catalyzed photochemical water-gas shift reaction.[26] Photochemical formic acid dehydrogenation catalysts are currently slower and less stable than corresponding thermal catalysts.[3, 27, 28] A deeper mechanistic understanding of photochemical formic acid dehydrogenation would provide guidance for improving these systems, which offer a promising, mild photochemical alternative to thermal reactions controlled by pressure or pH.

The mechanistic studies reported here reveal several new aspects of Cp*Ir-photocatalyzed formic acid dehydrogenation that helped guide significant improvements in stability, activity, and selectivity. Kinetic studies and *in situ* reaction monitoring indicate turnover-limiting photochemical H_2 release under most conditions, directing subsequent improvements by tuning the light source wavelength and intensity. Several deactivation pathways are also identified, guiding changes to the catalyst structure and reaction conditions that yielded more active and

longer-lived catalysts. The catalysts operate efficiently in basic conditions, where the evolved gas is comprised of >95% H_2 due to efficient sequestration of CO_2 by hydroxide. Our mechanistic findings lead to substantial improvements in performance, indicating that photochemical H_2 release is a promising strategy complementary to thermal reactions.

3.2 Results and Discussion

Scheme 3.1. Typical conditions for photochemical formic acid dehydrogenation by **1** and **1-OMe**.

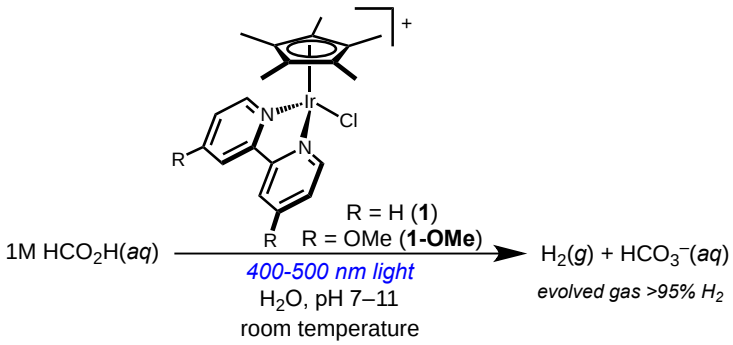

Initial catalytic studies.

The air-stable and water-soluble precatalysts **1** and **1-OMe** were prepared according to previously reported procedures.[29, 30] Initial catalytic runs were carried out in 20 mL scintillation vials containing 0.36 mM precatalyst in 10 mL of 1 M aqueous sodium formate, illuminated by a 460 nm LED lamp at room temperature (Scheme 3.1). The evolved gas was collected in an inverted burette eudiometer and analyzed by headspace GC in many cases (see Experimental Section for full experimental details).

When protected from light, solutions of **1** do not evolve appreciable amounts of gas at room temperature. Under 460 nm illumination, however, a pH 5 formate solution containing **1** produced 1.2 mL of gas in 2 h, corresponding to a TOF of ~4 h^{-1} (slightly higher than Ziessel's prior report, TOF = 0.5 h^{-1}).[24] Although prior reports only examined pH 5 conditions, we found that the catalyst is also active in basic solutions: upon photolysis of a pH 10 formate solution of

1, gas evolution commenced immediately and continued steadily. The methoxy-substituted catalyst **1-OMe**, which had not been studied previously as a photocatalyst for formic acid dehydrogenation, shows significantly improved photocatalytic activity relative to **1** (Figure 1.1). As shown in Figure 1.1, intermittent illumination (1 h cycles) confirmed the critical role of visible light in promoting the reaction. In the absence of catalyst, only traces of gas evolved over 6 h, with no response to light.

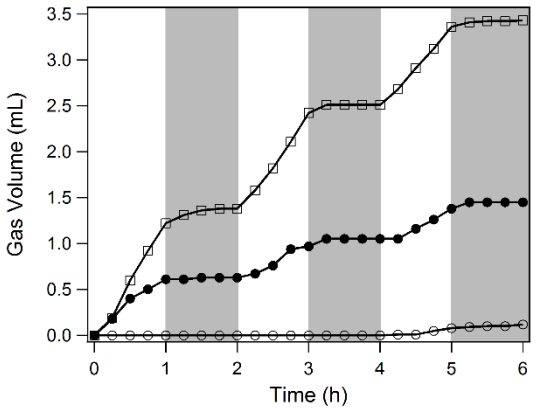

Figure 3.1. Gas evolution from formate solutions of **1** (filled circles), **1-OMe** (empty squares), and no catalyst (empty circles) during intermittent illumination (white background: lamp on, gray background: lamp off). Conditions: 0.32 mM Ir, pH 10 1 M $NaCO_2H(aq)$, 18 mM phosphate, 296 K.

Both catalysts exhibit gradually diminishing activity during prolonged illumination. While the initial yellow color of the solutions was maintained for the first 24 h, prolonged photolysis (beyond 48 h) in the eudiometer setup led to formation of a dark, *catalytically inactive* precipitate. The chloride complexes **1** and **1-OMe** are both air stable; however, a ~30% drop in activity was observed when the reactions were carried out under air. In order to avoid this decomposition and better understand the system, a series of mechanistic studies were carried out.

pH Dependence.

The pH dependence of the photochemical reaction was examined first. The volume of evolved gas dropped noticeably at higher pH, as shown in Figures 0.8 and 0.9 in Appendix B.

Rather than indicating a loss of activity, GC headspace analysis revealed that the decline in evolved gas correlated with a decrease in the amount of CO_2 released during the reaction. In fact, H_2 comprised 96(3)% of the evolved gas above pH 7, as shown in Figure 3.2a (the fuel cell poison CO was not detected). After prolonged illumination, reaction mixtures with initial pH between 6 and 10 were observed to approach a final pH of 8, while more acidic solutions showed no significant pH change during the reaction. This behavior is consistent with CO_2 sequestration and engagement of carbonate equilibria above pH 6, as in Equation 3.2 (an authentic sample of ~30 mM HCO_3^- in 1 M formate gave a pH 8 solution).

$$HCO_2^- + H_2O \leftrightarrows H_2 + HCO_3^- \quad \text{(Equation 3.2)}$$

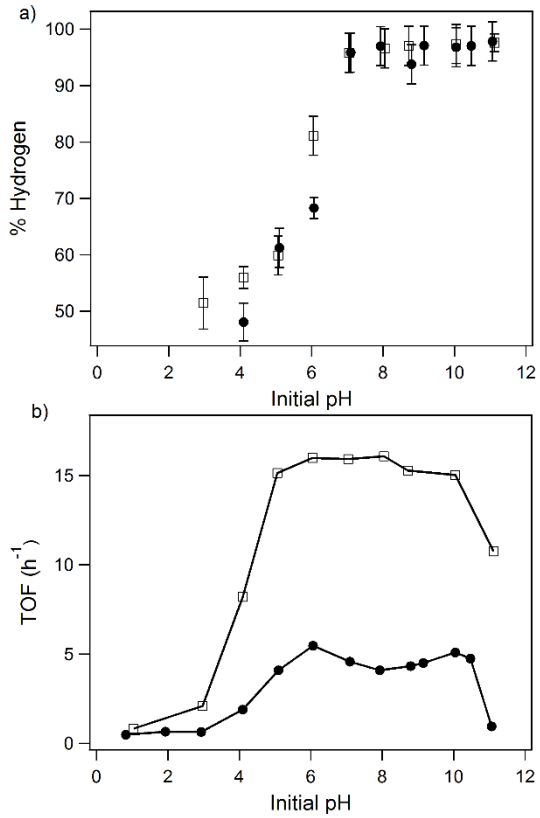

Figure 3.2. a) H_2 content of evolved gas as a function of pH for **1** (filled circles) and **1-OMe** (empty squares). b) Initial TOF (H_2 over 2 h) as a function of initial pH for **1** (filled circles) and **1-OMe** (empty squares). Conditions: 0.36 mM catalyst, 1 M $NaCO_2H$(*aq*), 296 K.

When the volume of evolved gas is corrected based on the H_2:CO_2 ratio of the evolved gas, it becomes clear that the rate of H_2 evolution is faster under more basic conditions (Figure 3.2b). Little H_2 release activity is observed below pH 3, but the rate increases sharply between pH 3 and 5 for both **1** and **1-OMe**. Both catalysts exhibit a roughly constant TOF between pH 5 and 10, with **1-OMe** operating roughly 3 times faster than **1** over this wide pH range. Catalyst **1** maintains good photocatalytic activity up to pH 10 and **1-OMe** performs well even at pH 11.

The broad region of pH independence is quite uncommon for aqueous formic acid dehydrogenation catalysts. Thermal aqueous formic acid dehydrogenation catalysts typically exhibit a sharp maximum between pH 3 and 4, close to the pK_a of formic acid (3.75).[17, 31-33] The ability of the photocatalysts **1** and **1-OMe** to maintain activity under alkaline conditions enables

the exciting observation of pure H_2 release. Only a few catalysts are capable of releasing a pure stream of H_2 from formic acid,[1, 3, 13, 14, 34] and this is the first example of photochemically-driven production of pure H_2.

The unusual ability to release H_2 from alkaline solutions is ascribed to the intermediate $[Cp^*Ir(bpy)(H)]^+$, which we have previously shown to be a photohydride: a species that becomes a stronger hydride donor upon illumination.[18, 19] Given that most catalysts produce 1:1 H_2:CO_2 mixtures in the "hydrogen release" step, photochemical methods offer a complementary selectivity for high purity hydrogen gas. Basic conditions also may facilitate integration with hydrogen storage reactions, because the best CO_2 and HCO_3^- hydrogenation catalysts thrive with added base,[17, 35] similar to the conditions where our catalysts are most active.

Pressure Dependence.

The dehydrogenation was carried out in a closed system to determine if H_2 inhibited the reaction. A thick-walled Pyrex glass pressure vessel was charged with a standard catalyst solution of **1-OMe** (20 mL in a ~40 mL vessel), equipped with either a 4.1 or 10.9 atm pressure gauge, and sealed under N_2. Hydrogen evolved with a TOF of 10 h^{-1} under 460 nm illumination at pH 9. When a higher-powered 443 nm LED lamp was applied instead, a higher initial TOF (20 h^{-1}) was obtained and the pressure in the vessel approached 4 atm. The initial rates in the pressure vessel were similar to initial rates observed by eudiometry (which maintains 1 atm H_2 during the reaction), and pressures over 4 atm were required before H_2 pressure appeared to inhibit the reaction. This pressure range is similar to a recently reported charge/discharge process for hydrogen storage.[13]

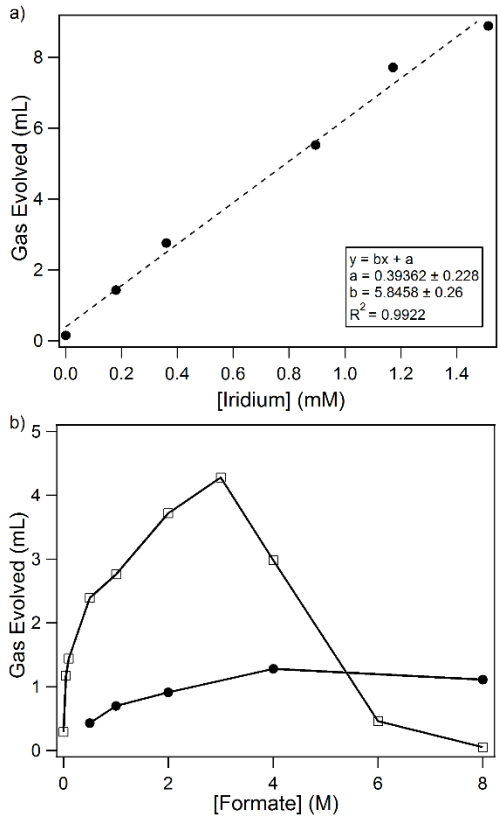

Figure 3.3. a) Gas volume measured from the eudiometer after 2 h irradiation with varying concentrations of precatalyst **1-OMe** in pH 9 1 M formate. b) Gas evolved after 2 h of 460 nm irradiation of 0.36 mM **1** (filled circles) and 0.36 mM **1-OMe** (empty squares) with varying concentrations of formate at pH 9.

Kinetic Analysis and *in situ* Monitoring.

Initial rates methods (linear fits of first 2 h of reaction) were used to determine the molecularity of the reaction. The rate of gas evolution exhibits a first-order dependence on the concentration of both catalysts **1** (Appendix B, Figure B.10) and **1-OMe** (Figure 3.3a). The reaction catalyzed by **1** exhibits saturation kinetics as a function of formate concentration, with the initial rate increasing at higher formate concentration before becoming formate-independent above 4 M (Figure 3.3b).

In contrast, an unexpected deactivation process was encountered in **1-OMe**-catalyzed reactions carried out at high formate concentrations (pH 9). As shown in Figure 3.3b, the rate

increases initially with increasing formate concentration, but slows down and eventually *loses activity* at formate concentrations around 6 M. The appearance of a yellow precipitate above 3 M formate correlates with the decrease in activity of **1-OMe**; further investigations of this deactivation process are described below.

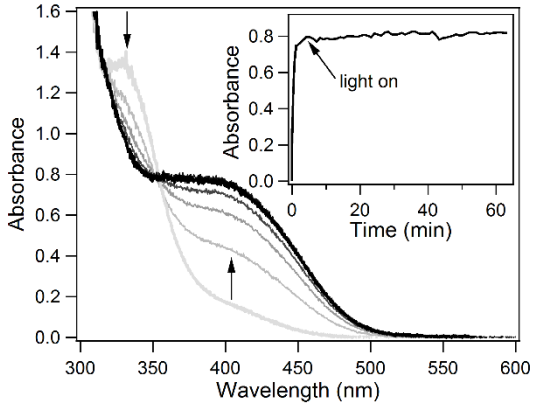

Figure 3.4. Absorbance profile after injection of 0.36 mM **1-OMe** into pH 9 1 M $NaCO_2H$(*aq*) at 296 K. The growth of **2-OMe** was observed in 20 s intervals for 1 min in the dark, followed by illumination. The inset follows the hydride absorbance at 390 nm; after 1 min in the dark, illumination with 460 nm light continued for 60 min.

The pale yellow charge transfer band of the chloride complex **1-OMe** (λ_{max} = 330 nm) provided a convenient handle for *in situ* UV-Vis spectroscopy studies. Initial studies were carried out protected from light to prevent turnover. The reaction was monitored over time immediately following injection of a stock solution of catalyst **1-OMe** to a cuvette containing a stirred solution of 1 M formate (pH 9). The characteristic charge transfer band of the hydride complex $[Cp^*Ir(bpy\text{-}OMe)(H)]^+$ (**2-OMe**, λ_{max} = 390 nm)[18] grew in over ~2 min (Figure 3.4). The hydride complex is a proposed intermediate in thermal formic acid dehydrogenation by Cp*Ir-based catalysts.[31, 36, 37] [31,36,37] Formation of hydride **2-OMe** occurs much faster than the observed rate of catalysis, suggesting that these dark processes are not rate-limiting.

Photocatalytic dehydrogenation was then spectroscopically monitored under continuous illumination to elucidate the resting state during catalysis. The cuvette was attached to a eudiometer to confirm that H_2 was indeed released during monitoring. The charge transfer band at 390 nm remained prominent during active catalysis (Figure 3.4), identifying hydride **2-OMe** as the resting state and indicating turnover-limiting photochemical H_2 release.

Table 3.1. Kinetic isotope effects of photochemical dehydrogenation.[a]

Formic acid isotopologue	Solvent	Kinetic isotope effect
HCO_2H	H_2O	–
DCO_2D	D_2O	2.6(3)
HCO_2H	D_2O	2.4
DCO_2D	H_2O	1.8

[a]Conditions: 0.36 mM **1-OMe**, 1 M formate, pH 8, 460 nm illumination for 2 h at 296 K. The formic acid OH proton is assumed to exchange with water protons.

A significant kinetic isotope effect (KIE) is anticipated if H_2 evolution is indeed the turnover-limiting process. The initial rate of gas evolution from HCO_2H/H_2O and DCO_2D/D_2O was determined in two separate experiments, providing a normal, primary KIE of 2.6(3), as shown in Table 3.1. This KIE is similar to the value of 2.6(1) reported for thermal formic acid dehydrogenation by [Cp*Ir(4,4-dihydroxy-bipyridine)(OH_2)]$^{2+}$, which was also proposed to involve rate-determining H_2 evolution.[37-39]

Table 3.1 shows KIE values obtained when other mixtures of isotopologues were examined. The observation that HCO_2H/D_2O mixtures produced a normal, primary KIE of similar magnitude to the DCO_2D/D_2O is inconsistent with rate-limiting hydride formation: conversion of Ir–O_2CH to Ir–H should only be sensitive to isotopic substitution on formate and a primary KIE would only be expected when comparing rates of formate with formate-*d*. On the

other hand, the KIE experiments are all consistent with a turnover-limiting process involving H−H bond formation.

Lamp Intensity and Wavelength Dependence and Quantum Yields.

A rate-limiting photochemical process could be limited by the kinetics of the photochemical reaction or by the light absorbing characteristics. To further probe this important step, the influence of light intensity was examined. A 443 nm LED lamp with programmable output intensity was used to perform formic acid dehydrogenation between 2 and 62 $mW \cdot cm^{-2}$ power density. The initial TOF increased from 3 h^{-1} at low intensity to 36 h^{-1} at high intensity (Appendix B, Figure B.19), again consistent with photochemical H_2 evolution limiting the rate of catalysis. A slight deviation from linearity was observed at high intensity, which might indicate that sufficient photon flux was present that other steps were starting to contribute to the rate.

To probe the role of overlap between the light source and the absorbing molecules, photocatalysis was performed under 406, 443, and 503 nm illumination at a constant, relatively low power density (~13 $mW \cdot cm^{-2}$) in a closed system (Appendix B, Figure B.18). Illumination with either the 406 nm or 443 nm lamp gave similar activity (10 h^{-1} for **1-OMe**). Under 503 nm light, the rate dropped to 5 h^{-1} for **1-OMe**. The chloride complex **1-OMe** does not absorb as much low energy light, nor with as much intensity as **2-OMe**, so the ability to operate with >400 nm light suggests that **2-OMe** is the active light absorber.[18] The performance trends correlate well with the predicted number of photons absorbed by hydride **2-OMe**; calculations suggest that **2-OMe** would absorb a similar number of 403 and 443 nm photons, but about 4 times fewer 503 nm photons (see derivation in the Experimental Section).

The conventional TON and TOF metrics of catalysis provide a convenient point of comparison with thermal catalysts, but photochemical reactions can also be assessed based on

the photon-to-chemical efficiency. The quantum yield, defined as the moles of product per photon absorbed by the catalyst, was determined under several conditions. Under typical conditions of 443 nm illumination at 13 $mW \cdot cm^{-2}$ intensity, $\Phi = 0.05$ is obtained for formic acid dehydrogenation by **1-OMe**. As the 443 nm lamp intensity was increased, the quantum yield decreases slightly, with $\Phi = 0.03$ at 62 $mW \cdot cm^{-2}$. As the irradiation wavelength was changed, only slight variations in quantum yield are observed, with $\Phi_{406\ nm} = 0.05$ and $\Phi_{503\ nm} = 0.10$ (Appendix B, Table 0.2). With relatively high photon efficiency maintained over the course of 2 h,[24, 26] and under a variety of illumination conditions, catalyst **1-OMe** has encouraging photochemical behavior.

Scheme 3.2. Proposed mechanism of photochemical formic acid dehydrogenation.

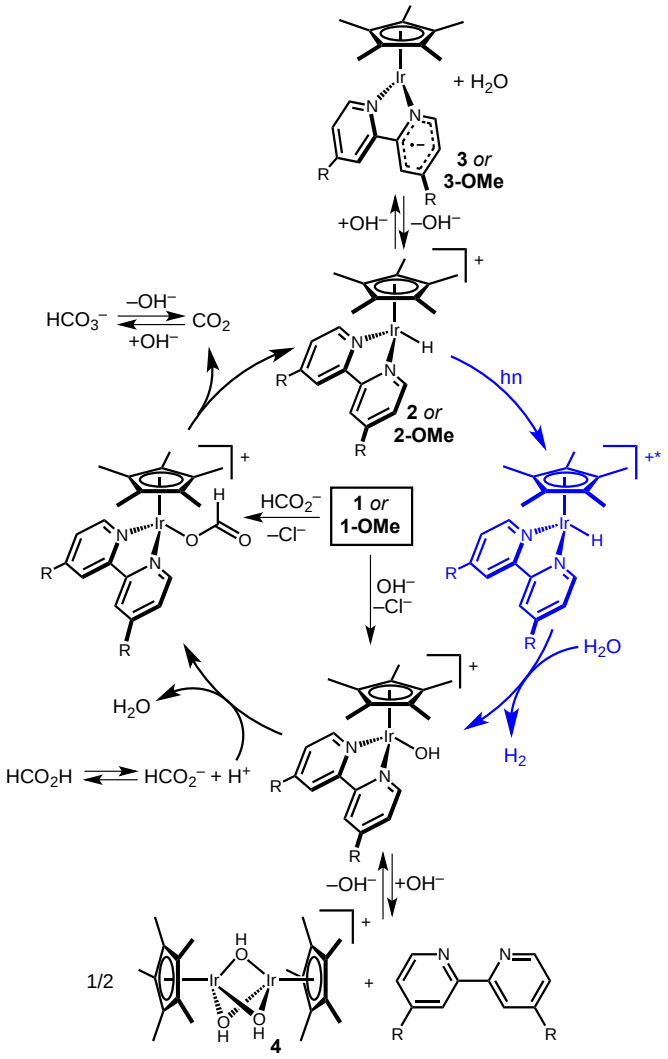

Mechanistic Proposal.

A plausible catalytic mechanism that is consistent with the preceding mechanistic studies is depicted in Scheme 3.2. Entry to the catalytic cycle is afforded by the chloride precatalysts **1** and **1-OMe**. Previous studies have shown that [Cp*Ir(bpy)(Cl)][Cl] undergoes facile ligand exchange in water,[18] and is readily converted to the hydride $[Cp^*Ir(bpy)(H)]^+$ in aqueous formate.[40] Ligand substitution processes are not turnover-limiting, as evidenced by the similar rates of dehydrogenation by chloride **1** and aquo $[Cp^*Ir(bpy)(H_2O)]^{2+}$ (TOF ~4 h^{-1} for each catalyst). Under basic conditions hydroxide substitution would be expected, based upon the

reported pK_a value for aquo $[Cp^*Ir(bpy)(H_2O)]^{2+}$.[29, 41, 42] Indeed, stirring either chloride **1** or aquo $[Cp^*Ir(bpy)(H_2O)]^{2+}$ in a pH 10 solution leads to the formation of the same product by NMR spectroscopy, assigned as the hydroxide complex $[Cp^*Ir(bpy)(OH)]^+$. Our *in situ* observations of rapid conversion of chloride **1-OMe** to hydride **2-OMe** in formate solutions in the dark suggest that formate binding and decarboxylation occur rapidly and without photochemical assistance.

Photochemical H_2 release (shown in blue in Scheme 3.2) has been identified as the turnover-limiting process at high concentrations of formate. The first-order dependence on Ir and saturation behavior with respect to formate concentration suggest that at lower formate concentrations a pre-equilibrium step involving formate (such as reversible formation of the formate complex) is also involved in the rate law. Observation of the hydride **2-OMe** as the resting state during photocatalysis strengthens this conclusion. Finding the reaction to be photon-limited holds promise for future catalyst development: improved reaction rates are possible by supplying a higher photon flux (see above), which can be accomplished by changing the photochemical reactor design or by employing more powerful lamps.[43-45]

The precise mechanism of photochemical H_2 release warrants further discussion.[46, 47] The primary event is likely excitation to the previously observed triplet excited state of **2**.[26, 48, 49] Once formed, the triplet excited state has a potent thermodynamic driving force for hydride transfer: the excited state is at least 20 kcal·mol^{-1} *more hydridic* than the ground state in acetonitrile.[19] While the kinetic details of excited state H_2 release from **2** remain the subject of ongoing studies in our laboratory, the photohydride reactivity of **2** clearly enables some of the unique features of Cp*Ir-based photochemical formic acid dehydrogenation. Light absorption renders the M−H fragment more hydridic — and therefore more reactive towards weak acids (H_2O in this case) — facilitating H_2 release under strongly basic conditions.

Photoelectrochemical H_2 evolution proceeds efficiently until pH 10,[18] in contrast to the acidic conditions (pH ~ 4) required by most aqueous formic acid dehydrogenation catalysts. Photochemically enabling H_2 release above pH 7 in turn facilitates the release of pure H_2 gas with concomitant trapping of CO_2 by hydroxide. The rarity of pure H_2 release likely stems from the fact that basic conditions are at odds with the fundamental organometallic chemistry underlying H_2 release: the metal hydride intermediates typically require acidic conditions to rapidly release H_2.

Typical thermal H_2 release pathways slow rapidly as the solution pH increases, as indicated by the narrow, acidic pH range at which most aqueous catalysts operate.[17, 31, 32] In contrast, catalysts **1** and **1-OMe** operate with similar TOF over a wide pH range. Although pH does not greatly impact the reaction rate, it does impose several restrictions based on the pK_a values of various species. The pK_a of formic acid (3.75) dictates the availability of formate anion and therefore the efficiency of the substitution process; under more acidic conditions formic acid is present and undergoes substitution more slowly, as observed in related systems that exhibit maximal performance near pH 4.[31, 32] The pK_a of the metal hydride limits the operational pH range in the basic regime. A pK_a of ~10 is estimated for hydride **2**, based on changes in electrochemical behavior,[18] at which point deprotonation forms an off-cycle Ir(II)-bpy$^{\bullet-}$ complex (**3**, Scheme 3.2).[49] When hydride **1** was stirred at pH 13, a purple precipitate formed; extraction into benzene confirmed that the precipitate was the deprotonation product **3**.[49]

Deactivation Pathways.

Understanding deactivation and/or decomposition processes of homogeneous catalysts can help identify molecular weaknesses and guide catalyst redesign.[50, 51] We sought to better understand the nature and origin of this decomposition. As described above, after 72 h

illumination of **1** in pH 8 or pH 10 formate solutions while collecting gases by eudiometry, formation of a dark blue solution was observed. A UV-Vis spectrum after the reaction revealed the growth of a broad new feature with λ_{max} = 750 nm that is consistent with nanoparticle formation.[40, 52] Nanoparticles could result from photochemical or thermal bpy dissociation, forming the photocatalytically inactive *tris*-hydroxide dimer **4** (Scheme 3.2),[41] which could go on to form insoluble aggregates or nanoparticles.

To prevent ligand loss, the reaction was run in the presence of free 2,2'-bipyridine. In parallel eudiometry experiments monitoring the ability of **1** to dehydrogenate 1 M formate solutions at pH 9, the catalyst produced more H_2 in the presence of 3 equiv free ligand (Appendix B, Figure B.21). Interestingly, analogous experiments in the sealed medium-pressure vessel showed little evidence of aggregation, suggesting that slow leaking of air into the eudiometer setup may also be partially responsible for nanoparticle formation. The more strongly donating methoxy-substituted bipyridine ligand in **1-OMe** may help avoid ligand loss during catalysis, as **1-OMe** maintains its initial rate for longer.

A deactivation process specific to **1-OMe** is encountered at high formate concentrations, as discussed above in the context of formate dependence from Figure 1.3b. To probe this process further, **1-OMe** was stirred in 8 M formate solutions protected from light. A yellow precipitate formed in the dark, ruling out photochemical degradation. When the solids were assessed by ATR-IR spectroscopy, a prominent Ir–H stretch was observed at 2046 cm^{-1}, closely matching the previously reported stretch for the hexafluorophosphate salt.[42] The solids dissolved readily in CD_3CN, and NMR and ESI−MS analyses confirm the presence of hydride **2-OMe** as well as some $[Cp^*Ir(bpy\text{-}OMe)(O_2CH)]^+$. Taken together, the data suggest that the formate salt of **2-OMe**, $[Cp^*Ir(bpy\text{-}OMe)(H)][O_2CH]$, is less soluble than the chloride salt, leading to

precipitation. The methoxy substituents apparently provide enough lipophilicity that the formate salt of **2-OMe** is substantially less water-soluble than the formate salt of **2**. It is noteworthy that activity can be restored simply by diluting the solution below 6 M formate.

Improved Catalytic Conditions.

Guided by our mechanistic findings, catalytic activity was re-assessed in a pressure vessel under conditions designed to minimize decomposition while maintaining optimal activity. When a 3 M aqueous formate solution at pH 8 was treated with 0.39 mM catalyst **1** at 296 K and illuminated with a 443 nm lamp, the initial TOF exceeds 12 h^{-1} and TON > 360 is achieved. Under analogous conditions with 0.37 mM **1-OMe**, the initial TOF exceeds 50 h^{-1} and TON > 500 is achieved over 30 h illumination. After 30 h, nearly 5 atm had built up in the sealed vessel. In addition to outperforming other photocatalysts that we are aware of, photocatalyst **1-OMe** also produces H_2 in 96% purity according GC analysis.

3.3 Conclusions

Mechanistic studies of a Cp*Ir-based photochemical formic acid dehydrogenation catalysts have led to a detailed understanding of the active catalyst cycle as well as decomposition and deactivation pathways. Direct spectroscopic evidence for every proposed intermediate was accumulated. Kinetic evidence identified the turnover-limiting process as photochemical H_2 release, via the photohydride $[Cp^*Ir(bpy)(H)]^+$, which is capable of producing H_2 beyond pH 10 and consequently enables the release of pure H_2 from formic acid in basic water. CO_2 is trapped in the alkaline solution, and no CO is produced, leading to headspace gas compositions of 96(3)% H_2. The H_2 levels are remarkably impervious to the makeup of the catalytic system, as H_2 levels above 90% were obtained regardless of catalyst loading and formate concentration (Appendix B, Figure B.7). Guided by these mechanistic findings,

improved visible light photocatalysis was realized at room temperature, even at elevated pressures of H_2. These findings offer a promising outlook for photochemical H_2 release as a strategy for hydrogen storage involving the CO_2/HCO_2H couple.

3.4 Experimental Section

General Considerations.

Manipulations were performed under the inert nitrogen atmosphere of a Schlenk line or a glovebox. Water was thoroughly degassed by sparging with nitrogen before use. D_2O, DCO_2D, NaOD(*aq*), and DCl(*aq*) were purchased from Cambridge Isotopes Laboratories, Inc. $[Cp^*Ir(Cl)_2]_2$,[53] [Cp*Ir(bpy)(Cl)][Cl] (**1**),[29] and [Cp*Ir(bpy-OMe)(Cl)][Cl] (**1-OMe**)[30] were synthesized following established procedures. All other materials were readily commercially available and were used as received. UV-Vis spectra were obtained with an Ocean Optics USB2000+ spectrometer with a DT-MINI-2GS deuterium/tungsten halogen light source controlled by OceanView software. ^{1}H NMR spectra were recorded on 400 or 600 MHz spectrometers at 25 ºC. Chemical shifts are reported with respect to residual proteo solvent.[54] ESI-MS data was acquired on a Thermo Scientific LTQ-FT-ICR Mass Spectrometer. Infrared spectroscopy was carried out with a Bruker Alpha FT-IR equipped with an ATR module.

Visible light photolysis was carried out using either an EagleLight 460 nm (± 12 nm at half-max intensity) LED lamp (500 lumens at 15 W; ~2 $mW \cdot cm^{-2}$ in typical experimental conditions) or a ThorLabs multi-wavelength LED source containing 406 ± 10 nm, 443 ± 9 nm, and 503 ± 13 nm LED lamps controlled by a ThorLabs LED driver for tunable power density. A Coherent $FieldMax_{II}$ Laser Power/Energy Meter (photodiode) was used for electronic photon flux measurements (to determine the number of incident photons on a sample). The quantum yield of the reaction was determined based on the moles of H_2 produced divided by the moles of

absorbed photons after 2 h of irradiation. Measurements of pH were obtained with either a Fisher AccupHast pH probe, a Hanna pH probe, or a Hach ISFET silicon chip pH probe.

Photocatalytic Formic Acid Dehydrogenation Procedures.

General Procedure A: Eudiometry.

Reactions were carried out in 20 mL scintillation vials containing a stir bar, 10 mL pH adjusted aqueous formate, and the desired precatalyst [Cp*Ir(bpy)(Cl)][Cl] (**1)** or [Cp*Ir(bpy-OMe)(Cl)][Cl] (**1-OMe**). Formate solutions were made by dissolving the appropriate amount of $NaCO_2H$ in HPLC grade water; pH adjustments were made by addition of dilute HCl(*aq*) and/or KOH(*aq*). In a typical reaction, an aqueous precatalyst solution containing 3.6 µmol **1** or **1-OMe** was delivered to a scintillation vial containing 10 mL pH-adjusted formate via micropipette. Specialized vial caps were constructed using septum caps, PTFE tubing, needles, parafilm, and grease (Appendix B, Figure B.1). Caps were sealed on each vial with grease and parafilm for an air-tight seal. Once capped and sealed, the reaction vial was wrapped in aluminum foil to shield the reaction from light. A large recrystallization dish was then filled halfway with water and a graduated centrifuge tube, filled with water, was inverted in the water of the recrystallization dish. The PTFE tubing attached to the reaction vial was placed into the inverted centrifuge tube, completing the eudiometer setup (Appendix B, Figure B.1). All reaction vials were then degassed with N_2 from a Schlenk line by inserting a needle through the septum cap to the bottom of the solution. After degassing for at least 15 min, the eudiometer tube was once again filled with water and any trace N_2 gas left in the eudiometer (typically < 0.1 mL) was recorded and subtracted from subsequent data. After removing the aluminum foil, the samples were illuminated with a 460 ± 12 nm LED lamp with constant stirring from a magnetic stir bar. The gas evolved from these reactions was collected, via the PTFE tubing, in the inverted-burette style

eudiometer suspended in water and the volume of evolved gas was recorded for the duration of the experiment.

A representative photocatalytic dehydrogenation procedure, following General Procedure A, is included for completeness. In a beaker, 1.701 g (0.025 mol) $NaCO_2H$ was dissolved in HPLC grade water; a volumetric flask was used to dilute the total solution volume to 25 mL, resulting in a 1.0 M formate solution. This solution was transferred to a beaker equipped with a stir bar. The pH was adjusted by addition of small volumes of KOH(*aq*). A 20 mL scintillation vial was then filled with 10 mL of the pH adjusted solution using a micropipette. A second scintillation vial was prepared the same way and stir bars were added to both vials. A 76.9 µL aliquot of a 0.042 M stock solution of **1-OMe** (3.25 µmol) was added to the first vial with a micropipette. The second vial was used as a control and contained no precatalyst. The specialized caps were then put on the two vials, and the vials were sealed with grease and parafilm around the cap-vial junction. Aluminum foil was wrapped around each vial to shield from light. A long needle connected to a Schlenk line was then inserted into the solution through the septum cap. The PTFE tubing was immersed into the inverted centrifuge vial. N_2 was then bubbled through the solution from the Schlenk line for at least 15 min. The inverted centrifuge vial was then refilled with water, while the end of the PTFE tubing was kept submerged. The tubing was then reinserted in the centrifuge vial. Under constant stirring, the aluminum foil was removed from the vials and the 460 nm LED lamp was turned on. Volume measurements were made periodically by inspection of the water level in the inverted centrifuge vial and recording the volume of collected gas.

General Procedure B: Pressure Vessel.

Reactions were performed in ~40 mL Pyrex glass pressure vessels equipped with a stir bar and capped with a pressure gauge (60 or 160 psig). Each vessel was charged with 20 mL of 1 M formate at pH 8-9, prepared according to the general procedure above. In a typical experiment, 100 mL of 1 M formate was prepared, transferred to a small bomb, and degassed for 20-30 min prior to being pumped into an N_2-filled glovebox. Next, 4.5-5.2 mg (7.32-8.46 μmol) **1-OMe** was weighed into a vial, and a micropipette was used to deliver 20 mL of the 1 M formate solution to the vial. The dissolved catalyst was then added to the pressure vessel along with a stir bar. The vessel was then capped with the pressure gauge to create an air-free, closed system. The vessel was then removed from the glovebox and placed in a photolysis hood. Under constant stirring, the vessel was monitored in the dark for ~10 min prior to irradiation. After 10 min in the dark (allowing for equilibration in any temperature change between the glovebox and photolysis hood), the vessel was irradiated with LED light. At periodic intervals, the light was turned off, the pressure gauge was checked, and the pressure buildup was recorded.

Control Reactions.

Light Dependence.

A series of three 20 mL scintillation vials were each charged with 10 mL of 1.0 M formate at pH 10.2 following the method described in General Procedure A. A 181.0 μL aliquot of 1.0 M phosphate buffer (0.181 mmol) was added to the first vial along with a 65.0 μL aliquot of a 0.049 M stock solution of **1** (3.19 μmol) using a micropipette. A second scintillation vial was charged with a 181.0 μL aliquot of 1.0 M phosphate buffer (0.181 mmol) along with a 132.3 μL aliquot of a 0.024 M stock solution of **1-OMe** (3.19 μmol) using a micropipette. A third scintillation vial was prepared the same way, but without the addition of **1** or **1-OMe**; the third

vial was used as a control and contained no precatalyst. Stir bars were added to the vials and the samples were degassed for at least 15 min. After degasing, the vials were irradiated in 1 h intervals with volume measurements taken every 15 min. After each 1 h of irradiation, the light was turned off and the vials were covered with aluminum foil to protect from room light. Volume measurements were also taken every 15 min with the light turned off, and the light was turned back on after 1 h. The process was repeated twice more for a total of 6 h (3 h light on, 3 h light off).

Catalyst Dependence.

A series of three 20 mL scintillation vials were each charged with 10 mL of 1.0 M formate at pH 8.7 following the method described in General Procedure A. The first vial was used as a control and contained no precatalyst. The second vial was charged with a 321.9 µL aliquot of a 0.011 M stock solution of **1-OMe** (3.61 µmol) using a micropipette. The third vial was charged with 2.8 mg (4.12 mmol) $[Cp^*Ir(OH_2)_3]^{2+}$, synthesized following established procedure.[32, 55] $[Cp^*Ir(OH_2)_3]^{2+}$ exhibited solubility issues in 1 M formate, and was evaluated as a stirring suspension. The vials were prepared following General Procedure A, and were irradiated with 460 nm light for 2 h.

Stability in Air.

A 20 mL scintillation vial was charged with 10 mL of 1.0 M formate at pH 8.7 following the method described in General Procedure A. The vial, run under the same conditions as vial 2 in Part B above but *without* an N_2 sparge, was charged with a 149.7 µL aliquot of a 0.024 M stock solution of **1-OMe** (3.60 µmol) using a micropipette. The vial was prepared following General Procedure A, and was irradiated with 460 nm light for 2 h. The TON was determined to

be 22 and was compared to vial 2 in Part B above (TON 31); the catalyst retained ~70% of its activity after 2 h without sparging.

Mechanistic Studies.

Monitoring the pH Change of Reaction Mixtures.

Trapping CO_2 released during formate dehydrogenation was expected to alter the solution pH by engaging carbonate equilibria. The pH was tested before and after most photocatalytic experiments, leading to the conclusion that factors such as the catalyst concentration (**1** or **1-OMe**), formate concentration, or presence of phosphate do not impact the change in pH during the reaction. In samples showing good catalytic activity ($5 < pH < 11$) a final value of pH ~ 8 was achieved (Figure 3.5). The final pH for experiments ran at very high or very low pH (where the reaction does not progress) does not deviate from the initial pH, consistent with CO_2 produced during catalysis being responsible for the pH change.

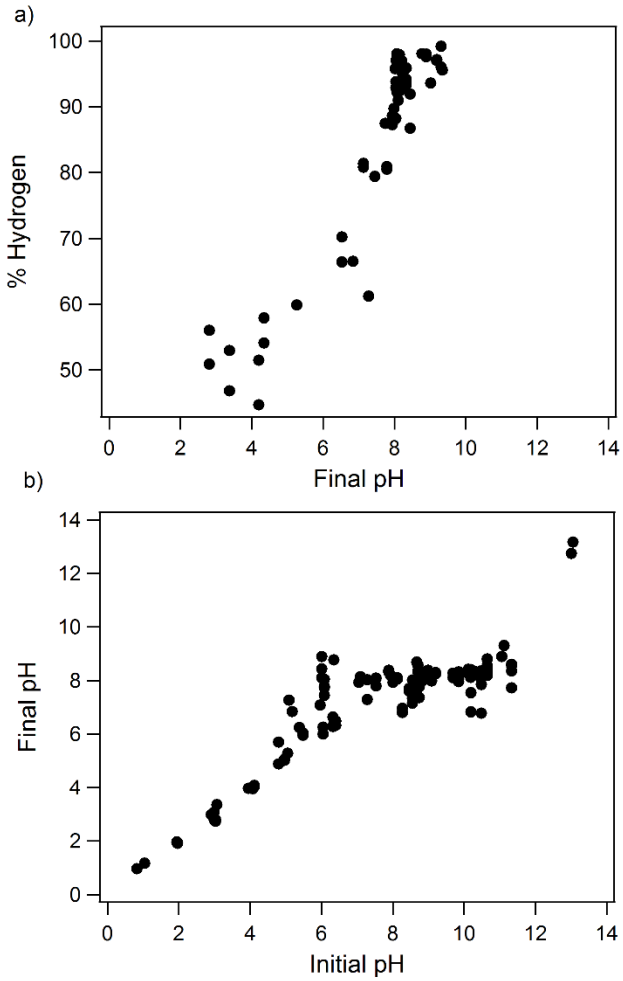

Figure 3.5. a) H_2 content of evolved gas as a function of final pH for **1** and **1-OMe** under a wide variety of reaction conditions. b) Final pH after photocatalytic formate dehydrogenation compared to initial pH measured before the reaction. Conditions: 0.18 – 1.50 mM **1** or **1-OMe**, 0.5 – 4 M $NaCO_2H$(*aq*), 296 K, 0 – 36 mM phosphate, 0 – 4 mM free ligand.

CO_2 sequestration via engagement in carbonate equilibria in water was tested by preparing authentic samples of $NaHCO_3$ in 1 M formate. Three vials were charged with 10 mL of 1 M formate, a stir bar, and 22.0, 43.5, and 65.8 mg (0.26 – 0.78 mmol) $NaHCO_3$, respectively. After stirring for a few minutes, a pH of 8.1 was recorded for all three vials.

pH Dependence of Catalysis.

According to General Procedure A, 1.0 M formate solutions containing 0.36 mM **1** or **1-OMe** were evaluated as photocatalysts at various pH values. Control reactions prepared without

any Ir catalyst were also evaluated. Figures 0.9 and 0.10 show the evolved gas volume after 2 h of illumination with the 460 nm lamp.

Order in Iridium.

According to General Procedure A, a series of three reaction vessels were prepared in pH 6.1 formate (1.0 M) and 50 eq. phosphate, varying the concentration of **1** from 0.18 mM to 0.72 mM. Appendix B, Figure B.11 shows the gas evolved after 2 h illumination at 460 nm. In an analogous experiment, six reaction vessels were prepared in pH 8.7 formate (1.0 M), varying the concentration of **1-OMe** from 0.18 mM to 1.51 mM. Appendix B, Figure B.12 shows the gas evolved after 2 h illumination at 460 nm.

Optical Spectroscopic Monitoring.

Photocatalytic formic acid dehydrogenation was monitored *in situ* by UV-Vis. A cuvette was charged with 2.5 mL of pH 9.2 formate (1.0 M) and a stir bar. The cuvette was fitted with a septum cap threaded with PTFE tubing leading to a eudiometer and was degassed (see General Procedure A). A file writer in the OceanView program was started, collecting data every second for ~8 min. The reaction was initiated by injection of 65.0 µL of a 0.011 M stock solution of **1-OMe** (0.72 µmol) and monitored over 8 min (Appendix B, Figure B.13). The growth of the characteristic band of hydride **2-OMe** (λ_{max} = 390 nm) was observed over about 120 seconds.

A similar experiment probed the resting state during active photocatalysis. After allowing the hydride to form while protected from light, the sample was irradiated with the 460 nm lamp and monitored for 2 h (Appendix B, Figure B.14). The concentration of the hydride remained constant during irradiation, suggesting that **2-OMe** is the resting state during turnover. After 23 h of illumination, gases collected in the eudiometer corresponded to TON = 35. These experiments were reproducible; Figure 3.4 in the main text is based on data from a closely related experiment.

Kinetic Isotope Effect.

A HCO_2H/H_2O sample was adjusted to pH ~8 in a 2 mL volumetric flask inside a N_2 glovebox. A 86.9 µL aliquot of a 0.008 M stock solution of **1-OMe** (0.72 µmol) was added to the flask and H_2O was added to produce a 2 mL 1.0 M formate solution (pH 7.5). The solution was then transferred to a 4 mL vial, capped, and removed from the glovebox. Following General Procedure A, the evolved gas volume was recorded periodically under 460 nm irradiation for 2 h. A DCO_2D/D_2O sample was prepared analogously using vials and a stir bar rinsed with D_2O and oven-dried prior to use. A 2 mL volumetric flask was charged with 0.9 mL D_2O (99.96% D) and a stir bar. A 80.1 µL aliquot of DCO_2D (98% D_2) was added to the flask, and the pH was adjusted to ~8 with NaOD and DCl. A 76.7 µL aliquot of a 0.009 M stock solution of **1-OMe** (0.72 µmol) was added to the flask and D_2O was added to produce a 2 mL 1.0 M formate solution (pD 8.4, where pD = pH + 0.4). Because photocatalytic reactions have pH drift during the course of the reaction (see above), slight differences in the initial pH were assumed to be negligible. The solution was then transferred to a 4 mL vial, capped, and removed from the glovebox. According to General Procedure A, the evolved gas volume was recorded periodically under 460 nm irradiation for 2 h.

The KIE experiment was run twice to ensure reproducibility of the KIE value. The second experiment was scaled up to better observe evolved gases. After 2 h irradiation, the headspace was sampled to determine the hydrogen percentage. The hydrogen percentage was found to be 97.2% for the deuterated sample and 98.1% for the proteo sample. The final pH was 8.8 for the proteo sample, while the final pD was 9.2 for the deuterated sample. The average KIE was determined to be 2.6(3).

Mixed H/D KIE experiments were performed using DCO_2D/H_2O and HCO_2H/D_2O. The DCO_2D/H_2O sample was adjusted to pH ~9 in a 5 mL volumetric flask inside a N_2 glovebox. A 299.5 µL aliquot of a 0.006 M stock solution of **1-OMe** (1.80 µmol) was added to the flask and H_2O was added to produce a 5 mL 1.0 M formate solution (pH 9.5). The HCO_2H/D_2O sample was prepared analogously using vials and a stir bar rinsed with D_2O and oven-dried prior to use. The HCO_2H/D_2O sample was adjusted to pD ~9 (using NaOD and DCl) using in a 5 mL volumetric flask inside a N_2 glovebox. A 293.4 µL aliquot of a 0.006 M stock solution of **1-OMe** (1.80 µmol) was added to the flask and D_2O was added to produce a 5 mL 1.0 M formate solution (pD 9.8). After 2 h irradiation, the headspace was sampled to determine the hydrogen percentage. The hydrogen percentage was found to be 97.4% for the HCO_2H/D_2O sample and 98.3% for the DCO_2D/H_2O sample. The final pH was 8.9 for the DCO_2D/H_2O sample, while the final pD was 9.3 for the HCO_2H/D_2O sample. The KIE values for the DCO_2D/H_2O and HCO_2H/D_2O samples were determined to be 1.8 and 2.4, respectively.

Wavelength Dependence Studies.

To directly compare the 406, 443, and 503 nm LEDs, the power density was matched to ~13 $mW \cdot cm^{-2}$ using a Coherent FieldMax energy meter and photodiode while varying the current setting on the LED driver. Using the general pressure vessel procedure, three experiments were performed using the 406, 443, and 503 nm LEDs adjusted to a power density of 13 $mW \cdot cm^{-2}$. For the 406 nm experiment, the vessel was charged with 20 mL of 1 M formate at pH 8.6, 5.2 mg (8.46 µmol) **1-OMe**, and a stir bar. For the 443 nm experiment, the vessel was charged with 20 mL of 1 M formate at pH 8.6, 4.7 mg (7.65 µmol) **1-OMe**, and a stir bar. For the 503 nm experiment, the vessel was charged with 20 mL of 1 M formate at pH 8.6, 4.9 mg (7.97

μmol) **1-OMe**, and a stir bar. Each sample was irradiated for 2 h, with pressure readings recorded every 30 min.

Similar performance for the 406 and 443 nm LEDs can be explained from the number of absorbed photons. From the power density given by the photodiode, the photon flux (defined here as the mol photons·s^{-1} of irradiation) at the irradiation wavelength was determined. The photon flux was then multiplied by the irradiation time (in seconds) to calculate the moles of *incident* photons. Then, using the percentage of light absorbed (by **2-OMe**) at the irradiation wavelength, the moles of *absorbed* photons were determined. Results are summarized in the table below.

Table 3.2. Absorption characteristics of **2-OMe** during catalysis.

Light source (nm)	Power Density: 13 mW·cm^{-2}			
	%A at $\lambda_{irradiation}$	**Mol photons·s^{-1} (x 10^{-7})**	**Mol incident photons (x 10^{-3})**	**Mol absorbed photons (x 10^{-3})**
406	96.9	5.38	3.87	3.75
443	89.7	5.85	4.21	3.78
503	18.6	6.76	4.87	0.91

Quantum yields (defined as moles of H_2 produced divided by the moles of *absorbed* photons after 2 h of irradiation) at different power densities using the 406, 443, and 503 nm LEDs are shown in the table below.

Table 3.3. Quantum yield of formate dehydrogenation catalysis by **1-OMe**.[a]

Light Source (nm)	Φ 13 mW·cm^{-2}	Φ 35 mW·cm^{-2}	Φ 62 mW·cm^{-2}
406	0.05	0.04	-
443	0.05	0.04	0.03
503	0.10	-	-

[a]Φ determined at power density given above after 2 h of irradiation. Dash indicates power density not available for a particular light source.

Light Intensity Dependence.

To determine the effect of light intensity on catalytic performance, a series of experiments were carried out using the 443 nm LED at different power densities while observing the TOF after 2 h of irradiation. Using the general pressure vessel procedure, experiments were performed using the 443 nm LED while varying the power density between 2–62 mW·cm^{-2}. For each experiment, the vessel was charged with 20 mL of 1 M formate at pH 8.6-8.8, 4.6-4.8 mg (7.48–7.81 μmol) **1-OMe**, and a stir bar. Each sample was irradiated for 2 h, with pressure readings recorded every 30 min.

Catalyst Deactivation.

Catalytic activity was found to decrease over time, leveling off after about 20 h of irradiation (Appendix B, Figure B.21). In some cases dark blue/black precipitates were observed after prolonged illumination, consistent with decomposition to Ir clusters or nanoparticles.

Excess Ligand Studies.

A series of two 20 mL scintillation vials were each charged with a stir bar and 10 mL of pH 9 adjusted 1.0 M formate solution according to the general procedure. A 166.6 μL aliquot of 0.022 M stock solution of **1** (3.61 μmol) was added to each vial. In the second vial, 1.7 mg

(0.011 mmol) free bpy ligand was added to the solution. Following the general procedure for eudiometer setup, gas evolution was monitored over time with 460 nm irradiation.

Order in Formate.

According to General Procedure A, experiments were carried out with 0.36 mM **1** or **1-OMe** in pH 8.7 formate ranging in concentration from 0.05 M to 8.0 M. Appendix B, Figure B.24 shows the gas evolution after 2 h illumination of each vial.

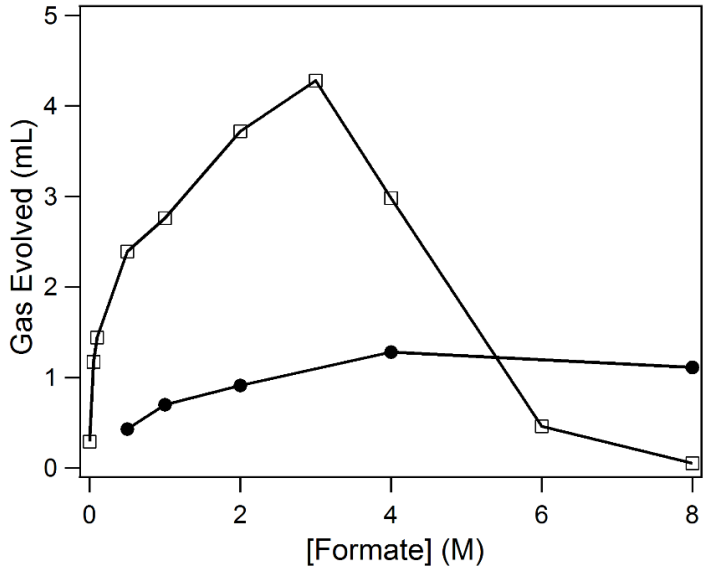

Figure 3.6. Gas evolved after 2 h of 460 nm irradiation with varying concentrations of formate with **1** (filled circles) and **1-OMe** (empty squares).

A yellow precipitate was noted under high formate concentrations with **1-OMe**. In an N_2-filled glovebox, an NMR tube was charged with 0.5614 g sodium formate (8.25 mmol), 654.0 µL D_2O, a 10 µL aliquot of a 0.935 M dioxane internal standard (9.35 µmol), and a 346.0 µL aliquot of a 0.009 M stock solution of precatalyst **1-OMe** (3.25 µmol) using a micropipette. A yellow precipitate formed immediately and was collected via filtration. Spectroscopic evidence suggests the complex to be [Cp*Ir(bpy-OMe)(H)][O_2CH], with the data closely matching the previously reported hexafluorophosphate salt in DMSO-d_6.[42] ^{1}H NMR (CD_3CN): 8.60 (d, J = 6.6 Hz, 2H), 8.44 (s, 1H), 7.88 (d, J = 2.8 Hz, 2H), 7.15 (dd, J = 6.6, 2.8 Hz, 2H), 4.03 (s, 6H), 1.79

(s, 15H), -11.27 (s, 1H). ESI-MS: calcd. m/z for $C_{23}H_{28}IrN_2O_4^+$ ([Cp*Ir(bpy-OMe)(O_2CH)]$^+$): 589.16838, observed m/z: 589.16746. IR (cm^{-1}): 3350s, 2046m, 1586vs, 1557vs, 1492s, 1428m, 1384m, 1343s, 1306m, 1255m, 1227m, 1033s, 1007m, 857m, 747w, 591w, 429w.

A yellow solution was noted under high formate concentrations with **1**. In an N_2-filled glovebox, an NMR tube was charged with 0.5635 g (8.29 mmol) sodium formate, 1 mL D_2O, a 10 µL aliquot of a 0.935 M dioxane internal standard (9.35 µmol), and a 149.3 µL aliquot of a 0.024 M stock solution of precatalyst **1** (3.61 µmol) using a micropipette. Spectroscopic evidence suggests the complex to be [Cp*Ir(bpy)(H)][O_2CH], with the data closely matching the previously reported hexafluorophosphate salt.[56] ^{1}H NMR (D_2O): 8.13 (d, *J* = 8.0 Hz, 2H), 7.96 (t, *J* = 7.9 Hz, 2H), 7.52 (t, *J* = 6.3 Hz, 2H), 1.69 (s, 15H), -11.92 (s, 1H). Fourth bpy resonance is hidden by formate peak at 8.48 ppm.

Complexes on Proposed Catalytic Cycle.

To accumulate spectroscopic data on each complex on the catalytic cycle, several experiments were performed to directly observe proposed intermediates on- and off-cycle. First, the presence of [Cp*Ir(bpy)(OH)]$^+$ was examined by adding chloride **1** and aquo [Cp*Ir(bpy)(H_2O)]$^{2+}$ in pH 9.6 carbonate buffer into two NMR tubes. Dioxane was added as an internal standard. The NMR spectra for the two samples were identical, with the data closely matching the previously reported triflate and tetrafluoroborate salts.[26, 57] ^{1}H NMR (D_2O): 8.99 (d, *J* = 5.6 Hz, 2H), 8.48 (d, *J* = 8.5 Hz, 2H), 8.24 (t, *J* = 8.1 Hz, 2H), 7.80 (t, *J* = 6.9 Hz, 2H), 1.64 (s, 15H).

The presence of the off-cycle Ir(II)-bpy$^{\bullet-}$ complex (**3**, Scheme 3.2 in the main text) was probed by setting up hydride **1** in basic conditions. In a 20 mL vial, 2.8 mg (4.4 µmol) [Cp*Ir(bpy)(H)][OTf], synthesized following an established procedure,[19] was added to 2 mL of

H_2O. Dilute NaOH was added and the pH was recorded as 13.1. The solution immediately turned purple-brown. After ~3 h stirring, a dark purple solution with a purple precipitate was observed. The precipitate was collected via filtration and dissolved in C_6D_6 for NMR characterization, which matched the previously reported Ir(II)-bpy$^{\bullet-}$ complex.[49]

Determination of the dark blue/black precipitates under prolonged irradiation was next investigated. After ~72 h of 460 nm irradiation, samples of 0.36 mM **1** in 1.0 M formate at pH 8 and 10 were found to exhibit a dark blue color. Following a 1:3 dilution in water, the λ_{max} was determined to be 750 nm by UV-Vis characterization. The spectrum matched well with a previously reported spectrum,[40] reported to be consistent with IrOx nanoparticle formation.

Improved Catalytic Conditions.

Eudiometer.

To obtain the best TON results, all factors that produce higher H_2 gas volumes were combined. Following the general procedure, a 20 mL scintillation vial was charged with a stir bar and 10 mL of 1.0 M, pH 6 formate solution. A 180.3 µL aliquot of 1.0 M phosphate buffer (0.180 mmol) was added to the vial along with a 89.7 µL aliquot of a 0.040 M stock solution of precatalyst **1** (3.61 µmol) using a micropipette. A second 20 mL scintillation vial was charged with a stir bar and 10 mL of 2.0 M, pH 6 formate solution. A 180.3 µL aliquot of 1.0 M phosphate buffer (0.180 mmol) was added to the second vial along with a 117.9 µL aliquot of a 0.031 M stock solution of precatalyst **1-OMe** (3.61 µmol) using a micropipette. Following the general procedure for eudiometer setup, gas evolution was monitored over time with irradiation. After ~ 1 day of irradiation for both samples, max TONs of 79 and 204 were obtained for **1** and **1-OMe** respectively.

Pressure Vessel.

Following the general pressure vessel procedure, the ~40 mL pressure vessel was charged with a stir bar and 20 mL of 1.0 M pH 8.5-8.8 formate solution. For the 406 nm experiment, the vessel was charged with 4.7 mg (7.65 μmol) **1-OMe**. For the 443 nm experiment, the vessel was charged with 4.8 mg (7.81 μmol) **1-OMe**. Each sample was irradiated over a couple days with their respective lamps, with pressure readings recorded periodically.

Finally, best TON results were obtained using **1** and **1-OMe**. The ~40 mL pressure vessel was charged with a stir bar and 20 mL of 3.0 M pH 8.1 formate solution. For **1**, the vessel was charged with 4.3 mg (7.75 μmol) **1**. For **1-OMe**, the vessel was charged with 4.5 mg (7.32 μmol) **1-OMe**. A webcam, connected to a computer, was set up to monitor the pressure gauge every 30 min over the course of the experiment. After 443 nm irradiation, the headspace was sampled to determine the hydrogen percentage. A balloon was used to completely envelop the pressure gauge and Teflon adapter. Loosening the Teflon cap allowed for collection of reaction gases in the balloon, enabling syringe sampling for GC analysis. The hydrogen percentage was found to be 96.5% and 96.0% for **1** and **1-OMe**, respectively.

GC Analysis.

H_2 quantification was performed using a Varian 450-GC with a pulsed discharge helium ionizer detector. A 1.0 mL Vici Pressure-Lok Precision Analytical gas-tight syringe was used to sample the headspace of the reaction vials by puncturing the septum cap. Calibration curves were constructed independently for H_2 and CO_2. Mixed gas samples for calibration were prepared by performing gas dilutions in sealed round bottom flasks. Data for each gas mixture was collected at least three times. The instrument is considerably more sensitive to CO_2, with even small amounts leading to substantial response. The resulting calibration curves for H_2 (Appendix B, Figure B.3) and CO_2 (Appendix B, Figure B.4) were validated by comparison with an authentic

sample of 50/50 H_2/CO_2, purchased from Airgas (certificate of analysis: 51 ± 2 % H_2). The commercial 50/50 H_2/CO_2 sample was 48 ± 2 % H_2 and 52 ± 4 % CO_2 according to the calibration curves.

Quantification of Catalytic Activity.

Turnover number (TON) is defined as the moles of H_2 produced divided by the moles of catalyst present in the reaction. Based on the H_2 composition of the evolved gas determined by GC, the moles of H_2 were calculated from the total volume of gas evolved. Turnover frequency (TOF) is calculated by dividing the TON by the time of reaction (the irradiation time). TOF values are typically calculated as initial rates, using the first 2 hours of the reaction, over which time the TOF was constant. Many experiments were run three times to ensure consistency and minimize experimental error. Error bars represent the standard deviation when two or more experiments were performed. When only one experiment was performed, uncertainty of ±3% was assigned based on typical run-to-run variation and the GC instrument response variation.

3.5 Acknowledgements

S.M.B. and S.A.S. performed all experiments in this study. We gratefully acknowledge funding from the University of North Carolina at Chapel Hill for the University Research Council's James Moeser Award and a J. Thurman Frieze Research Fellowship (S.A.S.), and from the NSF (Graduate Research Fellowship to S.M.B.; DGE-1144081). This research made use of an IR spectrometer funded by the UNC EFRC: Center for Solar Fuels, an Energy Frontier Research Center supported by the U.S. Department of Energy, Office of Science, Office of Basic Energy Sciences, under award number DE-SC0001011.

3.6 Associated Content

Appendix B: Additional experimental details, photographs of reaction setups, NMR spectra.

REFERENCES

1. Zaidman, B.; Wiener, H.; Sasson, Y., *Int. J. Hydrogen Energy* **1986,** *11*, 341.

2. Fukuzumi, S.; Suenobu, T., *Dalton Trans.* **2013,** *42*, 18.

3. Grasemann, M.; Laurenczy, G., *Energy Environ. Sci.* **2012,** *5*, 8171.

4. Enthaler, S.; von Langermann, J.; Schmidt, T., *Energy Environ. Sci.* **2010,** *3*, 1207.

5. Johnson, T. C.; Morris, D. J.; Wills, M., *Chem. Soc. Rev.* **2009,** *39*, 81.

6. Appel, A. M.; Bercaw, J. E.; Bocarsly, A. B.; Dobbek, H.; DuBois, D. L.; Dupuis, M.; Ferry, J. G.; Fujita, E.; Hille, R.; Kenis, P. J. A.; Kerfeld, C. A.; Morris, R. H.; Peden, C. H. F.; Portis, A. R.; Ragsdale, S. W.; Rauchfuss, T. B.; Reek, J. N. H.; Seefeldt, L. C.; Thauer, R. K.; Waldrop, G. L., *Chem. Rev.* **2013,** *113*, 6621.

7. Wang, W.; Wang, S.; Ma, X.; Gong, J., *Chem. Soc. Rev.* **2011,** *40*, 3703.

8. Jessop, P. G.; Joó, F.; Tai, C. C., *Coord. Chem. Rev.* **2004,** *248*, 2425.

9. Jessop, P. G.; Ikariya, T.; Noyori, R., *Chem. Rev.* **1995,** *95*, 259.

10. Fukuzumi, S., *Eur. J. Inorg. Chem.* **2008**, 1351.

11. Fukuzumi, S.; Yamada, Y.; Suenobu, T.; Ohkubo, K.; Kotani, H., *Energy Environ. Sci.* **2011,** *4*, 2754.

12. Fujita, E.; Muckerman, J. T.; Himeda, Y., *Biochim. Biophys. Acta, Bioenerg.* **2013,** *1827*, 1031.

13. Papp, G.; Csorba, J.; Laurenczy, G.; Joó, F., *Angew. Chem., Int. Ed.* **2011,** *50*, 10433.

14. Boddien, A.; Gärtner, F.; Federsel, C.; Sponholz, P.; Mellmann, D.; Jackstell, R.; Junge, H.; Beller, M., *Angew. Chem., Int. Ed.* **2011,** *50*, 6411.

15. Boddien, A.; Federsel, C.; Sponholz, P.; Mellmann, D.; Jackstell, R.; Junge, H.; Laurenczy, G.; Beller, M., *Energy Environ. Sci.* **2012,** *5*, 8907.

16. Hsu, S. F.; Rommel, S.; Eversfield, P.; Muller, K.; Klemm, E.; Thiel, W. R.; Plietker, B., *Angew. Chem., Int. Ed.* **2014,** *53*, 7074.

17. Hull, J. F.; Himeda, Y.; Wang, W. H.; Hashiguchi, B.; Periana, R.; Szalda, D. J.; Muckerman, J. T.; Fujita, E., *Nat. Chem.* **2012,** *4*, 383.

18. Pitman, C. L.; Miller, A. J. M., *ACS Catal.* **2014,** *4*, 2727.

19. Barrett, S. M.; Pitman, C. L.; Walden, A. G.; Miller, A. J. M., *J. Am. Chem. Soc.* **2014,** *136*, 14718.

20. Onishi, M., *J. Mol. Catal.* **1993,** *80*, 145.

21. Linn, D. E.; King, R. B.; King, A. D., *J. Mol. Catal.* **1993,** *80*, 151.

22. Boddien, A.; Loges, B.; Gärtner, F.; Torborg, C.; Fumino, K.; Junge, H.; Ludwig, R.; Beller, M., *J. Am. Chem. Soc.* **2010,** *132*, 8924.

23. Loges, B.; Boddien, A.; Junge, H.; Noyes, J. R.; Baumann, W.; Beller, M., *Chem. Commun.* **2009,** *28*, 4185.

24. Watson, K. J.; Ziessel, R., *Inorg. Chim. Acta* **1992,** *197*, 125.

25. Loges, B.; Boddien, A.; Junge, H.; Beller, M., *Angew. Chem., Int. Ed.* **2008,** *47*, 3962.

26. Ziessel, R., *J. Am. Chem. Soc.* **1993,** *115*.

27. Boddien, A.; Mellmann, D.; Gartner, F.; Jackstell, R.; Junge, H.; Dyson, P. J.; Laurenczy, G.; Ludwig, R.; Beller, M., *Science* **2011,** *333*, 1733.

28. Bielinski, E. A.; Lagaditis, P. O.; Zhang, Y.; Mercado, B. Q.; Würtele, C.; Bernskoetter, W. H.; Hazari, N.; Schneider, S., *J. Am. Chem. Soc.* **2014,** *136*, 10234.

29. Dadci, L.; Elias, H.; Frey, U.; Hoernig, A.; Koelle, U.; Merbach, A. E.; Paulus, H.; Schneider, J. S., *Inorg. Chem.* **1995,** *34*, 306.

30. Himeda, Y.; Onozawa-Komatsuzaki, N.; Sugihara, H.; Kasuga, K., *Organometallics* **2007,** *26*, 702.

31. Himeda, Y., *Green Chem.* **2009,** *11*, 2018.

32. Fukuzumi, S.; Kobayashi, T.; Suenobu, T., *J. Am. Chem. Soc.* **2010,** *132*, 1496.

33. Fukuzumi, S.; Kobayashi, T.; Suenobu, T., *ChemSusChem* **2008,** *1*, 827.

34. Wiener, H.; Sasson, Y., *J. Mol. Catal.* **1986,** *35*, 277.

35. Tanaka, R.; Yamashita, M.; Nozaki, K., *J. Am. Chem. Soc.* **2009,** *131*, 14168.

36. Himeda, Y.; Onozawa-Komatsuzaki, N.; Miyazawa, S.; Sugihara, H.; Hirose, T.; Kasuga, K., *Chem. - Eur. J.* **2008,** *14*, 11076.

37. Wang, W. H.; Xu, S.; Manaka, Y.; Suna, Y.; Kambayashi, H.; Muckerman, J. T.; Fujita, E.; Himeda, Y., *ChemSusChem* **2014,** *7*, 1976.

38. Wang, W. H.; Hull, J. F.; Muckerman, J. T.; Fujita, E.; Hirose, T.; Himeda, Y., *Chem. - Eur. J.* **2012,** *18*, 9397.

39. Wang, W. H.; Ertem, M. Z.; Xu, S.; Onishi, N.; Manaka, Y.; Suna, Y.; Kambayashi, H.; Muckerman, J. T.; Fujita, E.; Himeda, Y., *ACS Catal.* **2015,** *5*, 5496.

40. Miller, A. J. M.; Heinekey, D. M.; Mayer, J. M.; Goldberg, K. I., *Angew. Chem., Int. Ed.* **2013,** *52*, 3981.

41. Makihara, N.; Ogo, S.; Watanabe, Y., *Organometallics* **2001,** *20*, 497.

42. Ogo, S.; Kabe, R.; Hayashi, H.; Harada, R.; Fukuzumi, S., *Dalton Trans.* **2006**, 4657.

43. Garlets, Z. J.; Nguyen, J. D.; Stephenson, C. R. J., *Isr. J. Chem.* **2014,** *54*, 351.

44. Andrews, R. S.; Becker, J. J.; Gagné, M. R., *Angew. Chem., Int. Ed.* **2012,** *51*, 4140.

45. Elliott, L. D.; Knowles, J. P.; Koovits, P. J.; Maskill, K. G.; Ralph, M. J.; Lejeune, G.; Edwards, L. J.; Robinson, R. I.; Clemens, I. R.; Cox, B.; Pascoe, D. D.; Koch, G.; Eberle, M.; Berry, M. B.; Booker-Milburn, K. I., *Chem. - Eur. J.* **2014,** *20*, 15226.

46. Esswein, A. J.; Nocera, D. G., *Chem. Rev.* **2007,** *107*, 4022.

47. Teets, T. S.; Nocera, D. G., *Chem. Commun.* **2011,** *47*, 9268.

48. Suenobu, T.; Guldi, D. M.; Ogo, S.; Fukuzumi, S., *Angew. Chem., Int. Ed.* **2003,** *42*, 5492.

49. Ladwig, M.; Kaim, W., *J. Organomet. Chem.* **1992,** *439*, 79.

50. Widegren, J. A.; Finke, R. G., *J. Mol. Catal. A: Chem.* **2003,** *198*, 317.

51. Crabtree, R. H., *Chem. Rev.* **2012,** *112*, 1536.

52. Hoertz, P. G.; Kim, Y. I.; Youngblood, W. J.; Mallouk, T. E., *J. Phys. Chem. B* **2007,** *111*, 6845.

53. White, C.; Yates, A.; Maitlis, P. M., *Inorg. Synth.* **1992,** *29*, 228.

54. Fulmer, G. R.; Miller, A. J. M.; Sherden, N. H.; Gottlieb, H. E.; Nudelman, A.; Stoltz, B. M.; Bercaw, J. E.; Goldberg, K. I., *Organometallics* **2010,** *29*, 2176.

55. Ogo, S.; Makihara, N.; Watanabe, Y., *Organometallics* **1999,** *18*, 5470.

56. Abura, T.; Ogo, S.; Watanabe, Y.; Fukuzumi, S., *J. Am. Chem. Soc.* **2003,** *125*, 4149.
57. Hintermair, U.; Hashmi, S. M.; Elimelech, M.; Crabtree, R. H., *J. Am. Chem. Soc.* **2012,** *134*, 9785.

Chapter 4: PHOTOINDUCED HYDRODEHALOGENATION OF DICHLOROMETHANE BY IRIDIUM HYDRIDE COMPLEXES

4.1 Introduction

Hydrodehalogenations are an important class of transformations that exhibit great potential for a variety of real world applications, including organic synthesis[1] and decontamination of polluted water.[2-12] Hydrodehalogenation has been implemented in chemical synthesis for the purpose of removing a halide protecting group to enable new reactivity,[13, 14] to activate the α-position reactivity, and to simply dehalogenate to generate the desired product (Scheme 4.1).[15-17] Dehalogenation has also been used in biological applications to generate chiral alpha-methylamines from alkyl iodides of protected alpha-amino acids for drug development, inhibitors, and potassium channel modulators.[18,19] In water purification, the transformation may be applied to remove halogenated compounds[20] from drinking water via conversion to more easily removed hydrocarbon analogs. Additionally, photoredox catalysis has been used to promote light-driven hydrodehalogenation reactions.[1, 21, 22] Transition metal complexes, traditionally iridium and ruthenium polypyridyl species, are often applied to photoredox catalysis, serving as the light-absorbing photosensitizer that ultimately generates the redox equivalents for promoting desireable organic transformations using visible light irradiation.

Scheme 4.1. General hydrodehalogenation reaction of a) aromatic and b) aliphatic halides.

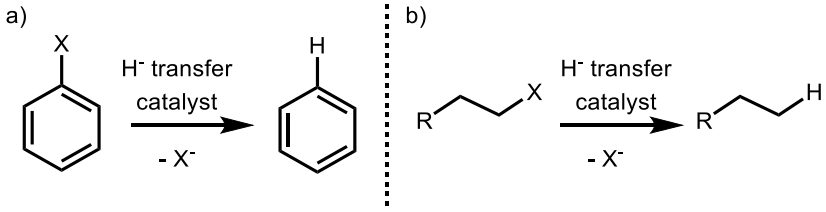

Careful mechanistic studies have been performed for hydrodehalogenation reactions involving aromatic and aliphatic substrates[1, 21-25] and aqueous reaction conditions.[26] Using $Ru(bpy)_3^{2+}$ photocatalyst, phenacyl-based electron acceptors, 9,10-dihydro-10-methylacridine ($AcrH_2$) as the electron donor, and 452 nm light, Fukuzumi observed a change in the mechanism for hydrodehalogenation under varying concentrations of $HClO_4$ acid.[23] Under low acid concentration, the reaction proceded via a radical reductive quenching pathway, where the excited state $Ru(bpy)_3^{2+}$* is quenched by electron transfer from the $AcrH_2$ electron donor. At high acid concentrations, however, a radical oxidative quenching pathway becomes dominant and the phenacyl halide oxidizes the excited state complex to $Ru(bpy)_3^{3+}$, a strong oxidant. Stephenson has applied the low acid, reductive quenching mechanism to a broad series of halides that are alpha to carbonyls and aryl groups.[24]

A conceptually similar switch in mechanism under differing reaction conditions with the same catalyst, this time between aromatic and aliphatic substrates instead of acid concentrations, has been observed by Jones.[25] Using a Cp^*ZrH_2 catalyst, hydrodehalogenations involving aliphatic substrates were found to operate via a radical chain mechanism, while hydrodehalogenations involving aromatic substrates were found to proceed through a direct hydridic attack from the metal hydride to the aromatic ring. Hydrodehalogenation involving hydride transfer to aromatic, aliphatic, and allylic substrates from a metal or metalloid hydride[2, 25, 27-32] have been proposed to go through several different reaction mechanisms, including radical chain,[33] nucleophilic attack,[34] and direct hydridic attack.[25, 34-36]

In one metal hydride example, a palladium heterogeneous catalyst is paired with a $NaBH_4$-TMEDA (tetramethylethylenendiamine) hydride source to achieve hydrodehalogenation of halogenated heterocycles at room temperature.[37] A dinuclear molybdenum paddlewheel was

invoked in combination with 1-methyl-3,6-bis(trimethylsilyl)-1,4-cyclohexadiene as an H-atom source, where kinetic studies reveal H-abstraction from cyclohexadiene to be the rate determining step.[38] A recent reported utilized silver nanoparticles (AgNPs) and an electrochemical hydrodehalogenation strategy to promote the reaction under mild reaction conditions and low energy consumption.[20] The NPs provide good yields whiles using lower metal loading and exhibit enhanced activity when compared to bulk silver.[39, 40] Several metals have been used in this strategy, including Ag, Pd, Cu, Pt, alloys, and cathode materials.[20, 39, 41-48] Additionally, hydrodehalogenation has been achieved using a variety of metal and metalloid hydrides,[2, 25, 28, 31, 32] utilizing hydride transfer from metal NPs to affect the transformation.[30]

By developing hydrodehalogenation under mild reaction conditions, widespread use of this transformation can be promoted. A recent report demonstrated that the reaction could be run in aqueous solutions with a Pd catalyst, showing the usefulness of the reaction in water purification applications,[26] including PdNPs that are recoverable via an external magnet.[49] Ogo demonstrated the ability of a $[Cp^*Ir(bpy)(OH_2)]^{2+}$ complex to hydrodehalogenate three water soluble alkyl halides using a formic acid hydride donor. The reaction was proposed to proceed via an S_N2 mechanism, with hydride transfer from the generated iridium hydride to the halogenated substrate causing a breakage of the C-X bond.

With a goal of achieving reactivity under mild conditions at room temperature and in the absence of strong reductants or oxidants, we wanted to see if $[Cp^*Ir(bpy)(H)]^+$ could be used to photochemically promote hydrodehalogenation. In the Miller lab, we have previously shown that photochemically excited $[Cp^*Ir(bpy)(H)]^+$ is an exceptionally potent hydride donor for reactions that include photoelectrochemical hydrogen production,[50] hydride transfer to organic acids,[51] and photochemical formic acid dehydrogenation.[52] By extending this reactivity to

hydrodehalogenation, we wish to harness light-driven hydride transfer from iridium hydride complexes to reduce halogenated compounds like dichloromethane, promoting new methods to achieve this reaction.

4.2 Results and Discussion

Scheme 4.2. Reaction of [Cp*Ir(bpy-OMe)(H)][OTf] and CH_2Cl_2 with visible light.

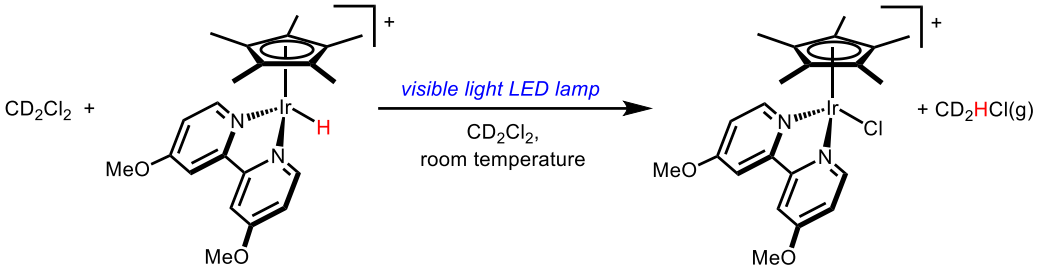

Towards our goal of hydrodehalogenating dichloromethane, we initially employed NMR spectroscopy to evaluate reactivity. Reactivity in CD_2Cl_2 was investigated by starting from the air- and light-sensitive $[Cp^*Ir(bpy\text{-}OMe)(H)]^+$ (**1**) or $[Cp^*Ir(bpy)(H)]^+$ (**2**), prepared from modified procedures (See Experimental Section). These two complexes have been previously shown to promote light-driven hydride transfer in water and acetonitrile,[50-52] and are stable in solution in the absence of light. In deuterated dichloromethane, chloromethane-d_2 could be readily observed with 460 nm LED illumination (Scheme 4.2). Chloromethane-d_2 is easily observed thanks to identifiable isotopic labeling; the expected pentet splitting pattern, due to deuterium coupling, provides a convenient spectroscopic handle to evaluate rates of reaction. The reaction was also carried out in proteo dichloromethane solvent, however the resultant chloromethane product (CH_3Cl), observed as a singlet, is far less distinct when compared against reactions run in deuterated dichloromethane. Importantly, control reactions of **1** or **2** in dichloromethane in the dark showed minimal reactivity; after one hour in the dark, 6% of hydride **2** had converted to **2-Cl**. For comparison, after one hour of 460 nm irradiation 94% of

hydride **2** had converted to **2-Cl** and a significant growth of the chloromethane-d_2 peak at δ 2.99 ppm was observed. This clearly indicates that the reaction is promoted by visible light.

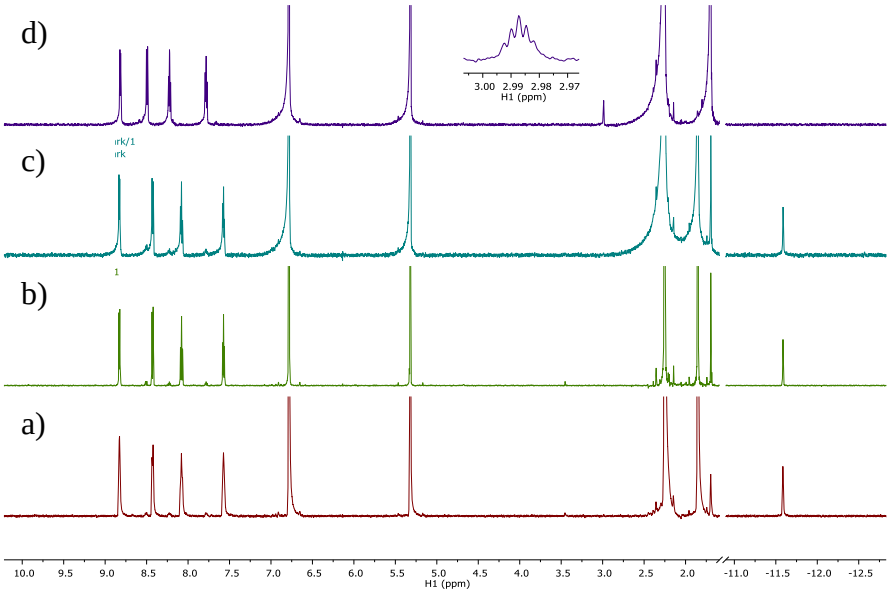

Figure 4.1. ^{1}H NMR spectrum of [Cp*Ir(bpy)(H)][OTf] (**2**) in a CD_2Cl_2/H_2O biphasic system in a) the initial dark tube b) the dark tube after 1 hour, c) the initial light tube, and d) the light tube after irradiation with 460 nm LED for 1 hour. Inset: CD_2HCl peak growth is observed at δ 2.99.

The photolysis of **1** and **2** in dichloromethane cleanly forms the chloride complex and chloromethane. No solvent bound product is observed, nor are any decomposition products noted. In the absence of dichloromethane reactants, more complex behavior is observed, with decomposition and iminoacyl adduct formation occurring in acetonitrile.[51] In addition, no H_2 release was observed by ^{1}H NMR for the reaction in dichloromethane.

Clean formation of the isotopically labeled chloromethane-d_2 in CD_2Cl_2 provides initial insight into the mechanism of photoinduced hydrodehalogenation. No other isotopologues are observed, and no H/D scrambling of the added hydride is noted. H/D scrambling might be expected if a radical mechanism was involved in this transformation. Instead, chloromethane-d_2 is the expected product in a net hydride transfer through a nucleophilic hydride transfer

mechanism. Similar net hydride reactivity was been proposed previously,[25, 34-36] with the notable example of the $[Cp^*Ir(bpy)(H)]^+$ complex promoting thermal hydride transfer to water soluble alkyl halide substrates.[53] Applying excited state reactivity to the alkyl halide system, however, does not yield improved hydrodehalogenation activity; instead, irradiation of **1** or **2** in D_2O with 2-bromopropanoic acid favored increased formation of H_2, observed as bubbles in solution. We have previously observed excited state production of H_2 in the presence of **1** or **2**, formed from net hydride transfer from the iridium complex to water, which serves as the proton donor to yield H_2.[50, 52] However, catalytic hydrodehalogenation activity in the dark was improved from the literature (9 TON)[53] by using **1**, resulting in up to 42 TON of propanoic acid. Increased activity of **1** has been demonstrated previously,[50] as **1** is a more active catalyst and is more stable over a wide pH range.[52]

Reactivity in the presence of additional substrates was evaluated next. Hydride **1** was generated in an aqueous formate solution from **1-Cl** precursor, followed by addition of 0.5 mL of either proteo bromohexane, bromocyclohexane, or 1,2-dichloroethane. Irradiation with 460 nm light did not yield any hydrodehalogenated product. Again, H_2 production was observed with illumination (confirmed with headspace GC analysis). Additionally, UV-Vis spectra of *in situ* reactions of hydride **2** and 2 mL of either dichloromethane, dichloroethane, chlorobenzene, or chlorohexane show that the hydride disappears within 30 min of irradiation. Analogous experiments carried out in NMR tubes in C_6D_5Cl with added dichloromethane, dichloroethane, chlorobenzene, or chlorohexane were irradiated for 30 minutes, with ^1H NMR spectra also showing disappearance of the hydride and production of H_2. These observations suggest that hydride **1** reacts with itself to form H_2 instead of reacting with the substrates present in C_6D_5Cl. It is particularly notable that no chloromethane was observed in the NMR tube containing

dichloromethane in C_6D_5Cl. In similar NMR experiments, hydride **2** was added to CD_3CN with added dichloromethane, dichloroethane, chlorobenzene, and chlorohexane. Upon 460 nm light, no hydrodehalogenation products were observed; instead, the bimetallic iminoacyl complex was noted (Scheme 4.3). These results suggest that hydride **2** will react with the CD_3CN solvent preferentially over added substrate to form the iminoacyl complex. NMR experiments in neat, deuterated dichloroethane, chlorobenzene, and chlorohexane will be explored in future work.

Scheme 4.3. Iminoacyl formation from **2** in CD_3CN.

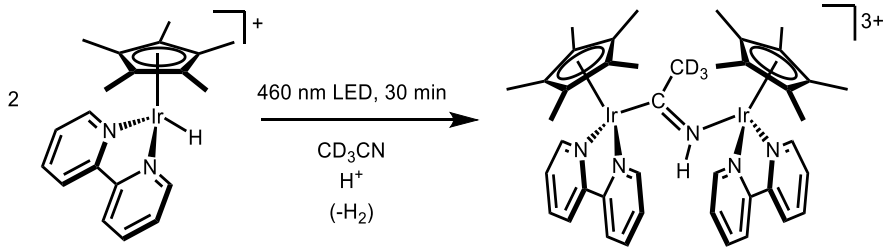

The reactivity of complexes **1** and **2** towards hydrodehalogenation of CD_2Cl_2 to form chloromethane-d_2 sparked our interest in better understanding the excited state reactivity and mechanism. Toward this goal, we set out to run careful kinetic studies to elucidate the mechanism. Hydrodehalogenation involving hydride transfer from a metal hydride to organic substrates have been previously reported,[2, 25, 27-32] and have been proposed to proceed through several different mechanisms including radical chain,[33] nucleophilic attack,[34] and direct hydridic attack.[25, 34-36] Reports of light-driven hydrodehalogenation are less numerous, but do exhibit, primarily in the field of photoredox catalysis.[1, 23, 24] The majority of these systems utilize either $Ru(bpy)_3^{2+}$ or $Ir(ppy)_3$ as photosensitizers for the reaction with an added electron donor species; a radical mechanism is proposed for these systems. From our previous studies,[51] complexes **1** and **2** have been shown to be more than merely serving as the photosensitizer. To understand the mechanism behind light-driven hydrodehalogenation of dichloromethane using hydrides **1** and **2**,

we began by monitoring the initial rate of the reaction with various iridium concentrations under visible irradiation using UV-Vis.

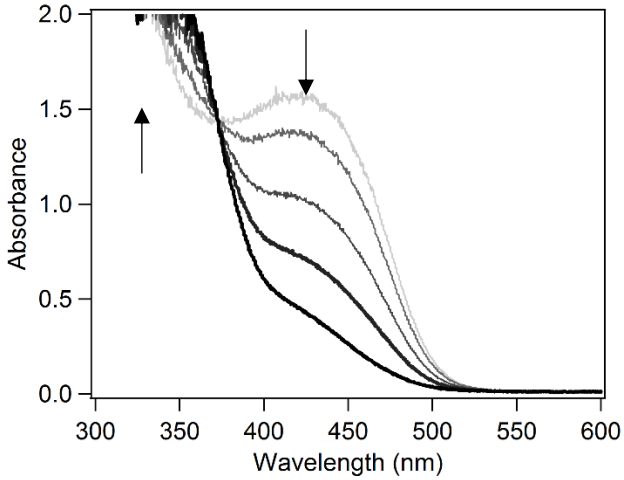

Figure 4.2. Absorbance profile of 0.56 mM **1** in CH_2Cl_2 upon 443 nm irradiation to form **1-Cl** (and chloromethane). The growth of **1-Cl** was observed between 0.15 – 30 min of irradiation.

The reaction proceeds very quickly with light; within 30 minutes of 443 nm irradiation, the reaction is essentially complete. After less than 1 minute of irradiation, the reaction reaches 10% conversion. Due to this rapid reactivity, the absorbance of the starting material can vary greatly within the period of a short, 30 minute experiment (Figure 4.2). The method of initial rates helps to minimize this dramatic change in absorbance, giving more reliable kinetic information to better understand the reaction mechanism. The starting hydride material and product chloride material have distinct, characteristic λ_{max} values that provide a convenient spectroscopic handle (420 nm for hydride, 350 nm for chloride, Figure 4.3). A slight spectral overlap between the hydride and chloride is observed, but the absorptivity between the hydride and chloride species is vastly different at the irradiation wavelength, ensuring that irradiated photons are absorbed almost exclusively by the hydride to productively promote activity. This slight spectral overlap further amplifies the importance of using the initial rates method to obtain the most reliable kinetic information. With a 443 nm light source and variable power output, we

were able to carefully tune the photon flux in order to observe reaction kinetics over longer time periods and collect additional data points.

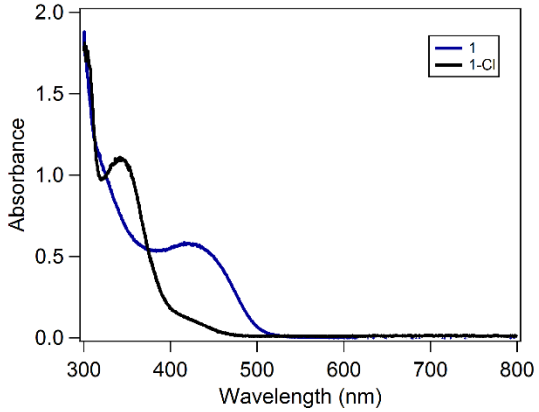

Figure 4.3. UV-Vis spectra of 0.21 mM **1** and 0.21 mM **1-Cl.**

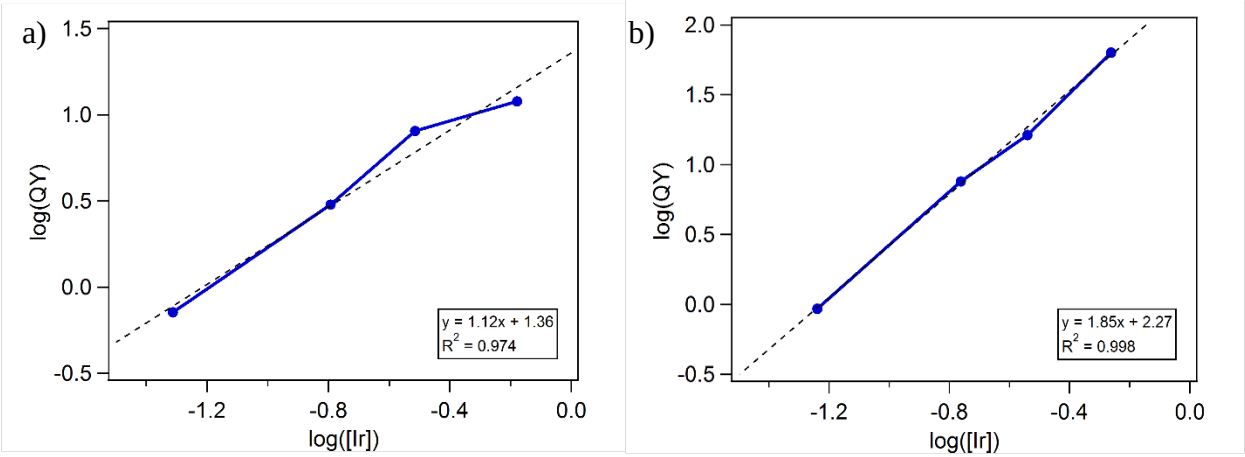

Figure 4.4. a) Log plot of quantum yield vs. [**1**] using 443 nm irradiation at 250 mA current and b) log plot of quantum yield vs. [**1**] using 443 nm irradiation at 10 mA current.

Varying the iridium concentration between 0.06 and 0.57 mM, initial rate data was obtained to determine the order of iridium within the reaction. A log-log plot of iridium concentration vs. initial rate was constructed and the data indicated that the reaction was second order in iridium. However, as discussed above, the absorbance of the reaction is changing as the reaction progresses, due to the changing concentration of **1**. Deviation from second order within initial rates plots can be explained through the change in absorbance of the hydride even over

these small irradiation times. A correction to this changing absorbance may be achieved by graphing log iridium concentration vs. log quantum yield. Importantly, the quantum yield term enables the correction of actual light (photons) absorbed by the sample over the initial points of the experiment. Performing this correction, a slope of one is noted for the quantum yield plot (Figure 4.4a), indicative that the reaction is second order in iridium.

A mechanism that is consistent with a reaction second order in iridium is proposed below (Equation 4.1 to Equation 4.5). First, a ground state hydride absorbs a photon and enters the excited state. Once excited, the excited state hydride is surrounded by ground state hydride and reacts with one equivalent of the ground state hydride. This bimetallic excited state electron transfer results in the formation of Ir^{IV}-H^{2+} and Ir^{II}-H intermediate species, where the Ir^{II}-H acts as a hydride donor to form Ir^{II}-Cl and chloromethane. The Ir^{IV}-H^{2+} intermediate oxidizes the generated Ir^{II}-Cl to form Ir^{III}-H^{+} and Ir^{III}-Cl^{+} product. The presence of this Ir-Cl product is experimentally observed in the UV-Vis experiments and matches the product seen in previous NMR experiments. The indicated second order iridium dependence is unusual for hydrodehalogenation, where radical mechanisms are often favored. Additional evidence towards this second order dependence has been found in preliminary data from the Miller lab, where light-driven reactions in both acetonitrile and water also exhibit a second order iridium dependence, suggesting theses reactions start with the same first two steps (Equation 4.1 and Equation 4.2). Excited state bimetallic electron transfer may be applicable not only to this particular solvent and substrate, but may be applied to iridium excited state reactivity more broadly, in different solvents and promoting different reactivity.

$Ir^{III}\text{-}H^{+} + hv \rightarrow Ir^{III}\text{-}H^{+*}$ (Equation 4.1)

$Ir^{III}\text{-}H^{+*} + Ir^{III}\text{-}H^{+} \rightarrow Ir^{IV}\text{-}H^{2+} + Ir^{II}\text{-}H$ (Equation 4.2)

$Ir^{II}\text{-}H + CH_2Cl_2 \rightarrow Ir^{II}\text{-}Cl + CH_3Cl$ (Equation 4.3)

$Ir^{IV}\text{-}H^{2+} + Ir^{II}\text{-}Cl \rightarrow Ir^{III}\text{-}H^{+} + Ir^{III}\text{-}Cl^{+}$ (Equation 4.4)

$Ir^{III}\text{-}H^{+} + hv + CH_2Cl_2 \rightarrow Ir^{III}\text{-}Cl^{+} + CH_3Cl$ (Equation 4.5)

Quantum yields for individual reactions varied from 0.01 to 0.18 at higher photon flux and up to 0.63 at lower light intensities; indicating an efficient use of absorbed light, particularly at higher iridium concentrations. These quantum yields are high, but are not unprecedented in the literature.[51, 52, 54, 55] It is important to mention the observed effect of light intensity on quantum yield and the slope of the log plots in Figure 4.4b; the quantum yield decreases with increasing photon flux. In preliminary data, the slope of the line in the log iridium concentration vs. log quantum yield plot also changed with varying photon flux. At lower light intensities, the slope approaches two.

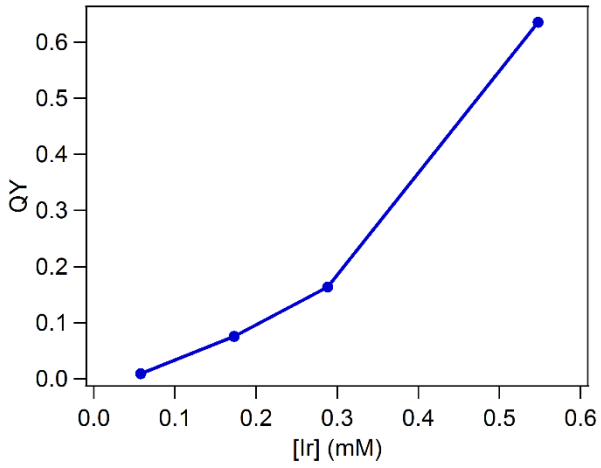

Figure 4.5. Changes in concentration of [**1**] vs. quantum yield of the reaction. Irradiated with 443 nm LED at 10 mA current.

To further improve the quantum yield, we considered adding electrolyte to the reaction. If a bimolecular excited state electron transfer is involved in the mechanism, added electrolyte should be able to more effectively transport generated charges. To support this hypothesis,

tetrabutylammonium hexafluorophosphate, [TBA][PF_6], was added to the reaction mixture to probe the effect of electrolyte on the observed reaction order under low light intensities. Adding 0.1 M electrolyte solution, quantum yields and reaction rates both increased (Table 4.1). A reaction order of two was observed with electrolyte; notably the log iridium concentration vs. quantum yield plot exhibited a slope of 1 (Figure 4.6). Therefore, the overall reaction order was found to be two with respect to iridium even at lower light intensities upon addition of electrolyte. These results support rate determining electron transfer, as increased electrolyte is expected to promote more efficient electron transfer.

Table 4.1. Effect of Electrolyte on Quantum Yield.

[**1**] (mM)	QY	QY with TBA^+
0.06	0.01	0.06
0.17	0.08	0.22
0.29	0.16	0.38
0.55	0.64	0.49

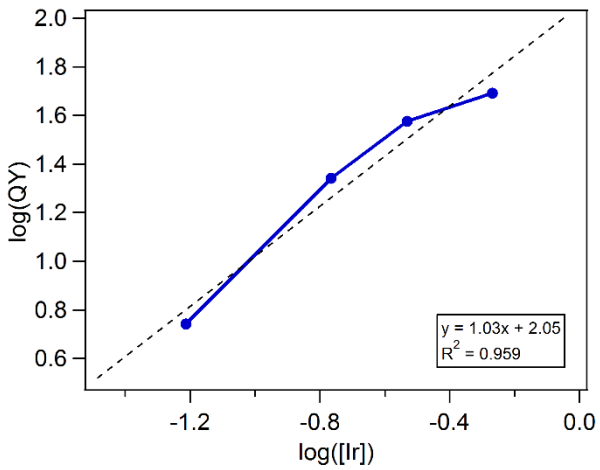

Figure 4.6. Plot of quantum yield vs. [**1**] using 443 nm irradiation at 10 mA current with the addition of 0.1 M tetrabutylammonium electrolyte.

From the mechanistic studies of stoichiometric reactivity of **1** and **2** to form chloromethane-d_2 in CD_2Cl_2 described above, we next wanted to see if the proposed excited state electron transfer could be converted from a stoichiometric to a *photocatalytic* hydrodehalogenation of dichloromethane. Biphasic reactions were used to probe activity, with an aqueous formate layer and an organic dichloromethane layer (Figure 4.7). Starting from precursors **1-Cl** or **2-Cl**, formic acid can be used to generate the active hydride intermediate in water.[54, 56-59] Once formed, the hydride complex migrates to the organic layer, where it is more soluble. The hydride will remain in the organic layer until the solution is irradiated; irradiation is performed only on the organic layer, as photolysis of the water layer produces significant amounts of H_2 (and CO_2) through photocatalytic dehydrogenation of formic acid.[52, 54] To prevent irradiation of the aqueous layer, the layer is kept in the dark using a foil mask.

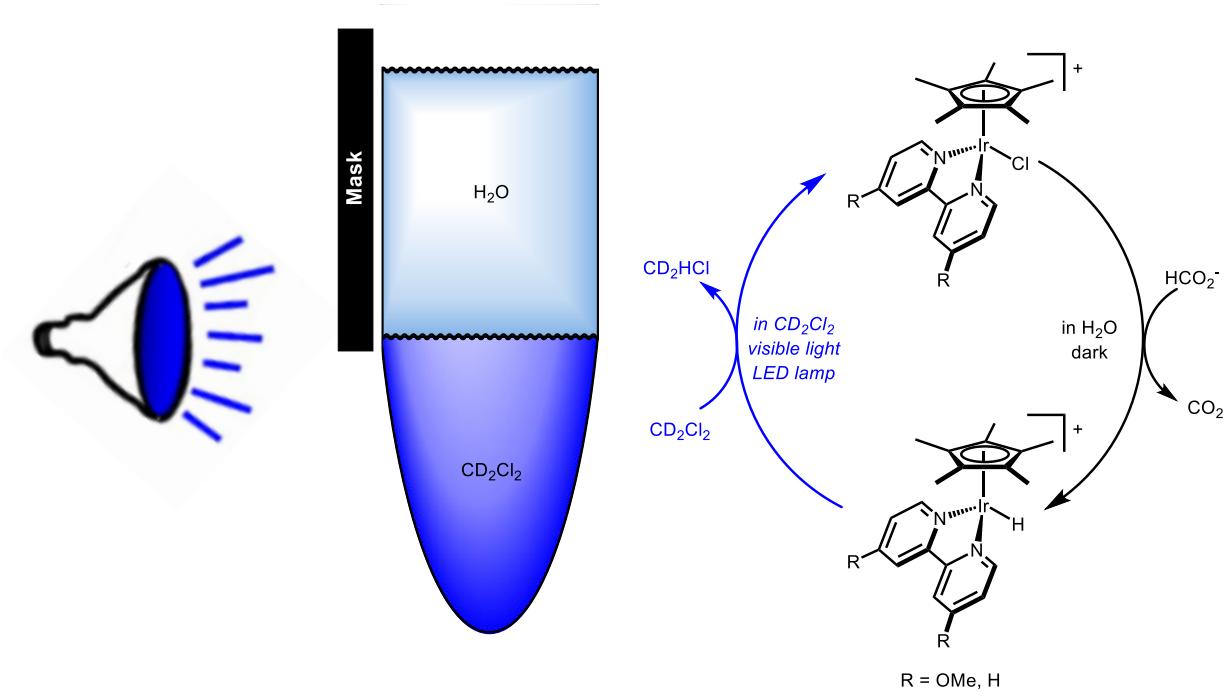

Figure 4.7. Biphasic reaction setup consisting of an aqueous formate layer and an organic CD_2Cl_2 layer in an NMR tube. A foil mask is used to prevent photolysis of the aqueous layer. Hydride **1** quickly forms in the aqueous formate layer from precatalyst **1-Cl**, then moves to the organic layer and is photolyzed to produce chloromethane and regenerate precatalyst **1-Cl**. Conditions: 9.4 mM **1-Cl**, 1.1 M $NaCO_2H$, 296 K, 443 or 460 nm irradiation.

To a 1.1 M formate solution in water, 9.4 mM precatalyst **1-Cl** was added and stirred in the dark for 15 minutes. The initial yellow color changed quickly to golden-yellow, indicative of hydride formation. CD_2Cl_2 was added to the solution, transferred to an NMR tube, and the organic layer of the biphasic reaction was irradiated with either 443 nm or 460 nm light. After 2, 5, and 12 hours of irradiation, illumination was stopped to evaluate catalytic performance relative to a mesitylene internal standard. After 2 hours of irradiation, greater than 1 TON of chloromethane was observed with 460 nm light; nearly 2 TON was observed using 443 nm light. After 12 hours of irradiation, TON exceeded 3 for both illumination setups. Notably, chloromethane is a gas and some product is expected in the headspace of the NMR tube. As additional support of greater than 3 TON, injection of the liquid sample into a GC gave similar

TON values, relative to a GC internal standard. Attempts to better quantify the amount of product in the headspace of the reaction is an area of future work.

Utilizing a biphasic reaction setup, **1** is capable of promoting *photocatalytic* hydrodehalogenation of dichloromethane (Scheme 4.4). Precatalyst **1-Cl** forms the formato complex in aqueous formate, which undergoes β-hydride elimination to lose CO_2 and form hydride **1**. Ground state **1** is excited with visible light to form **1***. **1*** reacts with a ground state **1** to release CD_2HCl and regenerate the **1-Cl** precatalyst. This last step in the cycle is expected to contain multiple steps, as proposed in Equation 4.1 through Equation 4.5.

Consistent with the proposed mechanism, growth of the chloromethane-d_2 product is observed via NMR, and precatalyst **1-Cl** is regenerated to complete the catalytic cycle. However, the system has yet to be optimized; turnover is relatively slow and catalytic performance is low. Hydride reactivity is fast, producing one equivalent of chloromethane quickly, but reformation of the hydride is slow; the solubility of **1-Cl** is higher in CD_2Cl_2 than H_2O. Allowing the biphasic reaction to rest overnight, **1-Cl** can diffuse into the aqueous layer, and the hydride is completely reformed and can be irradiated for additional catalytic performance. Shaking the NMR tube via vortexer does result in slightly quicker hydride reformation, but performance is still limited by the hydride reformation step.

Scheme 4.4. Proposed mechanism of photochemical dichloromethane hydrodehalogenation.

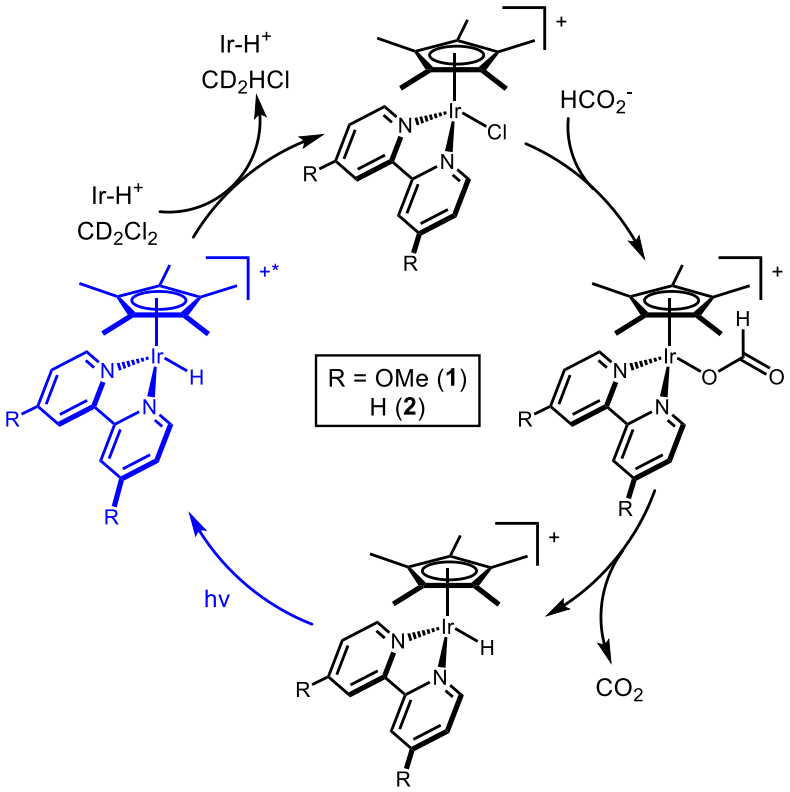

4.3 Conclusions

Mechanistic studies of Cp*Ir-based photochemical hydrodehalogenation catalysts have led to a better understanding of excited state reactivity. Kinetic evidence based upon the method of initial rates and quantum yields identified the mechanism to be second order in iridium, proposed to proceed through an excited state electron transfer from an excited hydride complex to a ground state complex. Generated hydride intermediates form the chloromethane product quickly while efficiently using absorbed light to achieve quantum yields exceeding 0.40. Biphasic experiments were utilized to test the photocatalytic hydrodehalogenation potential of the system. Turnovers greater than 3 were achieved, serving as a proof of concept for future catalytic reactions. The reactivity is achieved using mild reaction conditions using visible light irradiation to drive the hydrodehalogenation. Perhaps more importantly, the second order

dependence with respect to iridium may be applied more broadly to other solvents and additional reactions, proving a helpful insight into understanding Cp*Ir excited state reactivity and photoactivity. Future directions will focus on further understanding excited state reactivity, by identifying what properties and conditions lead to improvements in quantum yield, determining the lifetime of the species, and utilizing radical traps to rule out bimetallic radical mechanisms. Guided by these mechanistic findings, these results offer a promising outlook for light-driven hydrodehalogenation through net hydride transfer from transition metal hydride complexes.

4.4 Experimental Section

***General Considerations*.** Manipulations were performed under the inert nitrogen atmosphere of a Schlenk line or a glovebox. CH_2Cl_2 was dried and degassed with argon using a Pure Process Technology solvent system. CD_2Cl_2 was purchased from Cambridge Isotope Laboratories, Inc. and degassed by three freeze-pump-thaw cycles before drying by passage through a small column packed with activated alumina. $[Cp^*Ir(Cl)_2]_2$[60] and [Cp*Ir(bpy-OMe)(Cl)][Cl][61] were synthesized following established procedures. All other materials were readily commercially available and were used as received.

^1H and $^{13}C(^1H)$ NMR spectra were recorded on 400, 500, 600 MHz spectrometers at 25 ºC. Chemical shifts are reported with respect to residual proteo solvent.[62] UV-Vis spectra were obtained with an Ocean Optics USB2000+ spectrometer with a DT-MINI-2GS deuterium/tungsten halogen light source controlled by OceanView software. Visible light photolysis was carried out using an EagleLight 460 nm (± 12 nm at half-max intensity) LED lamp (500 lumens at 15 W) or a ThorLabs multi-wavelength LED source containing 406 ± 10 nm, 443 ± 9 nm, and 503 ± 13 nm LED lamps controlled by a ThorLabs LED driver for tunable power density. Photon flux measurements were determined using the ubiquitous potassium

ferrioxalate chemical actinometer. The quantum yield of the reaction was determined based on the disappearance of the hydride divided by the moles of *absorbed* photons after irradiation.

Chloromethane detection via GC was performed using either a Varian 450-GC with a pulsed discharge helium ionizer detector or an Agilent 6850 GC with a flame ionization detector. For the Varian 450-GC, a 1.0 mL Vici Pressure-Lok Precision Analytical gas-tight syringe was used to sample the headspace of the reaction vials by puncturing the septum cap. For the Agilent 6850 GC, a 10 µL gas tight syringe was used to sample either the headspace or solution of the reaction vial by puncturing the septum cap. A known amount of internal standard was injected to determine the amount of chloromethane detected.

Synthetic Procedures.

Synthesis of [Cp*Ir(bpy-OMe)(H_2O)][OTf]$_2$.

Using a modified procedure,[59] 73.5 mg (0.340 mmol) 4,4'-methoxy 2,2'-bipyridine was added to a stirring suspension containing 130.6 mg (0.164 mmol) [Cp*Ir$(Cl)_2]_2$ in 10 mL HPLC grade water. The 20 mL scintillation vial was heated to 40^{o}C to increase solubility. The solution slowly turned yellow and was heated overnight. The vial was allowed to cool, any remaining unreacted solids were removed via a frit packed with Celite. To the yellow solution, 168.6 mg (0.656 mmol) AgOTF were added. A white precipitate formed immediately and the suspension was stirred for 15 minutes. The AgCl solids were removed via a second frit packed with Celite. The yellow solution was again stirred for 15 minutes, allowing additional AgCl to precipitate. The solids were removed via filtration and yellow product was dried *in vacuo* to afford pure product (212.4 mg, 75% yield). ^{1}H NMR (D_2O): δ 8.85 (d, *J* = 6.6 Hz, 2H), 7.94 (d, *J* = 2.7 Hz, 2H), 7.37 (dd, *J* = 6.6, 2.7 Hz, 2H), 4.08 (s, 6H), 1.64 (s, 15H).

Synthesis of [Cp*Ir(bpy-OMe)(H)][OTf].

Using a modified procedure,[51] addition of 10 mL of 3 M formic acid at pH 5 to 212.4 mg (0.247 mmol) [Cp*Ir(bpy-OMe)(H_2O)][OTf]$_2$ in a 20 mL scintillation vial produced a dark brown solution that was protected from light and stirred for 4 h. After the first 2 hours, the reaction vessel cap was vented to release any CO_2 generated during the reaction. The cap was then replaced and the solution was stirred for an additional 2 hours. The product was extracted with 3 x 3 mL CH_2Cl_2. The extract was then washed with 3 x 3 mL aqueous LiOTf solution (147.2 mg, 0.944 mmol, in 10 mL water). The product was next washed with 3 x 3 mL of water. The final water wash was extracted with CH_2Cl_2 to recover any product lost to the aqueous layer. The yellow product was dried *in vacuo* to afford pure **1** (119.8 mg, 70% yield). ^{1}H NMR (DMSO-d_6): δ 8.65 (d, *J* = 6.6 Hz, 2H), 8.34 (d, *J* = 2.9 Hz, 2H), 7.32 (dd, *J* = 6.6, 2.8 Hz, 2H), 4.05 (s, 6H), 1.79 (s, 15H), –11.26 (s, 1H).

Synthesis of [Cp*Ir(bpy-OMe)(D)][PF_6].

A 20 mL scintillation vial was charged with 4.8 mg (7.81 μmol) [Cp*Ir(bpy-OMe)(Cl)][Cl], 3.7 mg (88.4 μmol) $NaBD_4$ (98% D), and 0.5 mL D_2O. The suspension was stirred for a few minutes and 3.7 mg (22.0 μmol) $NaPF_6$ was added to the vial. Solids were collected via a pipette filtration and were dissolved in CD_3CN for characterization. ^{1}H NMR (CD_3CN): δ 8.60 (d, *J* = 6.4 Hz, 2H), 7.86 (d, *J* = 2.9 Hz, 2H), 7.15 (dd, *J* = 6.5, 2.8 Hz, 2H), 4.04 (s, 6H), 1.80 (s, 15H). ^{31}P NMR (CD_3CN): δ -143.21 (m) from PF_6 counterion. Note: no ^{11}B peak was noted, indicating the complete removal of the BD_4 counterion.

Kinetics: Method of Initial Rates

Reactions were carried out in a 4-sided quartz cuvette and prepared in a glovebox. A representative method of initial rates procedure is included for completeness. In a typical

reaction, a stock solution of [Cp*Ir(bpy-OMe)(H)][OTf] was prepared by dissolving 4.0 mg (5.77 μmol) in a 1 mL volumetric flask. From this 5.77 mM stock solution, four samples were prepared; a 0.55 mM solution was prepared by adding 190 μL of the stock solution via syringe to a 2 mL volumetric flask, a 0.29 mM solution was prepared by adding 100 μL of the stock solution, a 0.17 mM solution was prepared by adding 60 μL of the stock solution, and a 0.06 mM solution was prepared by adding 20 μL of the stock solution. The samples were prepared immediately prior to photolysis and UV-Vis characterization. After an initial absorbance spectrum was recorded, the sample in the cuvette was irradiated with a 443 nm LED using the ThorLabs LED source and the LED driver was used to control current (and therefore the photon flux) of the lamp to ensure appropriate reaction times. The driver was set to 10 mA and the sample was irradiated at 0.25, 0.50, 0.75, 1.00, 1.5, 2.0, 2.5, 3.0, 3.5, 4.0 minutes with the absorbance recorded after each period of irradiation. The initial rates were obtained for the first 10% conversion of the reaction, disappearance of the hydride observed at 423 nm, the λ_{max}. Initial rates were recorded, and a log-log plot of iridium concentration vs. initial rates was created to show the reaction order in iridium. The experimental order in iridium was found to vary from 1.5-2.4, indicating a correction for absorbance was needed.

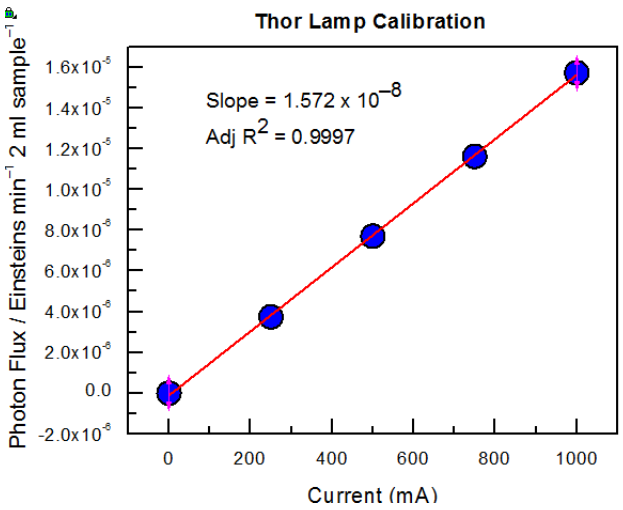

Figure 4.8. Photon flux measurements for the 443 nm ThorLabs LED lamp at varied current using the potassium ferrioxalate chemical actinometer.

This correction for absorbance was made possible by determining the quantum yield of the experiment. The absorbance correction is achieved by calculating the moles of photons absorbed by each sample (which includes an iridium concentration term). A potassium ferrioxalate chemical actinometer[63-67] was used to determine the photon flux of the light at the selected current. Combining the photon flux and absorbance of each sample, the quantum yield of each experiment was determined (Equation 4.6), with typical values ranging from 0.01 – 0.64. Taking a log-log plot of iridium concentration vs. quantum yield determines the reaction order beyond one (therefore, a slope of one suggests a second order reaction).

$$\text{QY} = \frac{\text{initial rate}\left(\frac{\text{mol}}{\text{min}}\right)}{[\%\text{ of irradiated light absorbed}]\left[\text{photon flux}\left(\frac{\text{mol photons}}{\text{min}}\right)\right]} \qquad \text{(Equation 4.6)}$$

Catalytic Hydrodehalogenation: Biphasic NMR Experiments

General Procedure. Catalytic reactions with dichloromethane were carried out on the NMR scale using a biphasic reaction mixture of CD_2Cl_2 and H_2O. Reaction mixtures in NMR

tubes were prepared in a nitrogen-filled glovebox as described in specific cases below, and the tubes were sealed and wrapped with parafilm. Experiments that were also probed via GC for catalytic chloromethane production were sealed with an NMR septum cap. After the initial NMR spectra were taken, one (light) sample was irradiated with the 460 nm LED for the desired time. The other (dark) tube was protected from light. The given reaction times for light samples are the time under active irradiation (time protected from light, where no background reaction was observed, is not counted); for dark samples, it is the total reaction time from initial reactant mixing. The reaction was monitored by NMR spectroscopy periodically. Product yields were determined from NMR integrations relative to a mesitylene or dioxane internal standard and are based upon the amount of iridium starting material present at the beginning of the reaction. The yields of chloromethane were established in representative examples as described below.

Catalytic Reaction of 1 or 2 with CH_2Cl_2: A 20 mL scintillation vial was charged with 11.5 mg (0.019 mmol) [Cp*Ir(bpy-OMe)(Cl)][Cl] and 1.0 mL H_2O. A stir bar and 75.4 mg (1.109 mmol) NaO_2CH was added to the vial and the solution was stirred in the dark for 15 min. An immediate color change of yellow to golden yellow was observed. In a second 20 mL scintillation vial, 2 mL CD_2Cl_2 and 40 µL (0.023 mmol) of a 0.58 M mesitylene stock solution were added. The aqueous solution was divided equally between two NMR tubes. The organic solution was then added, divided equally between the two NMR tubes. The tubes were inverted to place CD_2Cl_2 layer at the bottom of the tubes. After taking the initial spectra (no irradiation), one tube was irradiated with the 460 nm LED lamp, while the second tube was irradiated with the 443 nm LED at full power. The tubes were irradiated for 2, 5, and 12 h. NMR spectra were taken for each tube after each irradiation time. Determination of TON was made by integration of the mesitylene internal standard and the pentet product, CD_2HCl., at 2.99 ppm.

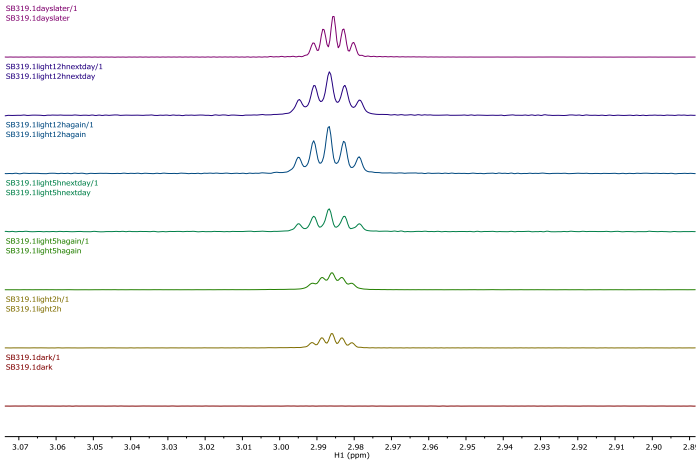

Figure 4.9. ^{1}H NMR spectrum of [Cp*Ir(bpy-OMe)(H)][OTf] in a biphasic setup with CD_2Cl_2 and H_2O after irradiation with 460 nm LED. CD_2HCl peak growth is observed after 2, 5, and 12 hours of irradiation. Spectra normalized to mesitylene internal standard.

To further support this determined TON, GC studies were also performed. A known amount of chloromethane was first injected into the instrument to record the retention time and instrument response. The NMR tube was sampled via a gas-tight syringe and the sample was injected into the GC. Comparison against the prior, known chloromethane sample provided the determination of TON by GC.

4.5 Acknowledgements

S.M.B. performed all experiments. We gratefully acknowledge funding from The University of North Carolina at Chapel Hill and a NSF Graduate Research Fellowship to S.M.B. (DGE-1144081). This research made use of instrumentation funded by the UNC EFRC: Center for Solar Fuels, and Energy Frontier Research Center supported by the U.S. Department of Energy, Office of Science, Office of Basic Energy Sciences, under award number DE-SC0001011.

4.6 Associated Content

Appendix C: Additional experimental details, NMR spectra.

REFERENCES

1. Narayanam, J. M. R.; Stephenson, C. R. J., *Chem. Soc. Rev.* **2011,** *40*, 102.

2. Alonso, F.; Beletskaya, I. P.; Yus, M., *Chem. Rev.* **2002,** *102*, 4009.

3. Voldner, E. C.; Li, Y. F., *Sci. Total Environ.* **1995,** *160–161*, 201.

4. Key, B. D.; Howell, R. D.; Criddle, C. S., *Environ. Sci. Technol.* **1997,** *31*, 2445.

5. de Wit, C. A., *Chemosphere* **2002,** *46*, 583.

6. Birnbaum, L. S.; Staskal, D. F., *Environ. Health Perspect.* **2004,** *112*, 9.

7. Breivik, K.; Sweetman, A.; Pacyna, J. M.; Jones, K. C., *Sci. Total Environ.* **2007,** *377*, 296.

8. Lohmann, R.; Breivik, K.; Dachs, J.; Muir, D., *Environ. Pollut.* **2007,** *150*, 150.

9. Adams, D. E. C.; Halden, R. U., *Contaminants of Emerging Concern in the Environment: Ecological and Human Health Considerations*. 2010; p 539.

10. O'Hagan, D., *J. Fluorine Chem.* **2010,** *131*, 1071.

11. de Wit, C. A.; Kierkegaard, A.; Ricklund, N.; Sellström, U., *Brominated Flame Retardants*. 2011; p 241.

12. Shen, Y.; Zhao, R.; Wang, J.; Chen, X.; Ge, X.; Chen, M., *Waste Manage.* **2016,** *49*, 287.

13. Capracotta, S. S.; Comins, D. L., *Tetrahedron Lett.* **2009,** *50*, 1806.

14. Liégault, B.; Petrov, I.; Gorelsky, S. I.; Fagnou, K., *J. Org. Chem.* **2010,** *75*, 1047.

15. Hartung, C. G.; Snieckus, V., The Directed ortho Metalation Reaction – A Point of Departure for New Synthetic Aromatic Chemistry. In *Modern Arene Chemistry*, Wiley-VCH Verlag GmbH & Co. KGaA: 2004; pp 330-367.

16. Snieckus, V., *Chem. Rev.* **1990,** *90*, 879.

17. Wagner, F. F.; Comins, D. L., *Eur. J. Org. Chem.* **2006,** *2006*, 3562.

18. Mandal, P. K.; Birtwistle, J. S.; McMurray, J. S., *J. Org. Chem.* **2014,** *79*, 8422.

19. Varzatskii, O. A.; Shul'ga, S. V.; Belov, A. S.; Novikov, V. V.; Dolganov, A. V.; Vologzhanina, A. V.; Voloshin, Y. Z., *Dalton Trans.* **2014,** *43*, 17934.

20. Lugaresi, O.; Encontre, H.; Locatelli, C.; Minguzzi, A.; Vertova, A.; Rondinini, S.; Comninellis, C., *Electrochem. Commun.* **2014,** *44*, 63.

21. Chelucci, G.; Baldino, S.; Pinna, G. A.; Pinna, G., *Current Org. Chem.* **2012,** *16*, 2921.

22. Wallentin, C.-J.; Nguyen, J. D.; Stephenson, C. R. J., *CHIMIA International Journal for Chemistry* **2012,** *66*, 394.

23. Fukuzumi, S.; Mochizuki, S.; Tanaka, T., *J. Phys. Chem.* **1990,** *94*, 722.

24. Narayanam, J. M. R.; Tucker, J. W.; Stephenson, C. R. J., *J. Am. Chem. Soc.* **2009,** *131*, 8756.

25. Kraft, B. M.; Lachicotte, R. J.; Jones, W. D., *J. Am. Chem. Soc.* **2001,** *123*, 10973.

26. Garrido, R.; Hernández-Montes, P. S.; Gordillo, Á.; Gómez-Sal, P.; López-Mardomingo, C.; de Jesús, E., *Organometallics* **2015,** *34*, 1855.

27. Grushin, V. V.; Alper, H., *Chem. Rev.* **1994,** *94*, 1047.

28. Kiplinger, J. L.; Richmond, T. G.; Osterberg, C. E., *Chem. Rev.* **1994,** *94*, 373.

29. Grushin, V. V.; Alper, H., *Activation of otherwise unreactive CCl bonds*. Springer-Verlag: 1999; Vol. 3.

30. Schrick, B.; Blough, J. L.; Jones, A. D.; Mallouk, T. E., *Chem. Mater.* **2002,** *14*, 5140.

31. Aresta, M.; Caramuscio, P.; De Stefano, L.; Pastore, T., *Waste Manage.* **2003,** *23*, 315.

32. Maron, L.; Werkema, E. L.; Perrin, L.; Eisenstein, O.; Andersen, R. A., *J. Am. Chem. Soc.* **2005,** *127*, 279.

33. Rettenmeier, C.; Wadepohl, H.; Gade, L. H., *Chem. – Eur. J.* **2014,** *20*, 9657.

34. Sadowsky, D.; McNeill, K.; Cramer, C. J., *Environ. Sci. Technol.* **2014,** *48*, 10904.

35. Artamkina, G. A.; Egorov, M. P.; Beletskaya, I. P., *Chem. Rev.* **1982,** *82*, 427.

36. Vlasov, V., *J. Fluorine Chem.* **1993,** *61*, 193.

37. Chelucci, G.; Figus, S., *J. Mol. Catal. A- Chem.* **2014,** *393*, 191.

38. Tsurugi, H.; Hayakawa, A.; Kando, S.; Sugino, Y.; Mashima, K., *Chem. Sci.* **2015,** *6*, 3434.

39. Minguzzi, A.; Lugaresi, O.; Aricci, G.; Rondinini, S.; Vertova, A., *Electrochem. Commun.* **2012,** *22*, 25.

40. Rondinini, S.; Aricci, G.; Krpetić, Ž.; Locatelli, C.; Minguzzi, A.; Porta, F.; Vertova, A., *Fuel Cells* **2009,** *9*, 253.

41. Klymenko, O. V.; Buriez, O.; Labbé, E.; Zhan, D.-P.; Rondinini, S.; Tian, Z.-Q.; Svir, I.; Amatore, C., *ChemElectroChem* **2014,** *1*, 227.

42. Scialdone, O.; Guarisco, C.; Galia, A.; Herbois, R., *J. Electroanal. Chem.* **2010,** *641*, 14.

43. Huang, B.; Isse, A. A.; Durante, C.; Wei, C.; Gennaro, A., *Electrochim. Acta* **2012,** *70*, 50.

44. Poizot, P.; Laffont-Dantras, L.; Simonet, J., *Electrochem. Commun.* **2008,** *10*, 864.

45. Perini, L.; Durante, C.; Favaro, M.; Agnoli, S.; Granozzi, G.; Gennaro, A., *Appl. Catal. B - Environ.* **2014,** *144*, 300.

46. Simonet, J., *J. Electroanal. Chem.* **2005,** *583*, 34.

47. Shiraishi, Y.; Takeda, Y.; Sugano, Y.; Ichikawa, S.; Tanaka, S.; Hirai, T., *Chem. Commun.* **2011,** *47*, 7863.

48. An, C.; Kuang, Y.; Fu, C.; Zeng, F.; Wang, W.; Zhou, H., *Electrochem. Commun.* **2011,** *13*, 1413.

49. Pélisson, C.-H.; Denicourt-Nowicki, A.; Meriadec, C.; Greneche, J.-M.; Roucoux, A., *ChemCatChem* **2015,** *7*, 309.

50. Pitman, C. L.; Miller, A. J. M., *ACS Catal.* **2014,** *4*, 2727.

51. Barrett, S. M.; Pitman, C. L.; Walden, A. G.; Miller, A. J. M., *J. Am. Chem. Soc.* **2014,** *136*, 14718.

52. Barrett, S. M.; Slattery, S. A.; Miller, A. J. M., *ACS Catal.* **2015,** *5*, 6320.

53. Ogo, S.; Makihara, N.; Kaneko, Y.; Watanabe, Y., *Organometallics* **2001,** *20*, 4903.

54. Watson, K. J.; Ziessel, R., *Inorg. Chim. Acta* **1992,** *197*, 125.

55. Ziessel, R., *J. Am. Chem. Soc.* **1993,** *115*.

56. Abura, T.; Ogo, S.; Watanabe, Y.; Fukuzumi, S., *J. Am. Chem. Soc.* **2003,** *125*, 4149.

57. Steckhan, E.; Herrmann, S.; Ruppert, R.; Dietz, E.; Frede, M.; Spika, E., *Organometallics* **1991,** *10*, 1568.

58. Lo, H. C.; Leiva, C.; Buriez, O.; Kerr, J. B.; Olmstead, M. M.; Fish, R. H., *Inorg. Chem.* **2001,** *40*, 6705.

59. Miller, A. J. M.; Heinekey, D. M.; Mayer, J. M.; Goldberg, K. I., *Angew. Chem., Int. Ed.* **2013,** *52*, 3981.

60. White, C.; Yates, A.; Maitlis, P. M., *Inorg. Synth.* **1992,** *29*, 228.

61. Himeda, Y.; Onozawa-Komatsuzaki, N.; Sugihara, H.; Kasuga, K., *Organometallics* **2007,** *26*, 702.

62. Fulmer, G. R.; Miller, A. J. M.; Sherden, N. H.; Gottlieb, H. E.; Nudelman, A.; Stoltz, B. M.; Bercaw, J. E.; Goldberg, K. I., *Organometallics* **2010,** *29*, 2176.

63. Prasad, R.; Sulaxna; Kumar, A., *J. Therm. Anal. Calorim.* **2005,** *81*, 441.

64. Kirk, A. D.; Namasivayam, C., *Anal. Chem.* **1983,** *55*, 2428.

65. Murov, S. L.; Carmichael, I.; Hug, G. L., *Handbook of Photochemistry*. 1993; p 298.

66. Kuhn, H. J.; Braslavsky, S. E.; Schmidt, R., *Pure Appl. Chem.* **2004,** *76*, 2105.

67. Gandolfi, M. T.; Moggi, L., *The Exploration of Supramolecular Systems and Nanostructures by Photochemical Techniques*. 2012; p 67.

APPENDIX A. PHOTOSWITCHABLE HYDRIDE TRANSFER FROM IRIDIUM TO 1-METHYLNICOTINAMIDE BY THERMOCHEMICAL CYCLES

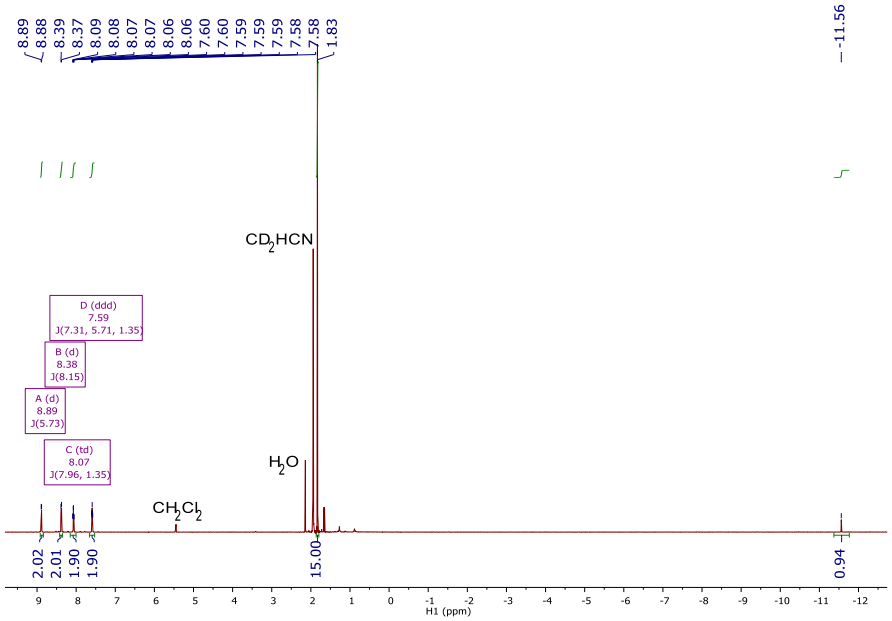

Figure A.1. ^{1}H NMR spectrum of [Cp*Ir(bpy)(H)][OTf] (**1**) in CD_3CN.

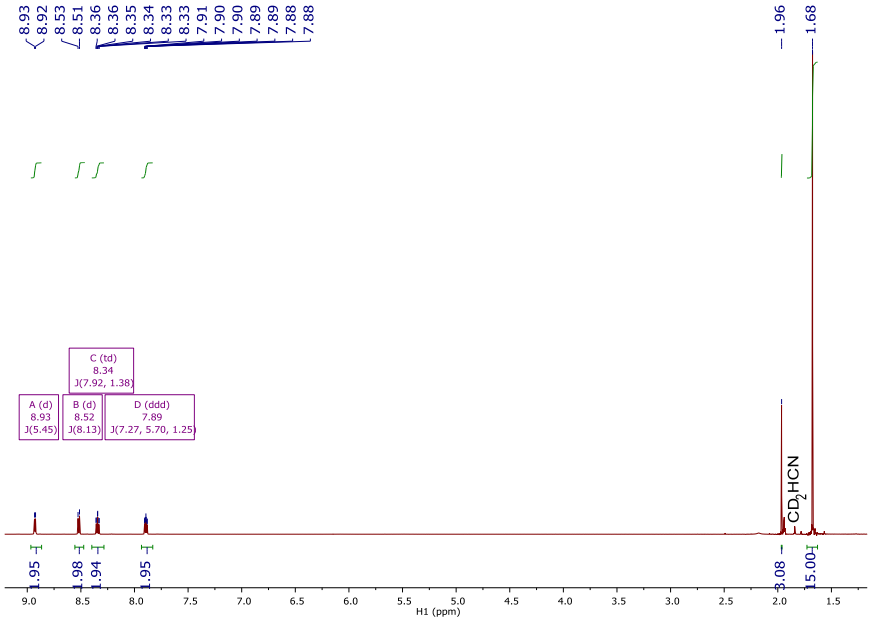

Figure A.2. ^{1}H NMR spectrum of [Cp*Ir(bpy)($NCCH_3$)][PF_6] (**2**) in CD_3CN.

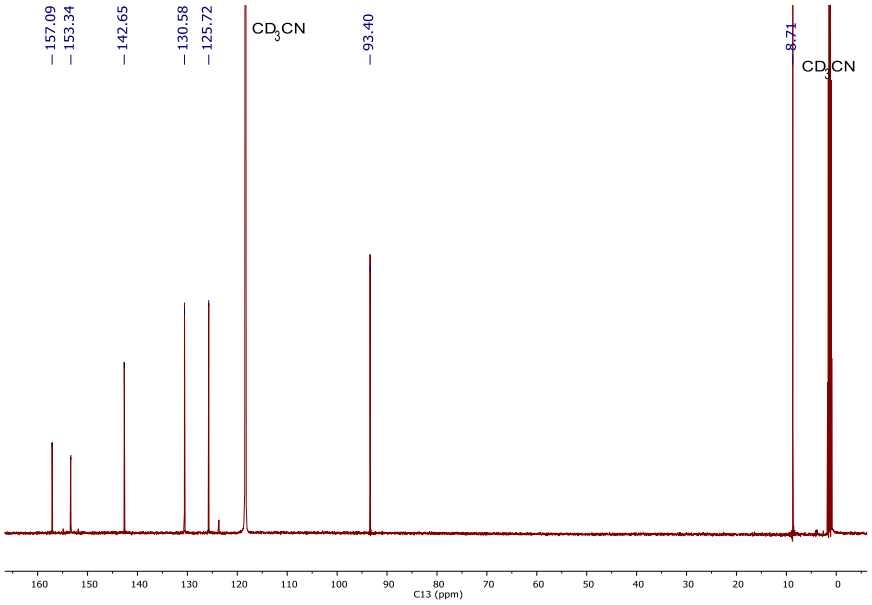

Figure A.3. $^{13}C(^{1}H)$ NMR spectrum of [Cp*Ir(bpy)($NCCH_3$)][PF_6] (**2**) in CD_3CN.

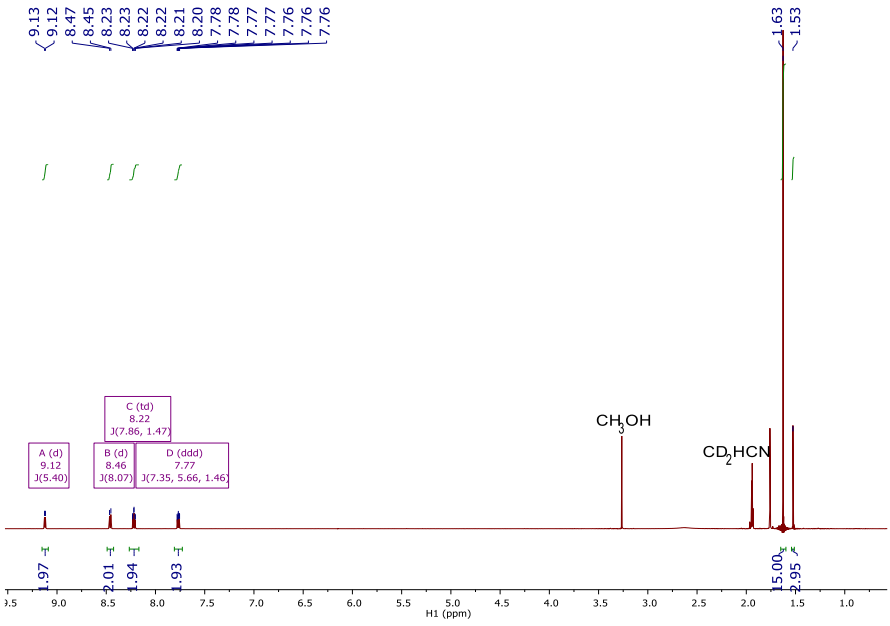

Figure A.4. ^{1}H NMR spectrum of [Cp*Ir(bpy)(OAc)][OAc] (**3**) in CD_3CN.

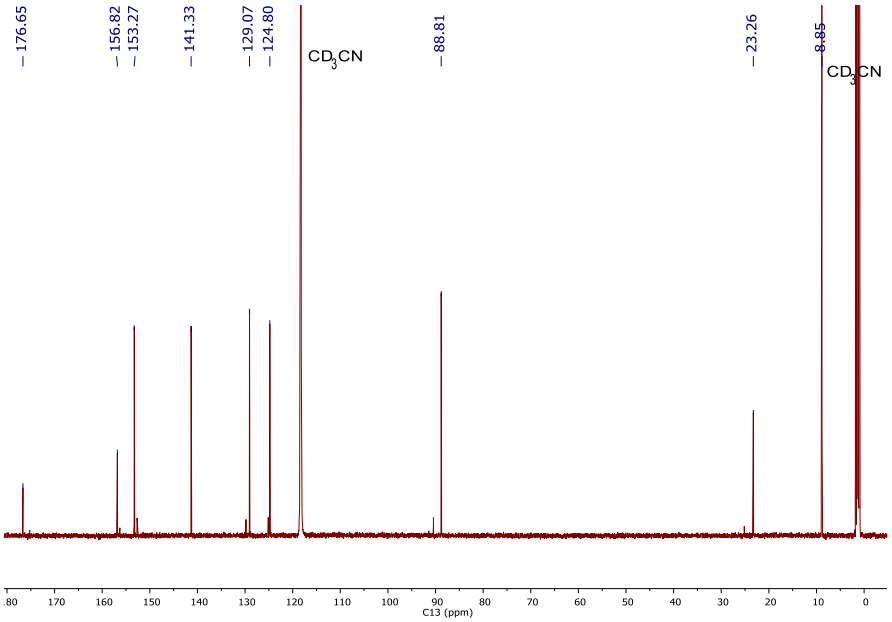

Figure A.5. $^{13}C(^{1}H)$ NMR spectrum of [Cp*Ir(bpy)(OAc)][OAc] (**3**) in CD_3CN.

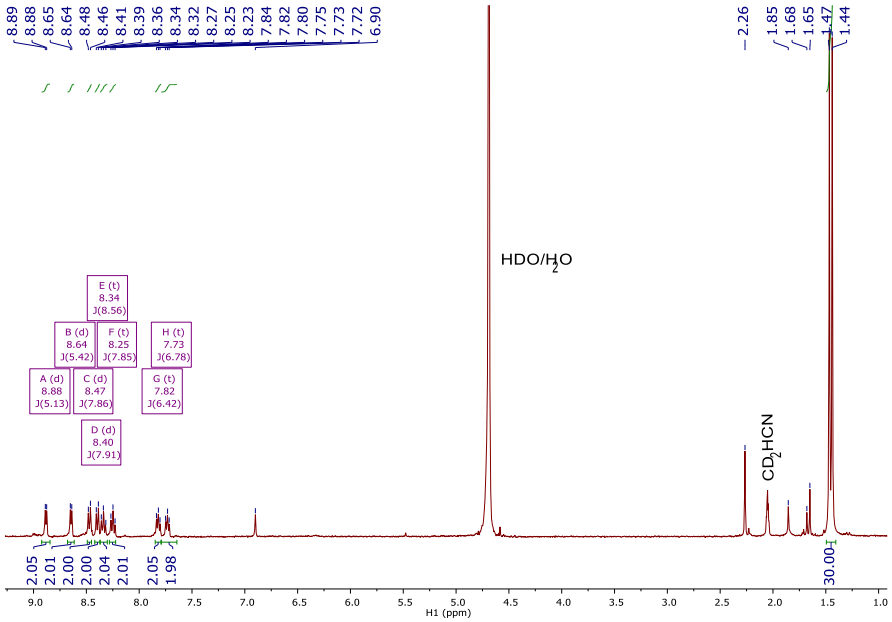

Figure A.6. ^{1}H NMR spectrum of **4-OTf** in CD_3CN containing mesitylene internal standard (δ 6.90, 2.26).

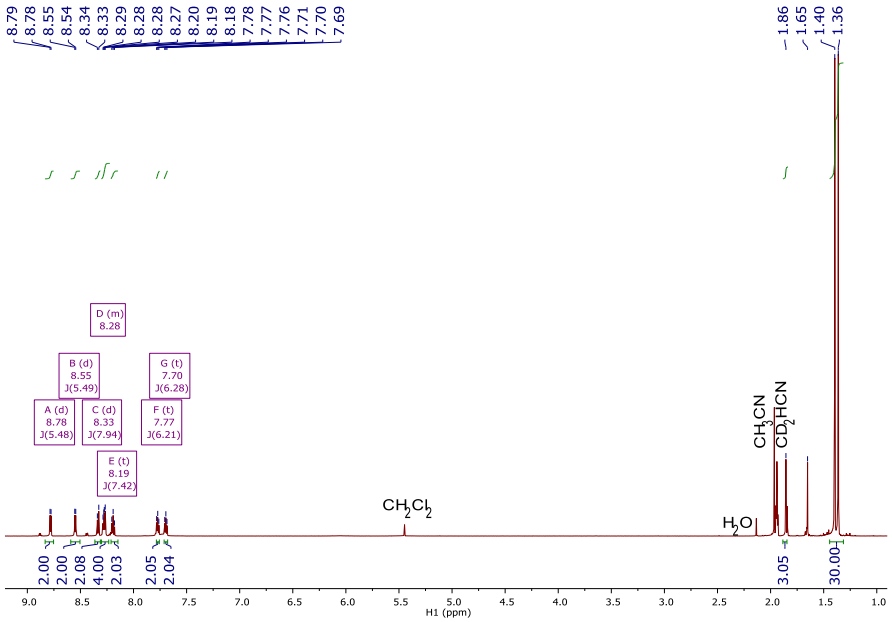

Figure A.7. ^{1}H NMR spectrum of [Cp*Ir(bpy)(μ-N(H)C(CH$_3$))(bpy)IrCp*][PF$_6$]$_3$ (**4-PF$_6$**) in CD_3CN.

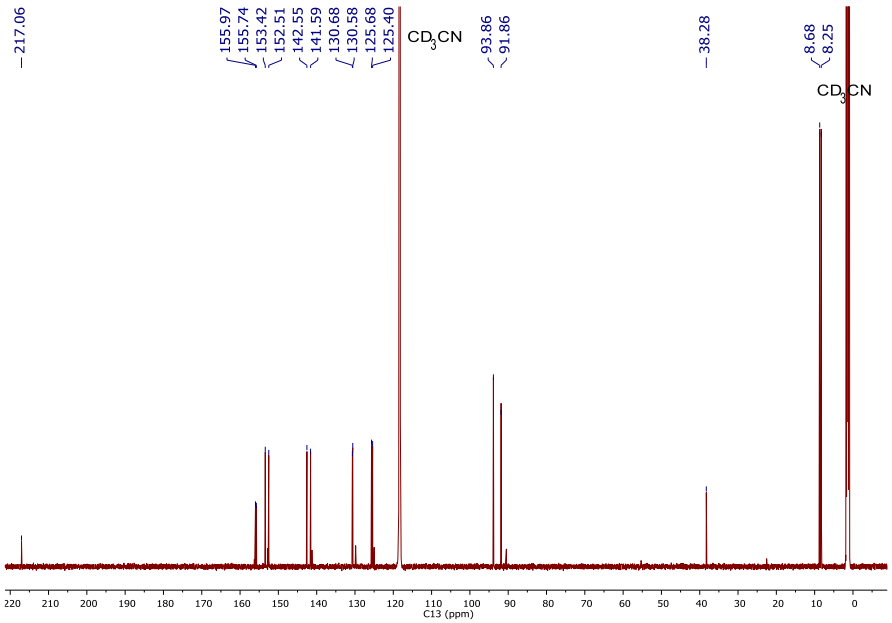

Figure A.8. ^{13}C(^{1}H) NMR spectrum of [Cp*Ir(bpy)(μ-N(H)C(CH$_3$))(bpy)IrCp*][PF$_6$]$_3$ (**4-PF$_6$**) in CD_3CN.

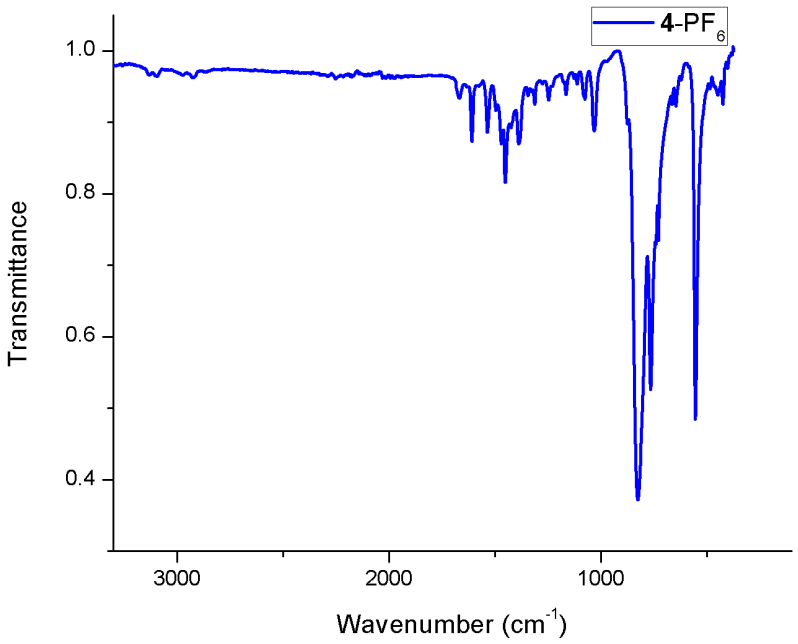

Figure A.9. IR spectrum of [Cp*Ir(bpy)(μ-N(H)C(CH_3))(bpy)IrCp*][PF_6]$_3$ (**4-PF_6**). P-F stretch dominates the spectrum (826 and 555 cm^{-1}). $\nu_{C=N}$ = 1536 cm^{-1}.

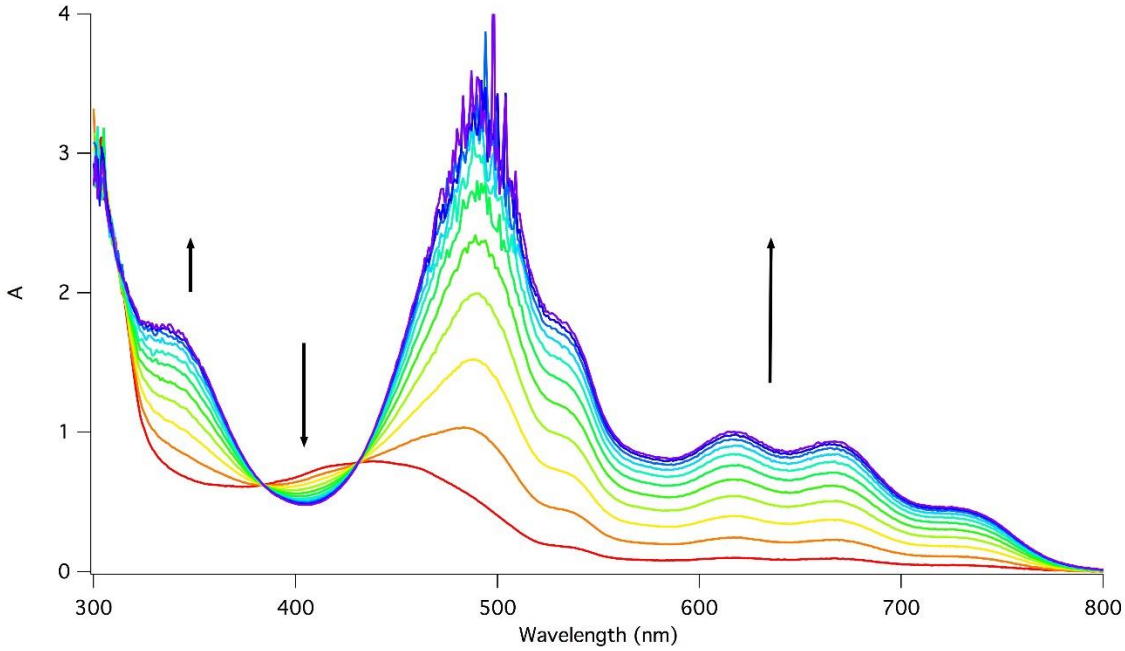

Figure A.10. UV-Vis spectra monitoring addition of DBU to **1** in CH_3CN.

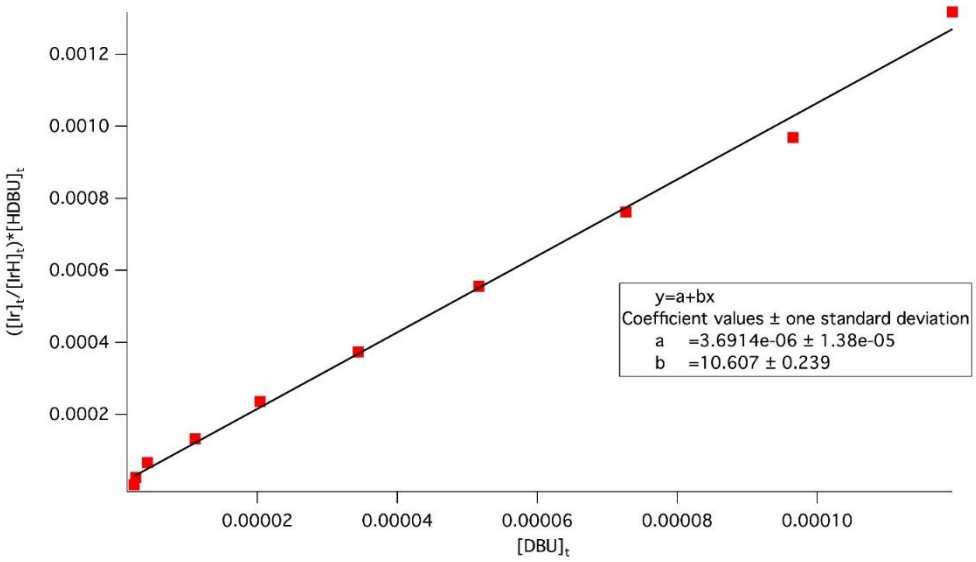

Figure A.11. Plot of $([Ir]_t/[IrH]_t)*[HDBU]_t$ vs $[DBU]_t$ generated from data points at 620 nm.

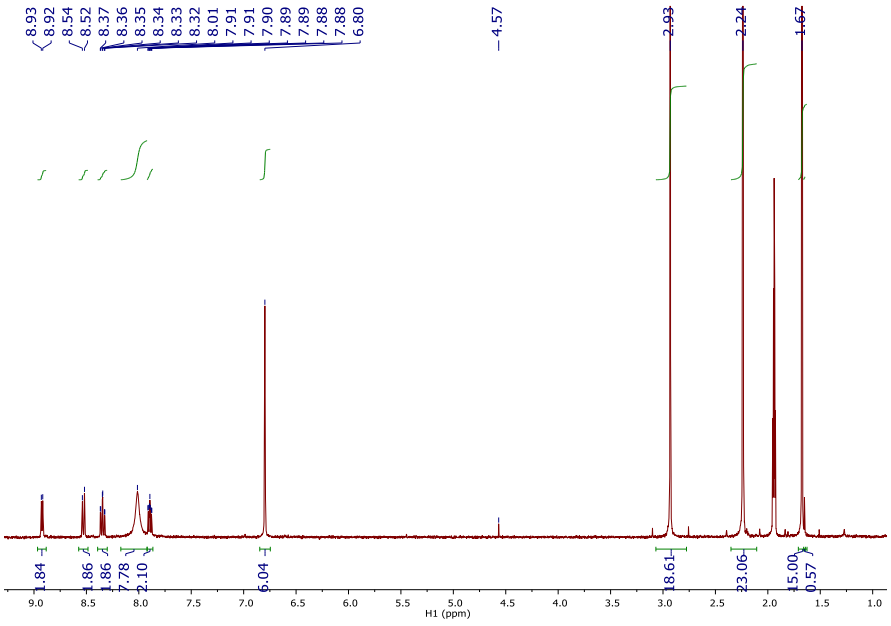

Figure A.12. ^{1}H NMR spectrum of methanesulfonic acid and **1** in CD_3CN after 1 h in the dark. The Cp* peak for **1** (δ 1.83) is notably absent, while the Cp* peak for the product (**2**) is seen (δ 1.67). Mesitylene (δ 6.80, 2.24), excess methanesulfonic acid (δ 8.01, 2.93), and hydrogen (δ 4.57) are also observed.

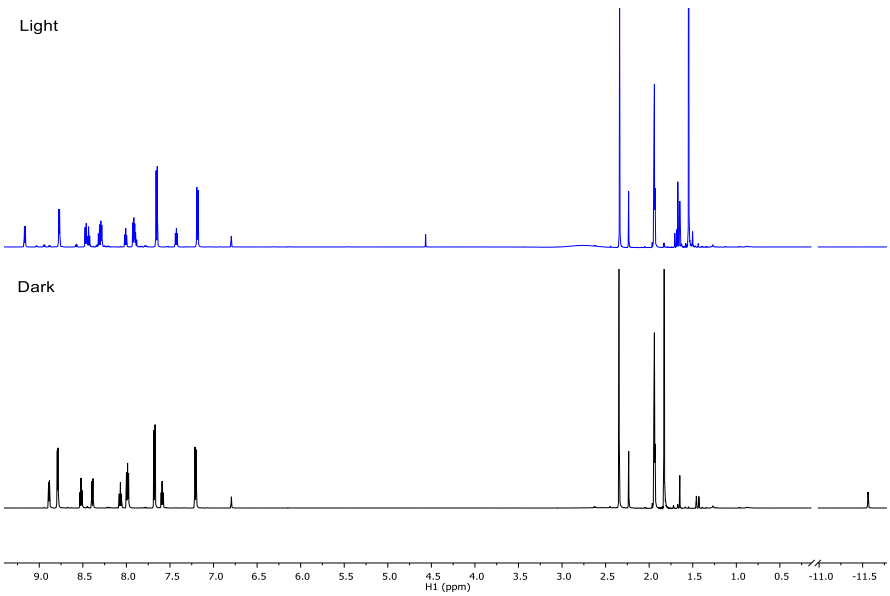

Figure A.13. ^{1}H NMR spectra of pyridinium and **1** in CD_3CN after 1 h in the dark (black) and after 1 h of irradiation (blue). The Cp* peak for **1** (δ 1.83) is notably absent after irradiation, while the Cp* peak for the product is seen (δ 1.55). Mesitylene (δ 6.79, 2.23), excess pyridinium (δ 8.77, 8.43, 7.91), and dihydrogen (δ 4.57) are also observed.

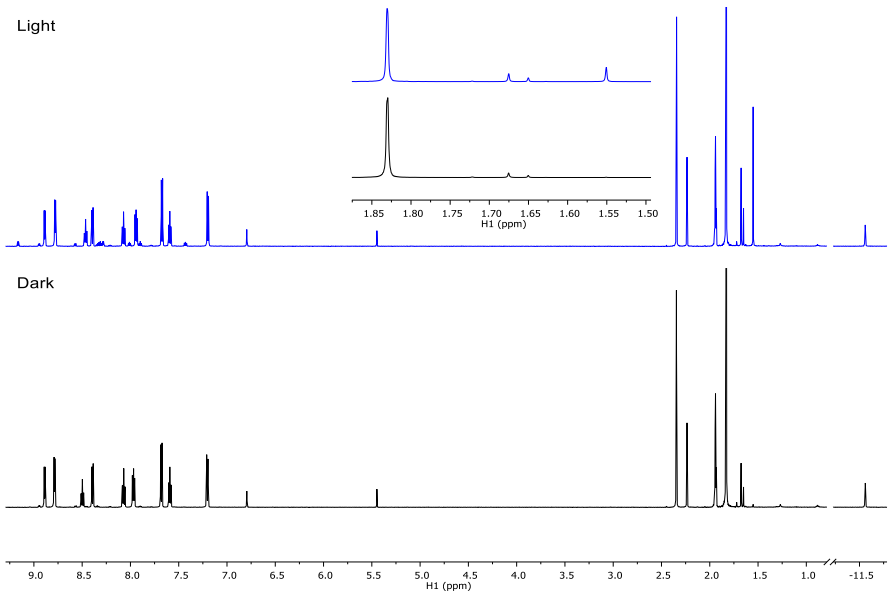

Figure A.14. ^{1}H NMR spectra of pyridinium and **1** in CD_3CN after ~10 min in the dark (black) and after heating at 80 ºC for 3 h in the dark (blue). Inset: ^{1}H NMR spectra (Cp* region).

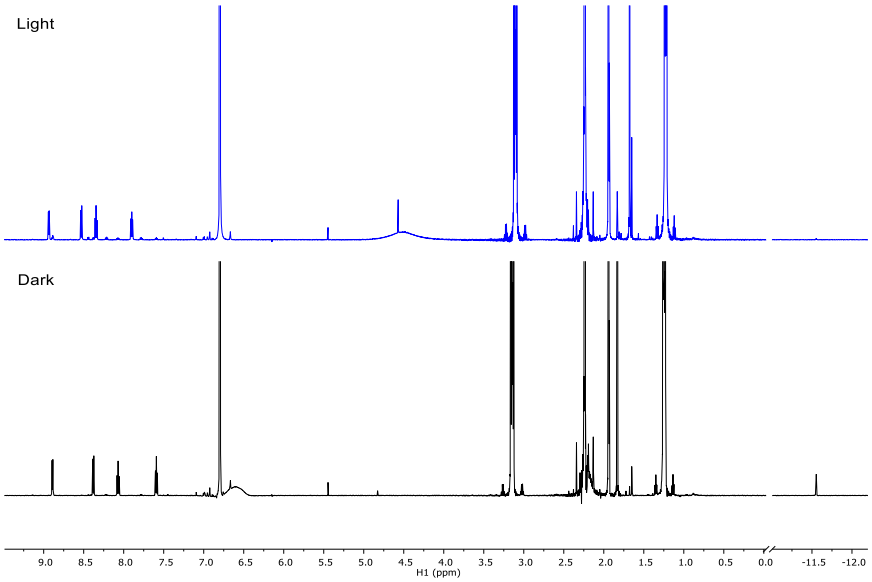

Figure A.15. ^{1}H NMR spectra of triethylammonium and **1** in CD_3CN after 10 min in the dark (black) and after 10 min of irradiation (blue). The Cp* peak for **1** (δ 1.83) is nearly absent, while the Cp* peak for the product (**2**) is seen (δ 1.68). Mesitylene (δ 6.79, 2.24), excess triethylammonium (δ 3.10, 1.23), and dihydrogen (δ 4.57) are also observed.

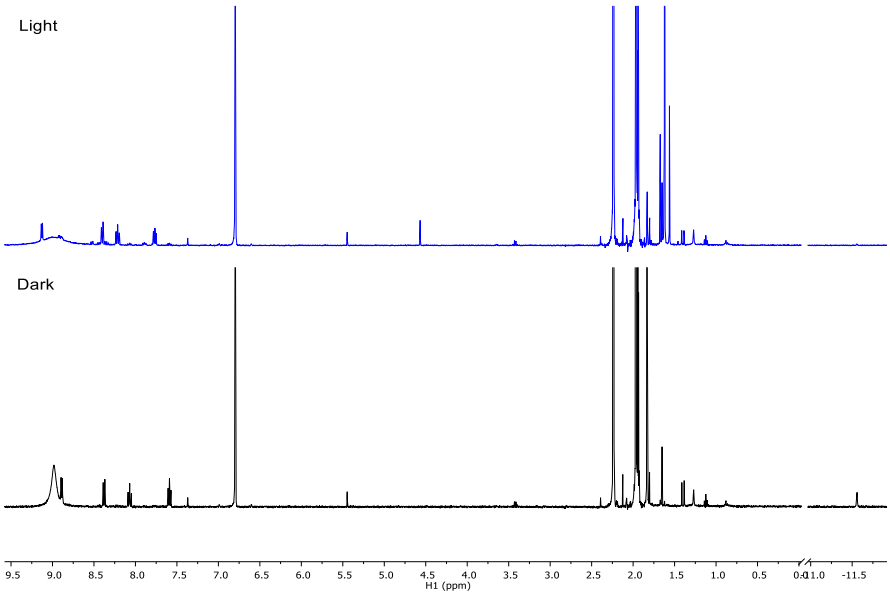

Figure A.16. ^{1}H NMR spectra of acetic acid and **1** in CD_3CN after 10 min in the dark (black) and after 10 min of irradiation (blue). The Cp* peak for **1** (δ 1.83) is nearly absent, while the Cp* peak for the product (**3**) is seen (δ 1.62). Mesitylene (δ 6.80, 2.24), excess acetic acid (δ 1.96), and dihydrogen (δ 4.57) are also observed.

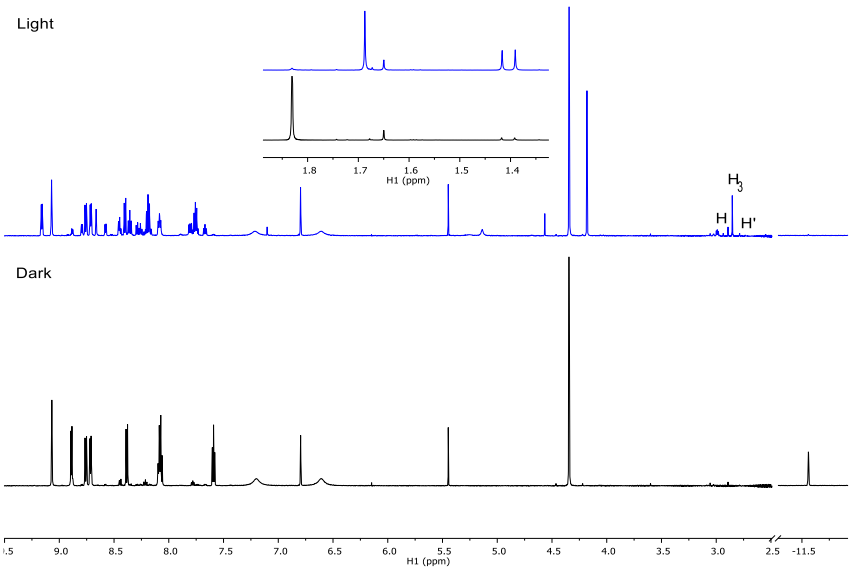

Figure A.17. ^{1}H NMR spectrum of **1** and [MNA][BF_4] (1:1.7) in CD_3CN after 1 h in the dark (black) and after 1 h of irradiation (blue). Inset: the Cp* peak for **1** (δ 1.83) is absent, while the Cp* peaks for the products $[Cp^*Ir(bpy)(MNA)]^{2+}$ (δ 1.69) and **4-OTf** (δ 1.41, 1.39) are observed. The methyl peak for $[Cp^*Ir(bpy)(MNA)]^{2+}$ is also seen (δ 4.18). Products MNA-H, MNA-H', and MNA-H_3 are labeled above as H, H', and H_3, respectively.

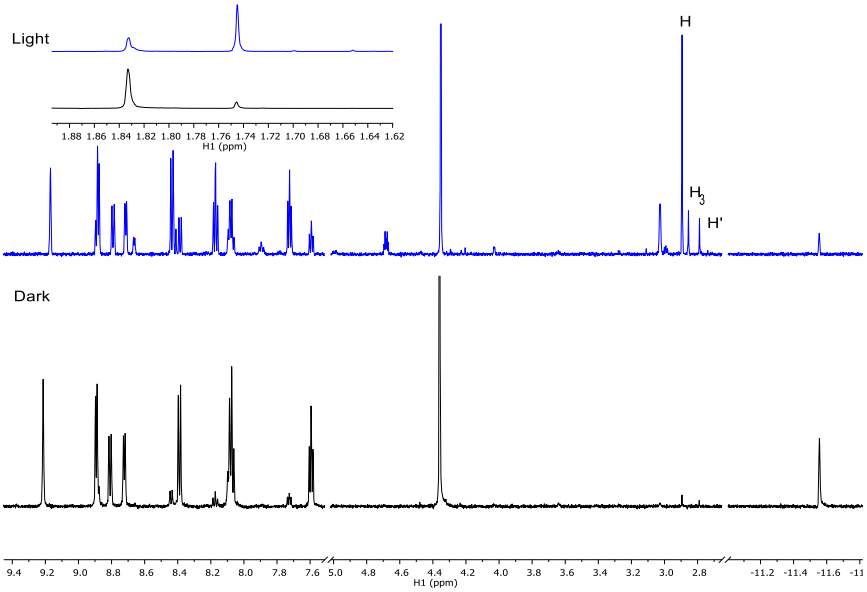

Figure A.18. ^{1}H NMR spectrum of **1** and [MNA][I] (1:1.5) in CD_3CN after 1 h in the dark (black) and after 3 min of irradiation (blue). Inset: the Cp* peak for **1** (δ 1.83) is significantly diminished, while the Cp* peak for the product $[Cp^*Ir(bpy)(I)]^{+}$ (δ 1.74), is observed. N-methyl group of products MNA-H, MNA-H', and MNA-H_3 are labeled above as H, H', and H_3.

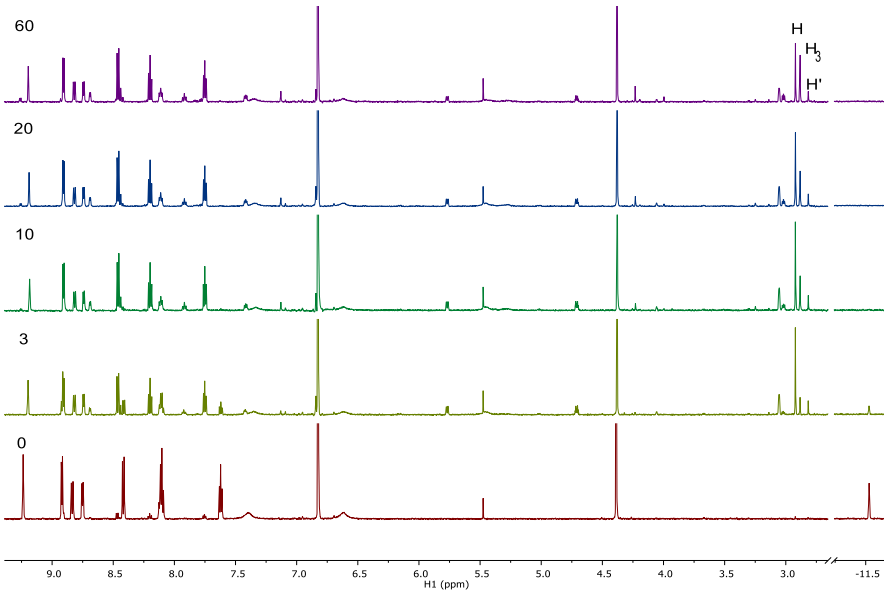

Figure A.19. ^{1}H NMR spectrum of **1** and [MNA][I] (1:1.5) in CD_3CN after 0, 3, 10, 20, and 60 min of irradiation. N-methyl group of products MNA-H, MNA-H', and MNA-H_3 are labeled above as H, H', and H_3, respectively.

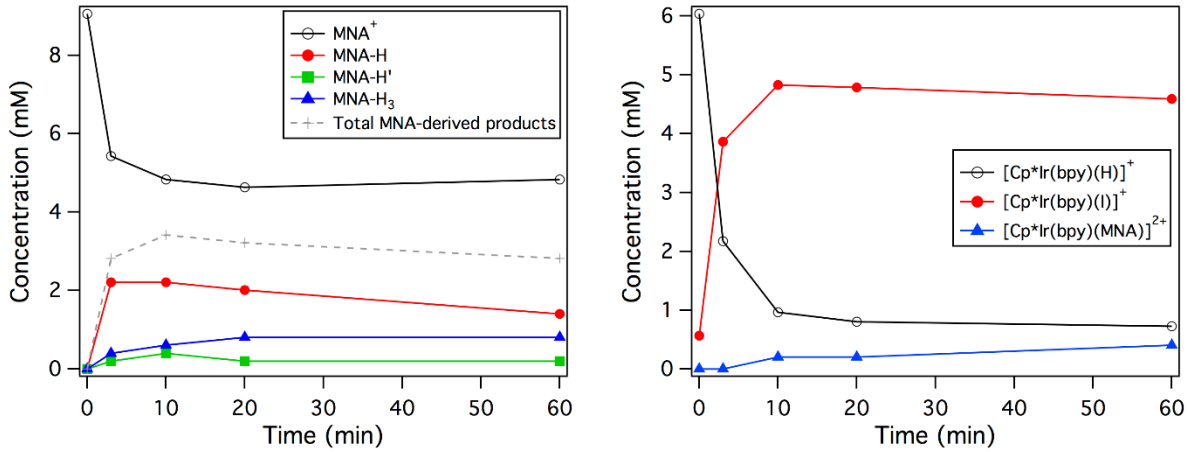

Figure A.20. Left: concentration of MNA-containing species as a function of photolysis time. Right: concentration of Ir-containing products as a function of photolysis time.

Table A.1. Visible light-promoted hydride transfer from $[Cp^*Ir(bpy)(H)]^+$ to MNA^+ (1:1.5).[a]

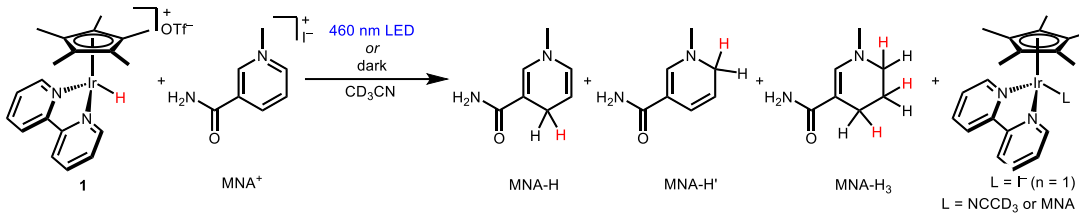

Time (min)	Yield of MNA-H (%)		Yield of MNA-H' (%)		Yield of $MNA\text{-}H_3$ (%)[b]		Yield of Ir-MNA (%)		Yield of Ir-I (%)	
	Dark	Light	Dark	Light	Dark	Light	Dark	Light	Dark	Light
0	-	0	-	0	-	0	-	0	-	9
3	-	37	-	3	-	7	-	0	-	64
10	0	37	0	7	0	10	0	3	9	80
20	0	33	0	3	0	13	0	3	11	79
60	3	23	3	3	0	13	0	7	10	76
360	17	7	7	3	0	20	0	10	42	62

[a]Yields determined by ^1H NMR and calculated relative to limiting reagent. Remainder of MNA species is MNA^+ starting material. [b]Maximum yield is 50%.

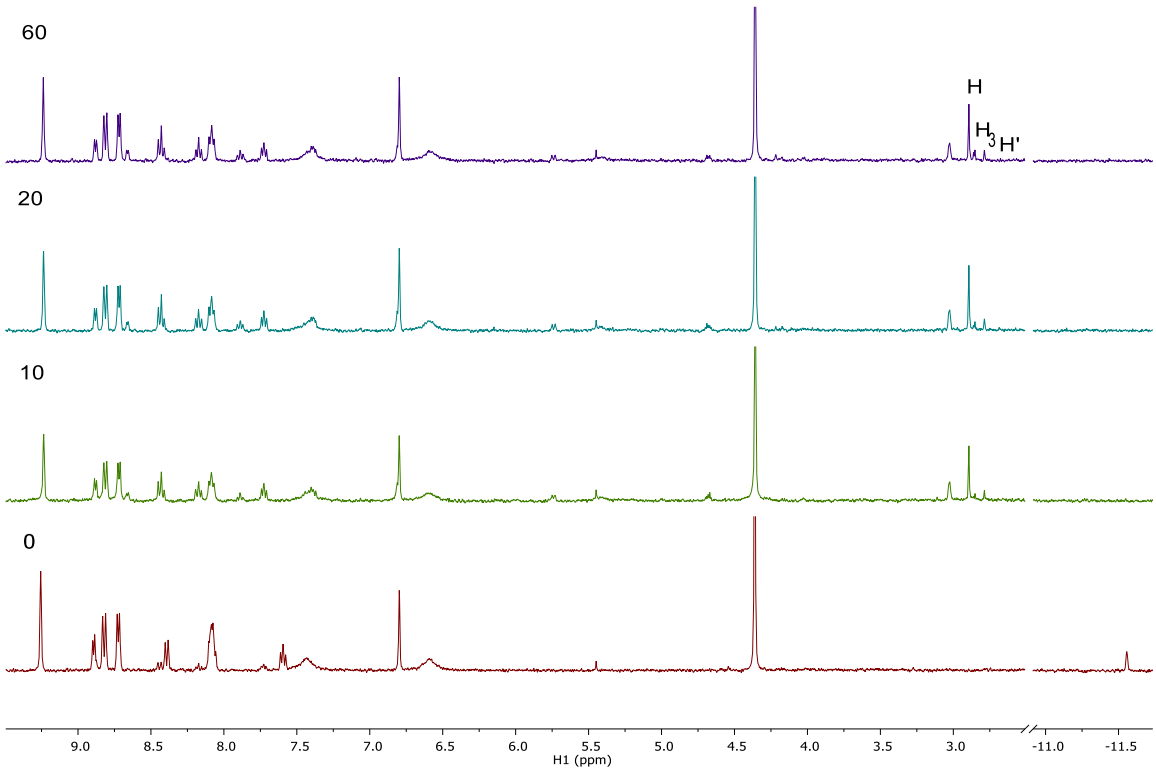

Figure A.21. ^{1}H NMR spectrum of **1** and [MNA][I] (1:4.4) in CD_3CN after 0, 10, 20, and 60 min of irradiation. N-methyl groups of products MNA-H, MNA-H', and MNA-H_3 are labeled above as H, H', and H_3, respectively.

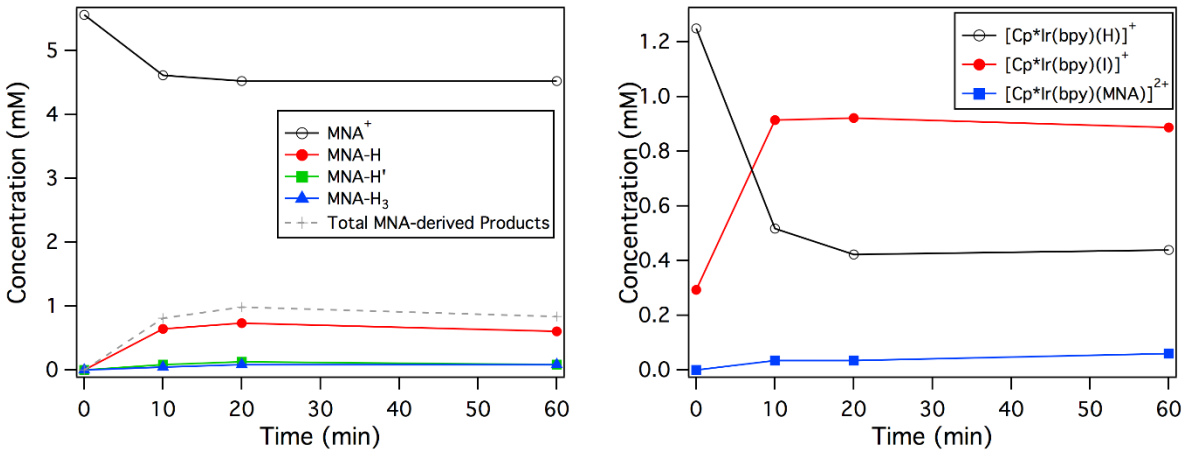

Figure A.22. Left: concentration of MNA-containing species as a function of photolysis time. Right: concentration of Ir-containing products as a function of photolysis time.

Table A.2. Visible light-promoted hydride transfer from $[Cp^*Ir(bpy)(H)]^+$ to MNA^+ (1:4.4).[a]

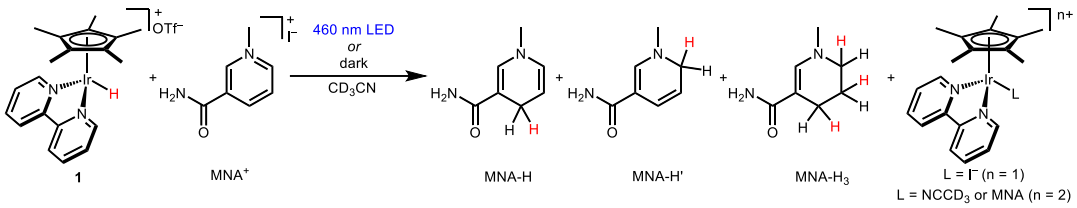

Time (min)	Yield of MNA-H (%)		Yield of MNA-H' (%)		Yield of $MNA\text{-}H_3$ (%)[b]		Yield of Ir-MNA (%)		Yield of Ir-I (%)	
	Dark	Light	Dark	Light	Dark	Light	Dark	Light	Dark	Light
0	-	0	-	0	-	0	-	0	-	23
10	0	52	0	7	0	3	0	3	18	73
20	0	59	0	10	0	7	0	3	19	74
60	0	48	0	7	0	7	0	5	21	71

[a]Yields determined by ^1H NMR and calculated relative to limiting reagent. Remainder of MNA species is MNA^+ starting material.
[b]Maximum yield is 50%.

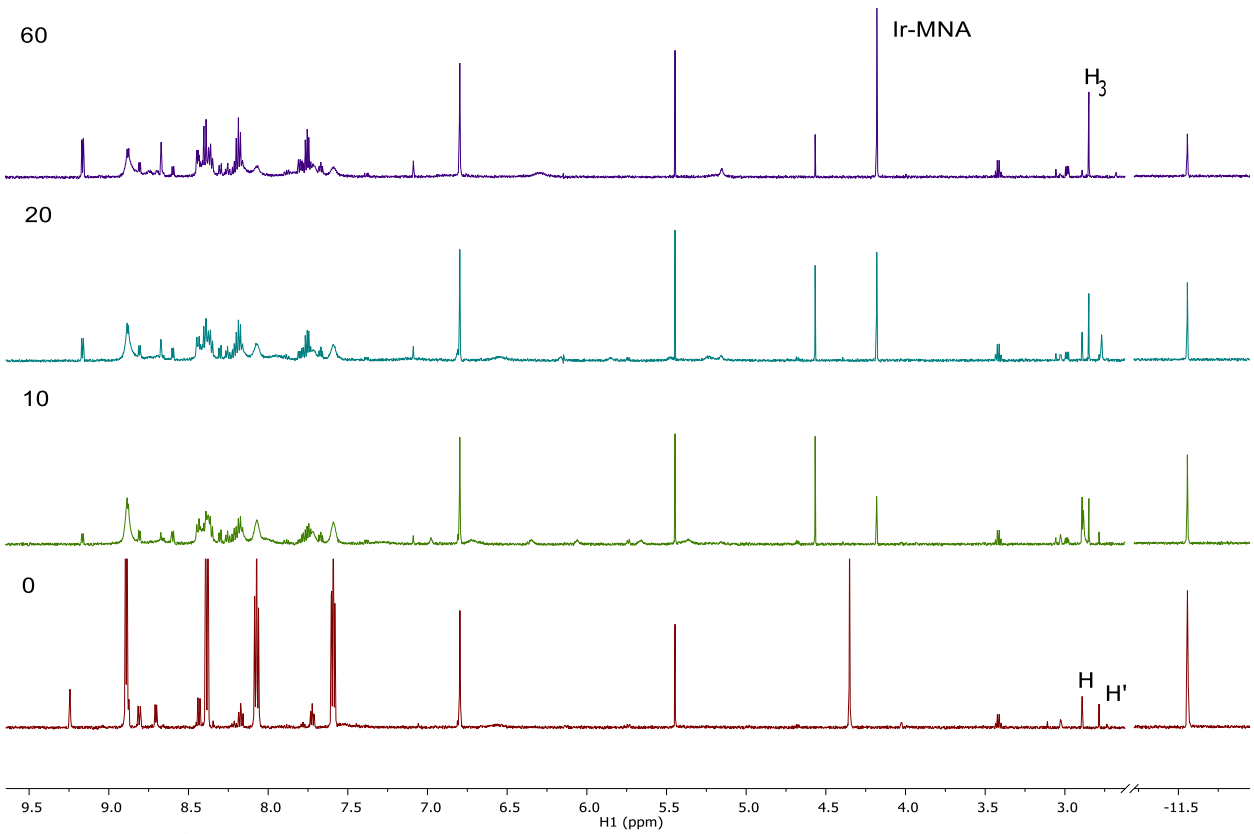

Figure A.23. ^{1}H NMR spectrum of **1** and [MNA][I] (4.0:1) in CD_3CN after 0, 10, 20, and 60 min of irradiation. N-methyl groups of products MNA-H, MNA-H', and MNA-H_3 are labeled as H, H', and H_3, respectively.

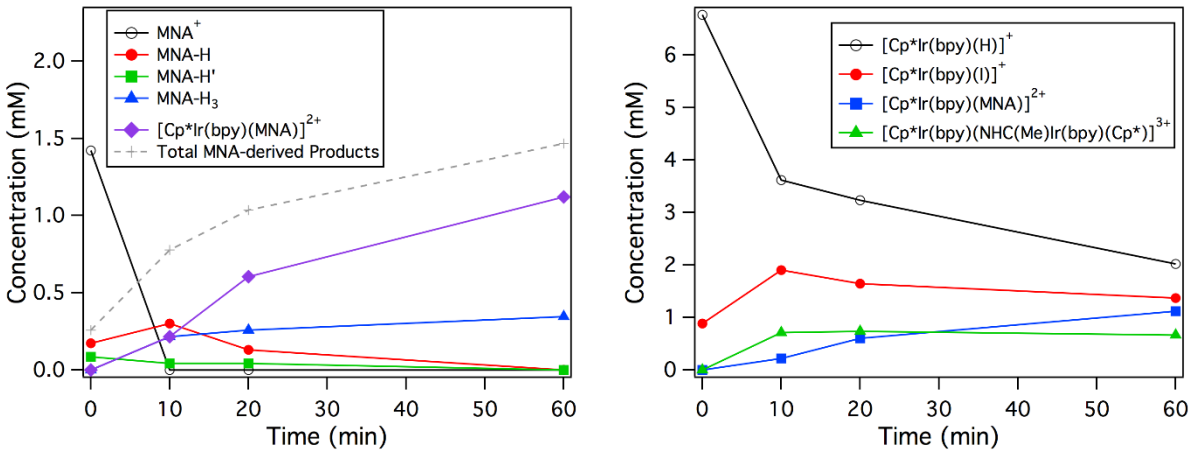

Figure A.24. Left: concentration of MNA-containing species as a function of photolysis time. Right: concentration of Ir-containing products as a function of photolysis time.

Table A.3. Visible light-promoted hydride transfer from $[Cp^*Ir(bpy)(H)]^+$ to MNA^+ (4.0:1).[a]

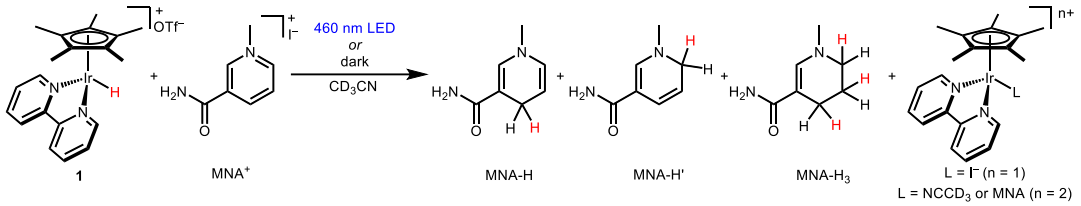

Time (min)	Yield of MNA-H (%)		Yield of MNA-H' (%)		Yield of $MNA\text{-}H_3$ (%)		Yield of Ir-MNA (%)		Yield of Ir-I (%)	
	Dark	Light	Dark	Light	Dark	Light	Dark	Light	Dark	Light
0	-	10	-	5	-	0	-	0	-	53
10	8	18	5	3	0	13	0	13	47	113
20	13	8	8	3	0	15	0	36	51	98
60	21	0	13	0	0	21	0	67	56	82

[a]Yields determined by ^1H NMR and calculated relative to limiting reagent. Remainder of MNA species is MNA^+ starting material.

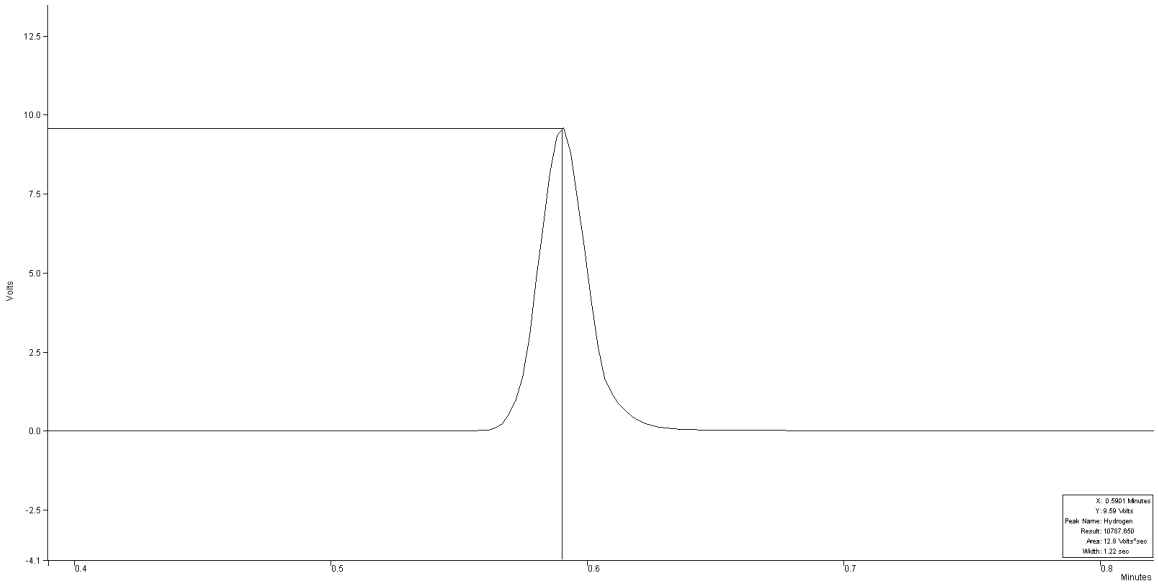

Figure A.25. GC trace of 0.15 mL injected headspace from NMR tube of **1** and HOAc following 20 min irradiation time. From the H_2 calibration curve and integral of the H_2 peak, H_2 yield was calculated to be 74%.

Table A.4. Quantum yield for visible light-promoted hydride transfer reactions from $[Cp^*Ir(bpy)(H)]^+$ to MNA^+.[a]

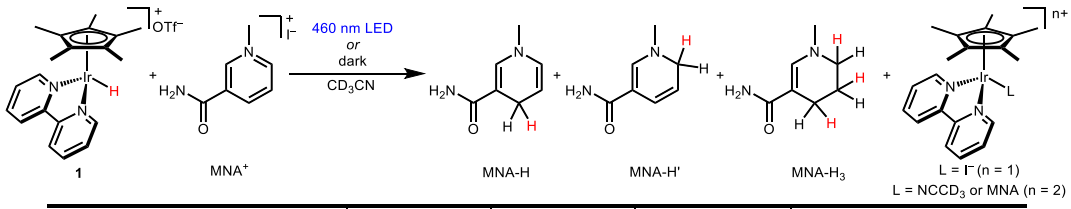

[**1**]:[MNA^+]	Time (min)	Φ MNA-H	Φ MNA-H'	Φ MNA-H_3	Φ Total Reduced MNA
1:1.5	10	0.169	0.031	0.046	0.246
1:4.4	10	0.049	0.007	0.003	0.059
4.0:1	10	0.023	0.003	0.016	0.043

[a]Φ determined from moles of product (from ^1H NMR relative to mesitylene internal standard) and photon flux after 10 min of irradiation (obtained from chemical actinometry).

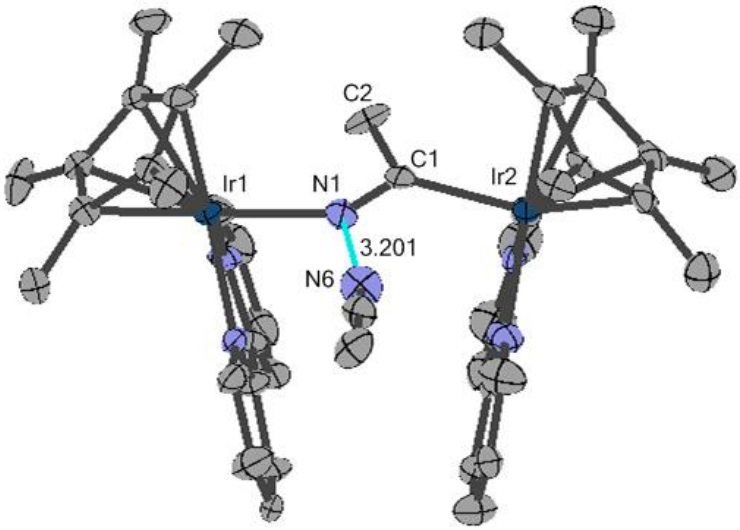

Figure A.26. Structural representation of 4 (ellipsoids at 50% probability) with a H-bonding interaction between N1−N6 (3.201 Å) from CH_3CN solvent. Three PF_6 ions, one CH_3CN molecule, and H atoms omitted for clarity.

Table A.5. Crystal Data and structure refinement for **4-PF_6** [sb106_c].

Identification code	sb106_c
Empirical formula	$C_{46}H_{56}N_7F_{18}P_3Ir_2$
Formula weight	1526.28
Temperature/K	100.15
Crystal system	orthorhombic
Space group	$Pna2_1$
a/Å	25.1101(3)
b/Å	11.0118(2)
c/Å	19.22650(10)
α/°	90
β/°	90
γ/°	90
Volume/$Å^3$	5316.27(12)
Z	4
$\rho_{calc}g/cm^3$	1.907
μ/mm^{-1}	11.345

F(000)	2968.0
Crystal size/mm^3	0.266 × 0.091 × 0.087
Radiation	CuKα (λ = 1.54178)
2Θ range for data collection/°	7.04 to 140.234
Index ranges	-24 ≤ h ≤ 29, -13 ≤ k ≤ 13, -23 ≤ l ≤ 23
Reflections collected	58370
Independent reflections	9803 [R_{int} = 0.0560, R_{sigma} = 0.0394]
Data/restraints/parameters	9803/760/699
Goodness-of-fit on F^2	1.046
Final R indexes [I>=2σ (I)]	R_1 = 0.0401, wR_2 = 0.0942
Final R indexes [all data]	R_1 = 0.0441, wR_2 = 0.0967
Largest diff. peak/hole / e Å^{-3}	1.96/-1.07
Flack parameter	0.37(2)

Table A.6. Bond Lengths for **4-PF$_6$** [sb106_c].

Atom	Atom	Length/Å	Atom	Atom	Length/Å
Ir1	N1	2.149(10)	C19	C21	1.41(2)
Ir1	N2	2.103(13)	C21	C22	1.47(2)
Ir1	N3	2.087(12)	C23	C24	1.38(3)
Ir1	C13	2.203(15)	C24	C25	1.38(3)
Ir1	C15	2.210(15)	C25	C26	1.39(3)
Ir1	C17	2.166(14)	C26	C27	1.38(2)
Ir1	C19	2.199(15)	C27	C28	1.50(2)
Ir1	C21	2.180(15)	C28	C29	1.43(2)
Ir2	N4	2.071(14)	C29	C30	1.34(3)
Ir2	N5	2.104(12)	C30	C31	1.36(3)
Ir2	C1	2.126(12)	C31	C32	1.39(2)
Ir2	C33	2.194(15)	C33	C34	1.53(2)
Ir2	C35	2.187(14)	C33	C35	1.37(2)
Ir2	C37	2.183(14)	C33	C41	1.34(2)
Ir2	C39	2.205(14)	C35	C36	1.48(2)
Ir2	C41	2.183(14)	C35	C37	1.46(2)
N1	C1	1.245(17)	C37	C38	1.50(2)
N2	C3	1.33(2)	C37	C39	1.35(2)
N2	C7	1.31(2)	C39	C40	1.46(2)
N3	C8	1.410(19)	C39	C41	1.48(2)

N3	C12	1.38(2)	C41	C42	1.60(2)
N4	C23	1.34(2)	P3	F13	1.474(15)
N4	C27	1.40(2)	P3	F14	1.583(15)
N5	C28	1.28(2)	P3	F15	1.708(13)
N5	C32	1.304(19)	P3	F16	1.584(13)
C1	C2	1.503(18)	P3	F17	1.590(12)
C3	C4	1.40(2)	P3	F18	1.639(14)
C4	C5	1.37(3)	P1	F1	1.615(12)
C5	C6	1.39(3)	P1	F2	1.586(10)
C6	C7	1.41(2)	P1	F3	1.587(6)
C7	C8	1.41(2)	P1	F4	1.597(13)
C8	C9	1.38(2)	P1	F5	1.589(13)
C9	C10	1.39(3)	P1	F6	1.599(6)
C10	C11	1.40(3)	P2	F7	1.617(14)
C11	C12	1.36(2)	P2	F8	1.486(15)
C13	C14	1.50(2)	P2	F9	1.506(17)
C13	C15	1.45(2)	P2	F10	1.472(14)
C13	C21	1.54(2)	P2	F11	1.474(15)
C15	C16	1.45(2)	P2	F12	1.714(18)
C15	C17	1.44(2)	N6	C43	1.133(13)
C17	C18	1.55(2)	C43	C44	1.466(14)
C17	C19	1.48(2)	N7	C45	1.135(13)
C19	C20	1.50(2)	C45	C46	1.468(16)

Table A.7. Bond Angles for **4-PF_6** [sb106_c].

Atom	**Atom**	**Atom**	**Angle/°**	**Atom**	**Atom**	**Atom**	**Angle/°**
N1	Ir1	C13	144.2(6)	C19	C17	C18	119.8(14)
N1	Ir1	C15	160.9(5)	C17	C19	Ir1	68.9(8)
N1	Ir1	C17	122.7(5)	C17	C19	C20	127.4(15)
N1	Ir1	C19	97.4(5)	C20	C19	Ir1	128.2(12)
N1	Ir1	C21	106.0(6)	C21	C19	Ir1	70.4(9)
N2	Ir1	N1	76.5(5)	C21	C19	C17	108.0(13)
N2	Ir1	C13	97.5(6)	C21	C19	C20	124.5(15)
N2	Ir1	C15	122.2(5)	C13	C21	Ir1	70.3(8)
N2	Ir1	C17	160.0(5)	C19	C21	Ir1	71.9(9)
N2	Ir1	C19	141.1(6)	C19	C21	C13	106.6(13)

N2	Ir1	C21	106.3(6)	C19	C21	C22	126.6(16)
N3	Ir1	N1	91.1(5)	C22	C21	Ir1	132.6(12)
N3	Ir1	N2	76.3(5)	C22	C21	C13	125.5(15)
N3	Ir1	C13	122.3(6)	N4	C23	C24	122.1(18)
N3	Ir1	C15	97.1(6)	C23	C24	C25	120.3(18)
N3	Ir1	C17	106.5(5)	C24	C25	C26	118.5(18)
N3	Ir1	C19	142.6(6)	C27	C26	C25	119.9(18)
N3	Ir1	C21	162.9(6)	N4	C27	C28	111.7(14)
C13	Ir1	C15	38.4(5)	C26	C27	N4	121.0(16)
C17	Ir1	C13	63.9(6)	C26	C27	C28	127.3(16)
C17	Ir1	C15	38.3(6)	N5	C28	C27	116.2(14)
C17	Ir1	C19	39.7(6)	N5	C28	C29	123.1(16)
C17	Ir1	C21	65.3(5)	C29	C28	C27	120.6(16)
C19	Ir1	C13	65.0(6)	C30	C29	C28	117.5(19)
C19	Ir1	C15	65.9(6)	C29	C30	C31	119.9(17)
C21	Ir1	C13	41.0(6)	C30	C31	C32	116.9(19)
C21	Ir1	C15	67.0(6)	N5	C32	C31	124.5(16)
C21	Ir1	C19	37.7(6)	C34	C33	Ir2	125.2(12)
N4	Ir2	N5	76.6(5)	C35	C33	Ir2	71.5(9)
N4	Ir2	C1	96.8(5)	C35	C33	C34	127.2(15)
N4	Ir2	C33	98.7(6)	C41	C33	Ir2	71.7(8)
N4	Ir2	C35	105.7(6)	C41	C33	C34	123.0(15)
N4	Ir2	C37	141.9(6)	C41	C33	C35	109.7(15)
N4	Ir2	C39	161.4(6)	C33	C35	Ir2	72.1(9)
N4	Ir2	C41	122.6(6)	C33	C35	C36	128.6(16)
N5	Ir2	C1	78.4(5)	C33	C35	C37	105.4(14)
N5	Ir2	C33	125.7(6)	C36	C35	Ir2	129.8(11)
N5	Ir2	C35	161.9(5)	C37	C35	Ir2	70.4(8)
N5	Ir2	C37	141.5(6)	C37	C35	C36	125.2(15)
N5	Ir2	C39	108.6(6)	C35	C37	Ir2	70.7(8)
N5	Ir2	C41	102.4(6)	C35	C37	C38	125.0(16)
C1	Ir2	C33	153.9(6)	C38	C37	Ir2	126.2(11)
C1	Ir2	C35	118.6(6)	C39	C37	Ir2	72.9(9)
C1	Ir2	C37	93.3(5)	C39	C37	C35	111.4(14)
C1	Ir2	C39	101.7(5)	C39	C37	C38	123.5(17)
C1	Ir2	C41	139.9(6)	C37	C39	Ir2	71.2(9)
C33	Ir2	C39	63.5(6)	C37	C39	C40	132.8(16)
C35	Ir2	C33	36.4(6)	C37	C39	C41	102.9(14)

C35	Ir2	C39	63.8(6)	C40	C39	Ir2	133.3(12)
C37	Ir2	C33	61.8(6)	C40	C39	C41	122.6(16)
C37	Ir2	C35	38.9(6)	C41	C39	Ir2	69.5(8)
C37	Ir2	C39	35.9(6)	C33	C41	Ir2	72.7(9)
C37	Ir2	C41	60.9(6)	C33	C41	C39	110.5(15)
C41	Ir2	C33	35.6(6)	C33	C41	C42	126.8(16)
C41	Ir2	C35	60.9(6)	C39	C41	Ir2	71.1(8)
C41	Ir2	C39	39.3(6)	C39	C41	C42	122.7(16)
C1	N1	Ir1	131.8(10)	C42	C41	Ir2	122.3(11)
C3	N2	Ir1	123.8(11)	F13	P3	F14	92.4(10)
C7	N2	Ir1	116.3(11)	F13	P3	F15	84.0(9)
C7	N2	C3	119.9(14)	F13	P3	F16	166.5(9)
C8	N3	Ir1	115.4(10)	F13	P3	F17	90.5(10)
C12	N3	Ir1	124.8(10)	F13	P3	F18	109.3(10)
C12	N3	C8	119.8(13)	F14	P3	F15	84.4(8)
C23	N4	Ir2	125.0(12)	F14	P3	F16	87.8(9)
C23	N4	C27	118.0(15)	F14	P3	F17	172.2(10)
C27	N4	Ir2	117.0(11)	F14	P3	F18	93.8(9)
C28	N5	Ir2	118.3(11)	F16	P3	F15	82.6(7)
C28	N5	C32	117.3(13)	F16	P3	F17	87.8(8)
C32	N5	Ir2	124.3(11)	F16	P3	F18	84.2(8)
N1	C1	Ir2	119.7(10)	F17	P3	F15	88.7(7)
N1	C1	C2	110.4(13)	F17	P3	F18	92.1(8)
C2	C1	Ir2	129.5(12)	F18	P3	F15	166.7(9)
C1	C2	N1	31.1(6)	F2	P1	F1	89.2(4)
N2	C3	C4	123.9(17)	F2	P1	F3	89.6(6)
C5	C4	C3	116.2(19)	F2	P1	F4	89.4(7)
C4	C5	C6	120.6(16)	F2	P1	F5	179.3(6)
C5	C6	C7	118.4(16)	F2	P1	F6	90.1(7)
N2	C7	C6	120.9(16)	F3	P1	F1	89.7(6)
N2	C7	C8	118.4(15)	F3	P1	F4	90.5(6)
C6	C7	C8	120.6(16)	F3	P1	F5	89.7(7)
N3	C8	C7	113.0(14)	F3	P1	F6	179.3(5)
C9	C8	N3	119.0(16)	F4	P1	F1	178.6(7)
C9	C8	C7	127.8(17)	F4	P1	F6	90.2(7)
C8	C9	C10	121.6(18)	F5	P1	F1	90.9(8)
C9	C10	C11	117.4(16)	F5	P1	F4	90.5(4)
C12	C11	C10	122.3(17)	F5	P1	F6	90.6(7)

C11	C12	N3	119.6(16)	F6	P1	F1	89.6(7)
C14	C13	Ir1	126.5(12)	F7	P2	F12	83.1(9)
C14	C13	C21	123.0(14)	F8	P2	F7	92.4(10)
C15	C13	Ir1	71.1(8)	F8	P2	F9	97.4(12)
C15	C13	C14	128.6(14)	F8	P2	F12	90.6(11)
C15	C13	C21	108.4(13)	F9	P2	F7	87.4(9)
C21	C13	Ir1	68.7(8)	F9	P2	F12	167.8(10)
C13	C15	Ir1	70.5(8)	F10	P2	F7	161.9(11)
C16	C15	Ir1	129.2(12)	F10	P2	F8	90.7(10)
C16	C15	C13	126.0(15)	F10	P2	F9	109.9(12)
C17	C15	Ir1	69.2(8)	F10	P2	F11	94.1(9)
C17	C15	C13	106.4(13)	F10	P2	F12	79.0(11)
C17	C15	C16	127.4(15)	F11	P2	F7	78.8(9)
C15	C17	Ir1	72.5(8)	F11	P2	F8	165.4(13)
C15	C17	C18	129.2(15)	F11	P2	F9	93.9(9)
C15	C17	C19	110.5(13)	F11	P2	F12	76.9(9)
C18	C17	Ir1	129.6(11)	N6	C43	C44	177(2)
C19	C17	Ir1	71.4(8)	N7	C45	C46	179(2)

APPENDIX B. PHOTOCHEMICAL FORMIC ACID DEHYDROGENATION BY IRIDIUM COMPLEXS: UNDERSTANDING MECHANISM AND OVERCOMING DEACTIVATION

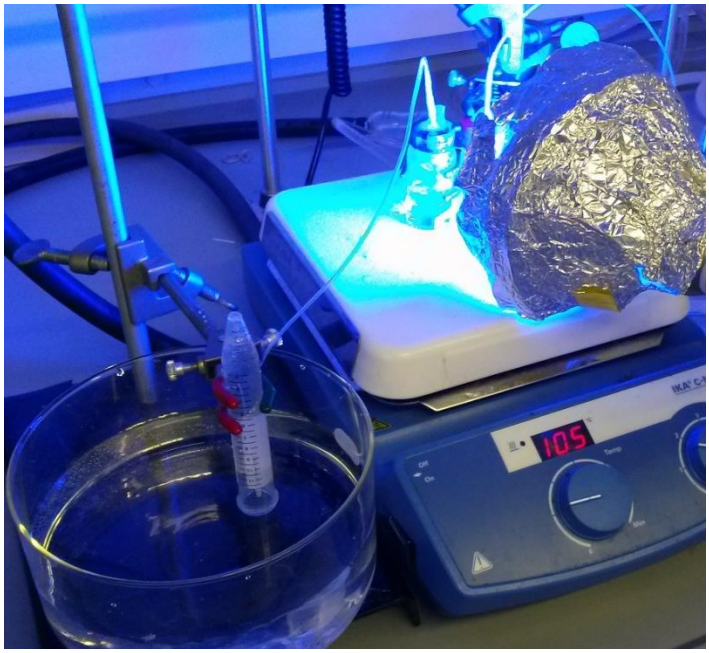

Figure B.1. Experimental set-up for gas-volume measurements using the inverted-burette style eudiometer. The reaction vial (right) is irradiated while evolved gases are collected in the eudiometer (left) using the PTFE tubing.

Figure B.2. Pressure vessel containing 20 mL of 1 M formate solution with **1-OMe**. Pressure gauge for this particular sample reads 37 psig (60 psig max) after irradiation.

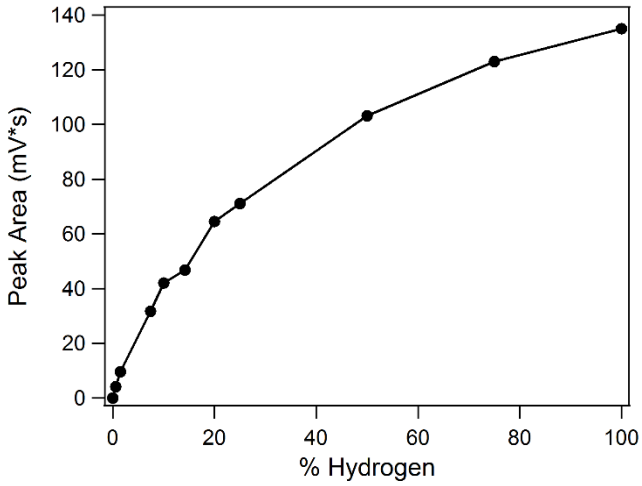

Figure B.3. Standard curve for H_2 on the Varian 450-GC.

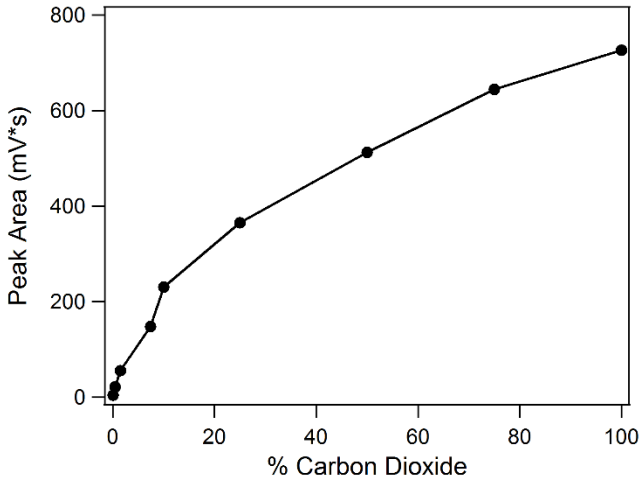

Figure B.4. Standard curve for CO_2 on the Varian 450-GC.

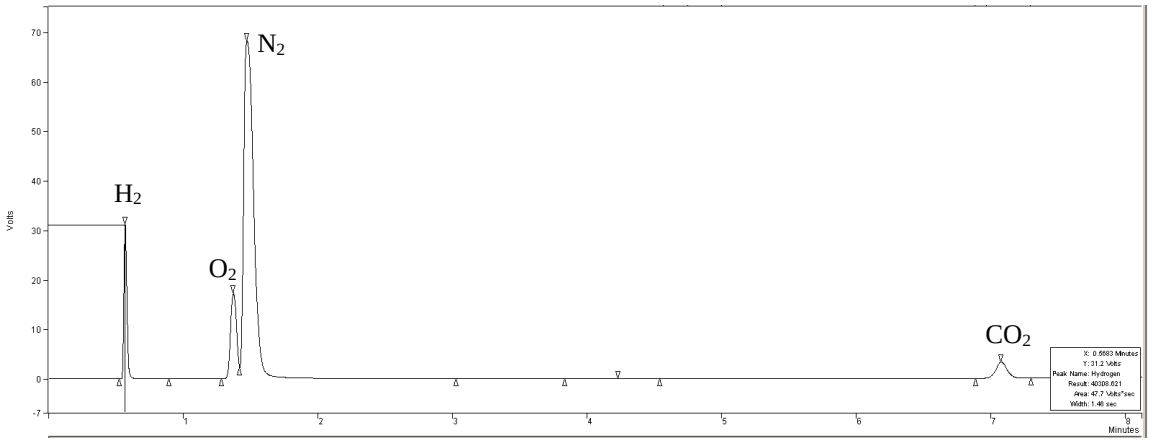

Figure B.5. Chromatogram showing evolved H_2 (0.6 min) and evolved CO_2 (7.1 min) for a sample after irradiation (O_2 and N_2 shown at 1.4 and 1.5 min, respectively). Conditions: 0.36 mM **1**, 1.0 M formate, pH 10.5. This sample was calculated to be 96.1% H_2.

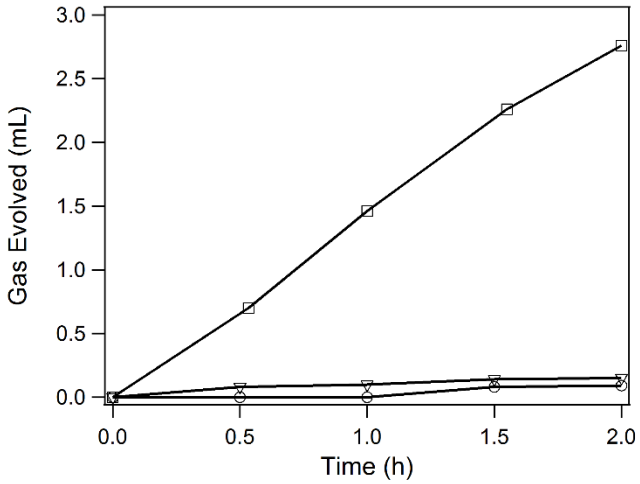

Figure B.6. Gas volume measured from the eudiometer over 2 h irradiation with precatalyst **1-OMe** (empty squares), no-precatalyst control (empty triangles), and $[Cp^*Ir(OH_2)_3]^{2+}$ (empty circles).

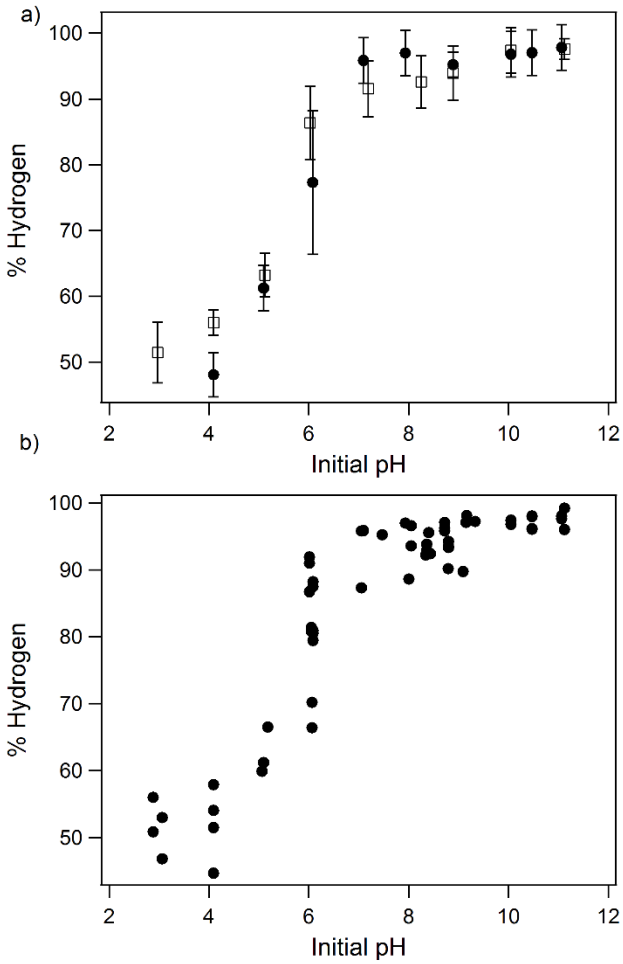

Figure B.7. H_2 content of evolved gas as a function of pH for **1** and **1-OMe** under a wide variety of reaction conditions. a) **1** (filled circles) and **1-OMe** (empty squares) with error bars. For small data sets, error bars were assigned based upon the average deviation for all data sets. b) **1** and **1-OMe** both displayed as filled circles. Conditions: 0.18 – 1.50 mM **1** or **1-OMe**, 0.5 – 4 M $NaCO_2H$ (aq), room temperature, 0 – 36 mM phosphate, 0 – 4 mM free ligand.

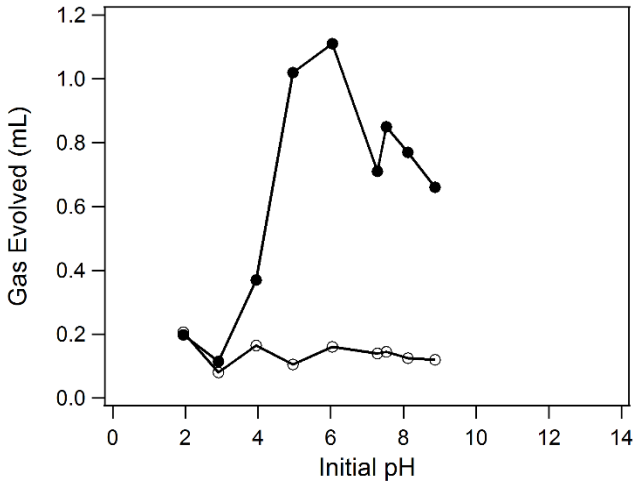

Figure B.8. Gas volume measured from the eudiometer after 2 h irradiation with precatalyst **1** (filled circles) and no-precatalyst control (empty circles).

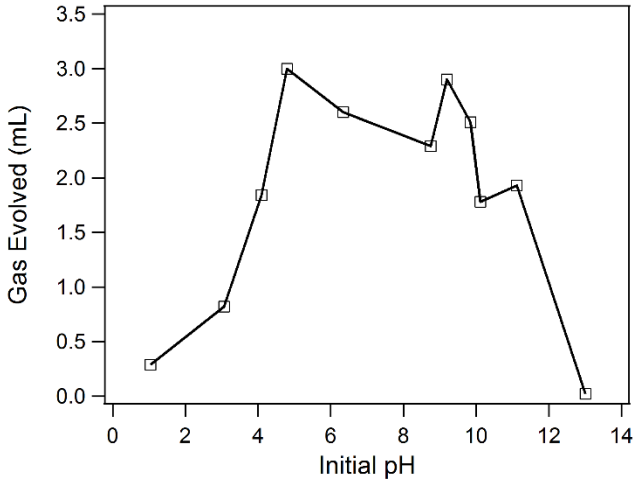

Figure B.9. Gas volume measured from the eudiometer after 2 h irradiation with precatalyst **1-OMe**.

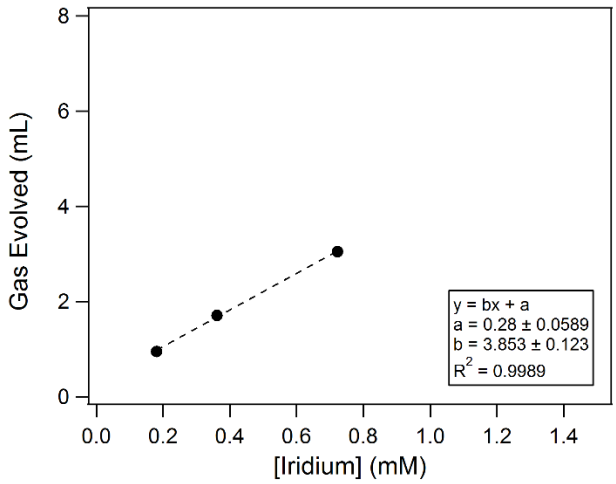

Figure B.10. Gas volume measured from the eudiometer after 2 h irradiation with varying concentrations of precatalyst **1**.

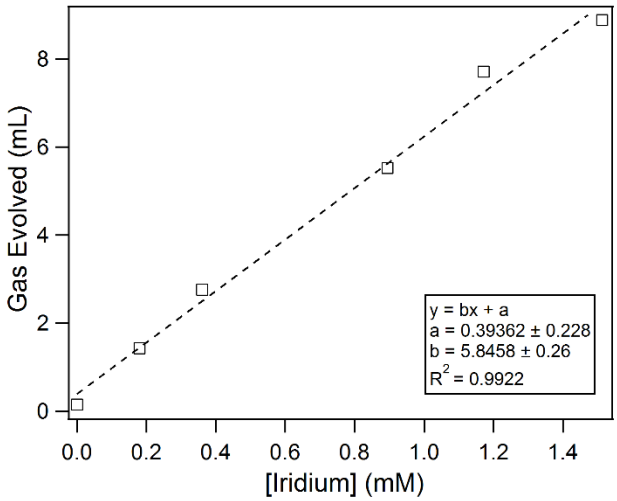

Figure B.11. Gas volume measured from the eudiometer after 2 h irradiation with varying concentrations of precatalyst **1-OMe**.

.

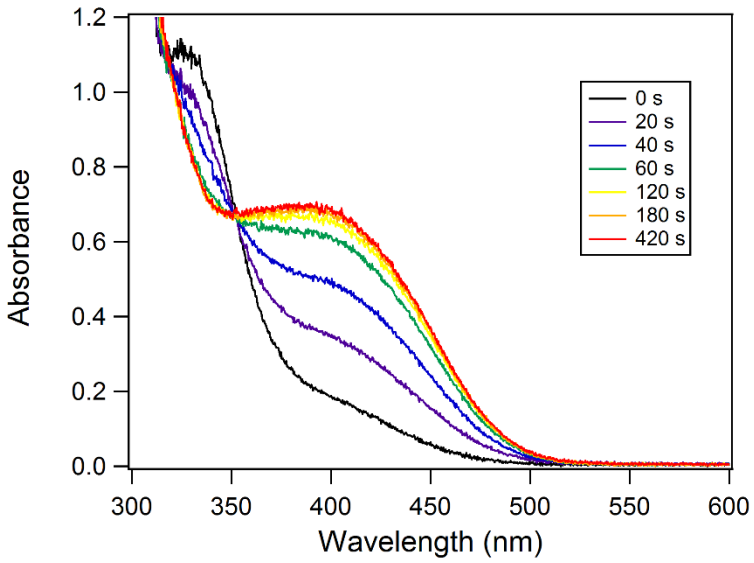

Figure B.12. *In situ* hydride formation monitored via UV-Vis in the dark starting from precatalyst **1-OMe** in 1 M formate.

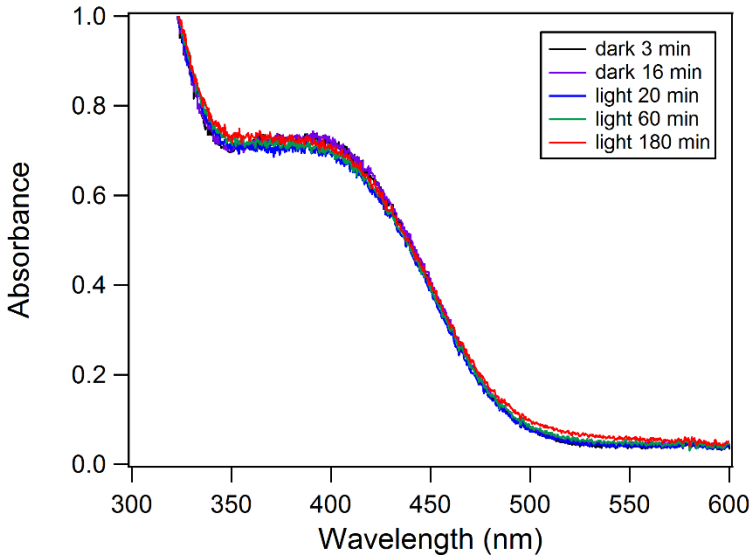

Figure B.13. *In situ* hydride formation monitored via UV-Vis in the dark starting from precatalyst **1-OMe** in 1 M formate, followed by 460 nm irradiation.

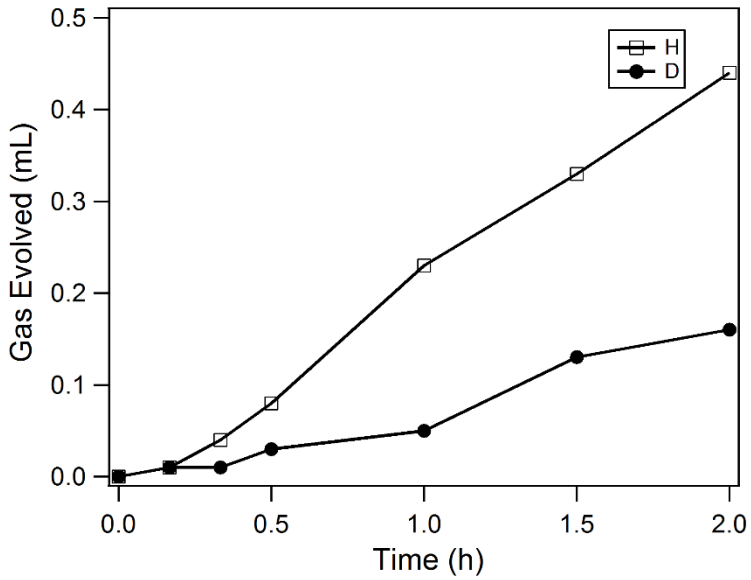

Figure B.14. Gas evolution traces over 2 h starting from precatalyst **1-OMe** in 1 M HCO_2H/H_2O and DCO_2D/D_2O with 460 nm irradiation.

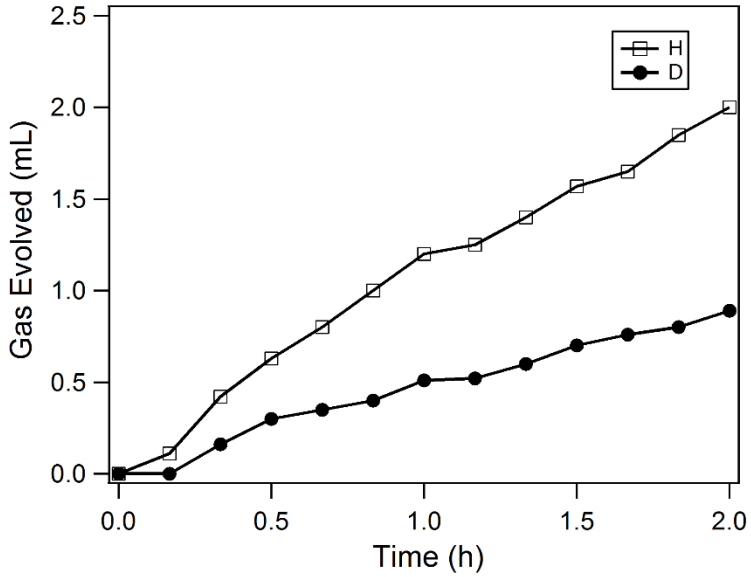

Figure B.15. Gas evolution traces over 2 h starting from precatalyst **1-OMe** in 1 M HCO_2H/H_2O and DCO_2D/D_2O with 460 nm irradiation.

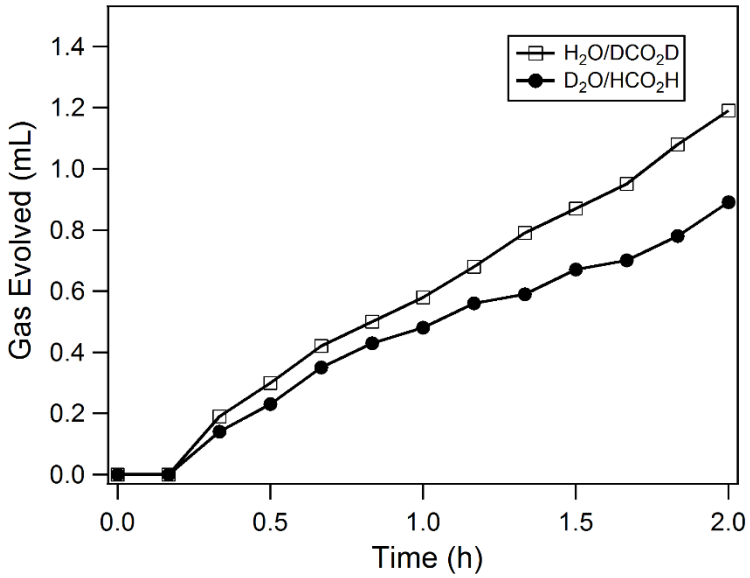

Figure B.16. Gas evolution traces over 2 h starting from precatalyst **1-OMe** in 1 M DCO_2D/H_2O and HCO_2H/D_2O with 460 nm irradiation.

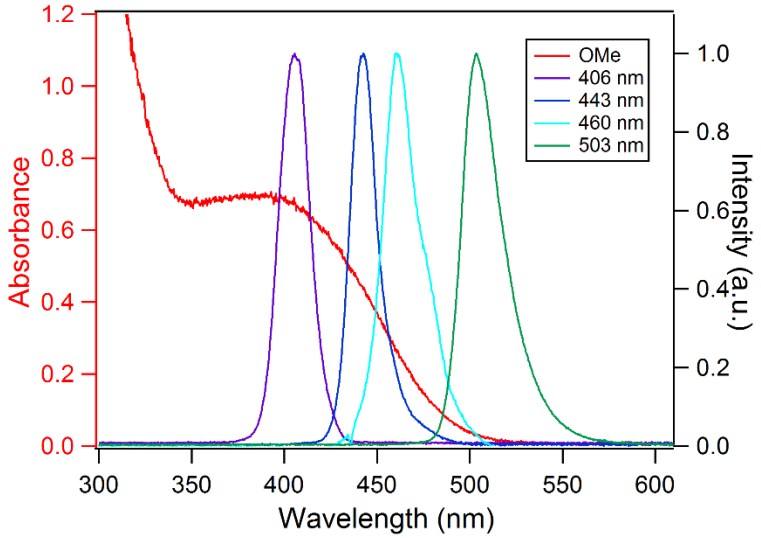

Figure B.17. Spectral overlap between $[Cp^*Ir(bpy\text{-}OMe)(H)]^+$ (**2-OMe**) and 406, 443, 460, and 503 nm LED sources.

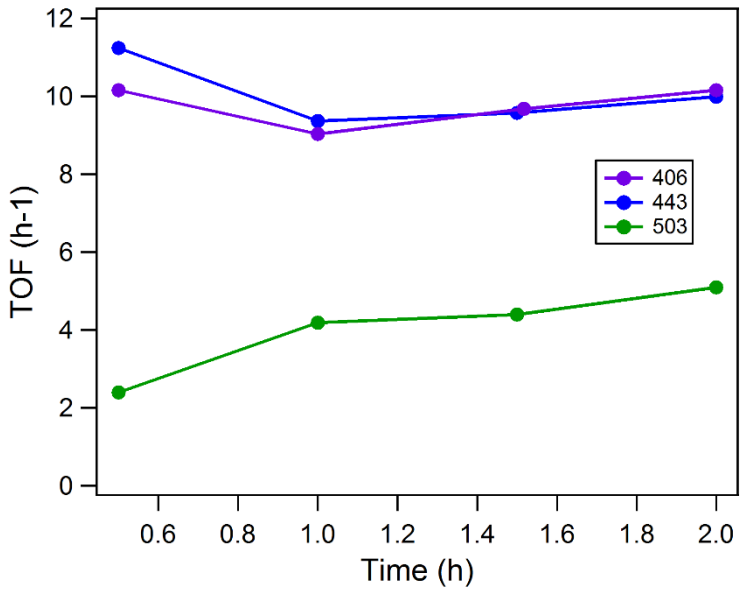

Figure B.18. TOF values from pressure vessel experiments with **1-OMe** under 2 h irradiation using 406, 443, and 503 nm LED sources.

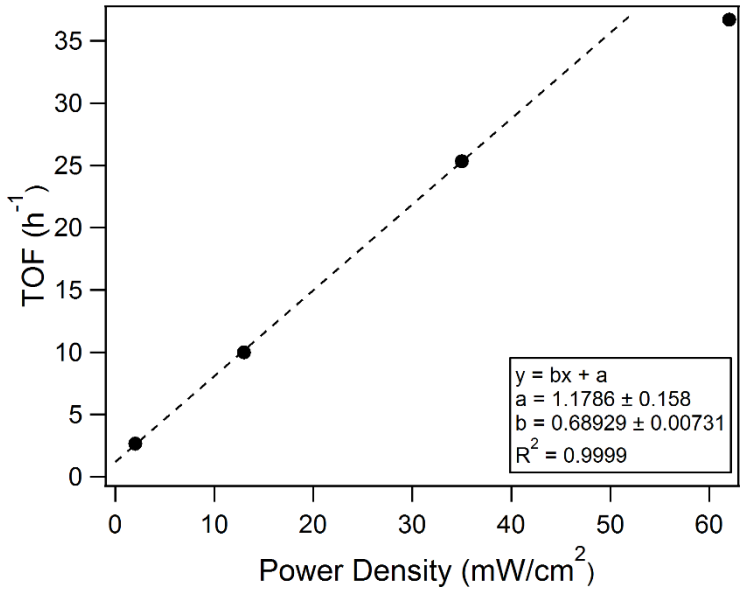

Figure B.19. TOF values after 2 h of 443 nm irradiation at different power densities with **1-OMe**. The dotted line is extrapolated from the first three data points.

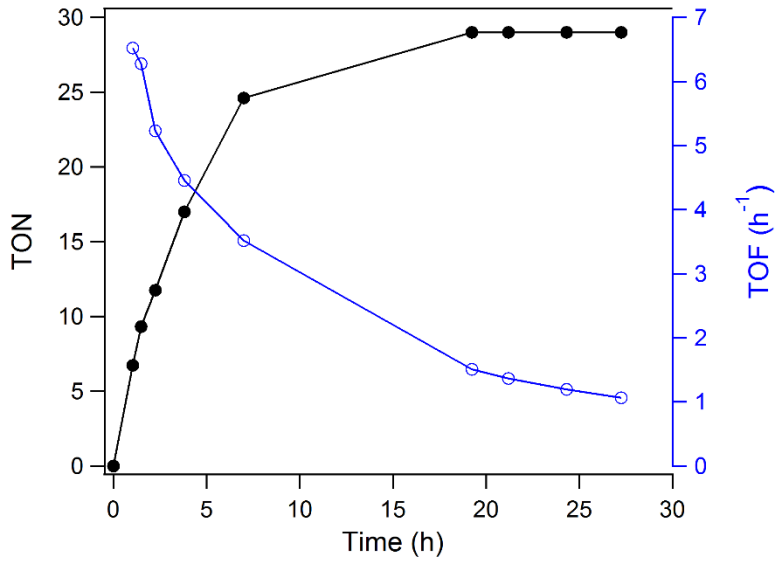

Figure B.20. Time course of catalyst TON (filled circles) and TOF (empty circles). Conditions: 0.37 mM precatalyst **1**, 1.0 M formate, pH 10.2, 25 eq. phosphate. The color of the trace corresponds to the color of the axis.

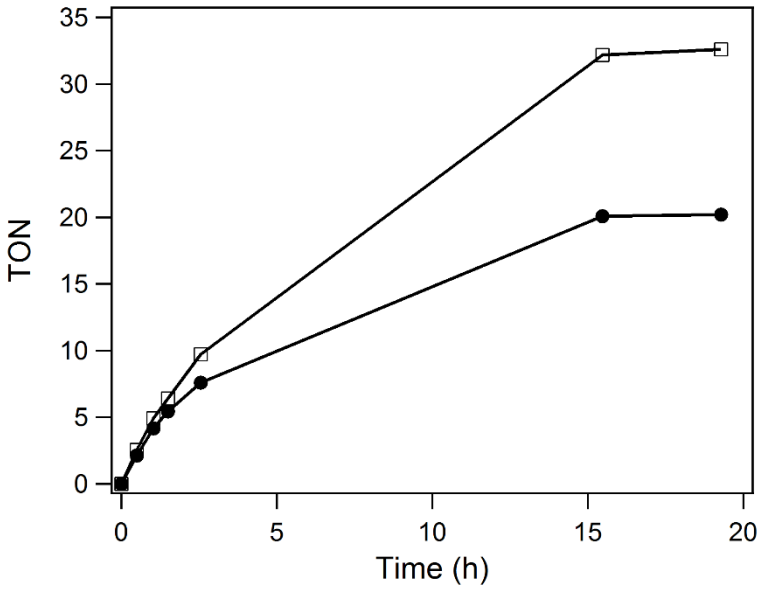

Figure B.21. Photocatalytic H_2 evolution activity of **1** alone (filled circles) and **1** in the presence of 3 equivalents bipyridine (empty squares). Conditions: 0.36 mM **1**, pH 9 1 M $NaCO_2H$(*aq*), 296 K.

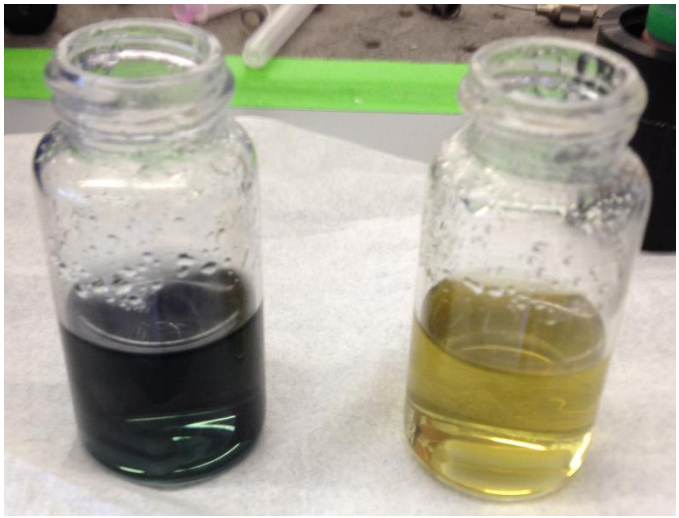

Figure B.22. After 20 h irradiation, Left: **1** without excess free ligand and Right: **1** with excess free ligand.

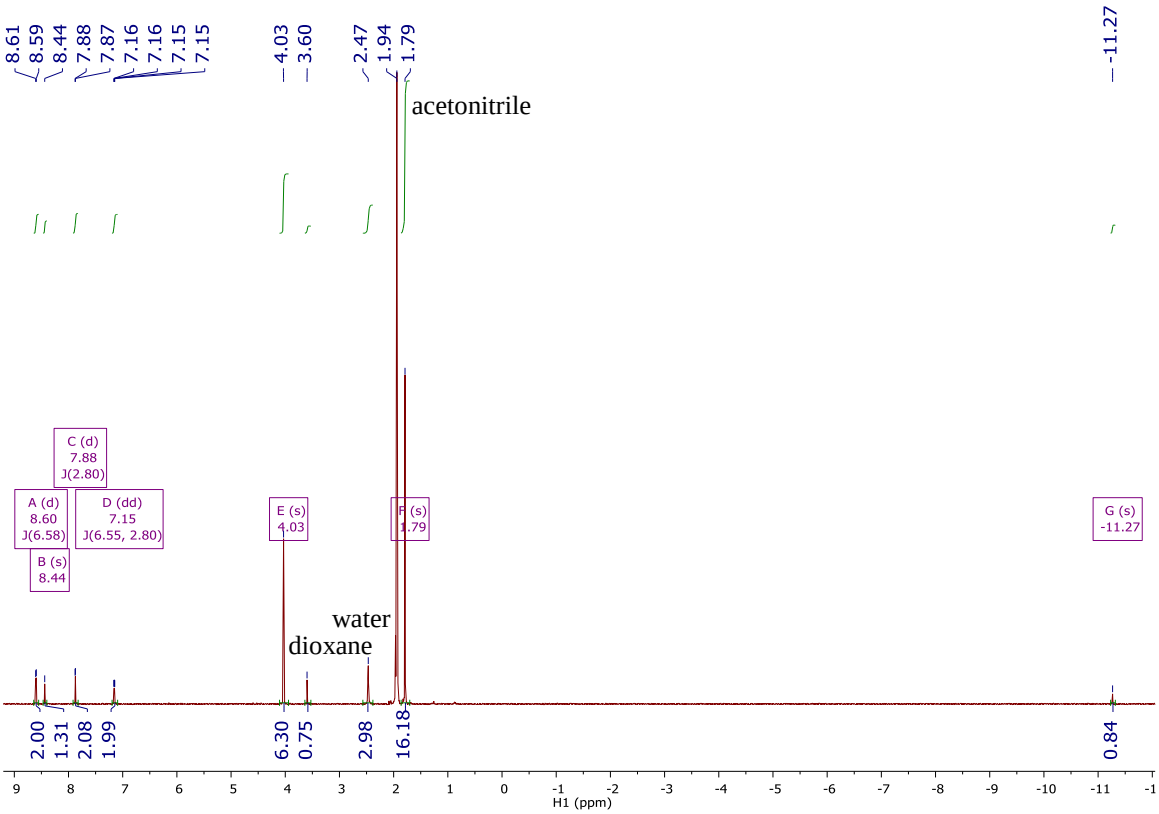

Figure B.23. ^{1}H NMR spectrum in CD_3CN after collecting [Cp*Ir(bpy-OMe)(H)][O_2CH] precipitate from mixing **1-OMe** in 8 M formate.

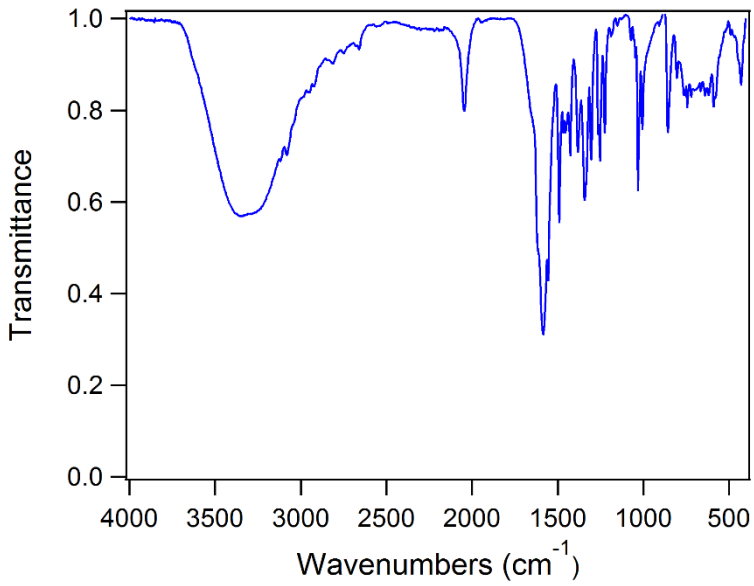

Figure B.24. IR spectrum of [Cp*Ir(bpy-OMe)(H)][O_2CH] precipitate from mixing **1-OMe** in 8 M formate. O-H stretch (3350 cm^{-1}) from water, and C-O stretch (1586 cm^{-1}) dominate the spectrum. Ir-H stretch seen at 2046 cm^{-1}.

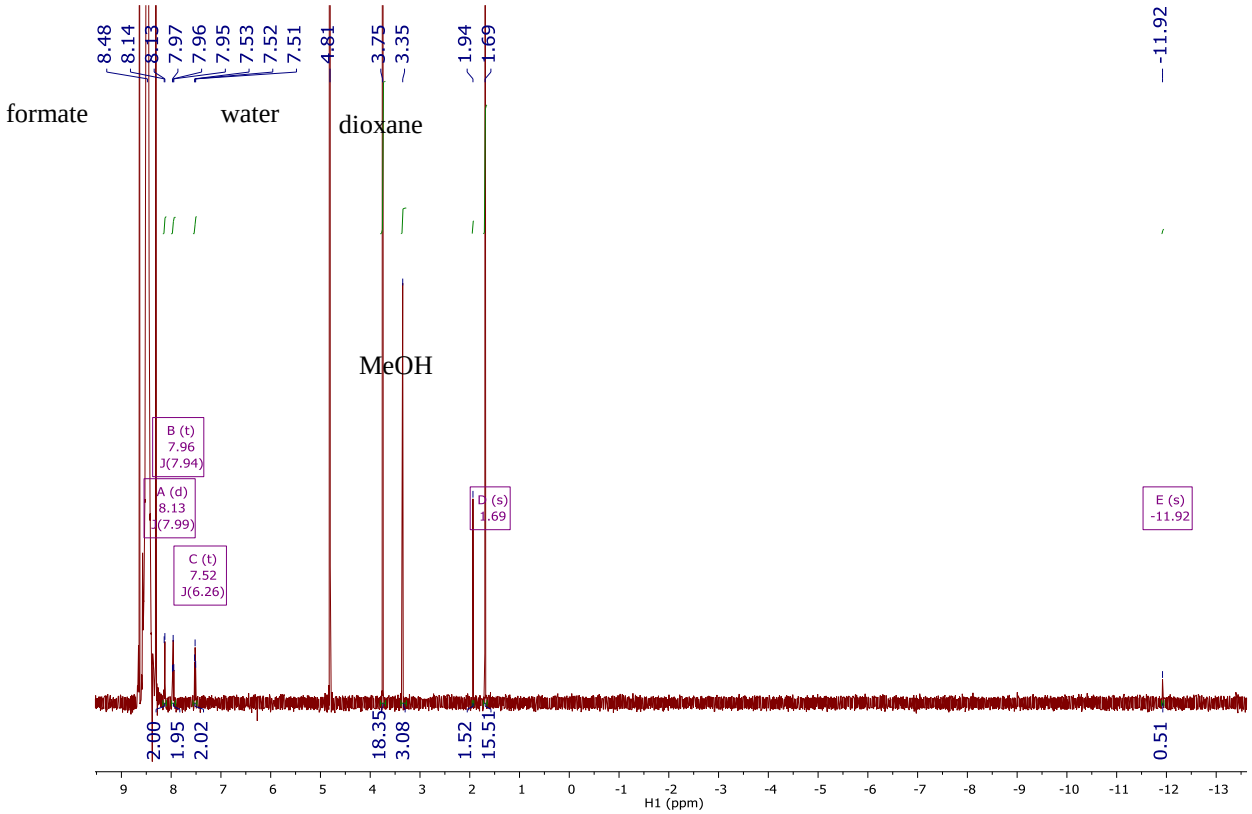

Figure B.25. ^{1}H NMR spectrum of [Cp*Ir(bpy)(H)][O_2CH] in D_2O from mixing **1** in 8 M formate.

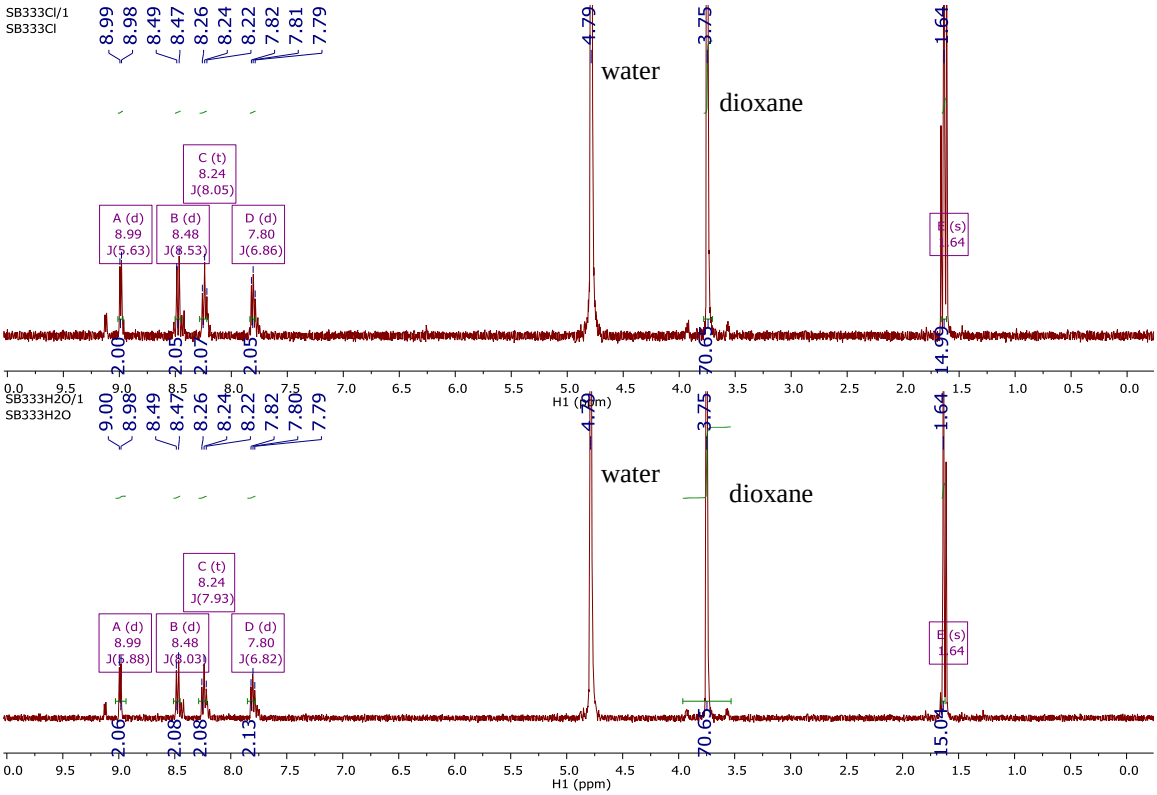

Figure B.26. ^{1}H NMR spectrum of chloride **1** and aquo $[Cp^*Ir(bpy)(H_2O)]^{2+}$ in pH 9.6 carbonate buffer.

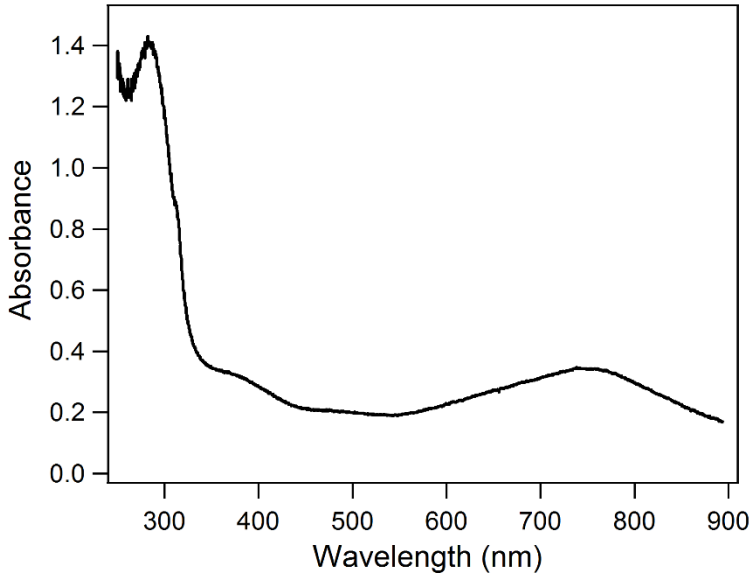

Figure B.27. UV-Vis spectrum of **1** after prolonged 460 nm irradiation.

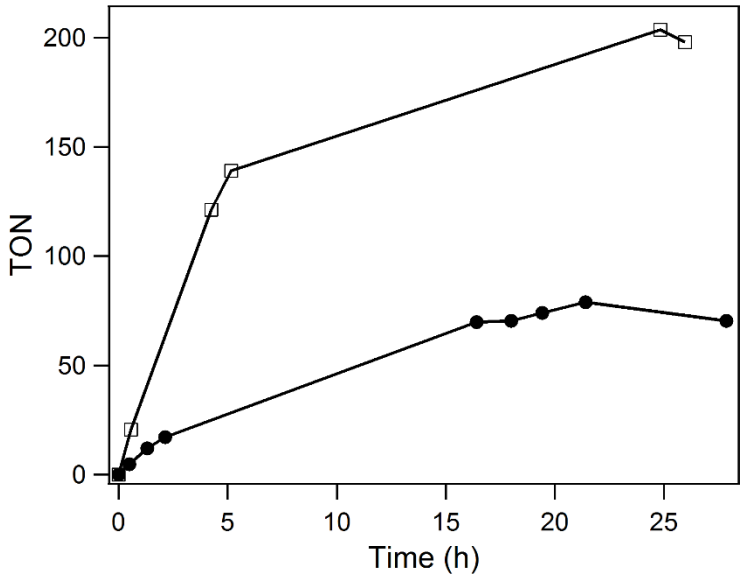

Figure B.28. Maximum TON runs for **1** and **1-OMe** using 460 nm irradiation.

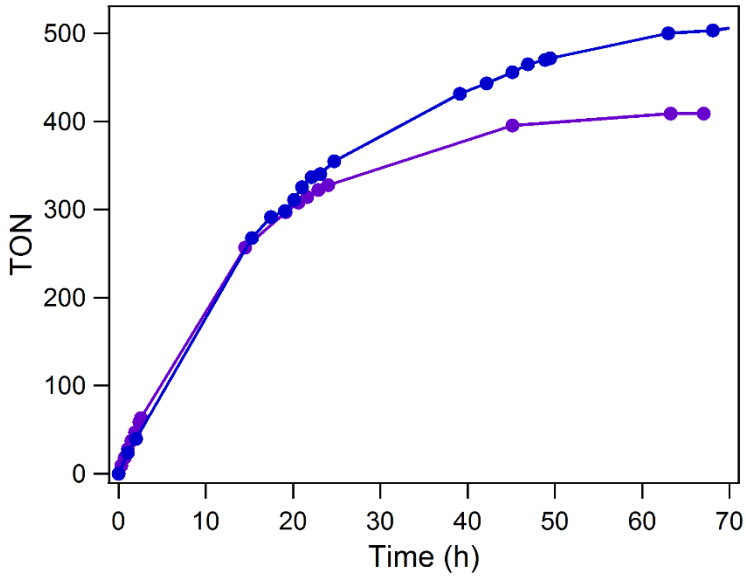

Figure B.29. Maximum TON runs for **1-OMe** using 406 (purple) and 443 (blue) nm irradiation.

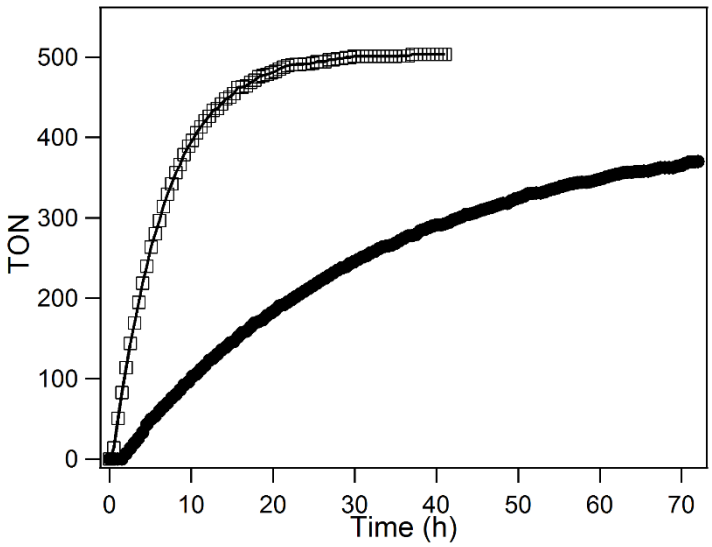

Figure B.30. Maximum TON runs for **1** and **1-OMe** using 443 nm irradiation.

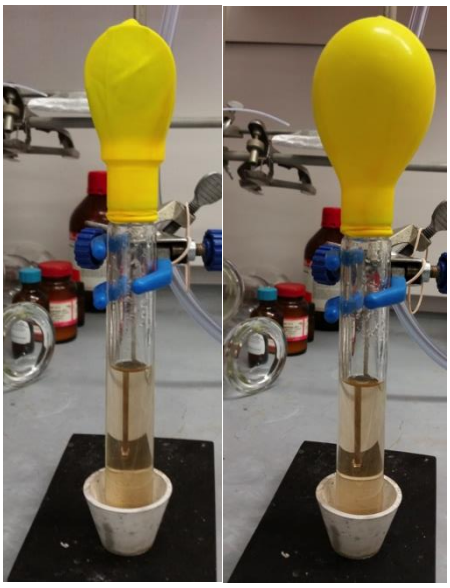

Figure B.31. Headspace sampling technique for pressure vessel using a balloon. Left: pressure vessel closed. Right: pressure vessel open.

APPENDIX C. PHOTOINDUCED HYDRODEHALOGENATION OF DICHLOROMETHANE BY IRIDIUM HYDRIDE COMPLEXES

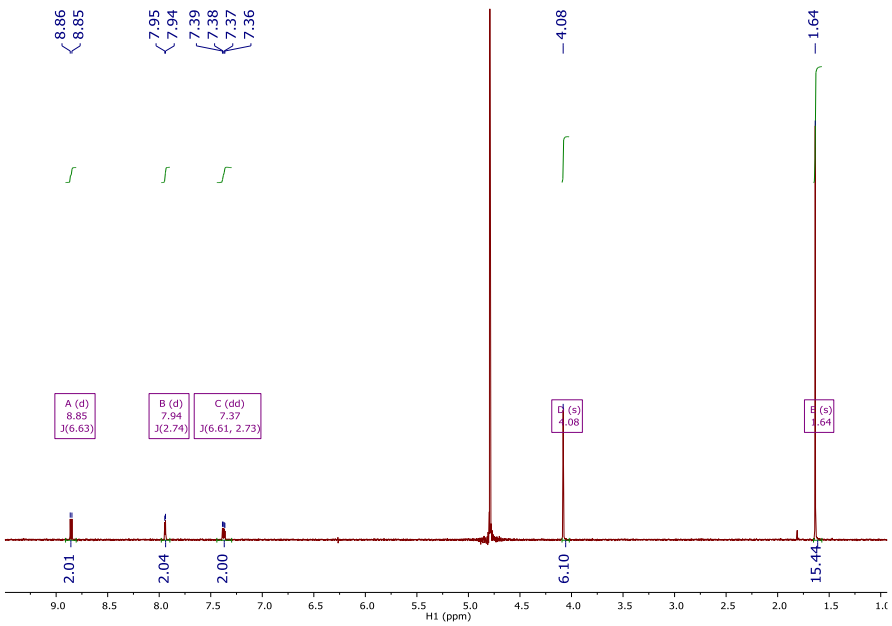

Figure C.1. ^{1}H NMR spectrum of [Cp*Ir(bpy-OMe)(H_2O)][OTf]$_2$ in D_2O.

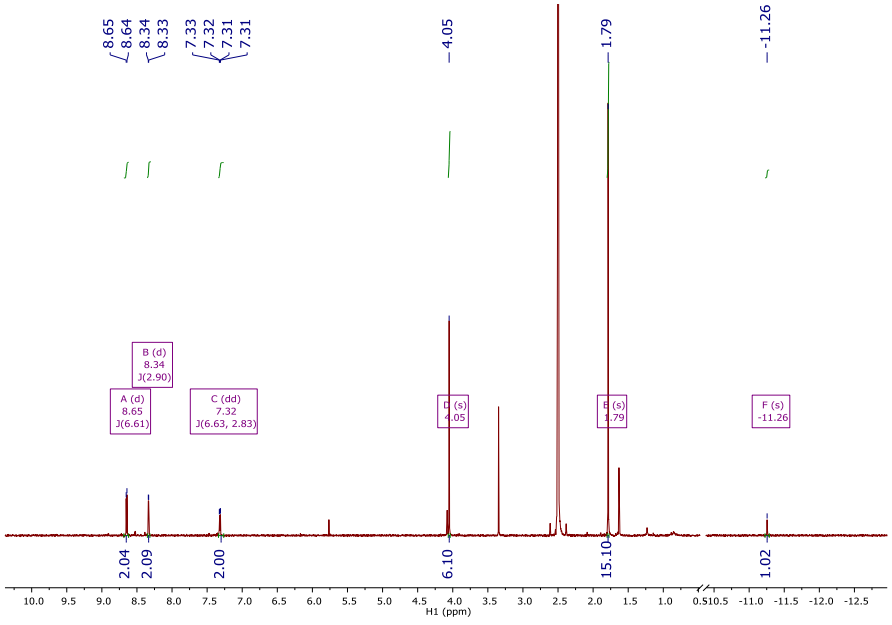

Figure C.2. ^{1}H NMR spectrum of [Cp*Ir(bpy-OMe)(H)][OTf] in DMSO-d_6.

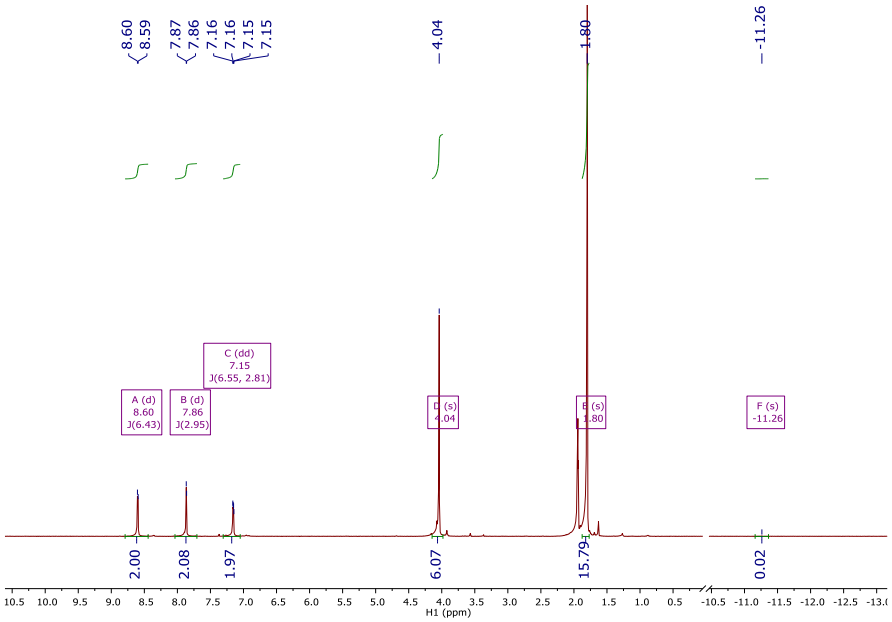

Figure C.3. ^{1}H NMR spectrum of [Cp*Ir(bpy-OMe)(D)][PF_6] in CD_3CN.

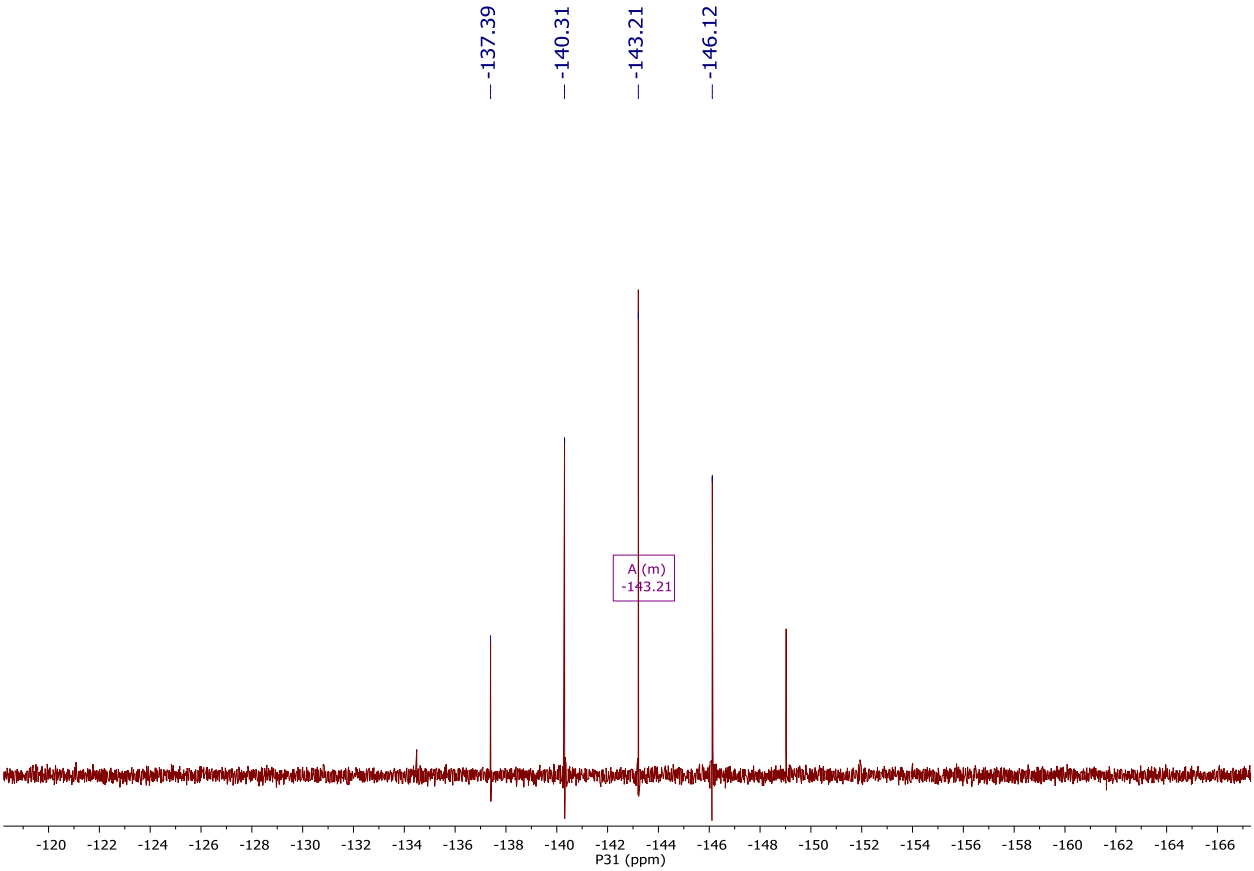

Figure C.4. ^{31}P NMR spectrum of [Cp*Ir(bpy-OMe)(D)][PF_6] in CD_3CN.